# Studies of turbulent burning rates and flame structures using 3D optical measurement techniques

---

By

Shaik Pervez Ahmed

MSc

Submitted in accordance with the requirements for the degree of Doctor of Philosophy

UNIVERSITY OF LEEDS

Institute of Thermo-fluids

School of Mechanical Engineering

September, 2019

## Intellectual Property and Publication Statements

The candidate confirms that the work submitted is his/her own, except where work which has formed part of jointly-authored publications has been included. The contribution of the candidate and the other authors to this work has been explicitly indicated below. The candidate confirms that appropriate credit has been given within the thesis where reference has been made to the work of others.

1- D. Bradley, M. Lawes, R. Mumby, Pervez Ahmed (2018), ‘‘The stability of laminar explosion flames’’, Proceedings of the Combustion Institute, 37(2), 1807-1813. *The Author of the present thesis provided the experimental data along with R. Mumby. Other Authors of this publication provided the technical discussions and guidance.*

2- D. Bradley, M. Lawes, R. Mumby, Pervez Ahmed (2018), ‘‘The stability of laminar explosion flames’’, 37th International Symposium on Combustion, Dublin, Ireland, 29th July -3rd August. *The Author of the present thesis provided the experimental data along with R. Mumby. Other Authors of this publication provided the technical discussions and guidance.*

3- Bradley, D., Shehata, M., Lawes, M., & Pervez Ahmed (2019), “Flame Extinctions: Critical Stretch Rates and Sizes”. (Submitted to Journal of Combustion and Flame journal, CNF-D-19-00657). *The Author of the present thesis provided the experimental data from swinging sheet technique. M. Shehata provided the schlieren experimental data and the other authors provided the technical discussions and guidance.*

4- Pervez Ahmed, Ben Thorne, Malcolm Lawes, (2019), “Development of Swinging Laser sheet technique to analyse 3D turbulent explosion flame structures”, (Internal Review). *The Author of the present thesis provided the experimental data from swinging sheet technique. Ben*

*Thorne provided technical assistance and the other authors provided the technical discussions and guidance.*

5- D. Bradley, M. Lawes, Pervez Ahmed (2019), “Experimental studies of burning rates of $n$-butanol/air mixtures”, (In preparation) *The Author of the present thesis provided the experimental data. Other Authors* provided the technical discussions and guidance.

6- Pervez Ahmed, Malcolm Lawes, Simone Hochgreb, (2019), “Three dimensional measurements of Surface Areas and Burning Velocities of Turbulent Spherical Flames”, (Submitted to the Proceedings of Combustion Institute). *The Author of the present thesis provided the experimental data from swinging sheet technique. Other authors provided the technical discussions and guidance.*

IN THE NAME OF ALLAH,

THE MOST GRACIOUS, THE MOST MERCIFUL

*In memory of my beloved mother,*

*Mehmooda Banu*

# Acknowledgements

I am grateful and thankful to Almighty Allah SWT for giving me the strength to pursue my PhD studies.

I would like to express my sincere gratitude to my supervisors Dr. Malcolm Lawes and Prof. Derek Bradley for their valuable guidance, advices and suggestions and their encouragement during my research. Also for their delightful farewell do treats, on the occasion of every colleague's PhD completion.

I would like to Thank The University of Leeds for funding my studies for three years. Also, Dr Malcolm Lawes for providing financial aid for the last few months.

I would like to thank the Laboratory staff Brian Leach, Mark Batchelor and Paul Banks for all their technical assistance in maintaining the experimental apparatus. I appreciate all their advices for safely handling the lasers.

Many thanks are due to colleagues Inna Gorbatenko, Dr Junfeng Yang for their inspiring conversations and Dr. Ben Thorne for giving a good introduction to experimental techniques. I really enjoyed it. Also, the discussions with Dr. Girish Nivarti are acknowledged.

I would like to acknowledge my friend and colleague Dr Moustafa Shehata for always being so warm whatever his circumstances. For all his help, discussions, the late nights tea and coffees and all the good times we spent in research.

I am truly grateful for my father and sister for their understanding, love and support, in particular my father without whose encouragement this journey would not have been possible. Finally, I would like to acknowledge my heartfelt appreciation for my wife and son, Ibrahim, for having the relentless patience and empathy to support me throughout my studies, to which I am indebted forever.

Thank You all

# Abstract

Burning velocities and Markstein numbers of premixed $n$-butanol explosion flames have been investigated under laminar and turbulent conditions at 360 K with pressures ranging between 0.1 to 1.0 MPa and equivalence ratios, $\phi$, from 0.7 to 1.4. For instabilities arising during laminar explosions, pressure dependencies were sought to exploit the leading role of the critical Peclet number in the phenomena. The critical Karlovitz number for flame stability decreased with increase in the strain rate Markstein number, $Ma_{sr}$. As a result, it is possible to predict the extent of the unstable regime for laminar flames as a function of $Ma_{sr}$ and pressure. It is shown that such data can be used to estimate the severity of large scale atmospheric explosions. For turbulent burning velocity, $u_t$, measurements, rms velocities, $u'$, between 0.5- 6.0 m/s were employed. Correlations of $u_t$ normalized by the effective rms turbulent velocity, $U$, were sought in terms of Karlovitz stretch factor, $K$, and the extent of validity of these correlations is extended to an $Ma_{sr}$ value of 9.

The present work also focuses on the development of a 3D swinging laser imaging technique to reconstruct 3D turbulent explosion flames. Experiments were conducted using $CH_4$ and $H_2$ air mixtures over a range of pressures, temperatures and $\phi$ covering different $Ma_{sr}$. Flame parameters such as total flame surface areas, $A$, and mean surface areas, $a$, were determined. Enhancement of the flame surface area, $A/a$, measured in both 2D and 3D is compared with the corresponding flame speed enhancement, $u_t/u_l$. As $K$ is increased, the 3D $A/a$ is unable to account entirely for the measured $u_t/u_l$ for negative $Ma_{sr}$ mixtures. For these mixtures, the discrepancy observed is tentatively explained by a theory based on turbulent diffusivity enhancement. Finally, quenched flame kernel mean diameters, $d_k$, are determined for a variety of fuels including $CH_4$, $H_2$, and $n$-butanol, at different $\phi$ and pressures. Normalised quenched flame kernel mean diameters, $d_k/\delta_k$, are correlated with $K$ and $Ma_{sr}$. Values of $d_k/\delta_k$ were found to increase with both $K$ and $Ma_{sr}$. The existing data on the onset of turbulent flame quenching are extended to higher $K$ and lower $Ma_{sr}$.

# Table of Contents

**Intellectual Property and Publication Statements** ..... **i**

**Acknowledgements** ..... **iv**

**Abstract** ..... **v**

**Table of Contents** ..... **vi**

**List of Figures** ..... **xi**

**List of Tables** ..... **xx**

**Nomenclature** ..... **xxi**

**Chapter 1 Introduction** ..... **1**

1.1 Foreword and overview ..... 1

1.3 Laminar premixed flames ..... 3

1.3.1 Flame radius and flame speed ..... 3

1.3.2 Flame stretch rate ..... 5

1.3.3 Laminar flame thickness ..... 8

1.3.4 Flame instabilities ..... 8

1.3.4.1 Development of flame instabilities ..... 10

1.4 Turbulent premixed flames and quenching ..... 11

1.4.1 Turbulent parameters and length scales ..... 12

1.4.2 Regimes in premixed turbulent combustion ..... 15

1.4.3 Turbulent burning velocities and their correlations ..... 17

1.4.4.1 Turbulent burning velocity definitions ..... 18

1.4.4.2 Correlations of turbulent burning velocity ..... 21

1.4.4 Flame quenching ..... 25

1.5 Review on burning velocities of *n*-butanol/air mixtures ..... 27

1.5.1 Laminar Flames ..... 27

1.5.2 Turbulent Flames ..... 28
1.6 Review on 3D analysis of turbulent flames ..... 30
1.7 Aims ..... 36
1.8 Thesis Outline ..... 37
**Chapter 2 Experimental Measurement Techniques ..... 38**
2.1 Combustion Vessel, CV, and ancillaries ..... 38
2.2 Ignition ..... 40
2.2.1 Spark Ignition ..... 40
2.2.2 Laser Ignition ..... 41
2.3 Diagnostic Techniques ..... 42
2.3.1 Pressure Measurement Technique ..... 42
2.3.2 Schlieren Imaging Technique ..... 43
2.3.2.1 Pixel size determination of the captured images ..... 44
2.3.3 3D Swinging Laser sheet Technique ..... 45
2.3.3.1 Optics for creating laser sheets ..... 47
2.3.3.2 Laser sheet geometry ..... 47
2.3.3.3 Synchronisation and control system ..... 52
2.3.3.4 Seeding particle generation ..... 55
2.4 Experimental Procedure ..... 56
2.4.1 Thermodynamic properties of all Fuel Mixtures ..... 58
**Chapter 3 Data Processing Techniques ..... 59**
3.1 Introduction ..... 59
3.2 Schlieren image processing ..... 59
3.2.1 Flame radius detection for laminar flames ..... 59
3.2.2 Flame speeds, laminar burning velocity, and Markstein length. ..... 62

3.2.3 Determination of Flame radius for turbulent flames ..... 62
3.2.4 Determination of turbulent flame speed and turbulent burning velocity ..... 62
3.2 Pressure Data Processing for Turbulent Burning Velocity ..... 64
3.3 3D swinging laser sheet image processing ..... 66
3.3.1 2D Laser Mie-scattered image processing ..... 66
3.3.2 3D flame reconstruction/assembly ..... 70
3.3.2.1 2D flame sheets assembly in a 3D matrix ..... 70
3.3.2.2 Interpolation, surface mesh generation and mesh smoothing ..... 70
3.3.3 3D reconstructed flame analysis ..... 73
3.3.3.1 Total flame surface area/ wrinkled flame area ..... 73
3.3.3.2 Validation of total flame surface areas using different geometries ..... 75
3.3.3.3 Calculation of mean flame area ..... 78
3.3.3.4 Calculation of burned gas volume ..... 81
**Chapter 4 Results ..... 82**
4.1 Introduction ..... 82
4.2 Laminar burning velocities, of *n*-butanol/air mixtures ..... 82
4.3 Laminar flame instabilities ..... 89
4.3.1 Critical Peclet number ..... 90
4.3.3 Onset of cellularity in terms of Critical Karlovitz number ..... 92
4.4 Turbulent burning velocities ..... 94
4.4.1 *n*-butanol/air mixtures ..... 94
4.4.1.1 Effect of *u'* on turbulent burning velocity ..... 99
4.4.1.2 Effect of pressure on turbulent burning velocity ..... 102

4.4.1.3 Effect of $\phi$ on turbulent burning velocity ..... 104

4.4.1.5 Enhancement of turbulent burning velocity ratio ... 109

4.4.2 $CH_4$/air and $H_2$ mixtures ..... 110

4.4.2.1 Enhancement of turbulent burning velocity ratio .. 114

4.5 3D turbulent flame results ..... 115

4.5.1 2D Mie-scattered images ..... 116

4.5.2 3D turbulent flame reconstructions ..... 120

4.5.3 Flame radius ..... 123

4.5.4 Flame Surface Area ratio ..... 130

4.5.4.1 Enhancement of flame surface area ratio ..... 135

4.6 Quenching of turbulent flames ..... 136

4.6.1 Flame quenching ..... 136

**Chapter 5 Discussions ..... 142**

5.1 Introduction ..... 142

5.2 Discussion of laminar burning velocities ..... 142

5.2.1 Comparison of $u_l$ with other studies ..... 142

5.3 Laminar flame instabilities ..... 144

5.4 Turbulent burning velocities: Comparisons and correlations ..... 154

5.4.1 Comparison of turbulent burning velocity of *n*-butanol with other hydrocarbons ..... 154

5.4.2 Correlations of $u_{tm}$ with $K$ ..... 157

5.5 3D turbulent flame structure analysis ..... 163

5.5.1 Analysis of raw flame images ..... 163

5.5.2 Flame surface area ratio ..... 164

5.5.3 Evaluation of probability of burning from 3D flame data .. 165

5.5.4 Evaluation of probability of burning from 2D flame sheets ..... 167

5.5.5 Proposed parameter Z ..... 170

5.6 Quenching of turbulent flame kernels ..... 173

5.6.1 Quenching of lifted jet flames ..... 174

5.6.2 Flame quenching on the *U/K* diagram ..... 175

**Chapter 6 Conclusions and Recommendations for Future Research ..... 179**

6.1 Laminar burning characteristics ..... 179

6.1.1 Flame Instabilities ..... 180

6.2 Turbulent burning characteristics ..... 180

6.3 3D flame surface area ratios ..... 181

6.4 Quenching of turbulent flames and extension of its limit on *U/K* diagram ..... 182

6.5 Recommendations for Future Research ..... 184

6.6 Summary of Conclusions ..... 185

**References ..... 186**

**Appendix A ..... 199**

**Appendix B Data Processing Algorithms in MATLAB ..... 206**

B.1 Turbulent Mass Burning Rate, $u_{tm}$, Code ..... 206

B.2 Total flame surface area and volume code ..... 207

B.3 Flame edge detector code ..... 208

B.4 Flame sheet assembly code ..... 209

B.5 polygon to voxel, Kroon D ..... 210

B.6 Mean flame area based on volume and mass balancing ..... 212

B.7 Strain rate Markstein number ..... 215

# List of Figures

Figure 1.1 Concentration and temperature profiles associated with one-dimensional, premixed adiabatic flame [22]. ..... 4

Figure 1.2 Structure of a wrinkled flame front showing the hydrodynamic streamlines and heat and mass diffusive fluxes [45]. ..... 9

Figure 1.3 Variation of $u'_k/u'$ with increasing $n_k$ for different $R_\lambda$ for *n*-butanol/air mixtures. ..... 15

Figure 1.4 Turbulent combustion regimes from Borghi [75] reproduced from [77]. ..... 17

Figure 1.5 Mie-scattered image showing the reference radii and masses of burned and unburned gas distribution [64]. ..... 19

Figure 1.6 Turbulent combustion regime as a function of $K$ and $Ma_{sr}$ [74]. ..... 23

Figure 1.7 Variations of $P_b^{0.5}$ as a function of $K$ and $Ma_{sr}$ [13]. ..... 25

Figure 2.1 Spherical stainless steel Leeds fan-stirred combustion vessel [150]. ..... 40

Figure 2.2 Spark plug assembly [152]. ..... 41

Figure 2.3 Top view of a laser ignition set up, all dimensions are in mm. ..... 42

Figure 2.4 Schematic diagram of the Schlieren imaging set up used in the present study, all dimensions are in mm. ..... 43

Figure 2.5 Image showing imprinted grid of 10 mm x 10mm on a transparent sheet. ..... 45

Figure 2.6 Schematic diagram of the 3D laser swinging sheet system. ..... 46

Figure 2.7 Top view of the mirror geometric offset and divergence of successive laser sheets. ..... 51

Figure 2.8 Synchronisation of all components for swinging sheet technique. ..... 54

Figure 2.9 Back view of an ignition laser controller showing the signals. .... 54

Figure 2.10 Signals involved during triggering of an experiment. ..... 55

Figure 3.1 Schlieren images of laminar $i$-octane/air flames at $\phi$ = 1.2, 0.5 MPa and 360 K. The time of each image from ignition within the captured sequence is shown. Cross symbol indicates the onset of cellularity. ..... 60

Figure 3.2 (a) Raw schlieren laminar flame image (b) Flame identification and spark plug masking (c) Identified flame edge shown as blue solid line and grey circle as best fit. Figure taken from Mumby [152]. ..... 61

Figure 3.3 (a) Raw schlieren image of a turbulent flame (b) Flame identification and spark plug masking (c) Identified flame edge shown as the boundary between white and black. ..... 63

Figure 3.4 Typical pressure record obtained during an explosion of $CH_4$/air, $\phi$ =1.25 at 365K and 0.5 MPa. ..... 64

Figure 3.5 Smoothed pressure/time data using Savitzky-Golay smoothing filter [9]. ..... 65

Figure 3.6 Calculated $u_{tm}$ against mean radius $r_m$ using four different frame lengths. ..... 66

Figure 3.7 (a) Raw Mie-scattered image (b) Binarised image. ..... 67

Figure 3.8 2D Mie-scattered images of flames at (a) $u'$=0.3 m/s, (b) $u'$=0.75 m/s, (c) $u'$=2.0 m/s. ..... 69

Figure 3.9 A view of the cross section through z-axis of (a) the assembled 2D sheets into 3D matrix with finite sheet spacing (b) the solid 3D flame structure after interpolation. ..... 71

Figure 3.10 3D reconstructed triangulated (a) unsmoothed (b) smooth surface mesh structure of a $CH_4$/air flame at $\phi$ =0.7, P=0.1 MPa, $T$=300K and at low turbulence of $u'$=0.3 m/s at 26.75 ms after ignition. ..... 72

Figure 3.11 Smoothed $CH_4$/air flame at $\phi$ =0.7, *P*=0.1 MPa, $T$=300K and at low turbulence of $u'$=0.3 m/s at 26.75 ms after ignition with (a) 2, 000,000 triangles (b) 20,000 triangles. ..... 74

Figure 3.12 Triangle with vertices P, Q and R and the vectors $a$ and $b$ resulting from PR and PQ respectively. ..... 74

Figure 3.13 Different geometries considered for validation of *A* (a) Sphere (b) Cylinder (c) Torus (d) Spheres on sphere (e) Symmetrical spinning top. Two views of the Symmetrical spinning top design are shown. ..... 77

Figure 3.14 Two different views of the same $CH_4$/air flame at $u'$=0.3 m/s, $\phi$ = 0.7, 300K and 01MPa. ..... 78

Figure 3.15 Variations of burned and unburned gas volume across $R_j$ with its increasing magnitude for the flame shown in Fig. 3.14. ..... 80

Figure 3.16 Variations of burned and unburned gas masses across $R_j$ with its increasing magnitude for the flame shown in Fig. 3.14. ..... 80

Figure 4.1 Measurements of a *n*-butanol/ air mixture at $T$=360 K and $P$ = 0.5 MPa (a) radius against time (b) flame speed against radius (c) flame speed against stretch. ..... 84

Figure 4.2 Variations of $S_n$, with $\alpha$, for different $\phi$ at 360 K for (a) 0.1 MPa (b) 0.5 MPa (c) 1.0 MPa. ..... 85

Figure 4.3 Variations of $ul$ with $\phi$ and $P$ for *n*-butanol/air mixtures at 360 K..... 88

Figure 4.4 Lewis numbers of *n*-butanol/air mixtures for different $\phi$..... 88

Figure 4.5 Variations of $L_b$, with $\phi$ and $P$ for *n*-butanol/air mixtures at 360 K..... 89

Figure 4.6 Variations of $Ma_{sr}$ with $\phi$ and $P$ for *n*-butanol/air mixtures at 360 K..... 89

Figure 4.7 Variations of $Pe_{cl}$, with $\phi$ and $P$ for *n*-butanol/air mixtures at 360 K..... 90

Figure 4.8 Variations of $Pe_{cl}$ with $Ma_b$ for *n*-butanol/air mixtures at 360 K. ..... 91

Figure 4.9 Variations of $Pe_{cl}$ variations with $Ma_b$ for propane/air mixtures at 360 K. ..... 92

Figure 4.10 Variations of $K_{cl}$ with $Ma_{sr}$ for *n*-butanol/air mixtures at 360 K. ..... 93

Figure 4.11 Variations of $K_{cl}$ with $Ma_{sr}$ for propane/air mixtures at 360 K. ..... 93

Figure 4.12 Flame radius with increasing time from ignition for different $u'$, at $\phi$ = 1 and 0.5 MPa, 360 K. ..... 95

Figure 4.13 Variations of $S_{sch}$ with increasing radii from ignition for different $u'$ at $\phi$ = 1 and 0.5 MPa, 360 K. ..... 96

Figure 4.14 Variations of $S_{sch}$ with increasing radius from ignition for different $u'$ at 360 K. ..... 97

Figure 4.15 Variations of $S_{sch}$ with increasing radii from ignition for different $u'$ at 360 K. ..... 98

Figure 4.16 Variations of $S_{sch}$ with increasing radii from ignition for different $u'$ at 360 K. ..... 98

Figure 4.17 Variations of $u_{tr}$ with increasing radii from ignition for different $u'$ at 360 K. ..... 99

Figure 4.18 Variations of $u_{tr}$ with increasing radii from ignition for different $u'$ at 360 K. ..... 100

Figure 4.19 Variations of $u_{tr}$ with increasing radii from ignition for different $u'$ at 360 K. ..... 101

Figure 4.20 Schlieren images of *n*-butanol/air mixtures at 0.5 MPa, 360 K $\phi$ =1.0 (a) $u'$ = 1.0 m/s (b) $u'$=6.0 m/s. ..... 101

Figure 4.21 Variations of $u_{tr}$ with increasing radii at 360 K $u'$=1.0 m/s (b) $u'$=2.0 m/s. ..... 103

Figure 4.22 Variations of $u_{tr}$ with increasing radii at 360 K. ..... 104

Figure 4.23 Variation of $u_{tr}$ with $\phi$ for *n*-butanol/air at $r_{sch}$ $rsch$= 30mm for different $u'$at 360 K (a) 0.1 MPa (b) 0.5 MPa (c) 1.0 MPa; solid line shows the best fit curve for the experimental data ..... 105

Figure 4.24 Variations of $u_{tr}$ with $u'_k$ for different $u'$ at 360 K. ..... 107

Figure 4.25 Variations of $u_{tr}$ with $u'_k$ for different $u'$ at $\phi$ = 0.8, 1.0, 1.2 and 1.4 at 0.5 MPa, 360 K. ..... 108

Figure 4.26 Variations of $u_{tr}$ with $u'_k$ for different $u'$ at $\phi$ = 0.7, 0.8 at 1.0 MPa, 360 K. ..... 108

Figure 4.27 Variations of $u_{tm}/u_l$ with $K$ for different $Ma_{sr}$ for *n*-butanol/air mixtures. ..... 109

Figure 4.28 Variations of $u_{tm}$ with $r_m$ for increasing $u'$ for $CH_4$/air at 365K, 0.5 MPa (a) $\phi$ =1.35 (b) $\phi$ =1.25. ..... 111

Figure 4.29 Variations of $u_{tm}$ with $r_m$ for increasing $u'$ for $CH_4$/air at 300K, 0.1 MPa (a) $\phi$ =1.3 (b) $\phi$ =0.7. ..... 112

Figure 4.30 Variations of $u_{tm}$ with $r_m$ for increasing $u'$ at 365K (a) $CH_4$/air $\phi$ =0.6, 0.1 MPa (b) $H_2$/air $\phi$ =0.3, 0.5MPa. ..... 113

Figure 4.31 Variations of $u_{tm}$ with $r_m$ for increasing $u'$ for $H_2$/air at $\phi$ =0.4, 0.5MPa, 365K. ..... 114

Figure 4.32 Variations of $u_{tm}/u_l$ with Karlovitz stretch factor, $K$ for the experimental conditions in Table 4.3. ..... 115

Figure 4.33 Set of raw flame image data in one sweep at one instant for $CH_4$/air, 300K, 0.1MPa, $\phi$ = 0.7, $u'$=0.3 m/s. ..... 118

Figure 4.34 Set of raw flame image data in one sweep at one instant for CH4/air, 300K, 0.1MPa, $\phi$ = 0.7, $u'$=1.5 m/s and 11.1 ms after ignition. ..... 119

Figure 4.35 3D reconstructed $CH_4$/air flames, $\phi$=0.7, 300K, 0.1 MPa with increasing time during an explosion at $u'$=0.3m/s. ..... 121

Figure 4.36 3D reconstructed $CH_4$/air flames, $\phi$=0.7, 300K, 0.1 MPa with increasing time during an explosion at $u'$=1.5m/s. ..... 122

Figure 4.37 $CH_4$/air flames at 0.5 MPa, 365K, $\phi$ = 1.35 (a) $r_v$ against time (b) $r_m$ against time for different $u'$. ..... 123

Figure 4.38 3D reconstructed $CH_4$/air flames, 0.1 MPa, 300K, $\phi$=0.7, 16.3 ms after ignition for three identical explosions, at $u'$=0.3m/s. .... 125

Figure 4.39 Comparison of $r_v$ and $r_m$ against time. ..... 126

Figure 4.40 Variations of $r_m$ against time for increasing $u'$ for $CH_4$/air at 365K, 0.5 MPa (a) $\phi$ =1.35, (b) $\phi$ =1.25..... 127

Figure 4.41 Variations of $r_m$ against time for increasing $u'$ at for $CH_4$/air at 300K, 0.1 MPa (a) $\phi$ =1.3 (b) $\phi$ =0.7..... 128

Figure 4.42 Variations of $r_m$ against time for increasing $u'$ at 365K (a) $CH_4$/air $\phi$ =0.6, 0.1 MPa (b) $H_2$/air $\phi$ =0.3, 0.5MPa..... 129

Figure 4.43 Variations of $r_m$ against time for increasing $u'$ for $H_2$/air, $\phi$ =0.4, 0.5 MPa, 365 K. ..... 130

Figure 4.44 Variations of $A/a_m$ with $r_m$ for increasing $u'$ for $CH_4$/air at 365K, 0.5 MPa (a) $\phi$ =1.35 (b) $\phi$ =1.25..... 131

Figure 4.45 Variations of $A/a_m$ with $r_m$ for $u'$ for $CH_4$/air at 300K, 0.1 MPa (a) $\phi$ =1.3 (b) $\phi$ =0.7. ..... 132

Figure 4.46 Variations of $A/a_m$ with $r_m$ for increasing $u'$ at 365K (a) $CH_4$/air $\phi$ =0.6, 0.1 MPa (b) $H_2$/air $\phi$ =0.3, 0.5MPa..... 133

Figure 4.47 Variations of $A/a_m$ with $r_m$ for increasing $u'$ for $H_2$/air at $\phi$ =0.4, 0.5MPa, 365K. ..... 134

Figure 4.48 Variations of $A/a_m$ with $K$ for the experimental conditions in Table 4.3. ..... 135

Figure 4.49 Radius against time for quenching of a $CH_4$/air kernel at 0.5 MPa and 365 K at $\phi$ =0.6. ..... 137

Figure 4.50 Temporal variation of $d/\delta_k$ and $u'_k$ from ignition for quenching of a $CH_4$/air kernel at 0.5 MPa and 365 K at $\phi$=0.6, $K$= 11.6 [172]. ... 138

Figure 4.51 Temporal variations of $d/\delta_k$ from ignition for $CH_4$-air at 365 K from (a) schlieren [172], and (b) laser swinging sheets. Complete mixture details on the figures. ..... 139

Figure 4.52 Temporal variations of $d/\delta_k$ from ignition for $H_2$/air at 365 K from laser swinging sheet 3D images, $u'$ = 0.75 m/s. Complete mixture details on the figures. ..... 140

Figure 4.53 Temporal variations of $d/\delta_k$ and $u'_k$ with time from ignition for *n*-butanol/air at 360 K, 0.5 MPa, $\phi$=0.7 and $u'$ = 2 m/s, $K$= 0.478, $p_{0.4}$..... 140

Figure 5.1 $u_l$, of *n*-butanol/air mixtures at 0.1, 0.5 and 1.0 MPa at 360 K. ..... 143

Figure 5.2 Variation of $u_l$ with $\phi$ and $P$ for *n*-butanol/air mixtures at 360 K. Symbols are experimental measurements, broken lines are the computed values using CHEMKIN [176] ..... 144

Figure 5.3 $Pe_{cl}$ variations with $Ma_b$ for different hydrocarbons and $H_2$ [171] at 0.1 MPa in the explosion vessel with data from large scale explosions [51-53]. Bold black symbols are Shell atmospheric explosions. ..... 145

Figure 5.4 $Pe_{cl}$ variations with $Ma_b$ for different hydrocarbon/air explosion vessel data. ..... 147

Figure 5.5 $K_{cl}$, expressed in terms of $Ma_{sr}$ for *n*-butanol/air (solid line) and ethanol/air [56] (broken line) mixtures. ..... 148

Figure 5.6 Values of $K_{cl}$ plotted against $Ma_{sr}$ for all hydrocarbon/air explosion vessel data. ..... 149

Figure 5.7 $K_{cl}$ variations with $Ma_{sr}$. Explosion vessel data for different hydrocarbon/air mixtures at different pressures. Crosses (0.1 MPa), open circles (0.5 MPa), filled squares (1.0 MPa). Solid curves shows best fits through these data. ..... 150

Figure 5.8 Solid curves show $K_{cl}$ variations with $Ma_{sr}$ from explosion vessel data at 0.1, 0.5 and 1.0 MPa alongside data for LS atmospheric explosions [51-53]..... 151

Figure 5.9 Comparison of $u_{tm}$, for ethanol (circles) at 358K, *n*-butanol/air (filled diamonds) [10] and $i$-octane/air (crosses) [68] at 360 *K* at $r_{sch}$ = 30mm against $\phi$ for different $u'$at 0.5 MPa. ..... 155

Figure 5.10 Strain rate Markstein numbers, $Ma_{sr}$ for ethanol (circles) at 358K, *n*-butanol [10] (filled diamonds) and $i$-octane/air (crosses, [68, 123]) flames at 360 K against $\phi$ at 0.5 MPa. ..... 156

Figure 5.11 $u_{tm}/u_l$ for ethanol (circles) at 358K, *n*-butanol [10] (filled diamonds) and $i$-octane/air (crosses, [68, 123]) flames at 360 K against $\phi$ at 0.5 MPa. ..... 156

Figure 5.12 Correlation of $u_{tm}/u'_k$ with *K* using schlieren experiments ..... 159

Figure 5.13 Correlation of $u_{tm}/u'_k$ with *K* using schlieren experiments (open triangles); and broken curve using the Eq.(1.48); solid curve shows the best fit for data from present schlieren experiments. ..... 160

Figure 5.14 $u_{tm}/u'_k$ plotted against *K* for positive $Ma_{sr}$..... 162

Figure 5.15 $u_{tm}/u'_k$ plotted against *K* for negative $Ma_{sr}$. ..... 162

Figure 5.16 Variations of $A/a_m$ with *K* for the experimental conditions in Table 4.3. ..... 165

Figure 5.17 Probability of burning, $P_b^{0.5}$, as a function of Karlovitz stretch factor, *K*..... 166

Figure 5.18 Flame surface area enhancement ratio, $A/a_m$ against, *K* using 2D flame data. ..... 168

Figure 5.19 Probability of burning, $P_b^{0.5}$, evaluated from 2D method, as a function of *K* ..... 169

Figure 5.20 $Z$ plotted against *K* for different $Ma_{sr}$. ..... 170

Figure 5.21 Symbols show probabilities of flame propagation for $d/\delta_k$ and $K$. Dotted curves show jet flame $D_b/\delta_k$ values at $U_b$* from [183]. Numbers adjacent to symbols are $p_b$ values. Flame quenching occurs beneath the curves. Symbols: △, for hydrocarbons, □, for $CH_4$, and, ○, for $H_2$, throughout the paper. ..... 175

Figure 5.22 Measured $K$ values at $p_{0.8}$ as a function of $Ma_{sr}$. Open symbols from [11], and solid symbols from the present study. ..... 176

Figure 5.23 $U/K$ diagram of showing regimes of turbulent combustion over a range of $Ma_{sr}$, including the new limits of quenching for $p_{0.8}$. Dashed curve is the limit reported in [74]. Symbols show the current experimental points. ..... 177

## List of Tables

Table 1.1 Some previous experimental studies of 3D imaging..... 34

Table 3.1 Total surface area, *A*, for different geometries considered..... 76

Table 4.1 Laminar flame properties at 0.1, 0.5, 1.0 MPa and 360 K. ..... 87

Table 4.2 Summary of experimental conditions at *T*= 360 K, *q* indicates flame quenching..... 95

Table 4.3 Experimental conditions for the present study, (+) represents the estimated value. (*) represents values from references for $u_l$ and $Ma_{Sr}$. ..... 110

Table 4.4 Experimental Quench Data [172]. ..... 141

Table 5.1 Experimental data sources for all the fuels used for laminar flame instabilities study ..... 153

Table 5.2 Data required for the analysis of present experimental study.... 172

# Nomenclature

| | | |
|---|---|---|
| $A$, $A_T$ | Total turbulent/wrinkled flame surface area | $m^2$ |
| $a$ | General turbulent mean flame surface area | $m^2$ |
| $a_m$, $a_v$ | Mean flame area based on mass and volume balancing respectively | $m^2$ |
| $A_m$ | Half the distance between RM parallel faces | m |
| $a_i$ | Geometric offset of each Imaging Laser | m |
| $\bar{c}$ | Reaction progress variable | - |
| $c_p$ | specific heat at constant pressure | J/kg.K |
| $D$ | Thermal diffusivity of the limiting reactant, flame average diameter, tube diameter | $m^2/s$ |
| $D_b$ | Limiting jet flame diameter at blow-off | m |
| $Da$ | Damköhler number | - |
| $d_f$ | Minimum waist diameter | m |
| $d_k$ | Mean diameter of a flame fragment | m |
| $f$ | Focal length | m |
| $f_{IL}$ | Imaging laser frequency | Hz |
| $f_s$ | Fan speed | rpm |
| $K$ | Karlovitz stretch factor | - |
| $Ka$ | Karlovitz number | - |
| $\bar{k}_{\eta k}$ | General dimensionless wave number | - |
| $k$ | Thermal conductivity of mixture | W/ m. K |
| $K_{ql}$ | Laminar flame extinction stretch factor = $\alpha_q \, \delta_l / u_l$. | - |
| $L$ | Integral length scale | (mm) |

| | | |
|---|---|---|
| $L_b$ | Burned gas Markstein length | m |
| $Le$ | Lewis number | - |
| $L_c$, $L_{cr}$ | Curvature Markstein length | m |
| $L_s$, $L_{sr}$ | Strain rate Markstein length | m |
| $m_b$ | Mass of burned gas | Kg |
| $m_u$ | Mass of unburned gas | Kg |
| $Ma_b$ | Burned gas Markstein number | - |
| $Ma_{sr}$ | Strain rate Markstein number | - |
| $Ma_{cr}$ | Curvature Markstein number | - |
| $n_k$ | Number of integral length scales | - |
| $n_f$ | Number of RM faces | - |
| $P$ | Pressure | MPa |
| $P_o$ | Initial pressure | MPa |
| $P_f$ | Peak pressure | MPa |
| $p_b$, $P_{bMa}^{0.5}$ | Probability of burning | - |
| $Pe$ | Peclet number | - |
| $r_u$ | Radius of cold front of flame | m |
| $r_{sch}$ | Schlieren radius | m |
| $r_{\bar{c}}$ | Radius at any value of $\bar{c}$ | m |
| $R_L$ | Integral scale Reynolds number | - |
| $R_\lambda$ | Taylor scale Reynolds number | - |
| $r$ | Radius of the flame kernel | m |
| $r_m$, $r_v$ | Mean flame radius based on mass and volume balancing | m |
| $R_r$, $R_t$, $R_j$ | root, tip and variable radius respectively | m |

| | | |
|---|---|---|
| $R_o$ | Inner radius of combustion vessel | m |
| $S_s$ | Unstretched laminar flame speed | m/s |
| $S$ | Flame speed factor | - |
| $\bar{S}(\bar{k}_\eta)$ | Non-dimensional power spectral density | - |
| $S_n$ | Stretched flame speed | m/s |
| $S_{sch}$ | Turbulent flame speed from schlieren | m/s |
| $T$ | Unburned gas temperature | K |
| $T_b$ | Burned gas temperature | K |
| $T_{ad}$ | Adiabatic flame temperature | K |
| $T_0$ | Preheat zone temperature | K |
| $t$ | time | s |
| $t_s$ | time between two sweeps | s |
| $t_{sIL}$ | time between two $IL$ successive sheets | s |
| $t_0$ | Initial time | s |
| $u_l$ | Unstretched laminar burning velocity | m/s |
| $u_\eta$ | Kolmogorov turnover velocity | m/s |
| $u_t$ | General turbulent burning velocity | m/s |
| $u'$ | RMS velocity | m/s |
| $u_n$ | stretched laminar burning velocity | m/s |
| $u_{tr}$, $u_{tv}$ | Turbulent burning velocity based on rate of production of burned gas | m/s |
| $u_{tm}$ | Turbulent mass burning rate | m/s |
| $u_{to}$ | Turbulent mass burning rate in absence of stretch | m/s |
| $u_k'$ | Effective rms turbulent velocity | m/s |

| | | |
|---|---|---|
| $U_b^*$ | Dimensionless flow number for flame blow-off in jets | - |
| $V$ | Total volume | $m^3$ |
| $v_i$ | Volume of voxel with index $i$ | $m^3$ |
| $X_m$ | Distance between centre of mirror face before and after rotation by $\theta_m$ | m |
| $Z$ | Proposed parameter | - |
| $z$ | Distance between mirror centreline and vessel | m |

**Greek**

| | | |
|---|---|---|
| $\alpha$ | Flame Stretch rate | $s^{-1}$ |
| $\alpha_s$ | Stretch rate due to strain | $s^{-1}$ |
| $\alpha_c$ | Stretch rate due to curvature | $s^{-1}$ |
| $\overline{\alpha}, \beta$ | Numerical constants | - |
| $\delta_l$ | Laminar flame thickness | m |
| $\delta_k$ | Preheat zone flame thickness | m |
| $\delta_t$ | Turbulent flame brush thickness | m |
| $\lambda$ | Taylor scale of turbulence | m |
| $\rho$ | Mixture density | $kg/m^3$ |
| $\varepsilon$ | Energy dissipation rate | $m^2/s^3$ |
| $\gamma_u$ | Unburned gas ratio of specific heats | |
| $\eta$ | Kolmogorov length scale | m |
| $\mu$ | Dynamic viscosity | N. s $/m^2$ |
| $\tau_\eta$ | Kolmogorov timescale | s |
| $\tau_c$ | Chemical time scale | s |

| | | |
|---|---|---|
| $\sigma$ | Unburned to burned gas density ratio | - |
| $\theta_m$ | Angle rotated by RM | radians |
| $\sum$ | Flame surface density | 1/m |
| $\Phi$, $\phi$ | Diameter, Equivalence ratio | m |
| $\rho_b$ | Burned gas density | kg/m$^3$ |
| $\rho_u$ | Unburned gas density | kg/m$^3$ |
| $\zeta_n$ | angle made by the $i^{th}$ sheet with the centreline of the CV | radians |
| $\nu$ | Kinematic viscosity | m$^2$/s |
| $\omega$ | rotating Frequency of mirror, perturbation growth rate parameter | radians/s |

**Subscripts and superscripts**

| | |
|---|---|
| $b$ | Burned |
| $cl$ | Critical value |
| $i$ | Inside, index |
| $l$ | Laminar |
| $m$ | Maximum value |
| $n$ | Stretched |
| $o$ | outside |
| $sch$ | Schlieren |
| $s$ | Unstretched |
| $t$ | Turbulent |
| $u$ | Unburned |

## Abbreviations

| | |
|---|---|
| ADC | Analogue to Digital Converter |
| CV | Combustion Vessel |
| CT | Computed Tomography |
| Nd:YAG | Neodymium Yttrium Aluminium Garnet |
| RM | Rotating mirror |
| DNS | Direct Numerical Simulation |
| EGR | Exhaust gas recirculation |
| FBE | Fibre-based endoscopes |
| HCCI | Homogeneous charge compression ignition |
| IL | Imaging laser |
| $I_gL$ | Ignition laser |
| LIF | Laser Induced Fluorescence |
| LII | Laser Induced Incandescence |
| LDV | Laser Doppler Anemometry |
| LES | Large Eddy Simulations |
| MRI | Magnetic Resonance Imaging |
| MRT | Minima reconstruction technique |
| PD | Photodiode detector |
| PIV | Particle Image Velocimetry |
| PLIF | Planar Laser Induced Fluorescence |
| TC | Tomographic chemiluminescence |
| UNFCCC | United Nations Framework Convention on Climate Change |
| VLIF | Volumetric Laser Induced Fluorescence |

# Chapter 1

# Introduction

## 1.1 Foreword and overview

Presently, emissions due to fossil fuels from engines and industries have become a major concern with respect to global warming and climate change. The Paris agreement on climate change that was sought within the United Nations Framework Convention on Climate Change (UNFCCC) in 2015 is to restrict the increase in global average temperature to below $2^0$C. Such issues of global warming provide exciting prospects for new fuels. As a result, a shift in research towards alternative fuels for energy supply has gained momentum [1, 2]. SHELL's carbon footprint programme [3] aims to achieve the UNFCC's target by reducing greenhouse gas emissions, by using renewable electricity, biofuels, and hydrogen, alongside oil and gas. In 2019, British Petroleum's (BP) Energy Outlook [4] reported measures to reduce greenhouse gas emissions by increasing the share of biofuels, up to 5%, in road transport and aviation sectors by 2040.

Biofuels, such as ethanol and $n$-butanol, are considered as promising alternatives with a higher efficiency and less pollution [5, 6]. In terms of future sources of viable energy, these are promising fuels with higher energy density [2], a higher calorific value and high octane numbers, almost comparable to those of gasoline, making them better alternative options in engines [2]. Engine operation will require little or no modification [7]. Among the many, $n$-butanol has some of the following advantages: lower vapour pressure reducing the chance of vapour lock and higher flash point (35 C), making it safer to handle. It is less hygroscopic making transportation easier with the existing pipelines, and is miscible with gasoline in any proportion [2].

Laminar burning velocities of conventional and alternative fuels are well understood through mathematical modelling, experiment, and long

experience. However, turbulent burning velocities of alternative fuels that approximately represent gasoline can have very different characteristics. If these fuels are to be efficiently used in engines, without loss of power and with reduced emissions, it is essential to improve fundamental understanding of their combustion process to generate accurate data on parameters that include burning rates, instabilities, stretch rate effects and flame structures.

Burning rates of turbulent premixed flames plays a significant role in many engineering aspects such as engines, gas turbines, furnaces, of energy demand [8, 9]. Although, these have been studied comprehensively for many decades, there are still unresolved questions. The effect of wrinkling on the flame structure in premixed turbulent flames is not fully understood and needs further investigation in terms of the flame surface areas, necessary to achieve faster burning rates. This is of direct relevance to engines [10-12]. Moreover, flame stretch rates influence turbulent burning velocities and a quantitative understanding of their effects is necessary in characterising turbulent flames [13]. To understand these fundamental properties, it is essential to look closely at the 3D structure of these turbulent premixed flames. Such knowledge of 3D structure can improve existing combustion devices and reduce exhaust gas emissions.

Laser techniques, with non-intrusive optical diagnostics offer flexibility in measurements, especially at high pressures and temperatures [14]. Various optical diagnostic techniques have been implemented in the combustion research, such as: Laser Doppler Velocimetry (LDV) [15], Mie scattering [16], Laser Induced Fluorescence (LIF) [17], Particle Imaging Velocimetry (PIV) [18], and the swinging Laser sheet technique [12].

The swinging laser sheet technique is a major focus in the present work. It is a unique technique that allows construction of an actual 3D flame surface revealing its structure and flame parameters such as surface area, reaction progress variable and flame surface densities that determine turbulent burning velocity, $u_t$. Calculating Markstein lengths, Markstein numbers, laminar burning velocities ($u_l$) also form part of the present study. Turbulent burning

rates of $n$-butanol are also investigated using the schlieren imaging technique. Moreover, flame quenching is not well understood and its limits to flame propagation are explored in fundamental terms involving limiting stretch rates and limiting flame kernel sizes. All these parameters are discussed in the following sections.

## 1.3 Laminar premixed flames

The laminar burning velocity is a fundamental characteristic of premixed combustion and is extensively used in the development of combustion engines. It is of vital importance in the understanding of the underlying combustion chemistry, the validation of turbulent combustion models and chemical kinetic mechanisms [19]. The unstretched laminar burning velocity, $u_l$, serves as a datum reference value in the analysis of pressure and temperature dependences for laminar and turbulent flames [20]. It is the velocity of the cold reactants, normal and into the plane that comprises the cold front of the flame [21]. It is dependent on the equivalence ratio, temperature and pressure of the mixture.

### 1.3.1 Flame radius and flame speed

Premixed homogenous mixtures of fuel and air, when centrally ignited, create an outwardly propagating spherical flame front burning in a thin reaction zone. Figure 1.1 shows concentrations of reactants, products and temperature profile through a one-dimensional, premixed, adiabatic flame. It is characterised by four zones. These are a cold reactant zone, pre-flame zone, a reaction zone, and a product zone [22]. In the pre-flame zone the reactants, at temperature $T_o$, are preheated through heat conduction, before further heating from chemical reaction. Chemical reaction and mass diffusion dominates the reaction zone. In this zone, the temperature increases further, and the chemical reaction rate rapidly increases due to the chain reactions causing a sharp density gradient across the flame front. Products appear at an adiabatic burned gas temperature, $T_b$, in the product zone.

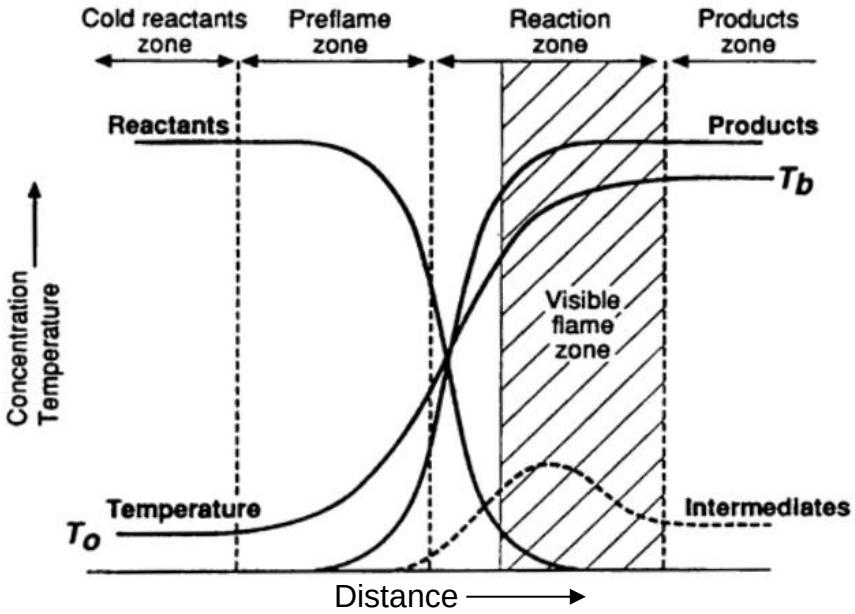


**Figure 1.1** Concentration and temperature profiles associated with one-dimensional, premixed adiabatic flame [22].

The increasing radius of the flame front can be captured using the schlieren imaging technique, described in Section 2.3.2, with an associated radius, $r_{sch}$. In their computational study of spherical flame propagation, Gu et al. [23] showed $r_u$ to be related to the flame front radius, $r_{sch}$, observed by schlieren imaging technique, by

$$r_u = r_{sch} + 1.95\,\delta_l \left(\frac{\rho_u}{\rho_b}\right)^{0.5}, \tag{1.1}$$

where $r_u$ is the cold front radius of the isotherm 5K above the temperature of the unburned reactants [21], $\rho_u$ the density of the unburned and $\rho_b$ that of the burned gas at the adiabatic flame temperature and $\delta_l$ is the laminar flame thickness, described in Section 1.3.3.

The unstretched flame speed, $S_n$, is calculated using $r_u$ with increasing time by [24]

$$S_n = \frac{dr_u}{dt} \tag{1.2}$$

Using the measured radius and calculated flame speed, parameters such as flame stretch and Markstein numbers, described in Section 1.3.2 can now be calculated.

### 1.3.2 Flame stretch rate

The flame stretch significantly affects both laminar and turbulent burning velocities [13, 21, 25]. It changes the total flame surface area, $A$, and the spatial distributions of temperature and species concentrations and, consequently, the burning velocity. For a spherically expanding laminar flame, $A = 4\pi r^2$, the total stretch rate is expressed in terms of $r_u$ and $S_n$ as [24, 26]

$$\alpha = \frac{1}{A}\frac{dA}{dt} = \frac{2}{r_u}\frac{dr_u}{dt} = \frac{2}{r_u}S_n. \tag{1.3}$$

A spherical flame is subjected to a total stretch, due to both curvature and strain rate [23, 27] and is given by

$$\alpha = \alpha_s + \alpha_c. \tag{1.4}$$

The flame stretch due to curvature at the cold front of a spherically outwardly propagating flame is given by [24]

$$\alpha_c = \frac{2u_n}{r_u}, \tag{1.5}$$

while that due to the flow field aerodynamic strain is given by

$$\alpha_s = \frac{2u_g}{r_u}. \tag{1.6}$$

Here $u_n$ is the stretched laminar burning velocity based on the propagation of the flame front, and $u_g$ the gas velocity due to the flame expansion at $r_u$ [24].

The flame speed $S_n$, is given by

$$S_n = u_g + u_n. \tag{1.7}$$

The effect of stretch on the laminar burning velocity is given by [27, 28]

$$u_l - u_n = L_c\alpha_c + L_s\alpha_s. \tag{1.8}$$

Here $u_n$ is the stretched laminar burning velocity based on the flame front propagation, $u_l$ is the unstretched laminar burning velocity, $\alpha_c$ and $\alpha_s$ are the stretch rates related to flame curvature and flow field strain and $L_c$ and $L_s$ are appropriate Markstein lengths. A measure of the influence of flame stretch rate upon the burning velocity for a stable flame is given by the Markstein numbers for strain rate and curvature [21, 29]. Dividing Eq. (1.8) by $u_l$ gives

$$\frac{u_l - u_n}{u_l} = K_c Ma_c + K_s Ma_s, \tag{1.9}$$

where $K_c = \alpha_c \delta_l / u_l$, *and* $K_s = \alpha_s \delta_l / u_l$ , are dimensionless stretch rates related to curvature and strain respectively while $Ma_c$ and $Ma_s$ are the corresponding Markstein numbers. For fully propagating flames, $Ma_s$ is usually dominant [30, 31].

The suffixes *s*, *c*, *n* in Eq. (1.8) are based on the rate of entrainment of cold unburned gas by the flame front. Alternatively, based on the rate of appearance of burned gas, a stretched burning velocity is represented by $u_{nr}$ and can be found using the equation given in [21]

$$u_{nr} = \frac{\rho_b}{\rho_u - \rho_b}(S_n - u_n). \tag{1.10}$$

These different stretched burning velocities arise as the rate of formation of burned gas is different from the rate of entrainment of unburned gas into the flame front for a spherical non-planar flame. Both $u_n$ and $u_{nr}$ when extrapolated to zero stretch should yield the same $u_l$ value as the flame spherical surface approaches a planar one. The associated Markstein lengths with $u_{nr}$ are indicated as $L_{sr}$ and $L_{cr}$ and are given by [21]

$$L_{sr} = (L_b - L_s)\frac{1}{(\rho_u/\rho_b) - 1} \tag{1.11}$$

and

$$L_{cr} = (L_b - L_c)\frac{1}{(\rho_u/\rho_b) - 1} \tag{1.12}$$

where $L_b$ is the burned gas Markstein length. These when divided by the laminar flame thickness, $\delta_l$, (See Section 1.3.3) yield associated Markstein

numbers $Ma_{sr}$ and $Ma_{cr}$ respectively. Values of $L_c$ and $L_s$ are obtained using multiple regression analysis, as detailed by Bradley et al. [21].

The extrapolation of $u_n$ through the stable flame regime to zero stretch yields $u_l$. Alternatively, the extrapolation of $S_n$ to zero stretch yields the unstretched flame speed, $S_s$. For cellular flames $S_s$ is obtained by extrapolating that part of the $S_n/\alpha$ curve prior to the onset of cellularity. The unstretched laminar burning velocity $u_l$ is then deduced from $S_s$ using the relation [21, 24]:

$$u_l = S_s \frac{\rho_b}{\rho_u}. \tag{1.13}$$

The relationship between $S_n$, $S_s$ and $\alpha$ is given as [28]

$$S_s - S_n = L_b \alpha, \tag{1.14}$$

The gradient of the best straight line fit to the experimental data in the $S_n/\alpha$ relationship gives $L_b$. Values of $u_l$ and $Ma_{sr}$ derived in this way, for the acquired data, are presented in Chapter 4.

Recent studies [18, 32] have shown that for heavy hydrocarbons such as $i$-octane, $n$-butanol, when the flame is stretched, the mean burnt gases temperature, $\bar{T}_b$, is not equal to the adiabatic temperature, $T_{ad}$. This is because of the effects of stretch and Lewis number, $Le$, on the adiabatic temperature, expressed in [32-34] as

$$\frac{\bar{T}_b - T_{ad}}{T_{ad}} = \left(\frac{1}{Le} - 1\right) \frac{D}{u_l} \alpha, \tag{1.15}$$

with $Le$ is the Lewis number of the limiting reactant, and $D$, the thermal diffusivity of the mixture. The effect of $\bar{T}_b < T_{ad}$ results in the mean burned gas density $\bar{\rho}_b$ to be greater than adiabatic burned gas density, $\rho_b$ i.e. $\bar{\rho}_b > \rho_b$. Therefore, to allow for this effect, laminar burning velocities, $u_l$, in the present study is calculated using the equation

$$u_l = S_s \frac{\bar{\rho}_b}{\rho_u}. \tag{1.16}$$

### 1.3.3 Laminar flame thickness

Various definitions of the laminar flame thickness have been suggested in the past [28, 35-37]. One based on hydrodynamic length has been used extensively and is given by [24, 38-40]

$$\delta_l = \nu/u_l, \tag{1.17}$$

in which $\nu$ is the kinematic viscosity of the unburned mixture and $u_l$ is the unstretched laminar burning velocity. This has been used in Section 4.2 and Sections 4.4 to 4.6. Because of the high diffusivity of hydrogen, a neglible chemically inert preheat zone exits in $H_2$ flames and the hydrodynamic definition of $\delta_l$ does not hold [41]. In theory [42], laminar flame thickness is characterised by Prandtl number, $Pr$ along with $\nu$ and $u_l$ and is given by

$$\delta_l = \delta_k = (\nu/u_l)/Pr, \tag{1.18}$$

where $Pr = C_p\mu/k,$ the Prandtl number. This definition has been used in Sections 4.3, 4.5-4.6.

### 1.3.4 Flame instabilities

Instabilities within the premixed laminar flame front can significantly affect the burning rate. A hydrodynamic theory of flame instabilities was first developed by Darrieus [43] and Landau [44] for a planar flame front. These hydrodynamics instabilities, also called D-L instabilities, are created by the propagation of a wave of density discontinuity due to flame interactions with hydrodynamic disturbances. Shown in Fig. 1.2 is the effect of such wave-like perturbation of a planar flame front. The disturbances occur within the reaction zone of a flame as a result of hot expanding products and generated vortices that converge and diverge the streamlines of oncoming unburned gas creating a wrinkled flame front [45]. If the flame front were to be stretched positively, it would have a neutralising effect on the developing instability. This can be partially neutralized by thermo-diffusive transport mechanisms comprising heat and mass fluxes, also indicated in Fig. 1.2. The heat flux from burned to

unburned mixture is shown by a solid arrow, while the mass diffusive flux of the limiting reactant from unburned to burned gas is shown by a broken line. The contribution of these fluxes is expressed by the Lewis number, $Le = k/\rho C_p D$ with $k$ the conductivity, $D$ the diffusive coefficient of the limiting reactant and $C_p$ the specific heat at constant pressure. Depending upon the value of $Le$, these fluxes, combined with the D-L instability, either stabilise or destabilise the flame front. For $Le < 1$, mass diffusive fluxes dominate over heat fluxes and are indicative of an unstable flame. Increased energy is converged at the crest of the flame front and the local burning velocity increases, while a contrary effect occurs in the trough, decreasing the burning velocity and local temperature due to diverging gas flow. As a result, the deformation increases and the flame becomes more unstable. On the other hand, for $Le > 1$, the D-L instability is neutralised by thermo-diffusive effects, that results in a reduced burning velocity at the crest of the flame front, thereby stabilising the flame.

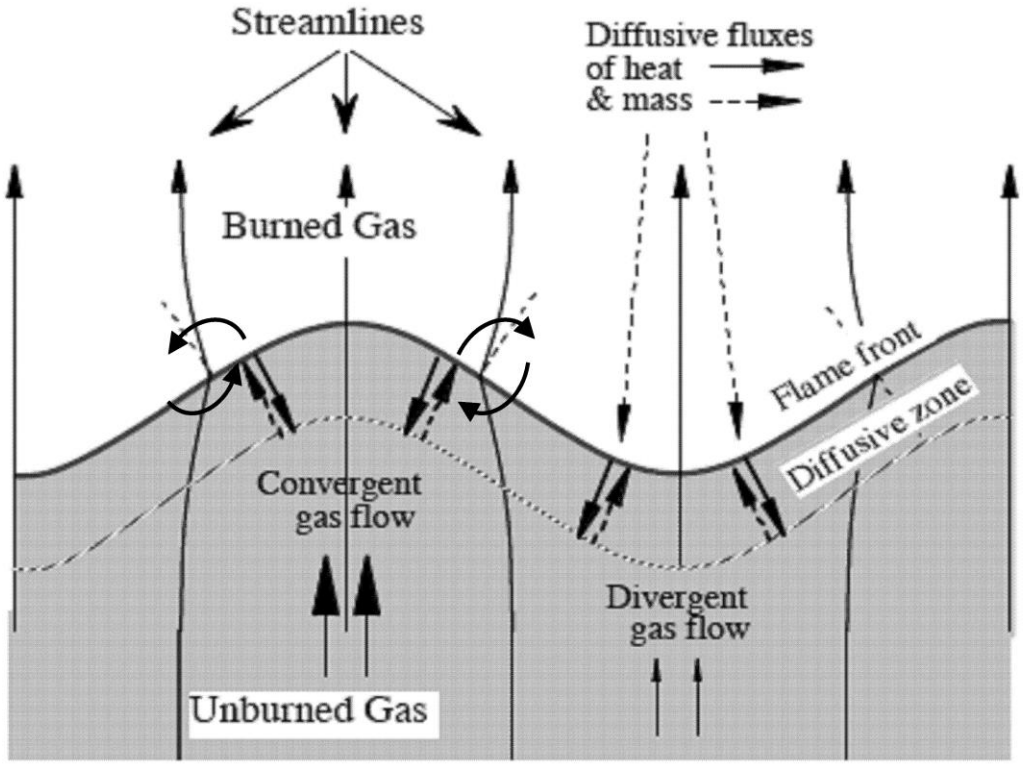


**Figure 1.2** Structure of a wrinkled flame front showing the hydrodynamic streamlines and heat and mass diffusive fluxes [45].

#### 1.3.4.1 Development of flame instabilities

The flame stretch rate decreases as the flame propagates, and when it falls below a certain threshold, the interactions of the D-L and thermo-diffusive instabilities create increasingly severe wrinkling of the initially smooth laminar flame surface, accelerating the flame speed and strengthening the associated pressure pulse, that arises from the rate of change of the heat release rate [46].

An important question is whether the wrinkled flame acceleration might lead to a detonation. The mathematical modelling of the increasing wrinkling of the flame surface, and the increasing flame speed present a severe challenge. Complete numerical simulations have only been possible up to a radius of a few cm. Consequently, semi-theoretical studies have involved a combination of fractal analyses [47, 48] and experiments [23, 24, 49, 50], some of which, in larger atmospheric explosions, have involved flame sizes of several metres [51-53]. Sivasinsky and co-workers [54, 55] have developed a mathematical technique that involves multiplying the reaction rate with a degree of folding of the wrinkled flame front.

A key parameter is the critical flame radius, $r_{cl}$, that marks the onset of the D-L and thermo-diffusive instabilities in flames, with developing cellularity and an increasing flame speed, $S_n$. It is defined by the change in the gradient in $S_n/\alpha$ plot. The appropriate dimensionless radius is the Peclet number, $Pe_{cl}$, comprised of $r_{cl}$, normalised by the laminar flame thickness, $\delta_l$.

The theoretical approach in [42] expresses the growth rate of the amplitude of the flame front perturbation, *A(n)*, for a given wave number, *n*, as:

$$A(n) = \omega\left(1 - (Pe_{cl}/Pe)\right). \tag{1.19}$$

*Pe,* the general Peclet number, is the flame radius, $r_u$, normalised by $\delta_l$, and $\omega$ is a perturbation growth rate parameter that depends upon *n*. As the flame grows, with $Pe < Pe_{cl}$ *A(n)* is negative, the amplitude diminishes, and the flame is stable. When $Pe > Pe_{cl}$, the sign becomes positive and the flame

becomes unstable. The relative contributions of the D-L and thermal diffusive instabilities to *A(n)* are in the ratio $(Pe_{cl}/Pe)$. The flame stability is increased by increases in strain rate Markstein number, $Ma_{sr}$, and $\sigma$, the ratio of unburned to burned gas density.

The creation of cells only occurs when the localised flame stretch rate at the cell surface is sufficiently reduced to allow the growth of an instability of shorter wavelength. The onset of cell formation at $Pe_{cl}$, provides the limiting stretch rate, below which flame wrinkling occurs. The critical Peclet number is a convenient measure for the onset of instability, and is associated with the flame stretch rate, $\alpha_{cl}$, multiplied by the chemical time, $(\delta_l/u_l)$, yielding a critical Karlovitz number, $K_{cl}$. For a spherical premixed laminar flame, this is expressed by [56]:

$$K_{cl} = (2\sigma/Pe_{cl})[1 + (2Ma_b/Pe_{cl})] - 1. \quad (1.20)$$

Here $Ma_b$ is the burned gas Markstein number, like $Pe_{cl}$, readily measurable. At normalised stretch rates below $K_{cl}$, the flame becomes unstable. Further details are provided in [24, 56], whilst Gaseq [57] provides data for evaluations of $Pr$ and $\delta_l$. The results of measured $K_{cl}$ are presented in Chapter 4.

## 1.4 Turbulent premixed flames and quenching

Mallard and Chatelier [58] recognised first the influence of turbulence on burning velocity of premixed flames. Later, Damköhler [59] envisaged turbulent flames as wrinkled laminar flames and highlighted the importance of eddy to chemical life time. He proposed that the large turbulent eddies wrinkle the flame front causing an increase in flame surface area and consequently the burning rate. The small scale turbulence only increase the transport properties within the reaction zone. It was concluded that turbulent burning velocity, $u_t$, is proportional to turbulence. He expressed the ratio of turbulent to laminar burning velocities in terms of ratio of total flame surface area and mean flame area. Because of the complexities of turbulent burning, it has

been the subject of extensive investigation in more recent times [10, 11, 60-67].

### 1.4.1 Turbulent parameters and length scales

For calculating $u_t$ of any reactive mixture, its laminar flame properties such as $u_l$, $\delta_l$, and turbulent flow field parameters such as rms turbulent velocity, $u'$ and turbulent scales must be known [68]. The turbulent flow is characterised by three length scales namely integral scale, $L$, Taylor scale, $\lambda$, and Kolmogorov scale, $\eta$. Integral length scale is the near largest scale while Kolmogorov scale is the smallest [69]. The integral length scales for the Leeds fan stirred Combustion vessel, CV, were determined by LDV and were found to be 20±1mm, are independent of fan speed between 1-6 m/s. However, at low fan speeds it measured 24 mm [15]. The turbulent length scales at different rms turbulent velocity and at different pressures are found in [68]. The Kolmogorov scale [40, 69] is the scale at which the turbulent kinetic energy is dissipated as heat by molecular viscosity. It is given by

$$\eta = (\nu^3/\varepsilon)^{0.25}, \tag{1.21}$$

where, $\nu$, is the kinematic viscosity and $\varepsilon$ , is the dissipation rate. The Taylor scales, $\lambda$, lies between the integral and the Kolmogorov scale, and is calculated from [70]:

$$\lambda = 15^{0.25} R_\lambda^{0.5} \eta. \tag{1.22}$$

where $R_\lambda$ is the Taylor scale Reynolds number given by

$$R_\lambda = u'\,\lambda/\nu, \tag{1.23}$$

The turbulent Reynolds number, based on $L$, is defined as

$$R_L = u'\,L/\nu\,. \tag{1.24}$$

Integral and Taylor length scales for isotropic turbulence, are related by

$$\frac{\lambda}{L} = \frac{A}{R_\lambda}. \tag{1.25}$$

Here $A$ is a numerical constant, $A$ = 16±1.5 [70]. From Eqs. (1.23) to (1.25):

$$R_\lambda^2 = AR_L, \tag{1.26}$$

With A = 16 Eq. (1.26) is expressed as:

$$R_\lambda = 4R_L^{0.5}, \tag{1.27}$$

An important dimensionless group based on the ratio of eddy lifetime to chemical lifetime is the Damköhler number, $Da$, given by

$$Da = (L/u')/(\,\delta_l/u_l). \tag{1.28}$$

The reciprocal of $Da$ is known as the Karlovitz stretch factor,$K$, given by

$$K = (\delta_l/u_l)/(\,\lambda/u'). \tag{1.29}$$

Eddy lifetime might also be expressed as the reciprocal of mean strain rate, $u'/\lambda$, and is defined by Taylor [71] as a function of the energy dissipation rate, $\varepsilon$, by

$$(u'/\lambda)^2 = \ \varepsilon/15\nu. \tag{1.30}$$

With $\delta_l = \nu/u_l$,and A $= 16$, $K$ is expressed as [72]

$$K = 0.25\left(\frac{u'}{u_l}\right)^2 R_L^{-0.5}. \tag{1.31}$$

If $K$ is small, the chemical reaction occurs within an eddy, and when it is large it is not completed during the eddy lifetime. This results in flame quench, discussed in Section 1.4.4.

Another dimensionless parameter for stretch is based on the turbulent length, $\eta$, and velocity scale, $u_\eta$, yielding a Karlovitz number, $Ka$ [8, 66] given by:

$$Ka = \frac{\delta_l/u_l}{\eta/u_\eta}, \tag{1.32}$$

where $u_\eta$ is the turnover velocity on the Kolmgorov scale, given by:

$$u_\eta = u'\,15^{1/4}/R_\lambda^{1/2}. \tag{1.33}$$

These correlations have been used by many researchers [10, 13, 68, 73, 74] to correlate turbulent burning velocities. To correlate turbulent burning velocities at a given instant, for a given rms turbulent velocity, $u'$, the effective rms turbulent velocity, $u_k'$ must be known. Calculating $u_k'$ for a given $u'$ is presented in the following section.

### 1.4.2 Variation of $u_k'$ through an explosion

For an established flame kernel, turbulent burning velocity, $u_t$, increases with flame radius. This is because as the flame propagates, it is wrinkled by increasing wavelengths of turbulence. As a result, the effective rms turbulent velocity, $u_k'$, is less than rms turbulent velocity, $u'$ [23]. As $u_k'$ approaches $u'$ the flame grows large enough to engulf the entire turbulent spectrum. The process of calculating $u_k'$ for a given range of wavelengths is detailed in [10]. The values of $u_k'$ during the propagation of a flame in an explosion is given by integrating the entire non-dimensional power spectral density, $\bar{S}(\bar{k}_\eta)$, over the range of wavelengths as [10]

$$u_k' = u' \left[ \frac{15^{0.5}}{R_\lambda} \int_{\bar{k}_{\eta 1}}^{\bar{k}_{\eta 2}} \bar{S}(\bar{k}_\eta) d\bar{k}_\eta \right]^{0.5} \tag{1.34}$$

$$\text{where } \bar{S}(\bar{k}_\eta) = \frac{0.01668R_\lambda^{2.5} + 3.74R_\lambda^{0.9} - 70R_\lambda^{-0.1}}{1 + (0.127R_\lambda^{1.5}\bar{k}_\eta)^{5/3} + (1.15R_\lambda^{0.622}\bar{k}_\eta)^4 + (1.27R_\lambda^{0.357}\bar{k}_\eta)^7}. \tag{1.35}$$

$\bar{k}_\eta$ is a dimensionless wavenumber, defined by $2\pi$/wavelength multiplied by $\eta$. The lower, $\bar{k}_{\eta 1}$, and the upper limits, $\bar{k}_{\eta 2}$, in the above integral are associated with the largest and the smallest possible wavelengths that can be evaluated using the general wave number, $\bar{k}_{\eta k}$ expression given by [10]

$$\bar{k}_{\eta k} = \frac{2\pi\eta}{n_k L} = \left( \frac{32\pi}{15^{0.25} n_k} \right) R_\lambda^{-1.5}. \tag{1.36}$$

Here $n_k$ is given by $n_k = 2r_{0.5}/L$, where $r_{0.5}$ is the mean flame radius. Typical values of $u_k'/u'$are plotted against increasing $n_k$ in Fig. 1.3 for different $R_\lambda$ values, associated with $R_L$ and $u'$. The maximum value of $u_k'/u' = 0.81$ corresponds to a value of $n_k$ slightly greater than 6. It is suggested in [10] that the value of $n_k$ for a non-quenching flame at the onset of developed linear regime is about 2. Therefore, for flame analysis at a value of $n_k$ above 2 should

well quantify the present experimental results. Values of $u_k'$ are used in correlations presented in Chapters 4 and 5.

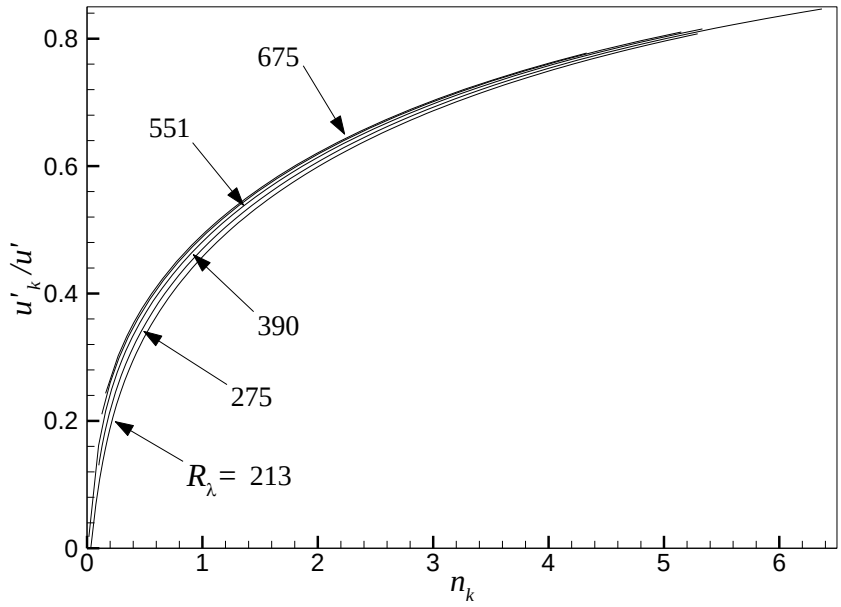


**Figure 1.3** Variation of $u'_k/u'$ with increasing $n_k$ for different $R_\lambda$ for *n*-butanol/air mixtures.

### 1.4.2 Regimes in premixed turbulent combustion

Much of our present understanding of turbulent flames is based on the laminar flamelet approach. Various combustion regime diagrams have been proposed [26, 38, 75, 76] to describe the interaction of flame and turbulent eddies. One of the best known is that of Borghi [75], the Borghi diagram. It employs the ratios $u'/u_l$ and $L/\delta_l$, as shown in Fig. 1.4, to identify the various premixed combustion regimes.

*(i) Laminar flame regime*

Where $R_L < 1$. $u'/u_l$ is low and $L/\delta_l$ is small. The flow is laminar. The line denoted by $R_L$=1, separates laminar and turbulent flames.

*(ii) Flamelet regime*

Where $Ka < 1$. In this regime, the chemical time scale, $\delta_l/u_l$, in Eq. (1.32), is smaller than the Kolmogorov time, $\eta/u_\eta$. There is little wrinkling and no effect on flame inner structure. The flame thickness is

smaller than the smallest turbulent scale $\eta$ [26]. This regime is further divided into two parts

a. *Wrinkled flamelet regime*

Where $u'/u_l < 1$, the eddy turnover velocity is small, and the flame structure is slightly wrinkled as it traverses through these eddies.

b. *Corrugated flamelet regime*

Where $u'/u_l > 1$, the eddy turn over velocity increases and the flame surface becomes highly convoluted upon passing them. Nevertheless, $Ka$ is still lower than unity and the flame retains its laminar flame characteristics.

*(iii) Distributed reaction zone or thickened flame regime*

Where $Ka > 1$ and $Da > 1$. In this regime $L/u' > \delta_l/u_l > \eta/u_\eta$. Chemical reaction cannot be completed during the smallest eddy lifetime. The smallest eddies can penetrate the preheat zone thickness and some pockets of fresh and burnt gases are formed. The boundary between the corrugated flamelets regime and distributed reaction regime is characterised by $Ka$=1, Klimov-williams criterion [26] where the flame thickness is equal to $\eta$.

*(iv) Well stirred reactor regime*

Where $Ka \gg 1$ and $Da \leq 1$. In this regime $\delta_l/u_l > L/u' > \eta/u_\eta$. I in this regime chemical, lifetime is longer than the turbulent scales. The smallest eddies can penetrate the reaction zone thickness and enhancing diffusion and hence energy transfer rates.

In the present work, the flamelet, distributed and well stirred reaction zones are of interest.

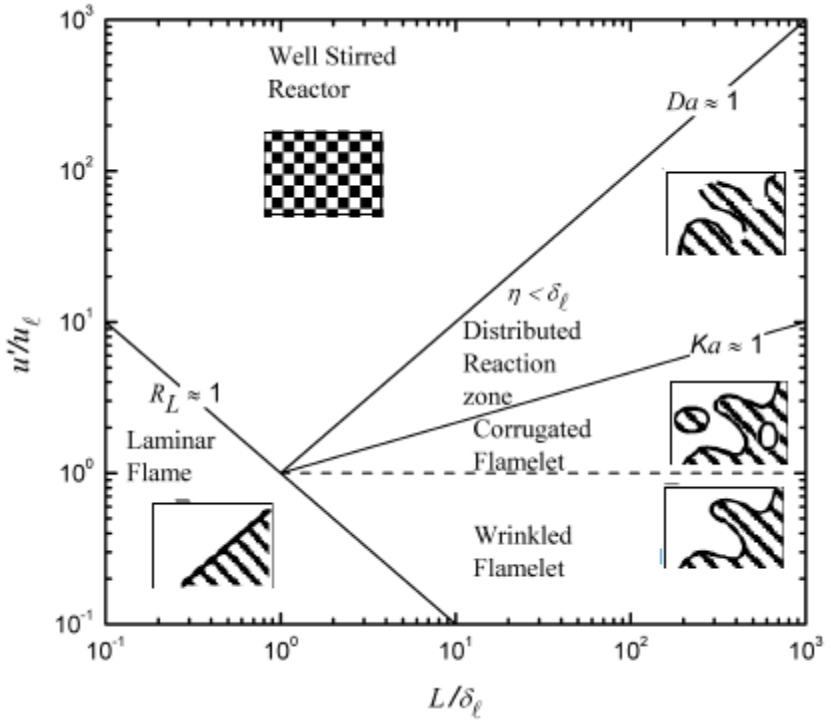


**Figure 1.4** Turbulent combustion regimes from Borghi [75] reproduced from [77].

### 1.4.3 Turbulent burning velocities and their correlations

Turbulent burning velocities, $u_t$, are of vital importance in determining the combustion characteristics of premixed turbulent flames which are highly wrinkled and stretched. These are defined based on either engulfment of unburned gas or the rate of production of burned gas [21]. Defining and accurately measuring $u_t$, remains one of the most serious challenges in combustion [11, 19, 61, 78]. Problems arise from the number of variables associated with it. For example the mass burning rate, which is based on mass rate of production of burned gas, is a function of the density, burning rate and the flame area, and any variation in these parameters, causes a change in its value [64].

Damköhler [59] introduced the concept of an instantaneous wrinkled turbulent flame surface to define $u_t$. The mean turbulent flame front was used to measure burning velocity relative to the unburned mixture. Turbulent burning velocities are directly affected by the structure of the turbulent flame and the total flame surface area that is available at a wrinkled laminar front [10, 11].

The mean flame area to be associated with $u_t$ must be carefully characterised. Many definitions of $u_t$ and the associated turbulent flame surfaces have been presented [10, 11, 60-67]and reviewed [79-81].

The influence of flame chemistry on turbulent premixed flames is usually expressed through parameters such as $u_l$, in laminar flamelet models, and Markstein number that describes the influence of stretch rates, due to molecular thermal-diffusive processes, on flame propagation [64, 82, 83]. Other physical parameters influencing $u_t$ include $u'$ and length scales of turbulence [11, 61, 62, 84]. Since, $u_t$, is an elusive parameter [68], many correlations and empirical formulae have been suggested to calculate it.

It is well established that for low to moderate turbulence $u_t$ increases linearly with $u'$ as a result of increased flame surface area [59]. At very low turbulence the role of laminar flame instabilities cannot be neglected, and this is further discussed in Chapter 6. With further increase in turbulence, the rate of increase of $u_t$ with $u'$ decreases and reaches a maximum followed by a decrease in what is called the bending phenomenon [60, 85]. Such a reduction has been attributed to increased local flame quenching due to excessive stretch [62, 67] and probably by merging of flamelet surfaces [61].

#### 1.4.4.1 Turbulent burning velocity definitions

The choice of mean flame radius is crucial and significantly affects $u_t$. Many definitions based on the associated flame front surfaces, located within the turbulent flame brush, have been presented to express the mean rate of burning. In general, a particular surface in the turbulent flame brush is identified based on the reaction progress variable, $\bar{c}$. This ranges from $\bar{c}$=0 in unburned gas to $\bar{c}$=1 in fully burned gas. Bradley et al. [64] measured turbulent mass burning velocities and flame speeds associated with different surfaces using schlieren imaging and Mie-scattering laser sheet images where $\bar{c}$=0.34.

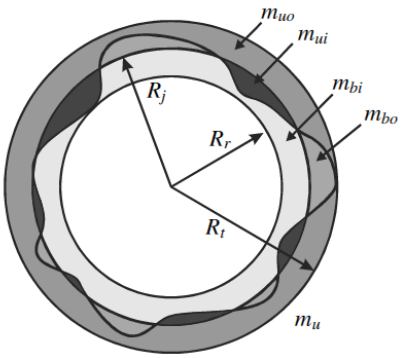


**Figure 1.5** Mie-scattered image showing the reference radii and masses of burned and unburned gas distribution [64].

With respect to the burned and unburned gas distribution in a Mie scattering image, three radii were defined as shown in Fig. 1.5. $R_t$ and $R_r$ represents the outermost tip and the innermost root radius, respectively, while $R_j$ is any general radius. $m_{bi}$, $m_{bo}$, $m_{ui}$, $m_{uo}$ represents the masses of burned and unburned gases inside and outside the general radius $R_j$. The subscripts '*b*' stands for burned, '*u*' for unburned, '*i*' for inside and '*o*' for outside. In the present study, $R_j$ is taken as a mean of the root and the tip radius, for calculating $u_t$, where the mass of unburned gas inside is equal to the mass of burned gas outside it. It was concluded from their study [64] that when the general radius $R_j$ is equal to a radius, $r_v$, at which the total volume of burned gas outside the sphere is equal to total volume of unburned gas inside it, $m_{ui}/\rho_u = m_{b0}/\rho_b$, then $u_t$ is given by [64]

$$u_{tr}(r_v) = \frac{\rho_b}{\rho_u}.\frac{dr_v}{dt}. \tag{1.37}$$

However, because it is more convenient to use schlieren images than Mie scattering sheets to derive $u_t$, an expression based on schlieren radius, $r_{sch,}$ is preferred. Consequently, this radius must be related to $R_j$. In [64] it was shown that a linear relationship exists between, $(\rho_b/\rho_u)(dr_{sch}/dt)$, calculated from schlieren experiments, and $u_{tr}(r_v)$ from Mie scattering whose gradient yields the expression for the mass burned turbulent burning velocity :

$$u_{tr} = u_{tr}(r_v) = u_{tv} = \frac{1}{1.11}\frac{\rho_b}{\rho_u}\frac{dr_{sch}}{dt} \tag{1.38}$$

This equation is employed in Section 4.4. Also, as discussed in Section 1.3.2, the turbulent burning velocities in Eqs. (1.37) and (1.38) are corrected for strain rate and $Le$ number effects simply by replacing $\rho_b$ with $\bar{\rho}_b$ evaluated at mean burned gas temperature, $\bar{T}_b$.

*Turbulent burning velocity from pressure records, $u_{tm}$*

For measurements of $u_t$ solely based on pressure records, a convenient radius is one where $R_j = r_m$ defined as $m_{ui} = m_{b0}$. The turbulent mass burning rate at $r_m$ is defined as $4\pi r_m^2 u_{tm} \rho_u$, where $u_{tm}$ is the mass based turbulent burning velocity [10].

It is usually assumed that the fractional pressure rise proportional to fractional mass burned [86]

$$m_b = (m_u + m_b)\left(\frac{P-P_0}{P_f-P_0}\right), \tag{1.39}$$

where $m_u$ and $m_b$ are the masses of all unburned and burned gas, $P_0$ and $P_f$ are the initial and peak pressures respectively. Bradley and Mitcheson [87] expressed this pressure rise as an equivalent sphere of radius $r_m$ within which all the gas is burned and outside which it is unburned and is given by

$$r_m = R_0\left\{1 - \left(\frac{P_0}{P}\right)^{1/\gamma_u}\left[\frac{P_f-P}{P_f-P_0}\right]\right\}^{1/3}. \tag{1.40}$$

Here $R_0$ is the combustion vessel radius, $\gamma_u$ is the ratio of specific heats for the unburned mixture. It is reported in [10] that the value of $\bar{c}$ at $r_m$ is evaluated as approximately 0.56. The associated turbulent burning velocity, $u_{tm}$, is given by

$$u_{tm} = \frac{R_0\left(\frac{P_0}{P}\right)^{1/\gamma_u}\frac{dp}{dt}}{3(P_f-P_0)\left\{1-\left(\frac{P_0}{P}\right)^{1/\gamma_u}\left[\frac{P_f-P}{P_f-P_0}\right]\right\}^{1/3}} \tag{1.41}$$

Alternatively, to obtain values of $u_{tm}$ from $u_{tv}$, measured from schlieren measurements using Eq. (1.38), is given by an attractively simple expression [10]

$$\frac{u_{tm}}{u_{tv}} = \left(\frac{r_v}{r_m}\right)^2 \tag{1.42}$$

The value of $r_v/r_m$ is reported to be 1.32 in [10].

#### 1.4.4.2 Correlations of turbulent burning velocity

Turbulent combustion measurements are complex and several correlations have been presented [62, 72, 74, 82, 88-92]. Some are discussed below.

Damköhler [59] first proposed that wrinkling due to increasing $u'$ increases the flame surface area of a turbulent flame. He hypothesised that the burning velocity ratio, $u_t/u_l$, increased in proportion to flame surface area ratio, $A/a$. Later, $A/a$ was related to $u'/u_l$ giving the simplest expression, $u_t \approx u'$. Clavin and Williams [88] introduced a simple formula in the form

$$\frac{u_t}{u_l} = 1 + \left(\frac{u'}{u_l}\right)^2. \tag{1.43}$$

However, the limitation in these simple expressions is that the influence of stretch rates is neglected. Flame stretch rates locally change laminar propagation speeds in flamelets and this necessitates the introduction of length scales [8, 89]. The correlation of Gülder [90] was developed for wrinkled flamelets experimentally, as a function of turbulent Reynolds number, $R_L$,

$$(u_t/u_l) - 1 = 0.6(u'/u_l)^{1/2}\, R_L^{1/4}. \tag{1.44}$$

A similar expression was derived by Zimont [91] using both empirical correlations and theoretical concepts, except that the adjustable constant, 0.6, was replaced by 0.4. It was later argued that at high values of $u'$, localised flame extinctions could become significant. The role of chemical to eddy lifetime should be involved in correlations, through either Karlovitz stretch factor [85] or Damköhler number [8].

Bradley et al. [62] had developed a correlation for $u_t$, based on experimental data generated over a wide range of conditions and fuels that involved $K$ and $Le$ to account for thermal diffusive/strain effects

$$u_t = 0.88u_k'(KLe)^{-0.3}. \tag{1.45}$$

$KLe$ varied between 0.01< $KLe$ <0.63.

Kobayashi et al. [82] derived an expression for turbulent burning velocity in their measurements of methane-air in a high pressure burner up to a pressure of 1.0 MPa, with

$$\frac{u_t}{u_l} = 5.04\left[\left(\frac{P}{P_o}\right)\left(\frac{u'}{u_l}\right)\right]^{0.38}. \quad (1.46)$$

This correlation was developed to demonstrate the influence of pressure on turbulent burning velocity. Without the pressure terms in the above equation, it is similar to the classical turbulent burning velocity expression given by Damköhler [40].

It was argued in [19, 83] that it was logical to use Markstein numbers in turbulent velocity correlations and subsequently Bradley et al. [72] improved their correlation, Eq. (1.45), by replacing $KLe$ with $KMa_{sr}$ as

$$u_t = 1.41u_k'(KMa_{sr})^{-0.43} \text{ for } 0.05 \leq KMa_{sr} < 19. \quad (1.47)$$

More recently, they [74, 92] presented a comprehensive correlation of $U = \frac{u_t}{u_k'}$, in terms of $K$ and $Ma_{sr}$, expressed by

$$U = \frac{u_t}{u_k'} = \bar{\alpha}\, K^{\beta}, \quad (1.48)$$

where $\bar{\alpha}$, $\beta$ are constants, given by [74].

For +ve Markstein numbers

$$\bar{\alpha} = 0.023(30 - Ma_{sr}) \quad (1.49)$$

$$\beta = 0.0103(Ma_{sr} - 30) \quad (1.50)$$

For -ve Markstein numbers

$$\bar{\alpha} = 0.085(7 - Ma_{sr}) \quad (1.51)$$

$$\beta = -0.0075(Ma_{sr} + 30) \quad (1.52)$$

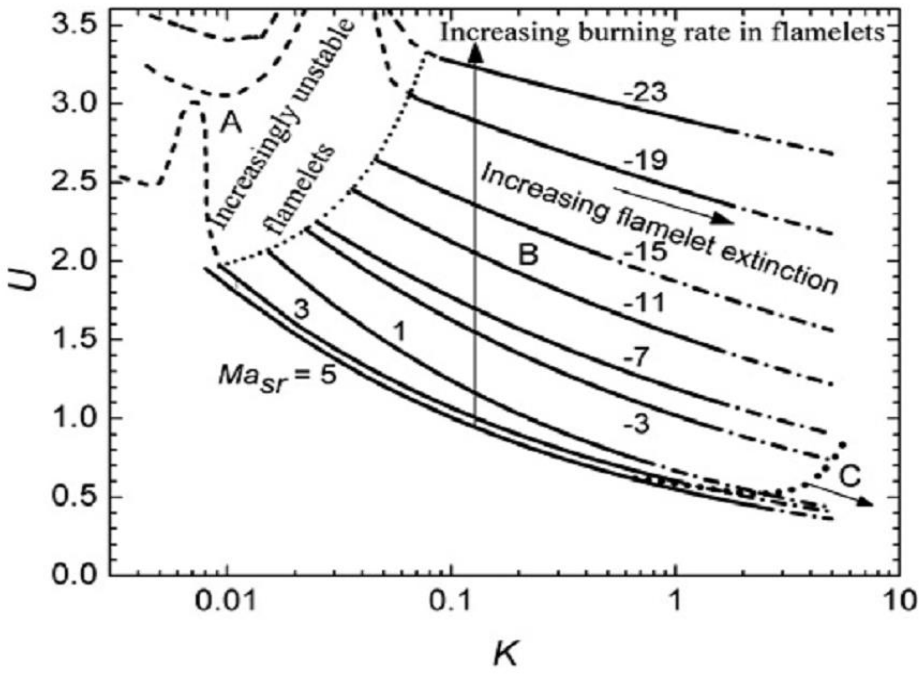


**Figure 1.6** Turbulent combustion regime as a function of *K* and $Ma_{sr}$ [74].

Equation (1.48) covers different turbulent combustion regimes and is based on a wide range of experimental data for different fuels (except $n$-butanol) the results of which are shown in Fig. 1.6 [74]. The entire regime is divided into three regimes: *A, B*, and *C.* Regime *A,* where *K*<0.1, represents that of unstable laminar flamelets with wrinkling due to instabilities. This regime is very complex because it involves the interaction between the laminar instabilities and the mild turbulence at low rms velocity, $u'$, close to zero. Regime *B* is where *K*>0.1 and the turbulence enhancement increases with increasing *K*. *U* also increases as $Ma_{sr}$ become increasingly negative. In Regime C, *K*>1.0 is not well established, but beyond the dotted lines, flame quenching is found to develop at high values of *K* and this is further discussed in Section 1.4.4.

Recently, Damköhler's hypothesis of $u_t/u_l$, proportional to $A/a$ has been revisited by many researchers [13, 84, 93, 94]. In his work, Bray [84] presented a factor $I_0$ that accounts for the influence of stretch rate on effective laminar burning velocity. This factor was in turn shown to be dependent on laminar Karlovitz stretch factor and Markstein number. Later, Bradley [78]

identified a factor named probability of burning, $P_b^{0.5}$, to allow the influence of stretch rate effects in Damköhler's hypothesis. $P_b^{0.5}$ was related to $u_t$, with that would exist in the absence of stretch, $u_{t0}$ as $P_b^{0.5} = u_t/u_{t0}$. This was accounted in Damköhler's hypothesis as given by the relation [13]

$$\frac{u_t}{u_l} = \frac{A}{a} P_b^{0.5}, \tag{1.53}$$

where $A$ is the total flame surface area given by the flame surface density, Σ, integrated over the entire volume, V, of the reacting flame brush as $A = \int_V \Sigma \, dv$, $a$, is mean surface area of the appropriate turbulent flame front, associated with $u_t$.

In their work, Bagdanavicius et al. [13] compared $A/a$ ratios for flames with positive and negative $Ma_{sr}$ values and demonstrated the effect of stretch on turbulent burning rate. They quantified these effects through $P_b^{0.5}$ that was found to increase with decreasing $Ma_{sr}$. However, the obtained $A/a$ ratios were inferred values using Eq. (1.53) and $P_b^{0.5}$ again evaluated in terms of $u_t$ and $u_{t0}$ as given by

$$P_{bMa}^{0.5} = \left(\frac{U_{Ma}}{U_0}\right) P_{b0}^{0.5} \tag{1.54}$$

where $P_{b0}^{0.5}$ was evaluated at $Ma_{sr} \approx 0$ through theoretical [72] and experimental [95] studies. Values of $P_b^{0.5}$ evaluated as described above are plotted against $K$ for different $Ma_{sr}$ in Fig. 1.7 taken from [13]. For negative $Ma_{sr}$, this shows an increase in $P_b^{0.5}$ with increasing $K$ that attains a maximum limit beyond which it reduces due to the onset of quenching. For positive $Ma_{sr}$, these remain constant with increasing $K$ before flame quenching, presented in Section 1.4.4, develop.

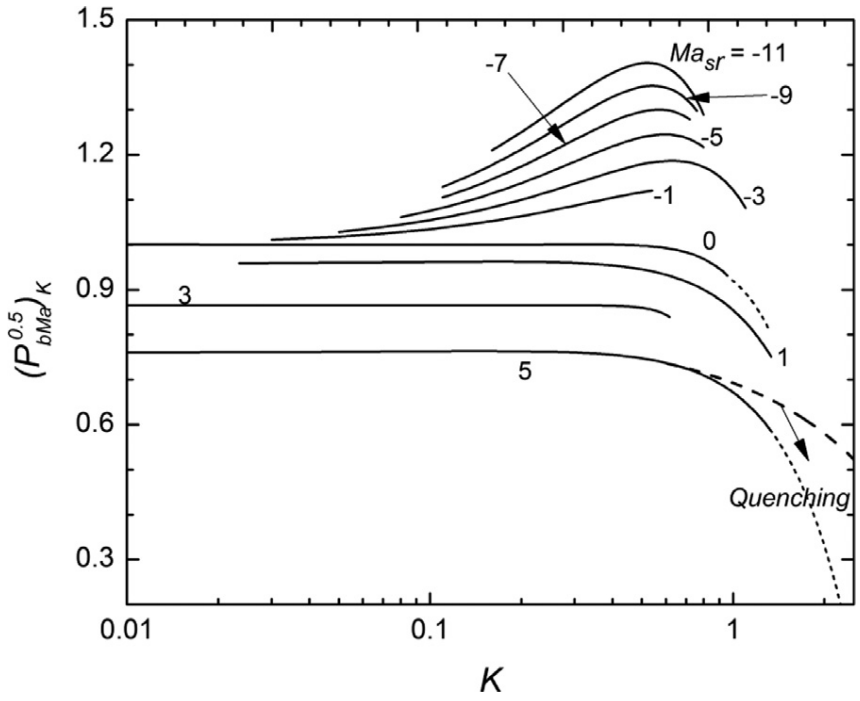


**Figure 1.7** Variations of $P_b^{0.5}$ as a function of $K$ and $Ma_{sr}$ [13].

### 1.4.4 Flame quenching

The premixed flame structure changes due to the turbulence, which in some cases increases the chemical reaction rate and in the other cases suppress it causing flame quenching. Therefore, it is vital to study this phenomenon. Quenching can be categorized as local quenching, as result of excessive flame stretching or heat losses which reduces the burning rate, and global quenching where the flame entirely extinct. Different effects have been argued to be the reason for the flame quenching. These include aerodynamic (straining), thermal (heat loss), and chemical. Flame quenching has been studied under varied experimental conditions, in burners [96-98], test tubes [99], orifices [100], and closed vessels [67, 101, 102]. Extinction stretch rates have been employed rather more widely than kernel extinction sizes in flame quenching studies [96]. It is convenient to generalise laminar extinction in terms of a Karlovitz laminar flame extinction stretch factor, $K_{ql}$, equal to the stretch rate, $\alpha_q$, normalised by the chemical time, the laminar flame thickness divided by the laminar burning velocity. In modelling, a turbulent flame is considered as an array of wrinkled laminar flamelets [84, 88]. Abdel-Gayed et

al. [103] measured turbulent quenching strain rate and found it to be higher than the laminar extinction stretch rate observed by Law et al. [104] and theoretical predictions of Stahl et al. [105] for the same mixture composition.

Klimov [106] and Williams [107] pioneered the study of turbulent flame quenching. They proposed a correlating parameter of the Kolmogorov scale strain rate multiplied by the laminar flame chemical time, comprised of the laminar flame thickness divided by the laminar burning velocity. This Klimov-Williams criterion for turbulent flame quenching suggested it occurred when the associated Karlovitz number exceeded unity. Kuznetsov [108] employed a similar chemical to eddy lifetime criterion, but with the latter given by $L/u'$, given in Eq. (1.28). Abdel-Gayed et al. [38] employed $\lambda/u'$ for this parameter as given by Eq. (1.29). They [38, 109], demonstrated the effect of Lewis number, $Le$, on the quenching phenomenon, using different mixtures of $i$-octane, hydrogen, propane-air mixtures under high turbulence conditions. They noticed that rich hydrogen-air and lean hydrocarbon mixtures were easily quenched. Later, Bradley et al. [101] reported that rich $i$-octane and $CH_4$ air mixtures tended to quench at pressures of 0.5 and 1.0 MPa, and near-limit lean hydrogen/air mixtures quenched at all pressure ranges until 1.5 MPa. Despite the importance of $Le$, in quenching criterion, $Ma_{sr,}$ was preferred as it varies with pressure at different *K* values [31, 72].

The probabilities of initial flame kernel propagation have been measured with fan speeds up to $u'$ = 7 m/s [101]. Probabilities of 80% ($p_{0.8}$) and 20% ($p_{0.2}$) for flame propagation were expressed as a function of *K* and $Ma_{sr}$ by [101]:

For ($p_{0.8}$)):

$$K(Ma_{sr}+4)^{1.8} = 34.4 \quad for \quad -3 \le Ma_{sr} \le 11 \qquad (1.55)$$

For ($p_{0.2}$):

$$K(Ma_{sr}+4)^{1.4} = 37.1 \quad at \quad -3 \le Ma_{sr} \le 11\,. \quad (1.56)$$

Using Eq. (1.55), a quenching regime boundary was plotted, as shown by the dotted curve in Fig. 1.6, based on measurements of explosions in the fan-

stirred explosion vessel [74]. The present study aims to revise this quenching curve. Just outside this regime of near quench is one in which an isolated flame kernel might briefly propagate to a maximum flame diameter, at which propagation ceases and the hot gases dissipate. A methodology was developed for measuring such a limiting mean quenching kernel diameters in the fan-stirred vessel. Experimental data at quench are presented for hydrocarbon and hydrogen mixtures at different pressures, temperatures, and rms turbulent velocities.

Measured quench diameters are normalised by the laminar flame thickness of the mixture, using Eq. (1.18), where $k$ and $c_p$ are the thermal conductivity and specific heat at constant pressure and at the inner layer temperature, $T_0$[41] below which there is no reaction. Values of all the required physicochemical data were obtained from the Gaseq code [57].

Analyses of turbulent quench flames are extended to non-premixed jet flames sustained by the entrainment of air by the fuel jet. This can quench the jet flame and cause flame blow-off at high jet velocities and small pipe diameters. Four major aspects are covered in the current research on quenching *(i)* Use of a swinging laser sheet to study kernel shape and whether a mean quenching diameter is a valid parameter, *(ii)* Measurement and correlation of normalised kernel quenching diameters, *(iii)* Development of a unified approach to both premixed and non-premixed jet extinctions. (*iv*) Extension of quenching limit on *U/K* diagram.

## 1.5 Review on burning velocities of *n*-butanol/air mixtures

### 1.5.1 Laminar Flames

Several studies have been conducted on laminar burning rates of premixed $n$-butanol/air mixtures in different configurations [1, 5, 110-116]. Laminar burning velocities were measured at elevated temperature and pressure by Gu et al. [110]. They also calculated the corresponding Markstein lengths over a range of equivalence ratios. Laminar flame speeds of butanol isomers at atmospheric pressure and 343 K were measured by Veloo and Egolfopoulos

[1] in a counter flow configuration. It was found that $n$-butanol possesses the highest laminar flame speeds among them. Zhang et al. [116] and Broustail et al. [114] measured laminar flame speeds and Markstein lengths of $n$-butanol/$i$-octane and ethanol/$i$-octane blends in a constant volume combustion chamber at 0.1 MPa and 393 K over a wide range of equivalence ratios. They showed that laminar flame speeds of fuel blends are enhanced with an increasing proportion of $n$-butanol. The laminar burning velocities of $n$-butanol were higher than those of $i$-octane, but less than of ethanol. Later in [115], they extended their study to higher temperatures of 423 K and pressures upto 1.0 MPa. They also reported the Markstein lengths of pure $i$-octane, ethanol and $n$-butanol at pressures from 0.1 MPa to 1.0 MPa. The differences in laminar burning velocities for alcohol fuels and $i$-octane were reduced as initial pressure increased. Recently, Zhang et al. [112] conducted an experimental and kinetic study of premixed laminar flames of acetone, ethanol and $n$-butanol/air (ABE) mixtures and found that those of ABE mixtures are closer to $n$-butanol. Beeckmann et al. [117, 118] investigated laminar burning velocities of alcohol fuels at 1.0 MPa, both experimentally and numerically. They suggested that the present numerical models for $n$-butanol under predict the experimental values at high pressures.

### 1.5.2 Turbulent Flames

Many investigations involving the effects of $n$-butanol/gasoline blends and $n$-butanol/diesel blends on the efficiency of spark ignition engines have been reported [6, 7, 119-121]. Alasfour [119] investigated the thermal efficiency of a single-cylinder engine, as well as $NO_x$ emission, with $n$-butanol/gasoline blends over a range of intake temperature and equivalence ratio. They compared the reductions in power with that of pure gasoline. Yao et al. [122] experimentally studied on $n$-butanol/diesel fuel blends in a heavy duty direct injection diesel engine. They concluded that $n$-butanol addition reduced soot and CO emissions significantly with no serious impact on specific fuel consumption. They also found that an increase in $n$-butanol in the fuel blend reduced the soot formation. Chen et al. [7] investigated combustion and

emissions with $n$-butanol/diesel ratio blends in a heavy-duty diesel engine. Their results show that combining a high butanol/diesel ratio blend with moderate exhaust gas recirculation (EGR) had the potential to achieve ultra-low NOx and soot emissions, while simultaneously maintaining high thermal efficiencies. Swaja and Naber [120] studied the combustion of pure $n$-butanol and its blends with gasoline in a sparked ignited engine at stoichiometric air-fuel ratios. It was concluded that $n$-butanol has the potential to perform as a direct substitute for gasoline, either as a pure fuel or blended with gasoline in a SI engine because of the similar thermo-physical properties. Pereira et al. [121] compared the performance of alcohol fuels such as butanol and ethanol with that of hydrocarbons, such as $i$-octane and gasoline in a direct injection spark ignition engine for stoichiometric and lean mixtures. They found that at higher temperatures butanol and ethanol fuels burn faster than gasoline and $i$-octane. Moreover, they suggested that alcohol fuels were most robust to changes in fuelling, in terms of combustion stability, under lean conditions than hydrocarbons.

Aleiferis et al. [2] conducted optical studies of $n$-butanol, ethanol, $i$-octane and methane fuel in an SI engine under stoichiometric and lean conditions and found $n$-butanol and ethanol to have comparable burning rates, while $i$-octane had the slowest. It was suggested that combustion of these fuels in controlled turbulent environments would reveal significant details that would improve their understanding.

Lawes et al. [68, 123] and a recent study by Bradley et al. [10] presented turbulent burning velocities for methane, $i$-octane, methanol and ethanol at high temperatures and pressures in a constant volume combustion vessel, CV, with isotropic turbulence. While few studies are reported on the use of $n$-butanol as a fuel in engines, there is no work reported on combustion of $n$-butanol in a controlled turbulent environment such as a CV. It is necessary to acquire fundamental turbulent combustion characteristics of $n$-butanol in well controlled turbulent environments to better predict the combustion performance under engine like conditions.

## 1.6 Review on 3D analysis of turbulent flames

The evaluation of turbulent flame parameters has been largely confined to 2D sheet imaging techniques in combustion vessels of uniform turbulence. For example, the experimental measurements of $u_t$, $\sum$ and $\bar{c}$ [10, 11, 13, 73, 74, 124-126] have been largely limited to 2D laser sheet techniques. These studies relied on the assumption that the flame surface detail witnessed was representative of the overall three-dimensional flame structure. It is often assumed that the average surface area per unit volume equals the average flame perimeter per unit area in the laser sheet to determine $\sum$ [80]. However, the limitation of this technique is that the behaviour of flames in the third dimension is not known. Moreover, flames in the early stages of development, particularly lean mixtures with slow laminar burning, are displaced from the centre by larger length scale eddies, thereby increasing the uncertainty of slicing a flame through its centre. As a result, flame parameters measured using the 2D techniques could be either underestimated, or overestimated, depending upon the location of the slicing. Therefore, 3D measurements are important to determine accurate flame parameters to achieve maximum burning rates for improved combustion engine efficiency and reduced pollutant emissions.

Modelling of turbulent flames employing $\sum$ and $\bar{c}$, has also been carried out extensively in both 2D and 3D by many researchers [60, 93, 127]. However, limited experimental data are available to test their validity. A summary of the 3D experimental work carried out, so far, is presented in Table 1.1. Researchers [128-131], in the past have proposed multiple simultaneous laser sheet imaging to overcome the 2D limitations. Yip et al. [128] used a traverse laser beam technique using a rotating mirror, RM, through an aerosol seeded gas jet, with a dye laser as the laser light source, to capture successive imaging of the jet. Mantzaras et al. [132] used a limited number of sheets, typically four, of different wavelengths for instantaneous multiple sheet imaging. However, to create a pseudo-instantaneous 3D flame structure, the laser sheet is required to traverse at a much higher frequency. Hult et al. [131]

applied a similar technique employing a neodymium yttrium-aluminium garnet (Nd:YAG) laser to study flames stabilized on a burner, whilst Nygren et al. [130] investigated combustion in a homogeneous charge compression ignition (HCCI) engine using a similar setup, with laser-induced fluorescence, LIF, to reveal chemical species as an indicator of the extent of combustion. More recently, Upton et al. [133] studied burner flames using computed tomography, CT, with 12 individual detectors equispaced around the flame. Lawes et al. [129] adopted the methodology of Yip et al. [128] to construct 3D turbulent flames at a faster laser frequency, while the flames were only analysed recently by Harker et al. [12, 134].

Ng and Zhang [135] demonstrated the stereoscopic imaging and reconstruction of turbulent impinging flames using a single camera to capture a pair of stereo images. However, their technique was limited to only low wrinkled flames, as well as to those flame surfaces viewable from two different points (complex flames). The technique also had difficulty in resolving transparent, or semi-transparent flames and recommended laser based techniques to be used. Bheemul et al. [136] developed an optical instrumentation system for the measurement of 3D geometric parameters of gaseous flames in real time using visual hull reconstruction. This involves a geometric shape obtained using silhouettes of flames as seen from a number of views. However, even with a large number of views, the result would not be the real representation of flames. Moreover, their method tends to be restricted to very low resolution reconstruction of ignition volume and ignition surface areas. Steinberg et al. [137] used cinema stereoscopic PIV technique to resolve the effect of 3D velocity fields on flame wrinkling. They showed that the flame contour using the particle gradient method (Mie-scattering) corresponds well to the true location of maximum gas density gradient obtained from CH-PLIF. However, their study indicated that the effect of eddies on the flame wrinkling cannot be resolved using conventional techniques. Tanahashi et al. [138] reconstructed 3D turbulent premixed flames in a noise-controlled, swirl-stabilized combustor by evaluating mean reaction progress variable, using 2D OH-PLIF images. The 2D images were

averaged over 100 temporal images to evaluate the mean reaction progress variable at 25 different planes, in order to reconstruct the 3D flame which was not instantaneous.

Kang et al. [139] demonstrated the feasibility of instantaneous 3D flame measurements using fibre-based endoscopes, FBEs, to gather projections from various orientations simultaneously. They reported the practical advantages of FBEs for overcoming optical access and reducing equipment cost. However, their technique was limited by the signal attenuation, due to the coupling and transmission loss in FBEs leading to a degradation of the image quality. More recently, from the same research group, Ma et al. [140, 141] demonstrated the feasibility and accuracy of 3D turbulent flame diagnostics, based on volumetric laser induced fluorescence, VLIF. The technique required five cameras to simultaneously capture CH radicals in the flame to reconstruct 3D flames. Wellander et al. [142, 143] and Kristensson [144] used dual-mirror laser scanning technique with Mie-scattering and OH planar laser-induced fluorescence, PLIF, for 3D reconstruction of dense sprays and low turbulent premixed flames respectively. They reported advantages and limitations of their technique with respect to spatial and temporal resolution. They concluded that this technique, with high frequency lasers and cameras, could be applied to highly turbulent flames.

Harker et al. [12, 134] presented a 3D study of developing turbulent flames in the Leeds fan-stirred combustion vessel, CV, using a multiple laser sheet imaging technique. An Oxford Lasers LS20-50 copper vapour laser, pulsed at a frequency of 18 kHz, was used to provide pulses of laser light. These were shaped into sheets using a number of lenses. The resulting laser sheets were swept through the CV by reflection off a rotating octagonal mirror. This allowed a number of “sweeps” through a flame during its development. Due to the small sheet height of 50 mm and the finite time required within and between each sweep, only low turbulence flames and in the early stages of growth could be imaged. The resolution of 0.7 mm per pixel in all directions allowed structures of the integral and Taylor length scales of turbulence (20 mm and 3 mm, respectively) to be resolved, but not the Kolmogorov scale (0.15 mm).

They suggested that this technique with improved resolution of captured images would allow more accurate analysis of faster burning mixtures at the high turbulence levels relevant to engines.

Turbulent combustion is certainly a complex phenomenon and only partially understood. Although 2D measurement techniques are designed to slice through the center plane of the flame, it is difficult to predict which part/plane of the flame has been captured as flame development is inherently 3D. Moreover, the third dimension of turbulent flames cannot be resolved by mere 2D flame imaging techniques. Therefore, it is necessary to analyse turbulent flames in 3D due to their inherent nature. Very limited 3D measurements have been carried so far and there remains a need for accurate 3D measurement data of the important structural parameters of turbulent flames [61, 124].

The rapid development of computational techniques, such as large eddy simulation, LES, and direct numerical simulation, DNS, a number of 3D numerical research [94, 145] is being carried out to investigate the turbulent flames, however, there is a lack of 3D experimental data to validate their work. Both LES and DNS can only be applied to flows of low Reynolds numbers, even with the state-of-the-art computing technology, and therefore the flame is only weakly wrinkled. The present swinging laser sheet technique suits this well and allows to analyse the flame in 3D without isotropic assumptions. Moreover, the spatial resolution of this technique is comparable to that of the VLIF techniques reported recently in [140, 141] and requires only one camera compared to five cameras for the later which increase the expenses. The swinging laser sheet technique demonstrated by Harker et al. [12, 134] has been significantly developed in the present study. The experimental data is processed using algorithms developed in MATLAB to determine flame parameters such as total surface area, $A$, and mean surface areas, $a$. These are subsequently compared with modeled data in DNS. More recently in a Leeds/Cambridge collaboration, the present $A/a$ data for turbulent flames obtained using this technique are being analysed in the light of Eq.(1.53), to better understand the limits of this equation's validity and discrepancies.

**Table 1.1** Some previous experimental studies of 3D imaging

| Authors | Year | Measurement Technique | Equipment | Voxel size | Apparatus | Frequency |
|---|---|---|---|---|---|---|
| Yip et al. [128] | 1987 | 3D, Aerosol concentration measurements | Rotating Mirror, 1 camera, thin multiple laser sheet | | Jet nozzle | 30 kHz |
| Mantzaras et al. [132] | 1988 | Mie-scattering technique | Four laser sheet | 0.35 mm | SI Engine | |
| Nygren et al. [130] | 2002 | PLIF, multiple imaging | Scanning mirror, | | HCCI Engine | 10 Hz |
| Hult et al. [131] | 2002 | LII | Scanning mirror, | | Burner | |
| Ng and Zhang. [135] | 2003 | Stereoscopic imaging | 1 camera | | Impinging burner | |
| Bheemul et al. [136] | 2005 | 3D digital imaging | 3 monochromatic CCD cameras | 0.23 mm x 0.21 mm | Burner | reported ign. SA |
| Steinberg et al. [137] | 2008 | Cinema Stereoscopic PIV, 3D velocity fields, CH-PLIF | 2 cameras | 0.14 mm | Bunsen burner | 1 kHz |
| Tanahashi et al. [138] | 2008 | 3D flames using 2D CH-OH PLIF + stereoscopic PIV, OH-PLIF | Multiple planes, 4 cameras | 0.023 mm, 0.05 mm | Swirl Burner | |
| Mason et al. [146] | 2009 | Minima Reconstruction Technique, MRT | 2 CCD cameras | | Burner | |

Cont'd

| | | | | | | |
|---|---|---|---|---|---|---|
| Upton et al. [133] | 2011 | 3D, Computed tomography (CT) | 6 cameras, | 0.25 mm | Burner | |
| Harker et al. [134] | 2012 | 3D, Mie-scattering technique | Rotating Mirror, 1 camera, multiple laser sheet | 0.7 mm | Explosion flames | 18 kHz |
| Kang et al. [139] | 2015 | FBE's, CH* chemiluminescence | 1 camera | 0.1x0.1x0.2 mm | Burner | 1 kHz |
| Wellander et al. [142, 143] | 2011, 2014 | OH-PLIF, Mie-scattering | 1-2 cameras | | Dense spray, burner | 1-2 kHz |
| Kristensson et al. [144] | 2011 | Mie-scattering | 1 camera | 512 512 pixels in 6.2x6.2 $mm^2$ | Dense Spray | 10 Hz |
| Meyer et al. [147] | 2016 | LII | 8 cameras | 0.13 $mm^2$ /pixel | Jet flame | 10 kHz |
| Lin Ma et al. [148] | 2015 | Tomographic chemiluminescence, TC and Fiber based endoscope, FBE, CH*emission | 2 cameras | 0.5 mm voxel size | Supersonic combustor, ignition | 20 kHz |
| Lin Ma et al. [141] | 2017 | 3D VLIF, CH radicals | Laser sheet slab, 5 cameras | 0.15 mm | Burner | 10 Hz |
| Lin Ma et al. [140] | 2017 | 2D LIF, 3D VLIF, CH radical, tomography with LIF | 6 cameras, Laser sheet, laser slab | 0.041mm for PLIF, 0.18mm for VLIF | Hi-Pilot Burner | 10 Hz |

## 1.7 Aims

Biofuels such as $n$-butanol are considered an important alternative in reducing greenhouse gas emissions and climate change. While few studies are reported on the use of $n$-butanol as a fuel in engines, there is no work reported on combustion of $n$-butanol in a controlled turbulent environment such as a CV. It is necessary to acquire fundamental turbulent combustion characteristics of $n$-butanol in well controlled laminar and turbulent environments to better predict the combustion performance under engine like conditions. Moreover, accurate 3D measurements of flame parameters are vital in improving engine efficiency and reduce pollutant emissions by determining the maximum possible burning rates and the likelihood of flames to quench. Therefore, the present study aims

1. To provide laminar burning characteristics of $n$-butanol/air mixtures at high temperature over a range of initial pressures and equivalence ratios. This includes accurate values of fundamental parameters such as $u_l$, $L_b$ and $Ma_{sr}$ of $n$-butanol using schlieren imaging technique.

2. To identify the low strain rate regime in which laminar flames become unstable and to ascertain the extent to which $K_{cl}/Ma_{sr}$ relationships might cover a wide range of fuels. To investigate whether small laboratory explosions can predict large atmospheric flame speeds.

3. To determine the variation of $u_t$ at different rms turbulent velocities and to correlate dimensionless burning rates, $u_t/u_k'$, with Karlovitiz stretch factor, $K$, in terms of $Ma_{sr}$. The present experimental data contribute to the database of turbulent combustion rates and can be used in validating chemical models or engine simulations using $n$-butanol as a fuel.

4. To measure fundamental parameters such as $A/a$ ratios directly from the 3D structure of turbulent premixed explosion flames and to re-examine Damköhler's first hypothesis [59] in the light of 3D flame surface area ratio measurements and understand its validity limits.

5. To investigate the behaviour of turbulent quenched flames at higher stretch rates and the probabilities of quenching. To determine, as part of a joint study with M. Shehata (2019) [149], the critical sizes for quenching flames of different mixtures including hydrogen, $CH_4$ and $n$-butanol. Also to develop a unified approach to both premixed and non-premixed jet extinctions.

The thesis concludes with details of ongoing work in collaboration with Cambridge University on the possible role of flame instabilities in the reported high values of $P_b^{0.5}$ for negative $Ma_{sr}$ mixtures and proposed explanations using fractal theory [78].

## 1.8 Thesis Outline

There are six chapters. The first chapter already described the motivation and theory for the present study along with the aims. A review of all the 3D flame analysis is also presented. Chapter 2 describes the apparatus and all the optical techniques along with details of their synchronisation set up used to conduct explosions and acquire data. Chapter 3 explains the different data processing analytical techniques. Chapter 4 presents the measured laminar burning velocities, flame instabilities and turbulent burning velocities obtained using the schlieren imaging technique and pressure records. It also presents the flame surface area ratios from 3D swinging laser sheet technique, along with quenching results.

Discussion related to the results, presented in Chapter 4, are addressed in Chapter 5. These include comparison of measured $u_l$ values of $n$-butanol with previous work; similarities of $K_{cl}/Ma_{sr}$ relationships with large explosions data; comparisons of $u_t$ of $n$-butanol with that of $i$-octane and ethanol and correlations of $u_t/u_k'$ with $K$ and their comparison with previous correlations. Furthermore, the discrepancies observed in $P_b^{0.5}$ values obtained from 2D and 3D techniques and the quenching of turbulent flame kernels in terms of their dimensionless critical sizes, along with a new quench boundary on the $U/K$ diagram are discussed. Finally the Conclusions from the present work and future work recommendations are presented in Chapter 6.

# Chapter 2

# Experimental Measurement Techniques

The present chapter describes the equipment and the optical techniques employed in this experimental study. The combustion vessel, CV, is described in Section 2.1 followed by the auxiliary systems for mixture preparation and ignition in consecutive sections. The diagnostic systems and techniques together with their synchronisation are described in Section 2.3 followed by the experimental procedure in Section 2.4.

## 2.1 Combustion Vessel, CV, and ancillaries

As shown in Fig. 2.1, the experimental rig consists of a 30 litre spherical stainless steel combustion vessel, CV, of 380 mm internal diameter and contained three pairs of orthogonal windows of 150 mm diameter viewable aperture, thickness of 100 mm. The vessel has been fully described in [10, 24, 64, 74, 92] and only brief descriptions are presented here. It is capable of withstanding the temperatures and pressures generated from explosions at initial values of 600 K and 1.5 MPa. Turbulence is generated in the CV by four identical, eight-bladed fans, each driven by an 8 kW electric motor. The four fans, arranged in a tetrahedron formation, were rotated by electric motors with independent and accurate speed control to within ±5% of each other [68] of the set speed in order to generate spatially uniform turbulence within the central region of the CV.

The mean and rms turbulence velocities, and integral length scale, have been determined using LDV and particle image velocimetry, PIV [21, 68]. The turbulence was found to be uniform and isotropic [15] within the optically accessable central region (150 mm diameter). The integral length scale is 20 mm, and independent of the fan speed between 1000 to 10,000 rpm, and at 500 rpm it was found to be 24 mm. The Taylor and Kolmogorov length scales

were found using the relations presented in Section 1.4.1. The rms turbulence velocity, $u'$, is given by

$$u'(m/s) = 0.00119 f_s\ (rpm) \tag{2.1}$$

where $f_s$ is the fan speed. This correlation is valid for all operating pressures, temperatures and mixture viscosities [68].

Most experiments required an initial mixture pressure and temperature of between 0.1 to 0.5 MPa and 300 to 365 K. Both static and dynamic pressure measurements were made during the course of the experiments. The static pressure measurement was made using a static pressure transducer (Druck PDCR 911) which can operate in a pressure range of 0-1.5 MPa. It was used to record the absolute pressure during mixture preparation and was isolated before triggering an explosion, using a swage lock ball valve, in order to avoid damage from any rapid/significant pressure rise.

The initial temperature prior to each explosion was monitored by a K-type thermocouple consisting of a 25μm chromel-alumel wire enclosed in a 1.5mm stainless steel case and mounted inside the CV such that the tip/junction of the thermocouple was 75mm away from the inner surface of the CV. Temperature readings were displayed on a LCD of a PID controller (CAL Controls, CAL3200). For high temperature explosions, the CV was typically pressurised to 0.2-0.3 MPa and then heated by 2kW coiled heaters to ensure uniform heat distribution. A safety mechanism was employed to prevent the heating coils operating unless the fans inside the CV were running. This was important as the running fans not only convected heat uniformly across the CV but also prevented any excessive hot spots that may lead to any pre-combustion of reactant mixture. Further details regarding the temperature control system are provided in [16].

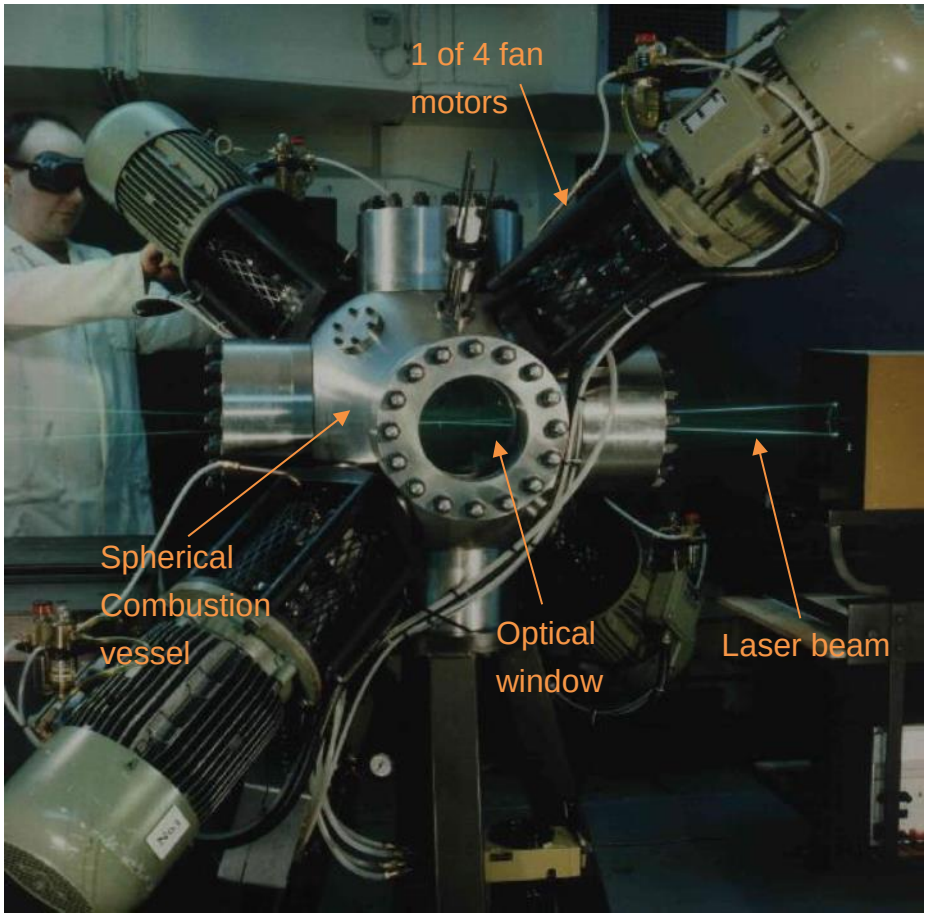


**Figure 2.1** Spherical stainless steel Leeds fan-stirred combustion vessel [150].

## 2.2 Ignition

As in previous studies in the present vessel, spark ignition was used to ignite the mixture in many experiments. This system has been fully described in [151] and is summarised in Section 2.2.1. However, for much of the work described in Chapters 4 and 5, it was necessary to use a laser ignition source, which is described in Section 2.2.2.

### 2.2.1 Spark Ignition

Figure 2.2 taken from [152], shows a miniaturised spark plug assembly consisting of a replaceable spark plug tip (anode), of 1.5 mm diameter, insulated in a ceramic material tube covered by a 6.35 mm diameter stainless steel body of which acts as a cathode. This unit was placed in an outer

stainless steel body that formed an electrical connection with the cathode. This was grounded via a high tension (HT) lead connector, secured in a PTFE insulator, to avoid any risk of uncontrolled ignition from residual ignition energy [153]. This simple spark plug assembly, capable of delivering 23 mJ [15] supplied by a 12 V transistorised automotive ignition coil, was designed at Leeds to minimise interference of the turbulence flow field and flame propagation. Fuller details are presented in [151, 152]. A second high spark ignition unit was used to ignite mixtures at near flammability limits. This unit was charged by a 600V DC power supply that employed a set of series resistors. This enabled the current to be varied between 3A to 12A and the spark duration between 0 to 1 ms. Fuller details of this ignition unit are presented in [77, 150].

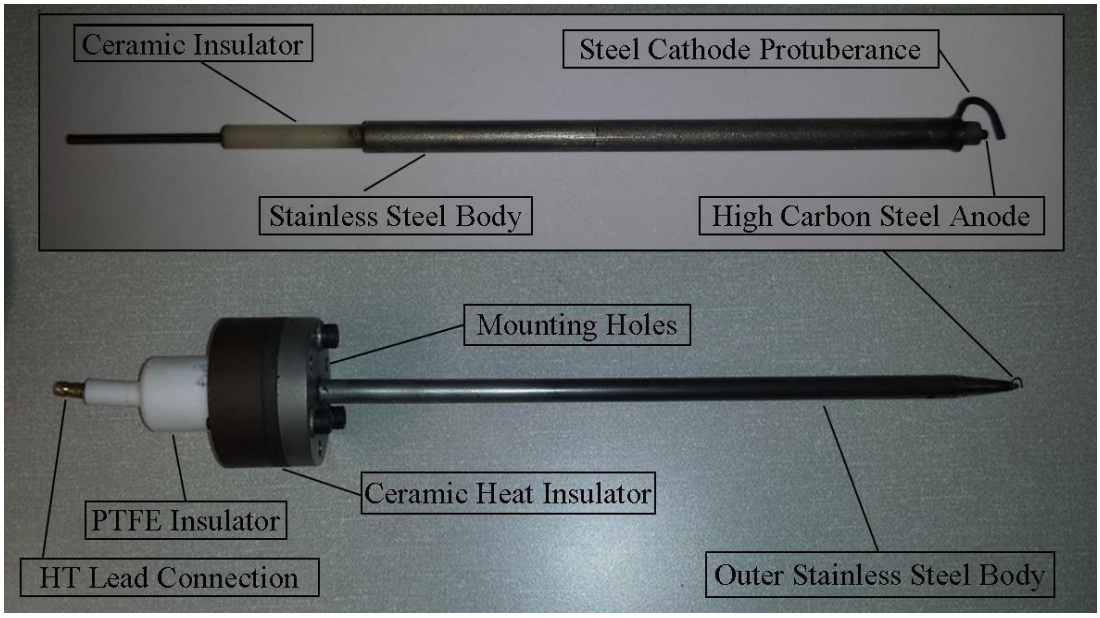


**Figure 2.2** Spark plug assembly [152].

### 2.2.2 Laser Ignition

The laser ignition system was used in conjunction with the 3D swinging laser sheet technique, described in Section 2.3.3, in order to avoid the interference caused by the spark plug in both turbulent flow field and captured flame images. Therefore, an adapted version of the laser ignition system presented in [154] was used.

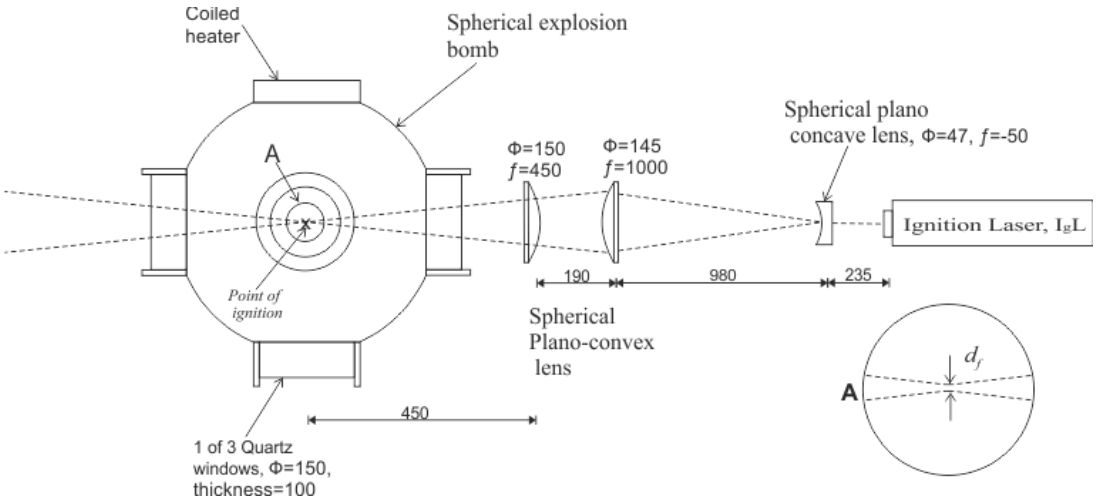


**Figure 2.3** Top view of a laser ignition set up, all dimensions are in mm.

Figure 2.3 shows a schematic top view of the laser ignition system employed in the present work. A New Wave solo 120 Nd:YAG laser, $\mathrm{I_gL}$, at a frequency of 532 nm capable of a maximum pulse repetition rate of 15 Hz was used for ignition. The laser beam from the ignition laser head was expanded, using a 47mm plano-concave lens, of focal length ($f$) -50mm, on to a plano-convex lens, of $f$=1000 mm and 145 mm in diameter, $\Phi$. It was then focused on to a second plano-convex lens, with $f$=450mm and $\Phi$ =150 mm, placed further downstream close to the CV window which in turn focused the laser beam at the centre of the CV to a minimum waist diameter ($d_f$) creating a spark for ignition. The higher laser convergence provided a more localised focus than otherwise, which minimised the risk of unwanted additional sparks at either side of the focus.

## 2.3 Diagnostic Techniques

### 2.3.1 Pressure Measurement Technique

Both static and dynamic pressure measurements were made during the course of the experiments. While the static pressure transducer was, in general, used to record only the initial pre-explosion pressure for all

experiments, the dynamic pressure during an explosion was measured using a Kistler 701A, dynamic pressure transducer with an accuracy of ±0.5%. It had an operating pressure range of 0-25 MPa and was mounted on the inner side of the CV. The charge from this transducer was sent to a charge amplifier, Kistler 5007, where it was converted to a +/- 10V analogue signal. It was then sent to a NI6361 DAQ analogue to digital converter, ADC, to be digitised and to be interpreted by the LABVIEW software. About 25K samples were collected for every explosion at a frequency of 50kHz. The voltage range for the associated pressure rise during an explosion was optimised by adjusting the charge amplifier volts/pressure range to 5volts/bar for initial static pressures of 0.1 and 0.5 MPa and 10volts/bar for 1.0 MPa. The synchronisation and triggering processes for initiation of pressure measurement recording are detailed in Section 2.3.3.3.

### 2.3.2 Schlieren Imaging Technique

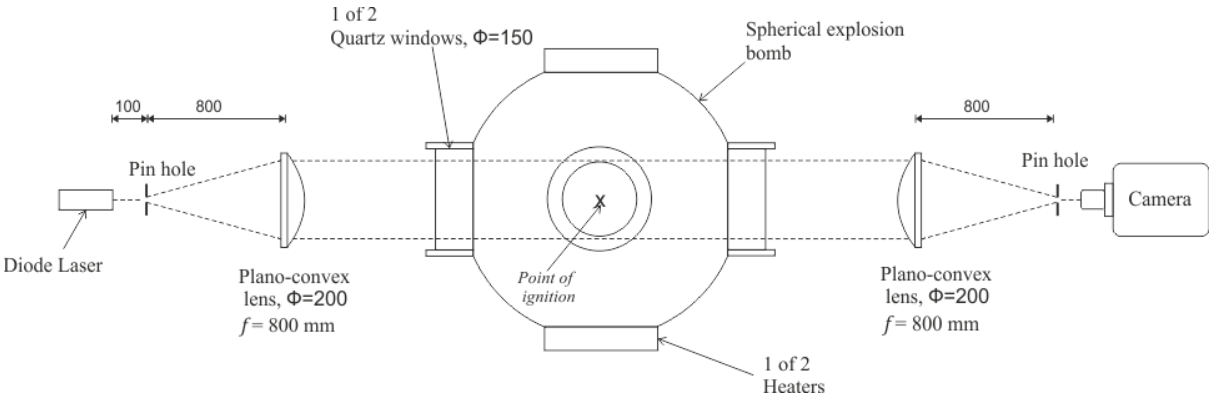


**Figure 2.4** Schematic diagram of the Schlieren imaging set up used in the present study, all dimensions are in mm.

High speed schlieren imaging was used to study laminar and turbulent flame explosions. This technique allows visual detection of the flame front through density gradients between the burned and unburned mixtures that cause varying degrees of light refraction. The captured flame images are processed to derive flame speeds, Markstein lengths, and laminar burning velocities. A schematic diagram of the schlieren set up is shown in Fig. 2.4. The synchronisation for the schlieren set up is presented in [152]. The flames were imaged using a class 3B, 5mW, 635nm LC, diode laser. It was collimated through the CV window using a plano-convex lens of focal length $f$=800 mm

and $\Phi$ =200 mm. It was then converged using a second plano-convex lens of aforementioned configuration. The camera was positioned such that the maximum field of view utilised the full window diameter of 150mm. The images are captured using a high speed Phantom Miro310 digital camera, with an exposure time of 6 μs, framing at 5400 frames per second (fps) with a resolution of 768x768 pixels.

#### 2.3.2.1 Pixel size determination of the captured images

The pixel size of the captured images was determined using a 10 mm x 10 mm grid imprinted onto a transparent sheet. This was mounted in the collimating beam area in centre of the CV. The high speed Phantom Miro310 digital camera captured the images of this imprinted transparent sheet with an image resolution of 768x768 pixels. This was repeated at two other positions within the collimated beam area to assure same grid size. An image of the transparent sheet is shown in Fig. 2.5. With the grid size known, using an image analysis tool in MATLAB the number of pixels within a grid is counted and thereby the pixel size is determined. This resulted in a recorded square view of 159 x 159 mm with a resolution of 0.207 mm/pixel. This resolution was found to be sufficient to capture the details of flame edges. Fuller details are provided in [14].

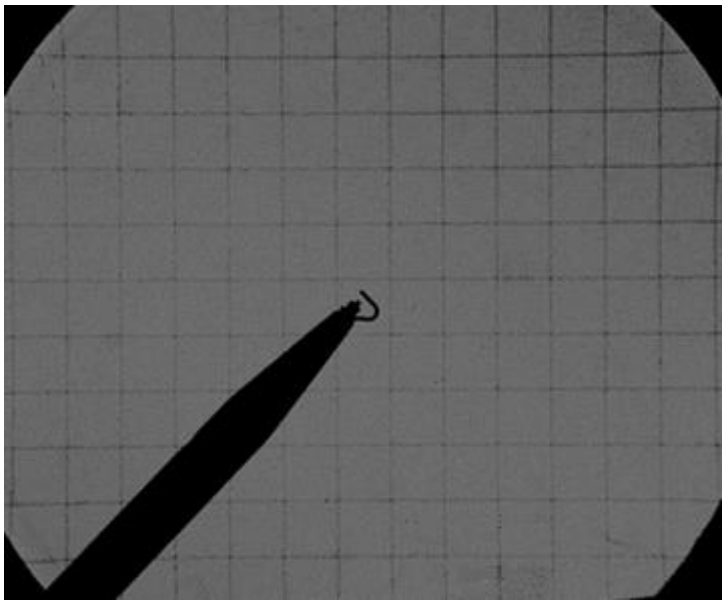

**Figure 2.5** Image showing imprinted grid of 10 mm x 10mm on a transparent sheet.

### 2.3.3 3D Swinging Laser sheet Technique

The 3D swinging laser sheet technique used in the current study is presented in this section. It allows to investigate the 3D turbulent premixed flames using high speed lasers and cameras. The formation of thin imaging laser sheets and the optics used for sweeping of these sheets through the flames is described in Section 2.3.3.1. Sections 2.3.3.2 and 2.3.3.3 describes the laser sheet geometry and synchronisation system for rotating mirror, the imaging laser, camera, ignition laser and the pressure recording equipment. Seeding particle characteristics for Mie-scattering are discussed in Section 2.3.3.4.

The swinging sheet technique creates multiple thin laser sheets sweeping, using a 16 faced rotating mirror, RM, through a propagating flame inside the fan stirred CV. A schematic diagram illustrating the formation of thin laser sheets is presented in Fig. 2.6. 2D Mie-scattered images are recorded by a digital camera at every position, 1mm apart, of the laser sheet in a sweep. For the Mie-scattering process, olive oil droplets measuring approximately 1 μm are used as seeding particles that reflects laser light. A high speed camera placed orthogonal to the imaging laser sheets captured the reflected laser light from these seeding particles. The 2D Mie-scattered images captured are used to reconstruct the 3-D flame.

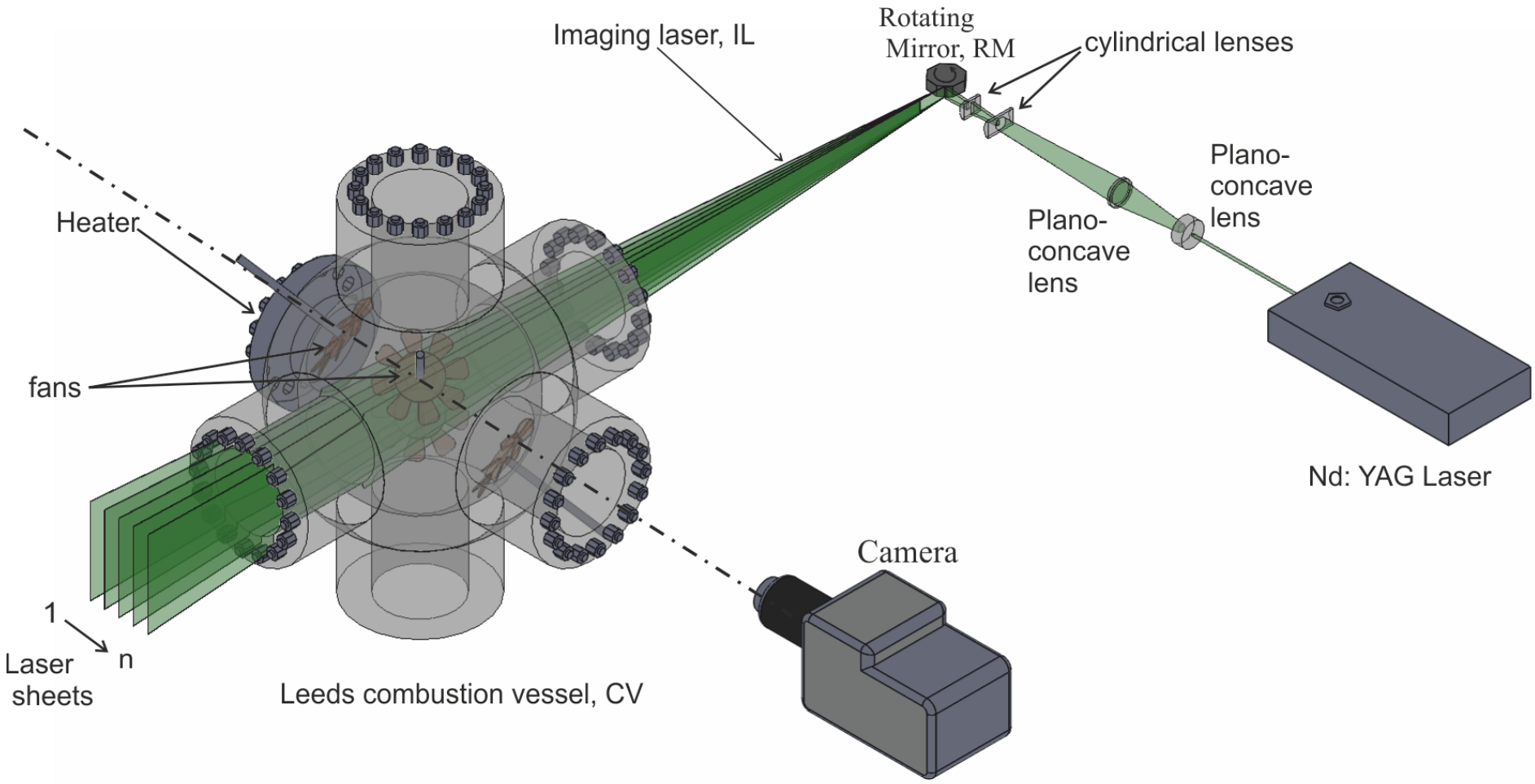


Figure 2.6 Schematic diagram of the 3D laser swinging sheet system.

### 2.3.3.1 Optics for creating laser sheets

A 532 nm Nd:YAG Imaging laser, IL, with two internal cavities each capable of repetition rates ranging from 5 kHz to 30 kHz, provided the pulsed light source with a pulse energy of 13mJ to 1.9 mJ respectively. Using a double cavity staggered pulsing, a maximum laser frequency of 60 Hz was achieved at a minimum pulse energy. The beam from the IL head was expanded through a 50.8 mm diameter, $\Phi$, plano-concave lens with focal length, $f$= -100mm, on to a plano-convex lens of $f$ =250 mm, and Φ =50 mm to focus at the centre of the CV in order to achieve a minimum sheet thickness of <0.6mm over a large focal distance of 100±5 mm. Using a pair of plano-convex cylindrical lens with focal lengths $f$ = 38.1 and $f$ = 25 mm, respectively, before the 16 facets rotating mirror RM, a vertically expanded IL sheet approximately 100 mm in height was generated across the central area of the CV. The details of optics and their distances are described in [12] and [155]. The RM was driven by a 30 V AC and 6 A motor. The speed of the RM was measured using a class 3B diode laser pointed towards it; a photo-diode, positioned to detect the diode laser beam. Images are recorded by a high speed Phantom digital camera, at frequencies 51k to 54k fps with an image resolution of 512x512 pixels. Laser ignition as discussed in Section 2.2.2 was used for initial spark. Synchronization of all the components such as the IL, $I_g$L and the camera, was critical, as time resolved data of flames were required [155] and this is discussed in Section 2.3.3.3.

### 2.3.3.2 Laser sheet geometry

The RM caused the IL sheet to reflect at an angle, from the centre plane of the CV, based on the RM speed. Therefore, it was important to understand the laser sheet geometry and its temporal variation before reconstructing the 3D flames. Shown in Fig. 2.7 are the details of the RM geometric offset and divergence of successive IL laser sheets. The IL sheet passing through the centre of the CV makes an angle 0 and is designated as $i = 0$, where $i$ is the

index of the sheet from the centre of the vessel. The angle between all the other sheets with respect to the centre of the CV is given by the equation

$$\zeta_n = \frac{360.\omega}{f_{IL}} i \quad (2.2)$$

where $\zeta_n$ is the angle made by the $i^{th}$ sheet with the centreline of the CV, $\omega$ is the angular rotating frequency of the RM in radians/s and $f_{\mathrm{IL}}$ is the imaging laser frequency in Hz. In addition to IL sheet divergence, the point of reflection on the RM causes a geometric offset, $a_i$, of each IL sheet from the centreline of the CV as illustrated in Fig. 2.7. It shows RM at time $t_0$ and after a time $t_0 + \frac{\omega}{dt}$ it rotates through an angle $\theta_m$. $A_m$ is half the distance between RM parallel faces. $X_m$ is the diagonal distance between the centre of the mirror face before and after rotation by angle $\theta_m$ and is given by

$$X_m = A_m Tan\theta_m \quad (2.3)$$

The geometric offset, $a_i$, is then calculated using the sine rule of a triangle given by

$$\frac{a_i}{sin\theta_m} = \frac{X_m}{\sin(45+\theta_m)}. \quad (2.4)$$

The time between two successive sheets is given by

$$t_{sIL} = \frac{1}{f_{IL}} \quad (2.5)$$

The time between two sweeps is given by

$$t_s = \frac{1}{\omega.n_f} \quad (2.6)$$

where $n_f$ is the number of faces on the RM. In the present study at ω=12 Hz and $n_f$=16, the time between two sweeps was 5.21ms. However, the time for each sweep with IL pulsing was around 1.44 ms. When RM rotates through an angle $\theta_m$, the angle of incident, $I_1$, made by IL with RM, does not change while the reflected ray $R_1$ shifts to $R_2$ and the normal shifts from $N_1$ to $N_2$. The new angle made by the $I_1$ with the new normal $N_2$ would be

$$\theta_{N2} = \theta_{N1} - \theta_m \quad (2.7)$$

The new angle of reflection, $R_2$,

$$\zeta = \theta_{N1} - [\theta_{N2} - \theta_m] = 2\theta_m \quad (2.8)$$

Therefore, for a given angle of rotation of $\theta_m$ for RM, the angle turned by each laser sheet was $2\theta_m$. The detailed calculations of laser beam diameters, required focal lengths of the lenses, the optical arrangement and the minimum waist diameter, $d_f$, of the IL, that determined the IL sheet thickness, are presented in [155].

For a given laser repetition rate, the rotating mirror speed determines both the sheet spacing and the number of sweeps through the combustion event. The lower the RM speed the closer the sheets, the lower the number of sweeps that could be recorded of the flame. Increasing the RM speed would have reduced the duration of each sweep allowing to capture more number of sweeps as the flame developed. Consequently, the number of sheets in each sweep would reduce and this would result in an increase in the distance between successive sheets, reducing the spatial resolution of the 3D reconstruction. A compromise was sought between these factors, to obtain a good 3D image resolution. Calculations were made to determine the number of images in a sweep and to ascertain the distance between two consecutive laser sheets was less than 1 mm. It was found that for the maximum IL frequency (54 kHz) that could be achieved with the present laser, the rotating mirror frequency of 12Hz delivered 78 images in a sweep. Given the sheet thickness of approximately 0.6 mm, the distance between two consecutive images was 0.7mm<1 mm. The detailed calculations to determine the number of sheets in a sweep are presented in APPENDIX A.

For the present work, IL and $I_g$L were pulsed at 51 up to 54 kHz and 12 Hz respectively. The frequency of the RM was kept at 12 Hz, typically, 73 to 78 sheets were recorded in each sweep of 1.44 ms. A high speed phantom V2012 digital camera placed orthogonal to the IL sheets captured the Mie-scattered images using a fixed macro lens of focal length 105 mm. The images

were captured with an exposure time of 6 μs, at a resolution of 512x512 pixels, and at a same sampling frequency of IL, however, with a finite lag between firing of IL and camera shutter opening.

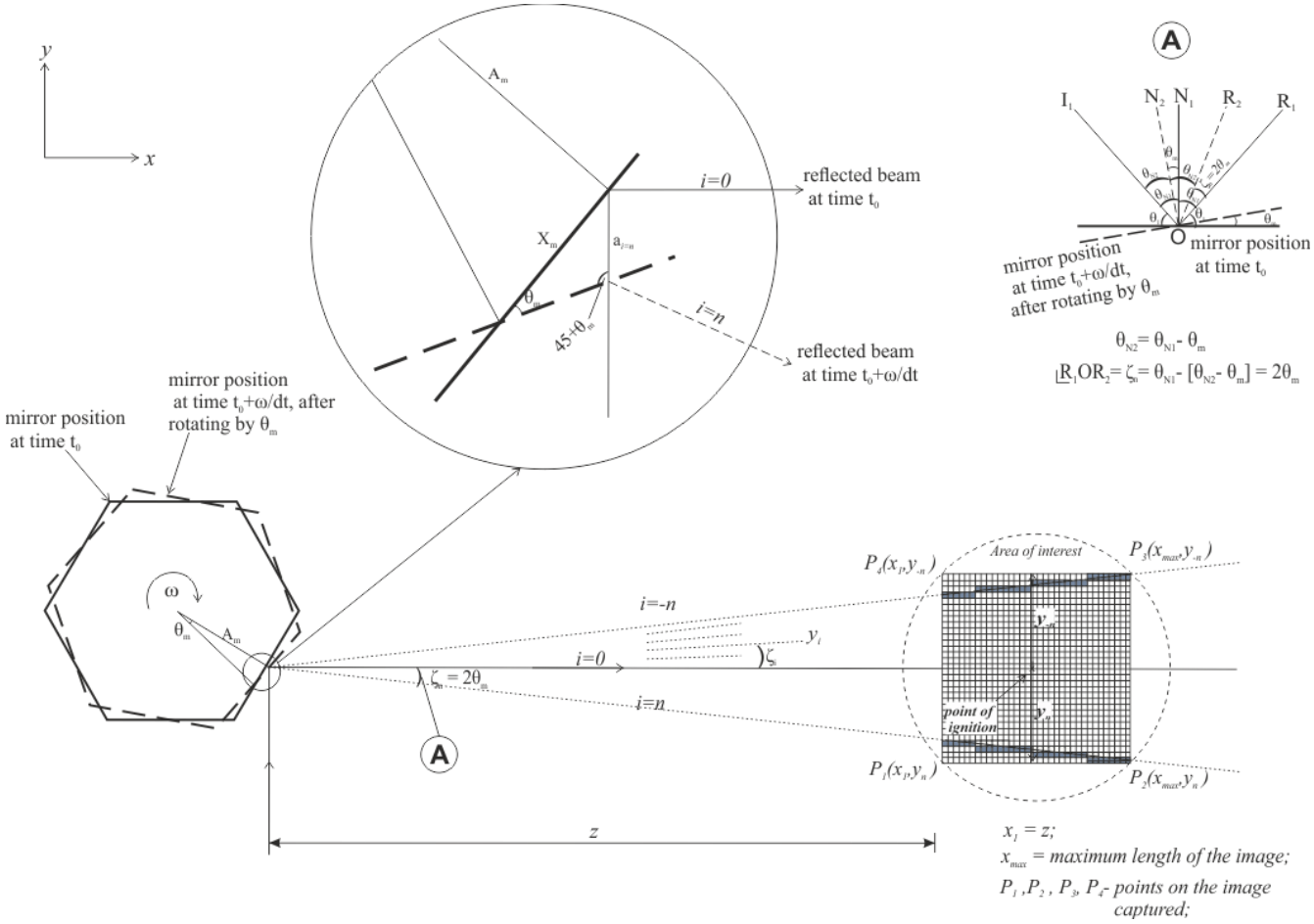


**Figure 2.7** Top view of the mirror geometric offset and divergence of successive laser sheets.

The pixel size of these Mie-scattered images was determined the same way as described in Section 2.3.2.1. However, because the recorded image size is a function of distance away from the recording camera, the recorded pixel resolution of individual laser sheets was also a function of their distance from the camera. The difference in distance of the first and last laser sheet in a sequence was 100 mm, resulting in the pixel resolution varying between 0.1827mm/pixel and 0.2095mm/pixel. This variation was taken into consideration during signal processing as described in Section 3.3.1.

As there is a finite time lag between the first flame image and the last flame image in one sweep of the IL sheet it was important to select flames that were slow enough that they do not grow significantly during the time of sweep. Consequently, only mixtures having a low laminar burning velocity, $u_l$ and at low turbulence levels could be investigated.

#### 2.3.3.3 Synchronisation and control system

The current synchronisation system was adopted from [155] and developed to include a New wave ignition laser, $\mathrm{I_gL}$. It was important to synchronise the Imaging Laser, Ignition Laser, rotating mirror and camera to obtain time-resolved data of the flames. Figure 2.8 shows the synchronisation system among all the components used in the present technique. All the components were required to be triggered relative to RM's position. Imaging laser, IL beam was directed on a given face of the mirror through a set of lenses and a continuous wave diode laser was projected at its opposite face. The reflected diode laser light was received by a photodiode (PD) detector. The relative positions of the mirror, PD detector and diode laser were adjusted such that the detector received light from the diode laser when the mirror was in its initial position to reflect the first IL sheet of light in a series. The path of the first IL sheet in a sequence could be fixed, by adjusting these components, so that the IL sheet just passed through the far end of the CV each time a new sweep starts.

Due to a weak output signal from the PD detector it was necessary to amplify the signal before it was supplied to a TGP 110 pulse generator to generate a gated signal. The IL pulsed laser light only when this gated signal was at its

maximum position. Therefore, by adjusting the gate signal pulse width, the sweep area of IL sheets and hence the position of the last IL sheet in the CV was set. This gate signal was sent to the IL controller, which was set to run at its own internal frequency.

The IL was pulsed in “Master/Slave” mode, whereby the first laser cavity controlled the second. The delay between pulsing of the Master and Slave cavities was set so as to symmetrically stagger the pulsing of the two cavities to achieve an overall pulse repetition frequency of 51 to 54 kHz. Only the Master cavity was capable of generating an sync output signal from the *IL* controller. This sync output signal at 25.5 to 27 kHz, was sent to a second TGP 110 pulse generator, where the signal was doubled to 51 to 54 kHz and inverted to produce a negative TTL signal. This negative TTL signal was then supplied to the camera, which recorded an image on each downward pulse it received. Each of the above mentioned signals, and their relationship to each other, are shown in Fig. 2.8.

The voltage amplifier, which received a signal of 192 Hz (12Hz RM x 16 faces) from PD detector also provided a signal to a frequency divider, FD, unit designed at Leeds. This FD unit converted the received input to a 12 Hz TTL signal by dividing it with a constant value of 16 to produce the required 12 Hz. This signal was supplied as an external frequency driving signal to the $I_gL$ controller, thereby, causing the ignition laser to trigger only once per complete rotation of the mirror.

While the IL synchronously pulsed with the RM continuously, the pressure and the image data were recorded only on the receipt of a trigger signal from the ignition laser controller. An image of the $I_gL$ and its schematic controller are shown in Fig. 2.9. The 12 Hz TTL signal from the FD was sent to a pulse generator 1. It was then sent to the $I_gL$ controller to Fire lamp, shown in Fig. 2.9. A delayed signal was also sent to a pulse generator 2 from PG1. This was further supplied to the $I_gL$ controller, as the second signal to Fire Q-switch, to activate the Q-switch for the ignition laser to pulse. Each of the signals synchronised are presented in Fig. 2.10.

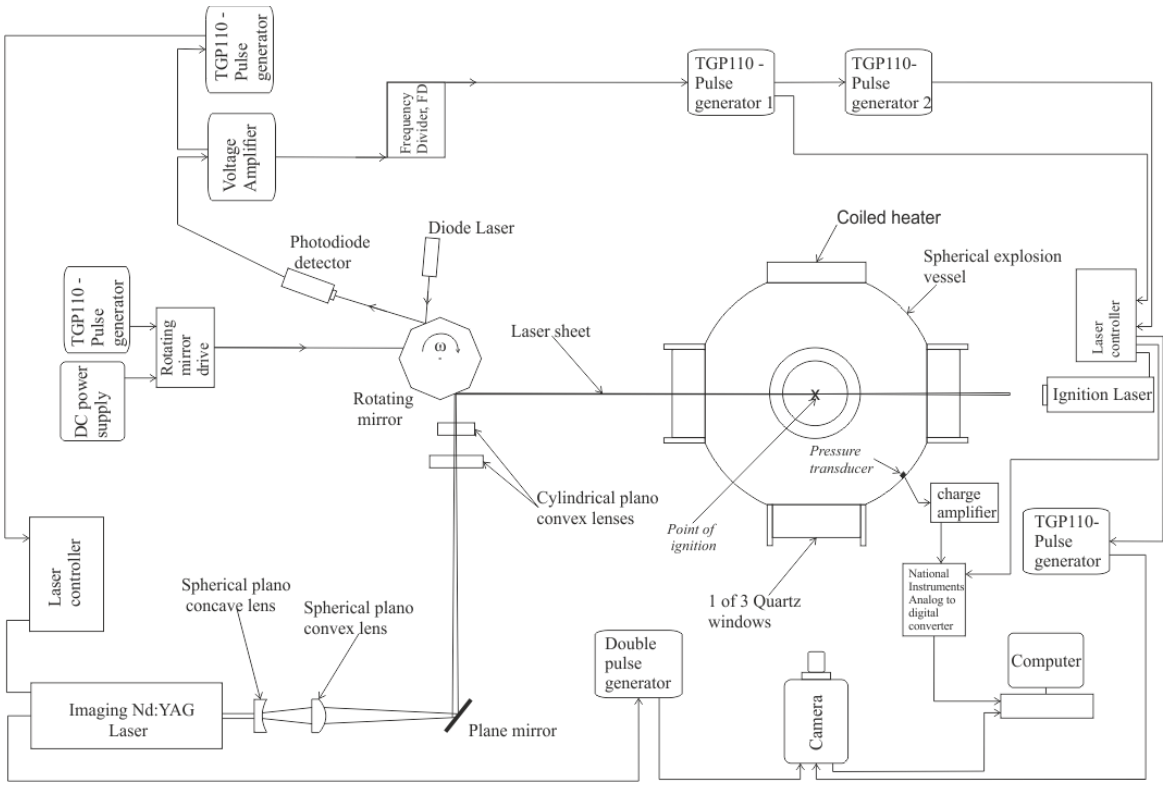


**Figure 2.8** Synchronisation of all components for swinging sheet technique.

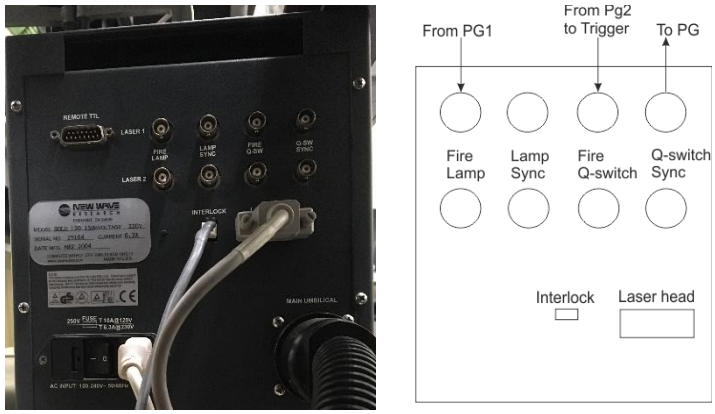


**Figure 2.9** Back view of an ignition laser controller showing the signals.

A synchronising CMOS output signal was generated by the ignition laser controller which was supplied to a further TGP110 pulse generator, converting it to a TTL signal before supplying it to the camera and the National Instruments ADC to initiate recording the data. Therefore, ignition occurred at recorded frame ‘0’ in the sequence of images and thus the time after ignition for each of these recorded images was known.

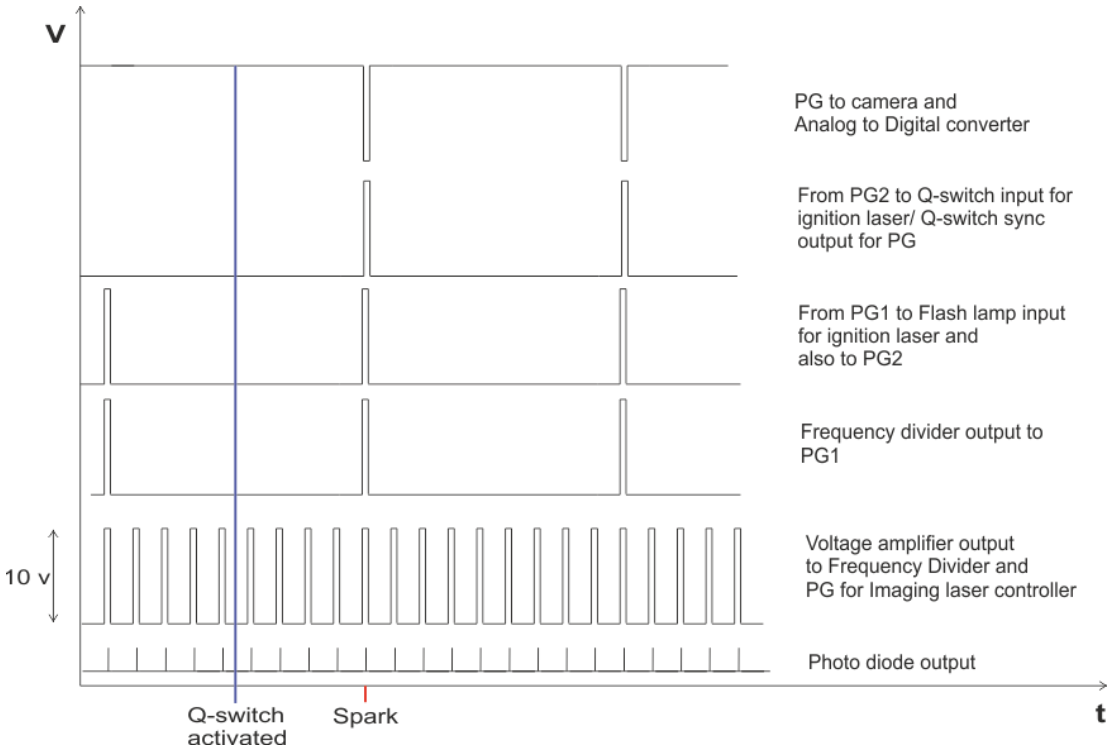


**Figure 2.10** Signals involved during triggering of an experiment.

### 2.3.3.4 Seeding particle generation

As discussed in Section 2.3.3, the present 3D swinging laser sheet technique requires Mie-scattering process to capture propagating flames. This was achieved by using olive oil droplets as seeding particles, with a typical diameter of 1.06 µm and a density of 970 kg/m$^3$ [156]. The role of seeding particles was essentially to reflect enough laser light from the unburned gas mixture, while remaining in suspension, to be captured by the high speed camera and also to evaporate readily in the presence of a flame. Many studies [156, 157] are conducted comparing different materials to be used as seeding particles in fluid flow analysis. Harker [157] at University of Leeds, conducted several tests using different seeding materials and concluded that olive oil droplets have the best desired characteristics of reflectance and entrainment time for Mie-scattering process. Therefore, for the present study these droplets were used. Moreover, it was important to ascertain that the amount of seeding particles do not influence the burning rates. Ben Thorne [155] studied the effect of seeding particles addition (between 0.015-0.02 MPa of

olive oil droplets) on the burning rates and found no significant change in the stretched flame speeds.

For a long suspension time, these olive oil droplets are required to have minimal diameters. However, they should be large enough to reflect sufficient laser light to be captured by the camera. Therefore, for the present study a PIVTech seed particle generator was used with three Laskin nozzles having two, four and eight orifices respectively with each nozzle supplied by a separate air supply control valve to vary the rate of seeding particles as required. This seeding particle generator operated at an inlet pressure of 0.15 MPa with a differential pressure of 0.05 and 0.07 MPa at inlet and outlet respectively. The preliminary tests results for this unit, supplied by the manufacturer, using di-ethyl hexyl sebacat (DEHS) seeding particles showed a peak particle size distribution of 0.9μm and a study conducted in [158] found the particle concentration of $1 \times 10^5$ particles/cm$^3$.

## 2.4 Experimental Procedure

Before starting the mixture preparation, an initial pressure leakage test was conducted to ascertain minimal leakage by pressurising the CV up to 0.5MPa and monitoring the static pressure every 10 seconds over a period of 10 mins. After a satisfactory pressure leakage test was conducted the CV was filled with air and vacuumed twice, up to $2.5 \times 10^{-3}$ MPa to ensure the CV was free from any residual gases. For all experiments the residual gases were kept as low as 0.06%. For high temperature experiments, the CV was pressurised with dry air and heated, by setting the desired value through the PID controller, to a much higher temperature than the required initial temperature for up to 2 hrs. Once the CV was found to be uniformly heated, it was allowed to cool down a few degrees higher than the required temperature before adding the fuel and air mixture.

1. Once the CV was ready and vacuumed, the fuel was added through the appropriate needle valve by monitoring the pressure on the digital static pressure gauge.

2. Up to 0.07 MPa Dry air was then added before the addition of seeding particles i.e. the olive oil droplets. 0.015 and 0.02 MPa amount of seeding particles were added to the mixtures for initial pressures of 0.1 and 0.5 MPa explosions respectively. This amount of seeding particles were found to give a reasonable compromise between laser light reflection and quality of the images captured. Some experiments were conducted using more than 0.2MPa of seeding particles which only resulted in extremely bright images, due to significant laser light scattering, and poor flame edge definition.
3. Following the addition of seeding particles, the CV was again filled with dry air up to the required initial pressure for explosion. While the mixture was being prepared, the fans were left running at 420 rpm i.e. at $u'$=0.5 m/s to aid temperature and mixture homogeneity.
4. The fans were run during mixture preparation, both to ensure full mixing and to assist uniform heat transfer. For laminar studies the fans were switched off for a period of 20 s, following mixture preparation, before ignition. For turbulent flame explosions, the fan speed was set to the desired speed and 4- 8 s of time was allowed for the mixture turbulence to develop and stabilise before igniting the spark.
5. Once the required temperature, pressure and rms turbulent velocity is reached, the inlet air supply and the static pressure transducer were isolated, and the Q-switch for laser ignition was activated to create spark for explosion.
6. After an experiment, the vessel was flushed with compressed air and then evacuated twice. Dry air from a cylinder was used in preparation of the combustible mixture. Liquid fuel was injected with a gas tight syringe, through a needle valve, and gaseous fuel was supplied directly.
7. After a successful explosion experiment, the exhaust valve was opened to release the combustion products and to depressurise the CV to a safe level following which the inlet air supply valve was reopened that flushed any remaining combustion products with dry air.

8. While the air supply valve continued flushing the CV, the acquired data such as the images captured by the camera and the pressure record by LabVIEW software were saved and the software systems were reset. The CV was then prepared for the next experiment by vacuuming and dry air filling in the same way as described above.

### 2.4.1 Thermodynamic properties of all Fuel Mixtures

The thermodynamic properties such as unburned, $\rho_u$, and mean burned gas densities, $\bar{\rho}_b$, kinematic viscosity, $\nu$, of fuel/air mixtures were calculated using a chemical equilibrium software called Gaseq [57], at constant pressure conditions (assuming no pressure rise during the flame propagation close to the vessel's windows) and mean adiabatic temperature, $\bar{T}_b$.

# Chapter 3

# Data Processing Techniques

## 3.1 Introduction

This chapter describes the data processing techniques used to process the acquired data, using the methods described in Chapter 2. Many algorithms were written in MATLAB by the author. Some of the algorithms inherited from other authors have been significantly improved to perform much faster. Nevertheless, due acknowledgement is provided wherever appropriate. In addition, an open source software called MeshLab was also used for surface smoothing of the reconstructed 3D images of flames. Moreover, MeshLab and SOLIDWORKS software were also used to validate the surface areas obtained using the present author's algorithms written in MATLAB.

## 3.2 Schlieren image processing

In the present study, the schlieren images obtained, using the technique presented in Section 2.3.2, were processed to obtain $u_l$ and $u_t$. Each recorded experiment consisted of several hundreds of schlieren images which were processed to define an appropriate flame edge in each image and to identify the onset of cellularity, if any, using algorithms developed by Sharpe [159].

### 3.2.1 Flame radius detection for laminar flames

Shown in Fig. 3.1 are typical images of a developing laminar flame captured during an explosion. Images were recorded at 5400 frames/second and every $8^{th}$ frame is shown. Flames moved outwards from the spark, consuming unburned gases. An algorithm developed in MATLAB was used to identify the outer edge of the flame front. The steps used to determine the flame edge are illustrated in Fig. 3.2, taken from Mumby [152]. The flame in Fig. 3.2(a)

represents a cellular flame. A spark plug protruding through the flame can be seen which was required to be removed before defining a flame edge. Using the image prior to ignition, shown in Fig. 3.1, the window edge and the spark plug tip were identified. As shown in Fig. 3.2(b), the spark plug region was masked off using a circa 22.5 degree section from either side of the spark plug tip. The resulting coordinates were saved and applied as a frame of reference to every subsequent flame image. Starting from the largest flame image within the observable window, the saved coordinates of the window and spark plug were superimposed and the flame edge was detected using a level set approach [150, 152, 160], highlighted as blue line in Fig. 3.2(c). A best fit curve was then obtained as shown by the solid grey circle. From the curve, the mean radius was obtained and this served as an initial level set starting point for the next flame image. The obtained mean radius from each flame image was saved to a file for further processing. Fuller details of the level set technique are presented in [160] and [150, 152].

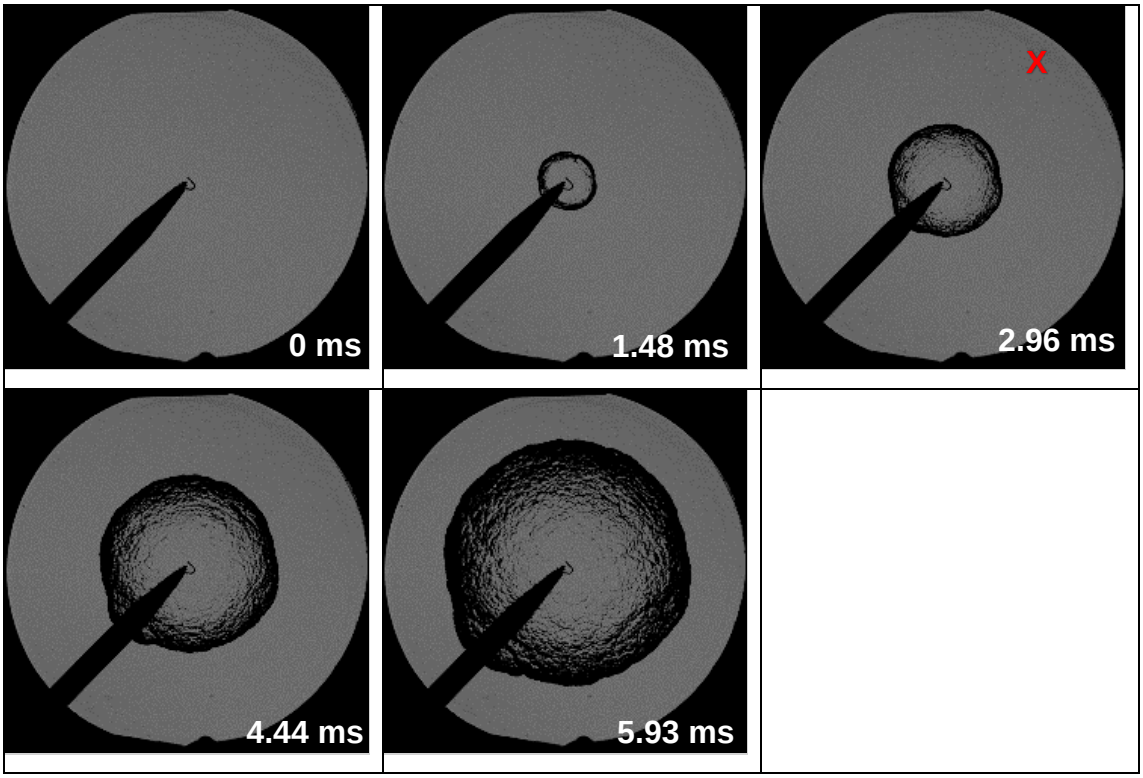


**Figure 3.1** Schlieren images of laminar $i$-octane/air flames at $\phi$ = 1.2, 0.5 MPa and 360 K. The time of each image from ignition within the captured sequence is shown. Cross symbol indicates the onset of cellularity.

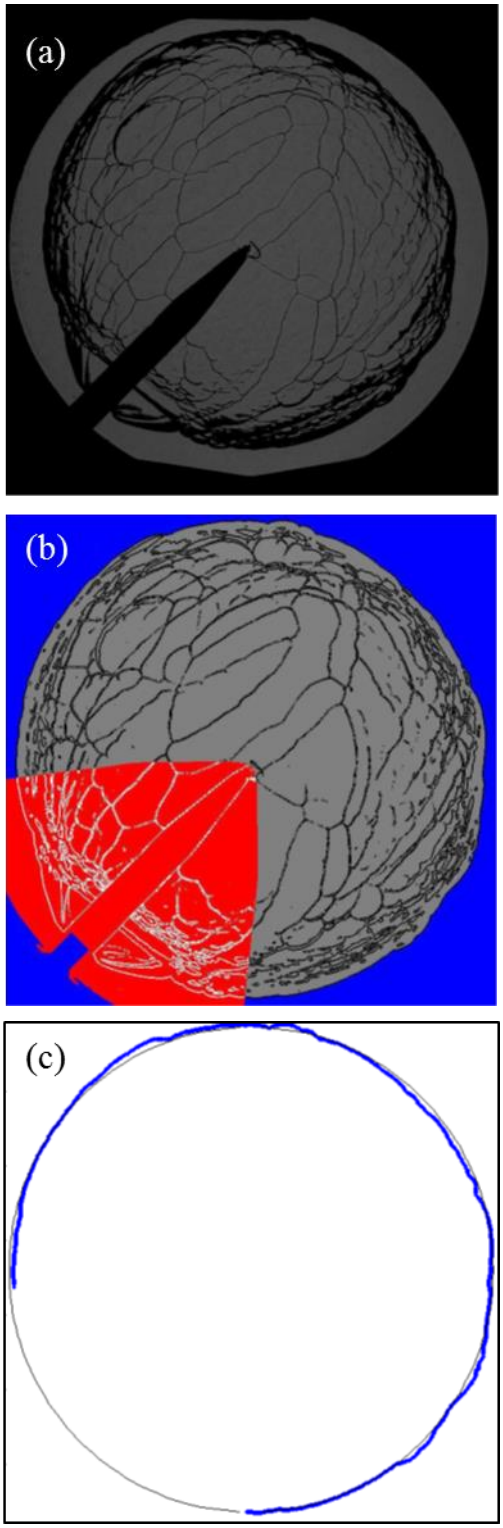


**Figure 3.2** (a) Raw schlieren laminar flame image (b) Flame identification and spark plug masking (c) Identified flame edge shown as blue solid line and grey circle as best fit. Figure taken from Mumby [152].

### 3.2.2 Flame speeds, laminar burning velocity, and Markstein length.

The process mentioned in Section 3.2.1 yielded a data set of radii as a function of time. Using this set of data, the stretched flame speed, $S_n$, as a function of stretch rate, $\alpha$, and radius, was calculated using Eqs. (1.1) to (1.3). The sequence of $S_n$ within the stable, non-cellular, regime was then extrapolated to zero stretch to yield the unstretched laminar flame speed, $S_s$. This was subsequently used to deduce $u_l$ and $L_b$ as described in Section 1.3.2. Fuller details for deducing these parameters are presented in [21, 152].

### 3.2.3 Determination of Flame radius for turbulent flames

Shown in Fig. 3.3(a), is a typical raw turbulent flame image. The process of identifying the window edge is the same as mentioned in Section 3.2.1. As shown in Fig. 3.3(b), the raw image was first rotated through an angle of 225.5°. The spark plug was then masked off (highlighted as red) by determining its coordinates from the image prior to ignition. The outer edge of the flame, shown in Fig. 3.3(b) with background as blue, is determined based on a similar level set threshold approach for laminar flames [150, 160] in MATLAB. After removing the spark plug, the flame edge points on either side of the spark plug is joined through a straight line to close the flame contour. Once the flame edge was detected, the image is binarised with flame represented by white pixels, as shown in Fig. 3.3(c), having a value of 1 while the rest of the image is made black with value 0. The projected area from the white pixels is calculated and is equated to the area of a circle to determine mean radius, $r_{sch}$.

### 3.2.4 Determination of turbulent flame speed and turbulent burning velocity

Once $r_{sch}$ is known, through the process presented in Section 3.2.3, as a function of time, the turbulent flame speed, $S_{sch}$, and turbulent burning velocity, $u_{tr}$, are calculated using Eq. (1.38).

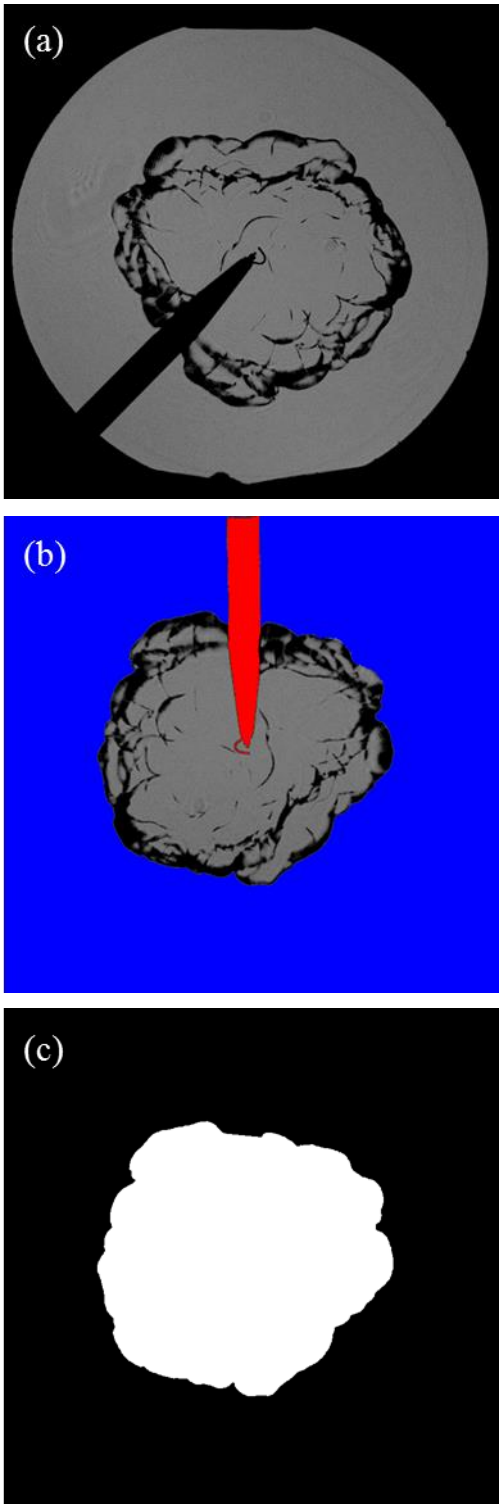


**Figure 3.3** (a) Raw schlieren image of a turbulent flame (b) Flame identification and spark plug masking (c) Identified flame edge shown as the boundary between white and black.

## 3.2 Pressure Data Processing for Turbulent Burning Velocity

Pressure measurements (Section 2.3.1) were used to obtain turbulent mass burning velocity, $u_{tm}$, by assuming that the fractional pressure rise is proportional to the fractional mass burned [87]. Values of $u_{tm}$ were evaluated based on a radius, $r_m$, within which resides the mass of all the burned gas and outside which resides the mass of all the unburned gas i.e $m_{ui} = m_{bo}$ [21] (See Fig. 1.5). Figure 3.4 shows a typical pressure against time record during an explosion of a $CH_4$/air mixture at $\phi$ =1.25, and initial temperature and pressure of 365K and 0.5 MPa.

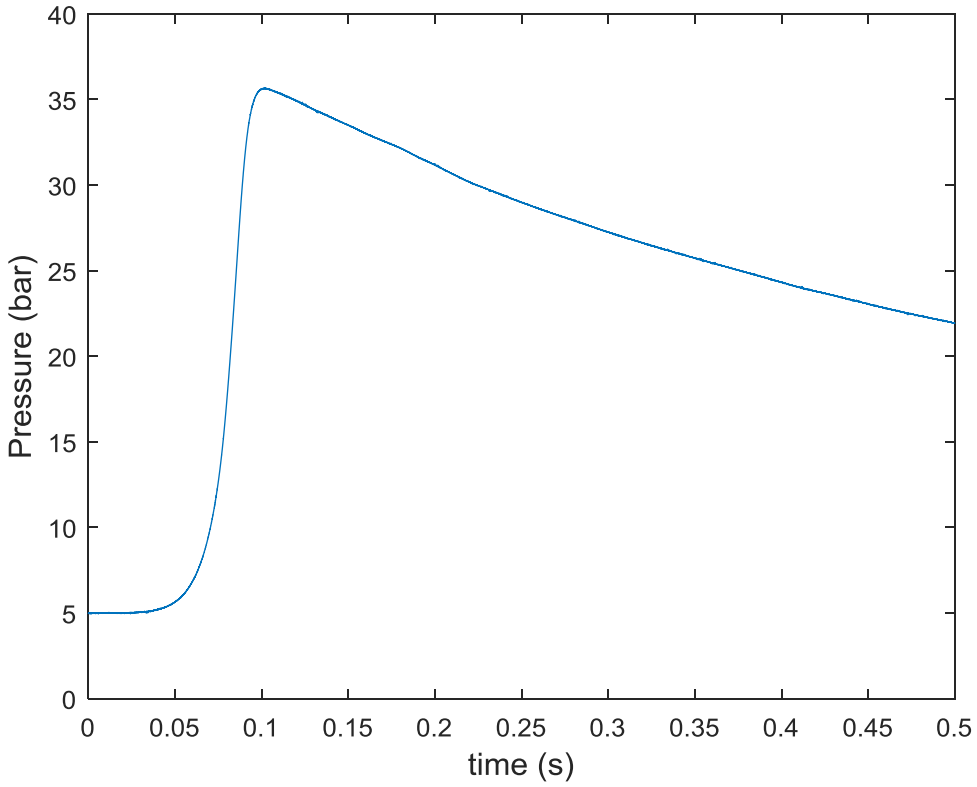


**Figure 3.4** Typical pressure record obtained during an explosion of $CH_4$/air, $\phi$ =1.25 at 365K and 0.5 MPa.

Before calculating $u_{tm}$, it was necessary to smooth the pressure vs time data to increase the signal to noise ratio without distorting the pressure signal. This was obtained using an algorithm (See Apendix B.1) developed in MATLAB by the present author. A Savitzky-Golay finite impulse response (FIR) smoothing filter [161] of order 1 and frame length of 15 was used that

smoothed the 25k data set points and yielded a smoothed data set of approximately 1660 data points for each explosion. The reduced smoothed data points are shown as orange crosses in Fig. 3.5 along with the original data points in blue. A magnified version is also presented in the same graph that shows the scatter in the original data set along with the smoothed data, set of orange crosses, closely following the original pressure signal.

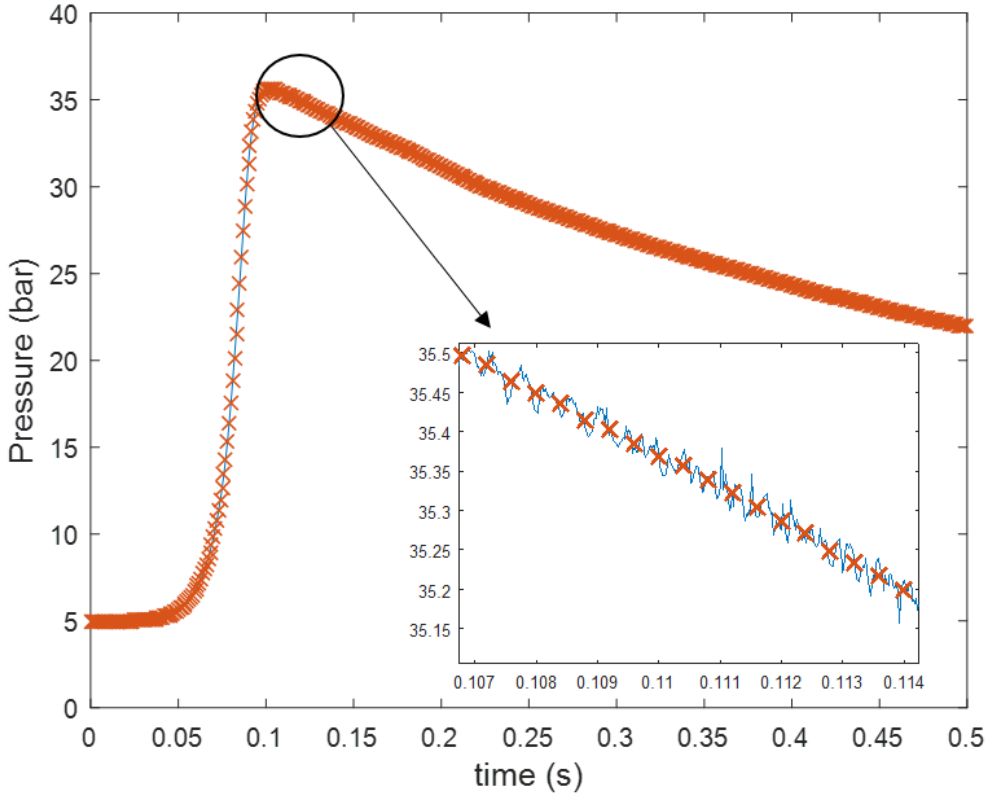


**Figure 3.5** Smoothed pressure/time data using Savitzky-Golay smoothing filter [9].

Once the data is smoothed, the peak pressure, $P_f$, is determined, the mean radius $r_m$ and the turbulent mass burning velocity, $u_{tm}$, are calculated using an algorithm developed by the present author in MATLAB based on the Eqs. (1.40) and (1.41), $u_{tm}$ values were also calculated choosing four different frame lengths to check its effect and is shown in Fig. 3.6. No noticeable difference in the values of $u_{tm}$ were observed until a flame radius of 150 mm. Differences can be seen beyond this radius, however, no data was used for the analysis in this region. Moreover, only after a radius of 30 mm, reliable $u_{tm}$ values were obtained because of a very little or no pressure rise during the

initial stages of flame development. More details of data processing technique for pressure measurements are presented in [77].

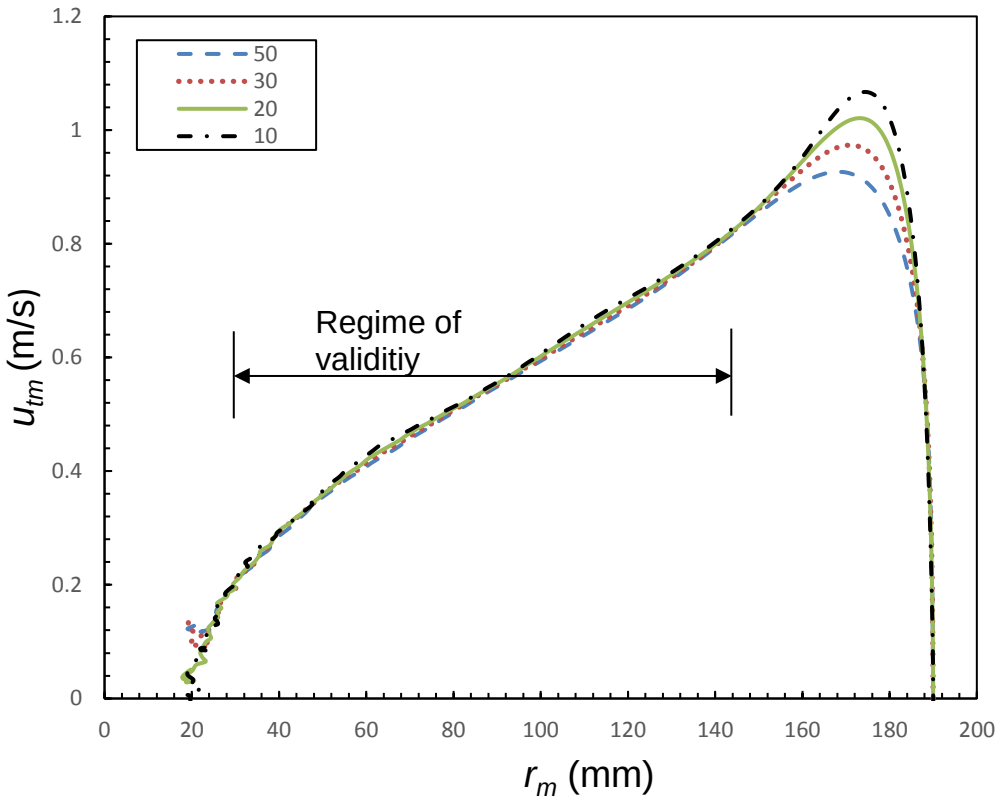


**Figure 3.6** Calculated $u_{tm}$ against mean radius $r_m$ using four different frame lengths.

## 3.3 3D swinging laser sheet image processing

For each explosion, depending on the speed of propagation of the flame, the 3D swinging laser sheet technique, described in Section 2.3.3, yielded a small number (between 2 and 9) of sweeps containing sets of 2D Mie-scattered images. The details of processing these images are presented in the following subsections.

### 3.3.1 2D Laser Mie-scattered image processing

Each sweep of the swinging laser sheet resulted in 78 greyscale TIFF images, at Imaging laser, IL, frequency of 54 kHz, through a developing flame. The resolution of each TIFF image was 512 x 512 pixels, however, as discussed in Section 2.3.3.2, the pixel size varied linearly between 0.1827 x 0.1827

$mm^2$/pixel and 0.2095 x 0.2095 $mm^2$/pixel for the closest and the farthest laser sheet image to the camera. Based on the distance of the 2D laser sheet image from the camera, the pixel sizes for each 2D sheet in the sequence (in each sweep) were determined before assembling them into a 3D matrix, described in Section 3.3.2.

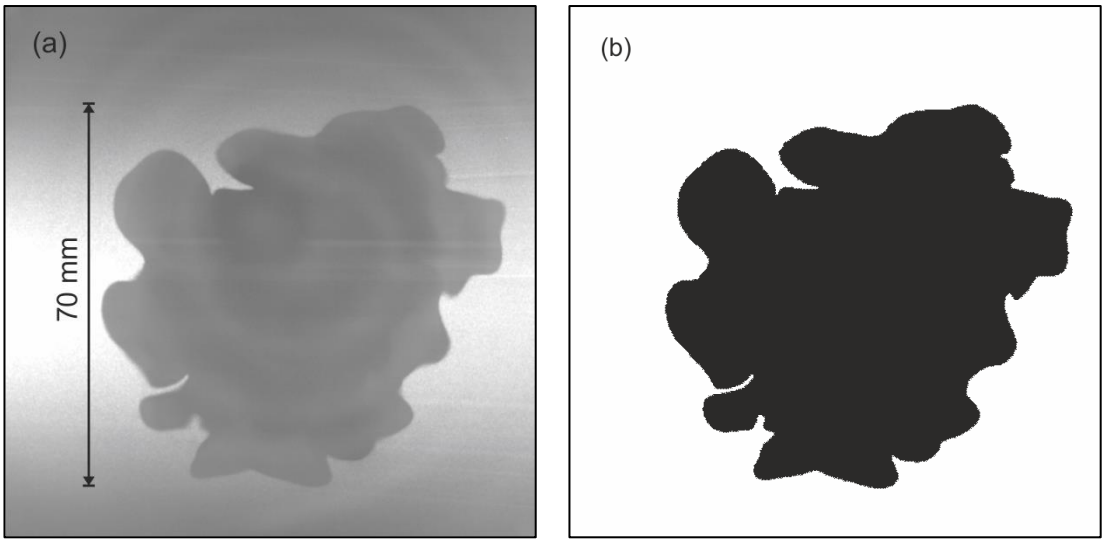


**Figure 3.7** (a) Raw Mie-scattered image (b) Binarised image.

Shown in Fig. 3.7(a) is a typical raw 2D Mie-scattered image acquired during the explosion for a $CH_4$/air explosion at $\phi$ =0.7, $P$=0.1 MPa, $T$=300K and at a fairly mild level of turbulence of $u'$=0.3 m/s. The dark region represents the presence of burned gas while the illuminated region is due to light scattered from seeding particles and represents the unburned mixture. The laser beam, and hence the generated laser sheets had a Gaussian intensity, with the sheet being brighter along its horizontal centreline than at its edges. This can be seen in Fig 3.7(a) by the brighter area in the approximately central horizontal third of the image. The flame imaged in Fig. 3.7(a) was mildly wrinkled and as a result, the flame edge was clearly defined. The height and width of each image was 100.35 mm.

These raw flame images were binarised, as shown in Fig. 3.7(b) before using them for 3D reconstruction. This was achieved using built-in filter functions in MATLAB such as *log* (Laplacian of Gaussian) edge detection algorithm. The Laplacian filter detects the flame edge based on a certain gradient, using

either the default value or a user defined value, while the Gaussian filter helps in reducing the noise. This two-step process resulted in a good compromise by successfully detecting the flame edges and minimising the spurious edge detection caused due to the intensity difference in the image background. Once the flame edge was detected, the enclosed area in the binary image is filled using *imfill* function, where the white (value 1) and black (value 0) pixels represent burned and unburned gas respectively. Furthermore, the noise in the resulting binary image was removed using different built-in filter functions in MATLAB that identify the noise/white spurious pixels against a certain user defined threshold to ascertain that small flame bits, particularly observed in high turbulence flames, were not accidentally removed. Finally, the function *imcomplement* was used to invert the pixel values thereby leaving the final binary image showing flame as black pixels and the background white.

Shown in Fig. 3.8 are slices through the centre of three flames of $CH_4$/air at $\phi$ =0.1.4, 0.1 MPa, 300K and at different values of $u$'. At the lowest $u$' of 0.3 m/s, shown in Fig. 3.8(a) the flame edge is well defined and are binarised as describe in above paragraphs. At a value of $u$' of 0.75 m/s, shown in Fig. 3.8(b), the flame surface is generally intact and well defined, but contains some wispy regions, as indicated by a broken circle. These regions are probably a result of some seed particles evaporating in highly turbulent regions. At the higher turbulence of $u$' of 2.0 m/s, at which Fig. 3.8(c) represents a typical image, edge detection proved to be problematic as wispy regions are more apparent. It is probably that wispy regions appear in Fig. 3.8(c) due to partial flame quenching, discussed in Section 1.4.4, where hot, partially quenched, combustion gases are mixed with the unburned reactants. This is supported by Fig. 1.6 in which the conditions for Fig. 3.8(c) ($Ma_{sr}$ =4, $K$= 0.79) show the flame to exist close to the quench regime. At higher turbulent intensities, the method adopted to binarise the raw images was to threshold the images such that wisps below a certain intensity were removed.

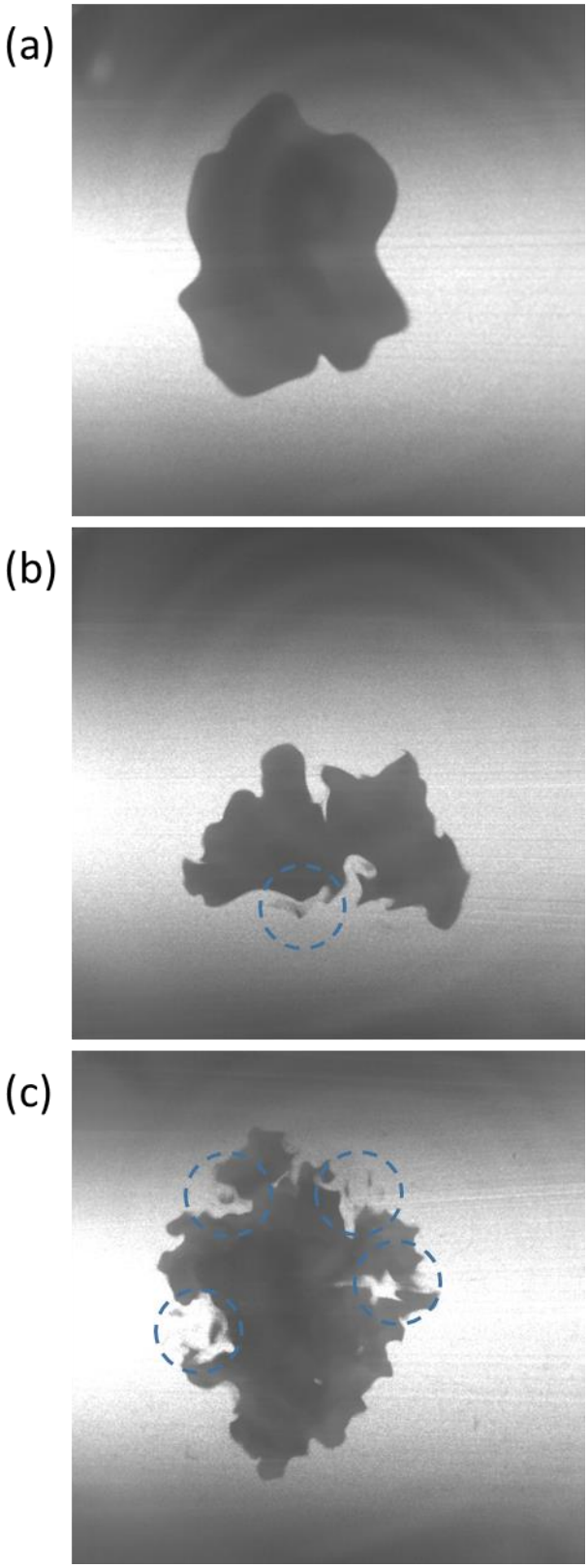


**Figure 3.8** 2D Mie-scattered images of flames at (a) $u'$=0.3 m/s, (b) $u'$=0.75 m/s, (c) $u'$=2.0 m/s.

### 3.3.2 3D flame reconstruction/assembly

The binarised 2D images after successful flame edge detection were assembled in a 3D matrix following which interpolation between the sheets was carried out to generate the 3D flame structure. Subsequently, a triangulated surface mesh was then generated, which upon smoothing, yielded a visual representation of the 3D flame. The steps involved in this process are described in detail in the following sub-sections.

#### 3.3.2.1 2D flame sheets assembly in a 3D matrix

A 3D volume matrix of 512 x 512 x 512 size was generated with each volume (3D) element, called voxel, pre-allocated a value of unity representing unburned mixture. The pixel values of each binary 2D flame sheet were then inserted into the 3D matrix based on its geometric offset ($a_i$) and the angle ($\theta_m$) made by it with the centre sheet. These parameters, calculated using the Eqs. (2.3) and (2.4), were used to generate a straight line equation given by

$$z = tan\theta_m \,.\, x + a_i \qquad (3.1)$$

Thus, for any x/y coordinate in the 2D image, the corresponding $z$ coordinate in the third dimension was calculated. The process was then repeated for all the 2D sheets in a sweep to insert the values of 2D pixels in the corresponding coordinates in the 3D matrix (shown as grid in Fig. 2.7 in the area of interest). Because of the finite resolution in the array, the values of $z$ coordinate were rounded off to the nearest integer. This resulted in a slightly stepped appearance of the inserted sheet, shown as filled squares in the grid in Fig. 2.7, where the stepped appearance has been exaggerated for clarity.

#### 3.3.2.2 Interpolation, surface mesh generation and mesh smoothing

Figure 3.9(a) shows a cross-section, through the Y-axis, of the assembled 2D sheets (into the 3D matrix) of a $CH_4$/air flame at 26.75 ms after ignition at $\phi$ =0.7, *P*=0.1 MPa, $T$=300K and at $u'$=0.3 m/s. The finite spacing between the successive sheets (seen in Fig. 3.9(a)) as discussed in section 2.3.3, was filled using a built-in interpolation function called *imdilate* in MATLAB. It was

necessary to interpolate between the sheets in order to generate a solid reconstruction and subsequent mesh generation of 3D flames. The *imdilate* function thickened the sheets to complete the existing spacing between the sheets. As a result, a solid 3D flame structure was generated whose cross-section through the z-axis is shown in Fig. 3.9(b).

The dilation method was selected over cubic/linear interpolation as the sheet spacing was only 2-3 pixels between successive sheets. This was insufficient to generate a reasonable line or a curve. Moreover, such algorithms can join incorrect closest points, especially in the areas of negative curvature, as shown by a blue dashed circle in Fig. 3.9(a), leading to erratic interpolation. These possible errors were minimised, though not entirely removed, using the current dilation method.

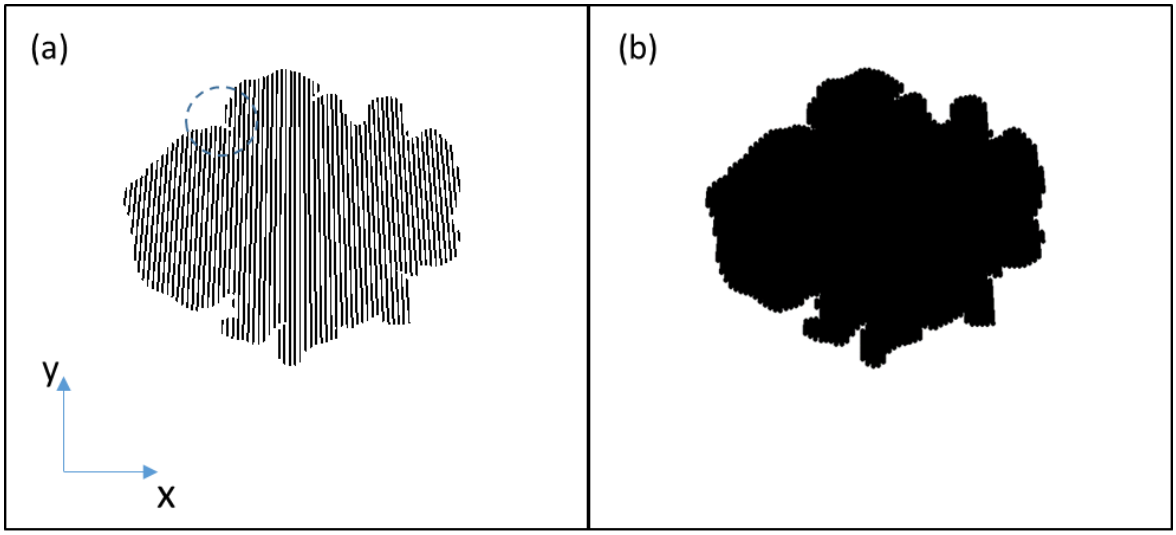


**Figure 3.9** A view of the cross section through z-axis of (a) the assembled 2D sheets into 3D matrix with finite sheet spacing (b) the solid 3D flame structure after interpolation.

Following interpolation, a triangulated surface mesh was generated using *isosurface* and *patch* functions in MATLAB. The *isosurface* command generates coordinates corresponding to a user defined isovalue positions, between 0 and 1 and in the present work a value of 0.5 was used. Using the list of isovalue coordinates, the *patch* function generated a triangulated surface mesh (shown in Fig. 3.12(b)), linked by vertices at the coordinates

returned by the *isosurface* function. Figure 3.10(a) shows the resulting surface mesh structure after importing it into MeshLab. The stepped appearance discussed in Section 3.3.2.1 can also be seen from this figure.

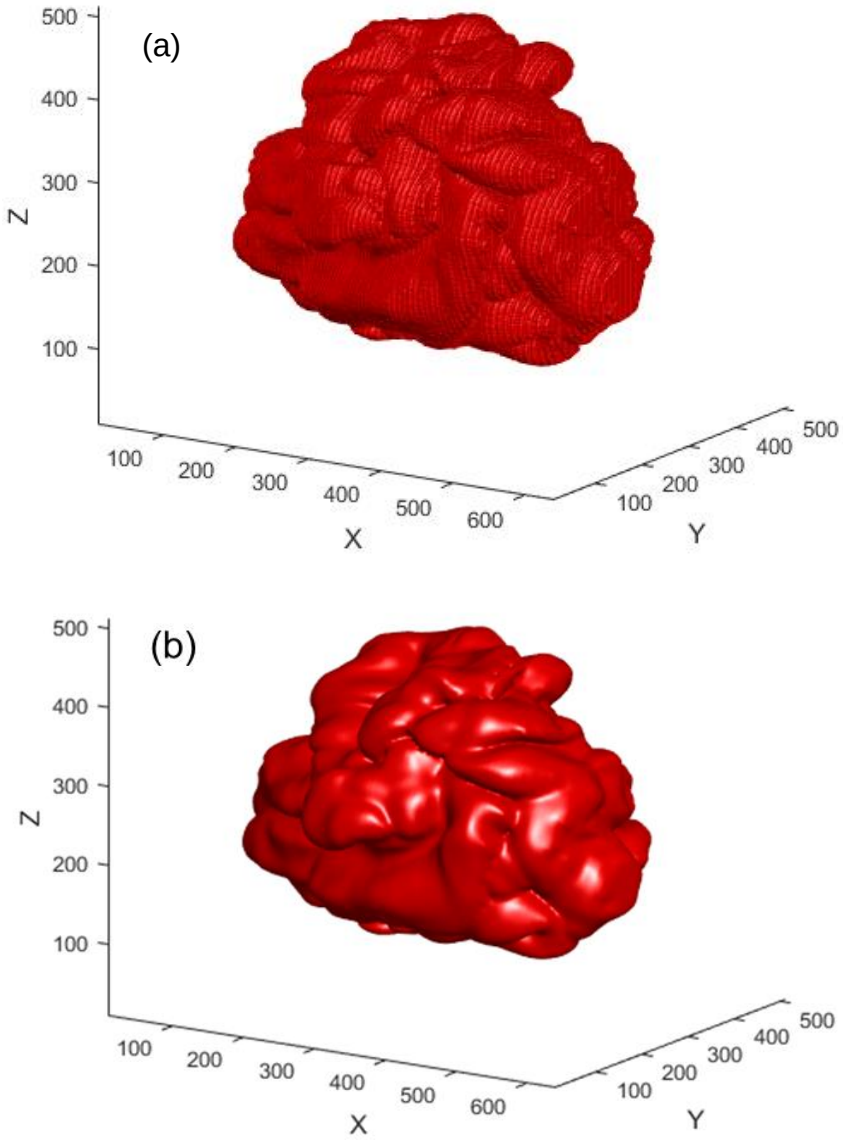


**Figure 3.10** 3D reconstructed triangulated (a) unsmoothed (b) smooth surface mesh structure of a $CH_4$/air flame at $\phi$ =0.7, P=0.1 MPa, $T$=300K and at low turbulence of $u'$=0.3 m/s at 26.75 ms after ignition.

The step and flat surfaces were later eliminated using interpolative smoothing algorithm given by Taubin [162]. This algorithm minimised shrinkage and retained the surface features of the reconstructed flame. This method operates by moving the vertices of the triangulated surface without altering

the connectivity of the faces. Therefore, the operated surface contains exactly the same number of verities and faces as the original surface. The unsmoothed image in Fig. 3.10(a), was smoothed and is shown in Fig 3.10(b). Flat faces and steps can be seen in the unsmoothed reconstruction, Fig. 3.10(a), while the smoothed version, Fig. 3.10(b), displays none of these leaving the surface features such as flame wrinkles intact. Details of quantitative analysis of the effect of surface smoothing and increasing $u'$ on total surface area are presented in [155].

### 3.3.3 3D reconstructed flame analysis

Three dimensional flame parameters such as total flame surface area, $A$, mean flame surface area, $a_v$ (based on balancing of burned and unburned volume) and $a_m$ (based on balancing of burned and unburned masses), flame volume, were evaluated. Such parameters are often readily obtained computationally [93], not adequately experimentally. This section presents the methodology used to obtain quantitative information on these aforementioned 3D parameters from the 3D reconstructions in the present work. The details of calculating each parameter are presented in the following sub-sections.

#### 3.3.3.1 Total flame surface area/ wrinkled flame area

Figure 3.11(a) shows a 3D reconstructed $CH_4$/air flame at time 26.75 ms after ignition. It is a triangulated mesh with 2,000,000 triangles with three Cartesian coordinates at each point of the triangle. Due to a large number of triangles, the flame in Fig. 3.11(a) looks smoother whereas in Fig. 3.11(b) the same flame is shown with only 20,000 triangles revealing the triangular structure. The total flame surface area, $A$, is now found by calculating the area of each triangle on the flame surface and then summing up areas of all the triangles using the method described below.

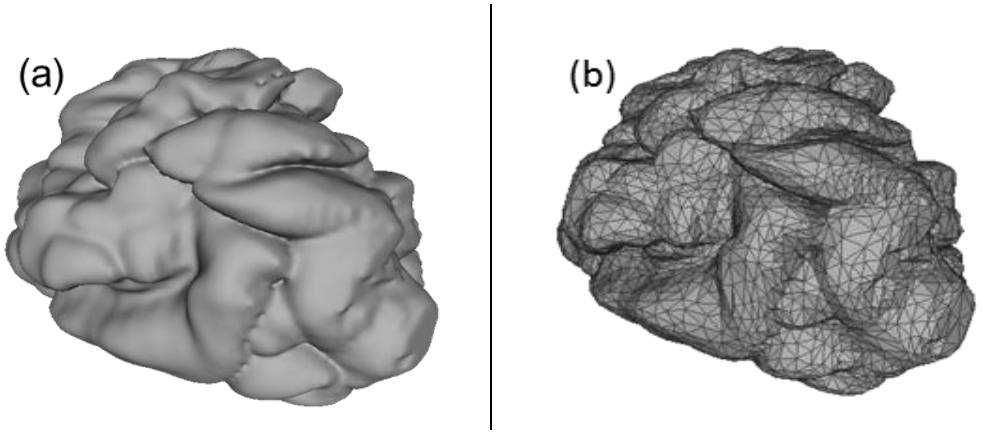


2,000,000 triangles 20,000 triangles

**Figure 3.11** Smoothed $CH_4$/air flame at $\phi$ =0.7, *P*=0.1 MPa, $T$=300K and at low turbulence of $u'$=0.3 m/s at 26.75 ms after ignition with (a) 2, 000,000 triangles (b) 20,000 triangles.

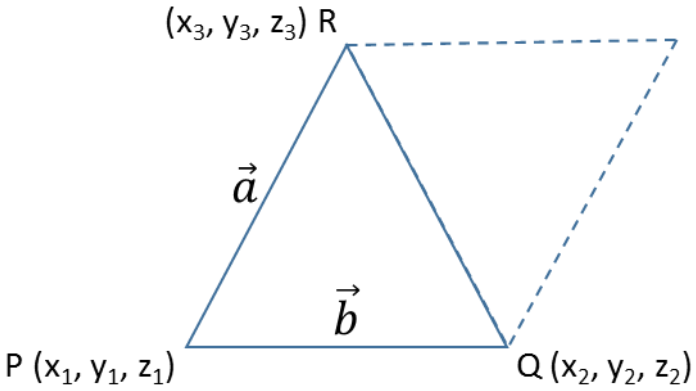


**Figure 3.12** Triangle with vertices P, Q and R and the vectors $\vec{a}$ and $\vec{b}$ resulting from PR and PQ respectively.

A surface area algorithm was developed in MATLAB, based on the concept of cross product of two vectors [163] which represent the sides of a triangle in a triangular mesh. Shown in Fig. 3.12 is a triangle with P, Q, and R as vertices and index I. If *i, j, k* are unit vectors in the x, y and z direction respectively then $\vec{a}$, $\vec{b}$ are vectors formed from vertices PR and PQ respectively. The magnitude of cross product of these two vectors, as sides of the parallelogram, gives the area of the parallelogram made by them. The area of the triangle formed by these vectors is then given by

$$A_I = \frac{1}{2}\left|\vec{a} \times \vec{b}\right| \qquad (3.2)$$

Now, the total sum of areas of all the triangles gives the total surface area, $A$, of the turbulent flame as

$$A = \sum A_I \qquad (3.3)$$

#### 3.3.3.2 Validation of total flame surface areas using different geometries

The algorithms developed for calculating total surface areas, $A$, in the present study were validated using two different software namely MeshLab [164] and SOLIDWORKS [165]. Five different geometries, as shown in Fig. 3.13, that include a sphere, cylinder, torus, spheres on sphere and a symmetrical spinning top geometry of known dimensions were created. For a better understanding, two different views of the symmetrical spinning top geometry consisting of both positive and negative curvature surfaces is shown in Fig. 3.13(e). Real flame shapes are complex due to the influences of the spectrum of turbulence and its possible interplay with thermos-diffusive instabilities (See the regime at low K in Fig. 1.6). Therefore, simplified geometries that represent all the possible shapes that may form part of the complicated flame shapes are chosen. A turbulent flame consists of combinations of cusps and a troughs that has negative and positive curvatures and this is clearly demonstrated through the simplified shape in Fig. 3.13(e). Moreover, the analytical solutions to these simplified geometries are well established that adds confidence to the present validation. These geometries were imported into the present authors algorithm developed in MATLAB and the values of $A$ were calculated. Furthermore, these geometries were also imported into MeshLab and SOLIDWORKS environment and the values of $A$ were evaluated again. The values of $A$ from all three algorithms in different software are tabulated in Table 3.1. The difference was found to be less than 1% thereby imparting confidence in the algorithms developed by the present author.

**Table 3.1** Total surface area, *A*, for different geometries considered

| | Total Surface Areas, $A$, ($cm^2$) | | | |
|---|---|---|---|---|
| | Present Algorithms (MATLAB) | MeshLab [164] | SOLIDWORKS [165] | % difference |
| Sphere | 12.562 | 12.561 | 12.566 | 0.03512 |
| cylinder | 25.118 | 25.118 | 25.132 | 0.05521 |
| torus | 118.414 | 118.415 | 118.435 | 0.01687 |
| Random design | 365.458 | 365.458 | 366.092 | 0.17338 |
| symmetrical spinning top | 56.0367 | 56.037 | 56.155 | 0.20952 |

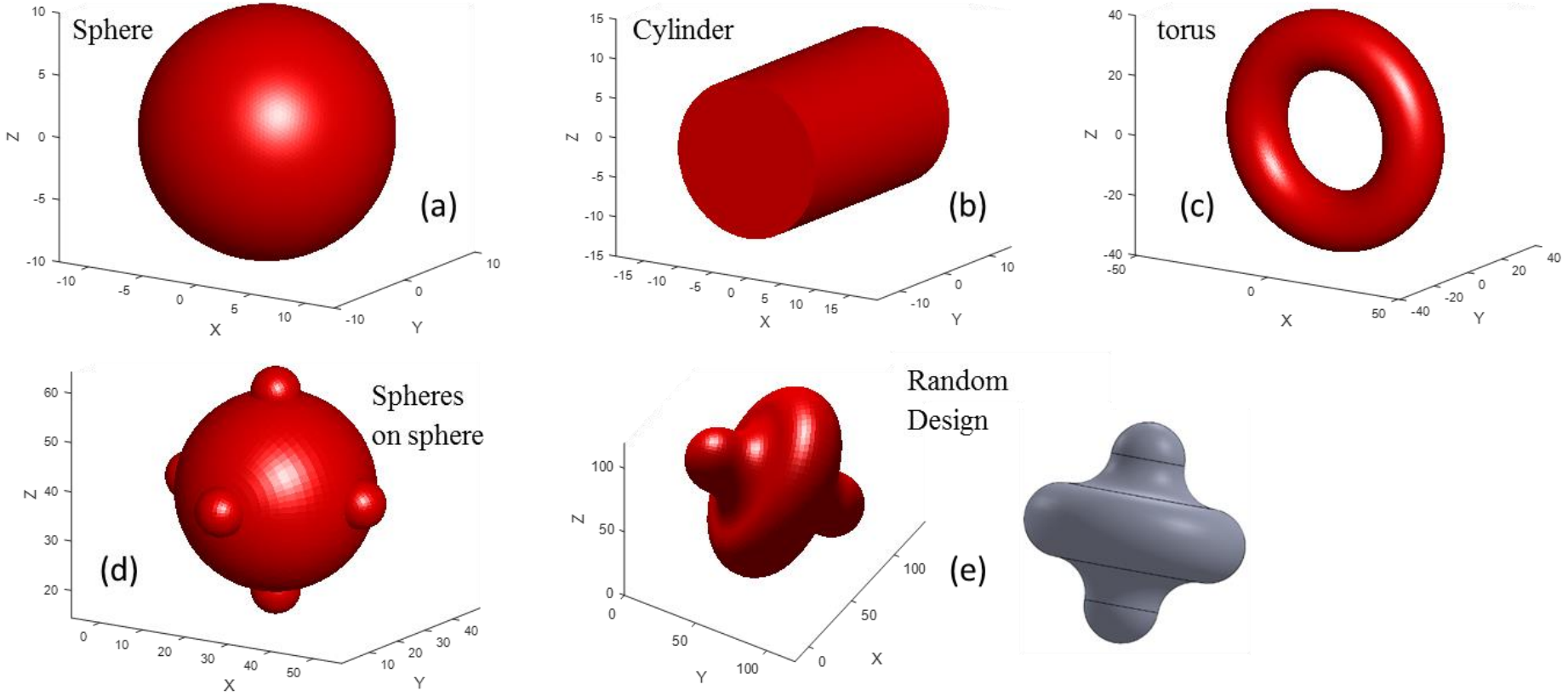


**Figure 3.13** Different geometries considered for validation of *A* (a) Sphere (b) Cylinder (c) Torus (d) Spheres on sphere (e) Symmetrical spinning top. Two views of the Symmetrical spinning top design are shown.

### 3.3.3.3 Calculation of mean flame area

Firstly, using an algorithm developed by Kroon [166] in MATLAB, the triangulated surface mesh was converted into a solid reconstruction consisting of voxels, a 3D pixel, representing burned gas. This algorithm discretises the triangulated surface by splitting and refining each face until the longest edge is smaller than half of a voxel. The voxel is then set beneath the vertex coordinates of the original face to a value of unity [155]. Therefore, with the volume of each voxel known and counting the number of voxels, the entire volume of 3D reconstructed flame was obtained.

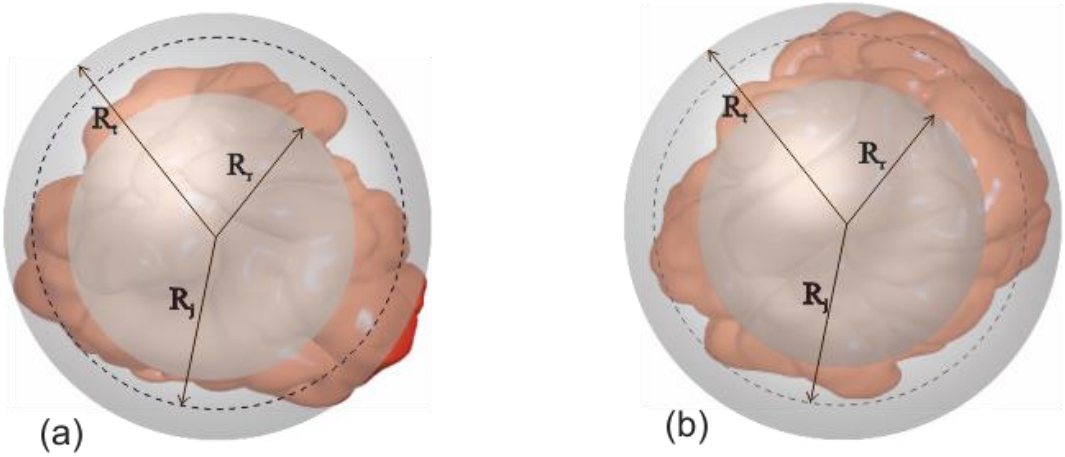


**Figure 3.14** Two different views of the same $CH_4$/air flame at $u'$=0.3 m/s, $\phi$ = 0.7, 300K and 01MPa.

Now, the mean surface area, $a$, can be calculated based on volume balancing, $a_v$, and also on mass balancing, $a_m$, of unburned and burned gases. Figure 3.14 shows two different views of the same turbulent flame for $CH_4$/air at $u'$=0.3 m/s and $\phi$ = 0.7, 300K, 01MPa, at t=26.75 ms after ignition. Similar to the 2D flame sheet, shown in Fig 1.5, $R_r$ and $R_t$ are identified as the root and tip radius of spheres drawn from the centroid of the 3D reconstructed flame to $\bar{c} = 0$ and $\bar{c} = 1$ respectively. A general radius $R_j$ lies in between these two radii within which and outside $R_r$, $m_{ui}$ and $V_{ui}$ are the total mass and total volume of unburned gas and $m_{bi}$ and $V_{bi}$ are the total mass and total volume of burned gas respectively. Outside $R_j$ and within $R_t$, $m_{uo}$ and $V_{uo}$ are the total

mass and total volume of unburned gas and $m_{bo}$ and $V_{bo}$ are the total mass and total volume of burned gas respectively. To calculate the mean area $a_v$ based on volume balancing, $R_j$ was found such that the total volume of unburned gas, $V_{ui}$, inside it is equal to the total volume of burned gas, $V_{bo}$ outside it [67]. Similarly, to calculate the mean area $a_m$ based on mass balancing, $R_j$ was chosen such that the total mass of unburned gas, $m_{ui}$, inside it is equal to the total mass of burned gas, $m_{bo}$ outside it [67]. The two different views in Fig. 3.14 demonstrate how $R_t$ could be miscalculated from 2D imaging because Fig. 3.14(a) shows the sphere $R_t$ slicing through the flame towards the bottom right of the image, while in fact it is passing through the farthest flame edge when viewed through a different angle as shown in Fig. 3.14(b).

The above discussed method was implemented in an algorithm which was written by the present author in MATLAB. Firstly, the centroid of all the burned gas was found by calculating the mean in *x*, *y* and *z* direction. The distance between the centroid and each burned voxel is then calculated and stored in a different array. The maximum and the minimum value in this array is then termed as $R_t$ and $R_r$ respectively. Now, starting from $R_j = R_r$ and iterating the loop until $R_j = R_t$, the respective unburned and burned gas volumes outside and inside it is calculated and is plotted against mean radius, varying between $R_t$ and $R_r$, an example of which is shown in Fig. 3.15. The point at which the unburned and the burned gas volumes intersect is taken as the mean $R_j = r_v$, using which $a_v$ is calculated from the Eq. (3.6).

Similarly, the respective unburned and burned gas masses outside and inside $R_j$ is calculated and is plotted against mean radius varying between $R_t$ and $R_r$, an example of which is shown in Fig. 3.16. The point at which the unburned and the burned gas masses intersect is taken as the mean radius, $R_j = r_m$, using which $a_m$ is again calculated from Eq. (3.6).

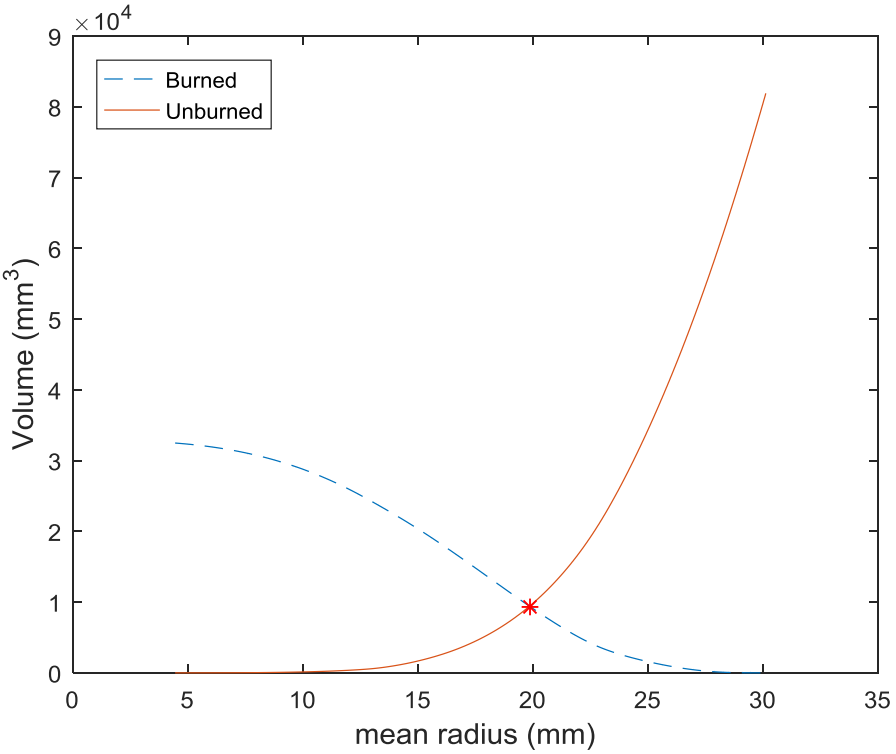


**Figure 3.15** Variations of burned and unburned gas volume across $R_j$ with its increasing magnitude for the flame shown in Fig. 3.14.

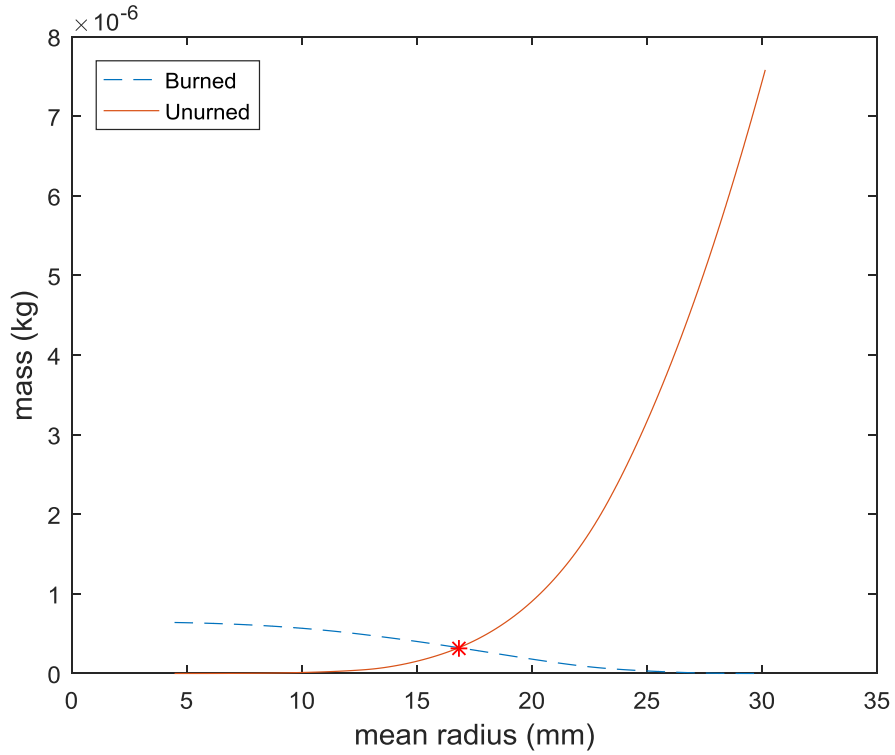


**Figure 3.16** Variations of burned and unburned gas masses across $R_j$ with its increasing magnitude for the flame shown in Fig. 3.14.

### 3.3.3.4 Calculation of burned gas volume

The mean radius, $a_v$, was also found from the volume, *V*, of the flame. Here *V* is calculated by summing up the volume of all the voxels that constitute the burned gas. The size/volume, $v_i$, of each voxel is determined based on camera resolution, in the present case is 0.0075 mm$^3$ (with each side of the pixel representing 0.196 mm) and is thus known. Therefore, the total volume of the flame is calculated using the equation below

$$V = \sum n.v_i \quad (3.4)$$

Here *n* is the number of burned (black) voxels. This volume, *V*, is equated to the volume of a sphere by using equation (3.4) and hence $r_v$ is calculated.

$$V = \frac{4}{3}\pi r_v^3 \quad (3.5)$$

Using $r_v$, the mean flame surface area $a_v$ is calculated as

$$a_v = 4\pi r_v^2 \quad (3.6)$$

# Chapter 4

# Results

## 4.1 Introduction

This chapter presents measured values of laminar burning velocities, $u_l$, of $n$-butanol air mixtures, details of laminar flame instabilities and values of turbulent burning velocities, $u_t$, of $n$-butanol, $CH_4$ and $H_2$/air mixtures. This is followed by 3D turbulent flame structure analysis. All data were obtained with the experimental and data processing techniques presented in Chapter 2 and Chapter 3. Finally, results of turbulent flame quenching studies are presented.

## 4.2 Laminar burning velocities, of *n*-butanol/air mixtures

Laminar burning characteristics of $n$-butanol/air mixtures at 360 K for pressures ranging from 0.1-1.0 MPa and $\phi$ from 0.7-1.4 were obtained with schlieren imaging, at an imaging frequency of 5400 Hz, using the techniques discussed in Sections 2.3.2 and 3.2.1, 3.2.2 respectively. Shown in Fig. 4.1(a) is a typical schlieren radius, $r_{sch}$, versus time curve for a stoichiometric $n$-butanol/air mixture at a temperature and pressure of 360±2K and 0.5 MPa. The flame speed, $S_n$, was calculated, as described in Chapter 1, and is plotted against $r_{sch}$ in Fig. 4.1(b). Figure 4.1(c) shows the measured $S_n$ variation with the corresponding stretch, $\alpha$, calculated using Eqs. (1.2) and(1.3). The Asterisk, *, in Fig. 4.1(b) denotes the radius at which the flame speed becomes independent of spark effects. This was found to be approximately 6-10 mm in previous studies [24, 152]. The cross symbol in Fig. 4.1(b) represents the critical flame radius, $r_{cl}$, at the onset of cellularity, also shown in Fig. 3.1. Beyond this, $S_n$ increases sharply due to increasing rate of surface area generation [24]. The corresponding critical stretch rate, $\alpha_{cl}$, at the onset of cellularity is shown as the cross symbol in Fig. 4.1(c). The solid line in Fig.

4.1(c) shows the linear extrapolation of $S_n$ through the stable region between the asterisk and the cross, to zero stretch rate to obtain an unstretched flame speed, $S_s$. The slope of the solid line gives the burned gas Markstein length, $L_b$ according to Eq. (1.14). Results for the stable flame regime are presented in this section, while those of the unstable region are presented in Section 4.3.

Measurements of flame speed, against stretch, $\alpha$, for pressures ranging from 0.1 MPa to 1.0 MPa and equivalence ratios between 0.7 and 1.4, are shown in Fig. 4.2. Those at 1.0 MPa, shown in Fig. 4.2(c), are limited to $\phi$ = 0.7 and 0.8, because a completely gaseous mixture of $n$-butanol was not attainable beyond $\phi$ = 0.8, as its required partial pressure would become higher than its vapour pressure, and vaporisation would be insufficient [152]. In each of these Figures, the solid lines and symbols have the same meaning as in Fig. 4.1. With increase in both $\phi$ and $P$, the stable regime to measure $S_s$ and $L_b$, becomes increasingly limited.

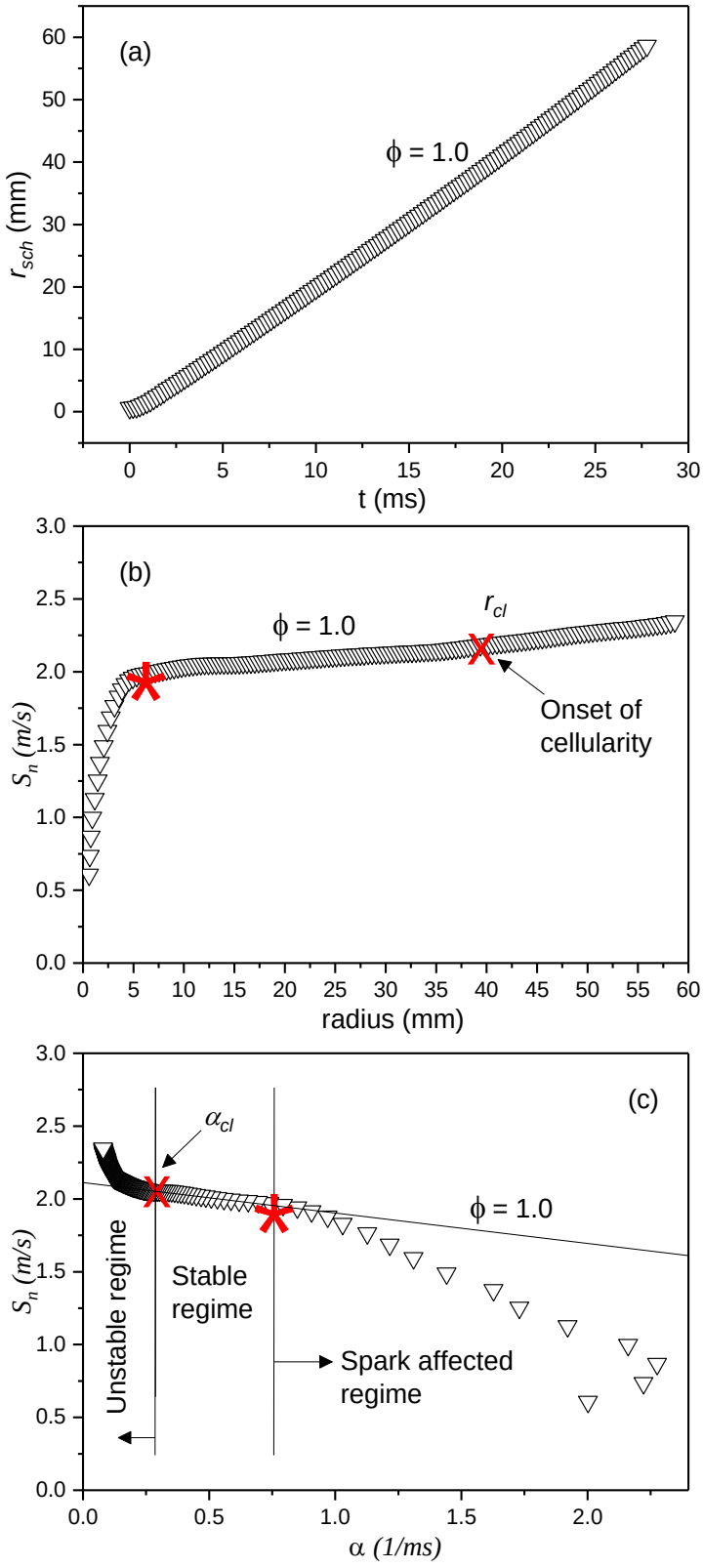


**Figure 4.1** Measurements of a *n*-butanol/ air mixture at $T$=360 K and $P$ = 0.5 MPa (a) radius against time (b) flame speed against radius (c) flame speed against stretch.

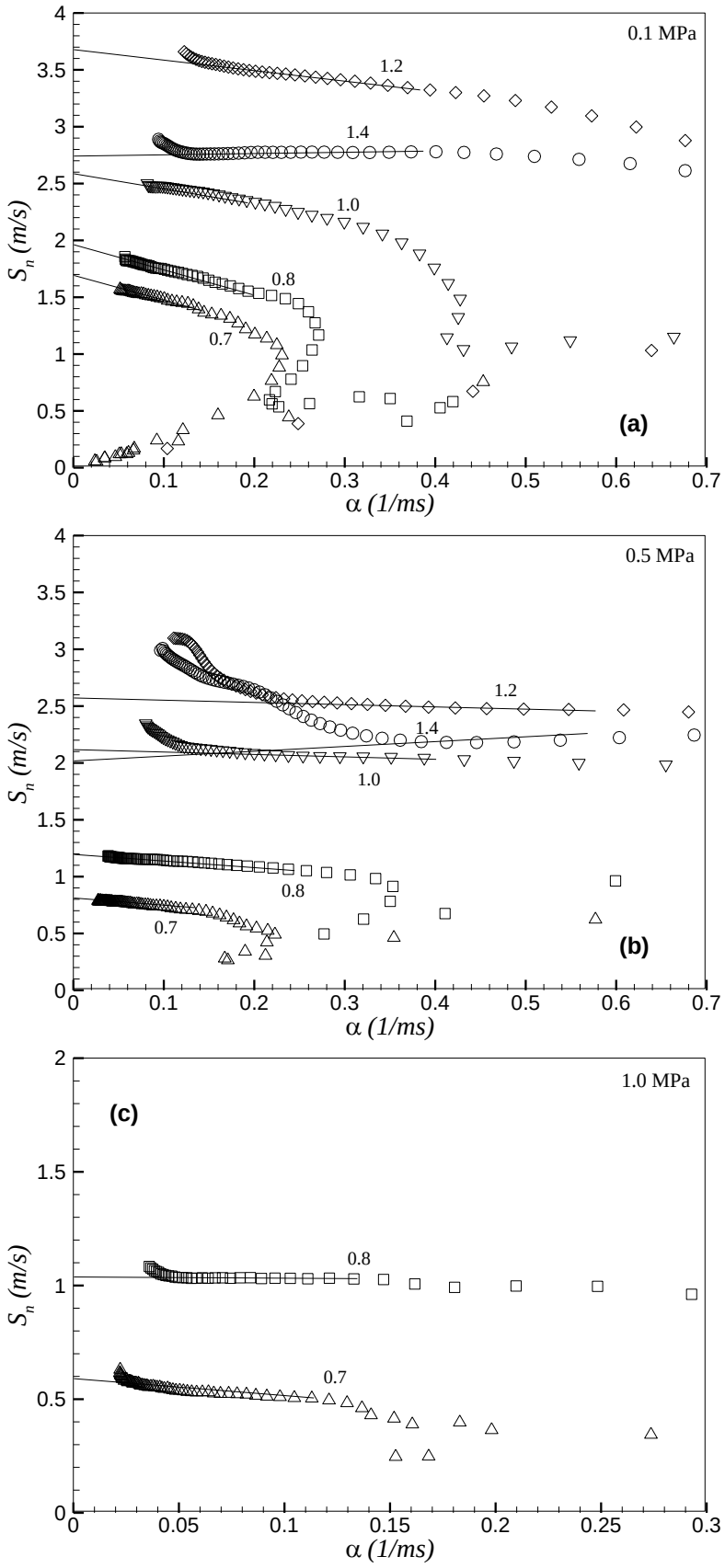


**Figure 4.2** Variations of $S_n$, with $\alpha$, for different $\phi$ at 360 K for (a) 0.1 MPa (b) 0.5 MPa (c) 1.0 MPa.

Unstretched laminar burning velocities, $u_l$, were derived from the data in Fig. 4.2 with Eq. (1.16). These are presented in Fig. 4.3. The necessary values of *Le,* required to calculate $T_b$ and $\bar{\rho}_b$, were taken from [167] and are presented in Fig. 4.4. All relevant data are summarised in Table 4.1. Three explosions were conducted at each experimental condition and the average values of $u_l$ are shown by filled symbols in Fig. 4.3. Error bars show standard deviations from their average, and the solid line is best line curve fits through the data. The limiting value of $\phi$, beyond which the fuel could not be fully evaporated, is indicated by asterisk. As shown in Fig. 4.3, $u_l$ decreased with increasing pressure. All data exhibited the expected trend of a maximum value of $u_l$ at approximately $\phi$ = 1.1, with significant reductions on the lean and richer sides. The corresponding values of $L_b$, are presented in Fig. 4.5. These decreased with increasing $P$ as well as increasing $\phi$. At 0.5 MPa, $L_b$ reached negative values with rich mixtures, indicating an increase in burning rate with stretch.

Strain rate Markstein numbers, obtained using the multiple regression analysis [21] employing Eq. (1.11) as described in Section 1.3.2, at different pressures over a range of $\phi$ are shown in Fig. 4.6. Values of $\delta_l$, were obtained using Eq. (1.17). The value of $\nu$, at each experimental condition is obtained with the software, Gaseq [57]. Each open symbol represents the average value of $Ma_{sr}$ from three explosions at the same condition and the error bar shows the uncertainty. Significant decreases in values of $Ma_{sr}$ were observed as $\phi$ is increased, becoming negative at high pressures.

**Table 4.1** Laminar flame properties at 0.1, 0.5, 1.0 MPa and 360 K.

| | 0.1 MPa | | | | | 0.5 MPa | | | | | 1.0 MPa | | | | |
|---|---|---|---|---|---|---|---|---|---|---|---|---|---|---|---|
| $\phi$ | $\rho_u/\rho_b$ | $\nu\,\mathbf{x10^{-5}}$ | $u_l$ | $L_b$ | $Ma_{sr}$ | $\rho_u/\rho_b$ | $\nu\,\mathbf{x10^{-6}}$ | $u_l$ | $L_b$ | $Ma_{sr}$ | $\rho_u/\rho_b$ | $\nu\,x\mathbf{10^{-6}}$ | $u_l$ | $L_b$ | $Ma_{sr}$ |
| 0.7 | 5.61 | 2.14 | 0.29 | 2.40 | 10.01 | 5.62 | 4.27 | 0.14 | 0.80 | 9.00 | 5.62 | 2.14 | 0.11 | 0.41 | 6.03 |
| 0.8 | 6.11 | 2.13 | 0.33 | 1.68 | 6.62 | 6.13 | 4.25 | 0.21 | 0.60 | 6.49 | 6.14 | 2.13 | 0.17 | 0.12 | 4.15 |
| 1.0 | 6.85 | 2.11 | 0.45 | 1.45 | 7.27 | 6.95 | 4.21 | 0.31 | 0.28 | 2.95 | - | - | - | - | - |
| 1.2 | 6.97 | 2.09 | 0.53 | 1.05 | 5.51 | 6.99 | 4.17 | 0.36 | 0.10 | -2.80 | - | - | - | - | - |
| 1.4 | 6.81 | 2.07 | 0.42 | 0.25 | 2.54 | 6.82 | 4.14 | 0.29 | -0.43 | -4.39 | - | - | - | - | - |

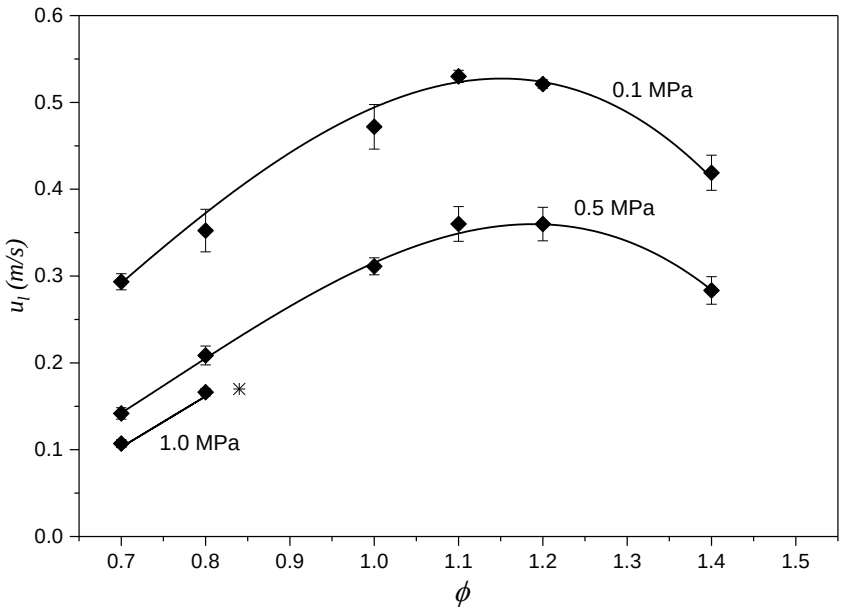


**Figure 4.3** Variations of $u_l$ with $\phi$ and $P$ for *n*-butanol/air mixtures at 360 K.

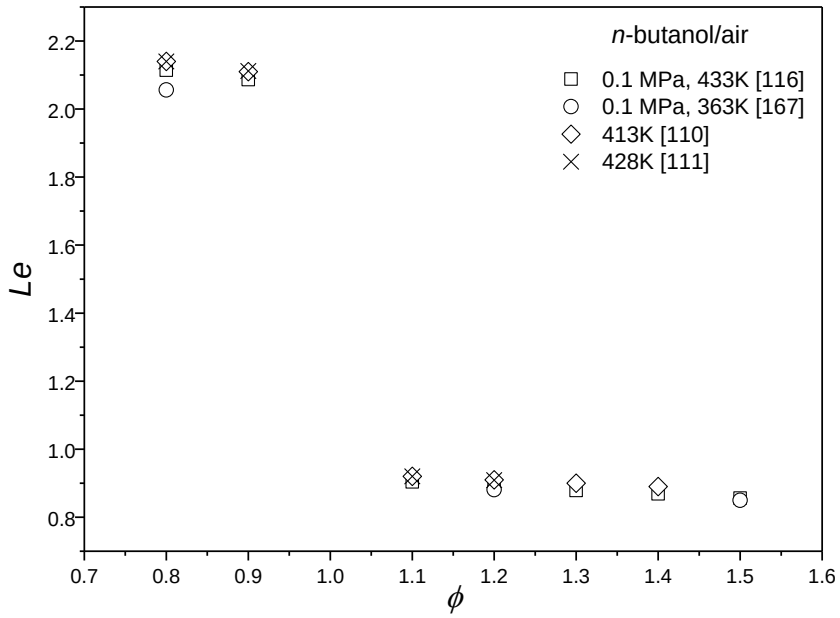


**Figure 4.4** Lewis numbers of *n*-butanol/air mixtures for different $\phi$.

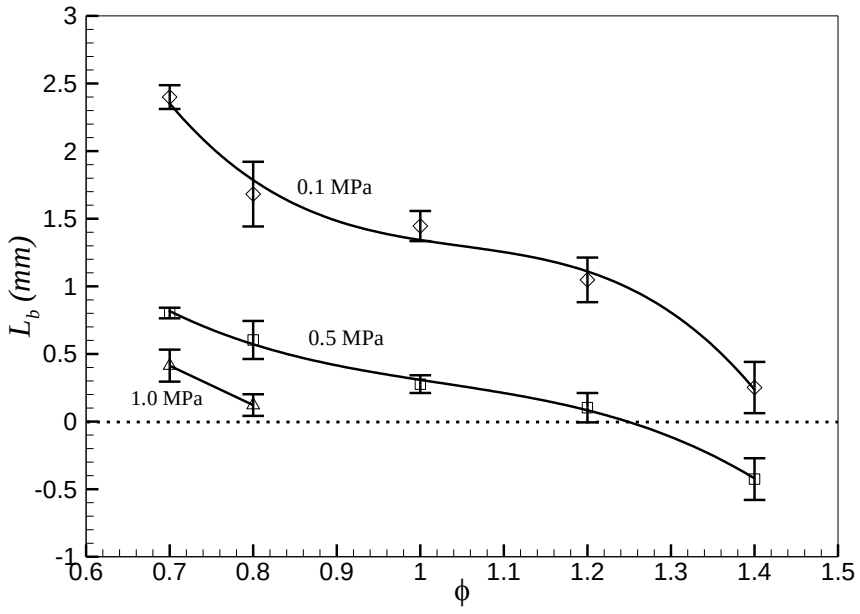


**Figure 4.5** Variations of $L_b$, with $\phi$ and $P$ for *n*-butanol/air mixtures at 360 K.

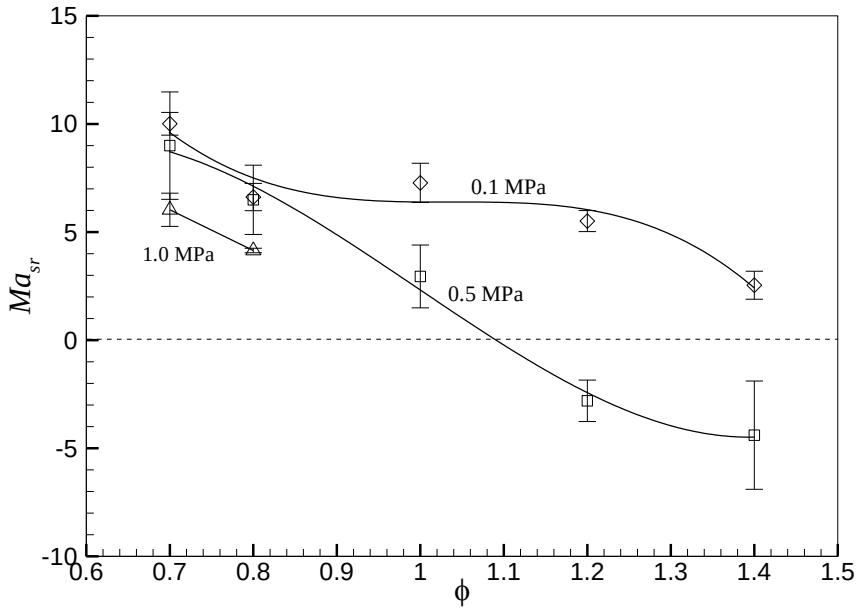


**Figure 4.6** Variations of $Ma_{sr}$ with $\phi$ and $P$ for *n*-butanol/air mixtures at 360 K.

## 4.3 Laminar flame instabilities

This section focuses on the results obtained from the unstable regime, shown in Fig. 4.1(c). The critical flame radius, $r_{cl}$, is an important parameter that marks the onset of cellularity and the increase in flame speeds. As the flame

propagates, the stretch rate decreases. When this falls below a certain threshold, $\alpha_{cl}$, the interactions of the Darrieus-Landau and thermo-diffusive instabilities create increasingly severe wrinkling of the initially smooth laminar flame surface, accelerating the flame speed and strengthening the associated pressure pulse. The latter arises from the rate of change of the heat release rate [46]. Such phenomena, described in Section 1.3.4, were observed only for the richest mixtures at low pressures, while high pressure explosions readily developed cellularity at relatively low $\phi$, enabling the acquisition of more $r_{cl}$ data.

### 4.3.1 Critical Peclet number

Critical flame radii were expressed in terms of the critical Peclet number, $Pe_{cl}$, as described in Section 1.3.4.1. They are presented for the $n$-butanol air mixtures at pressures of 0.1, 0.5 and 1.0 MPa in Fig. 4.7, over a range of $\phi$ and at 360 K. Values of $Pe_{cl}$ decreased with both $P$ and $\phi$.

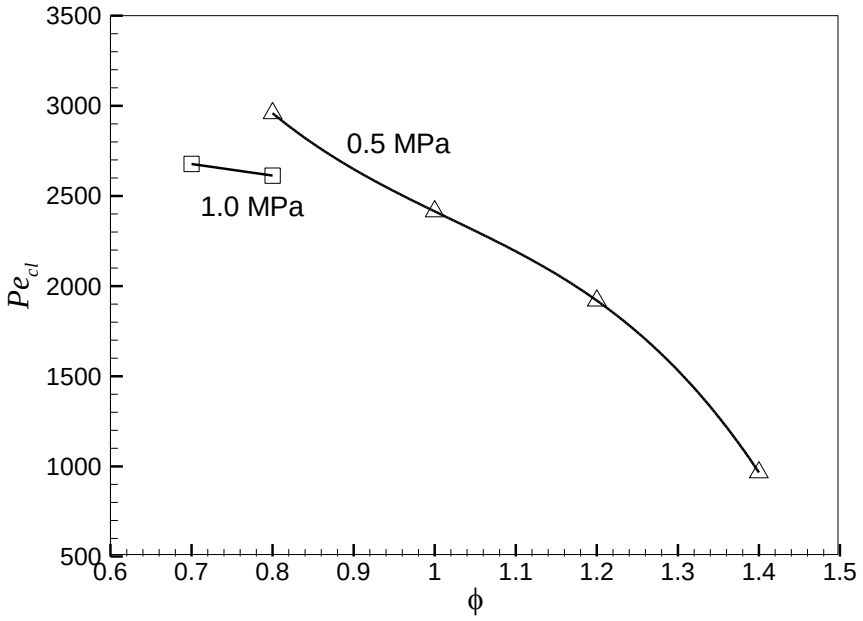


**Figure 4.7** Variations of $Pe_{cl}$, with $\phi$ and $P$ for *n*-butanol/air mixtures at 360 K.

From Fig. 4.2, the onset of cellularity is dependent on $L_b$. Higher values of $L_b$ indicate flame stability while lower values decrease it. Bradley et al. [168] suggested that $Pe_{cl}$ can be generalised by plotting it against the burned gas Markstein number, $Ma_b$ (which is a function of $L_b$). This is shown in Fig. 4.8

for the data in Fig. 4.7. Each experimental point gives the mean value from three identical explosions. Solid lines are the best fit curves through the data. Data of $Pe_{cl}$ for several fuels are available in the literature and are compared with the present data in Chapter 5, however, there is a lack of relevant data for propane. Therefore these were obtained in the present work, at 360 K and pressures 0.1, 0.5 and 1.0 MPa. They are presented against their corresponding $Ma_b$ in Fig. 4.9. The corresponding, $S_n$ against $\alpha$, curves to obtain $Pe_{cl}$ data for these mixtures, are presented in APPENDIX A (See Fig. A.6). Values of $\phi$ ranged from 0.7 to 1.4 for propane-air mixtures.

For both mixtures, $Pe_{cl}$ increased with increasing $Ma_b$. There are more $Pe_{cl}$ data points at 0.5 and 1.0 MPa, a consequence of a reduction in $\delta_l$ with pressure. For both mixtures, the gradient of $Pe_{cl}$ against $Ma_b$ at 1.0 MPa is smaller than at 0.5 MPa, while the relative magnitudes are reversed and the two curves intersect at about $Ma_b$=5, as can be seen from Fig. 4.9.

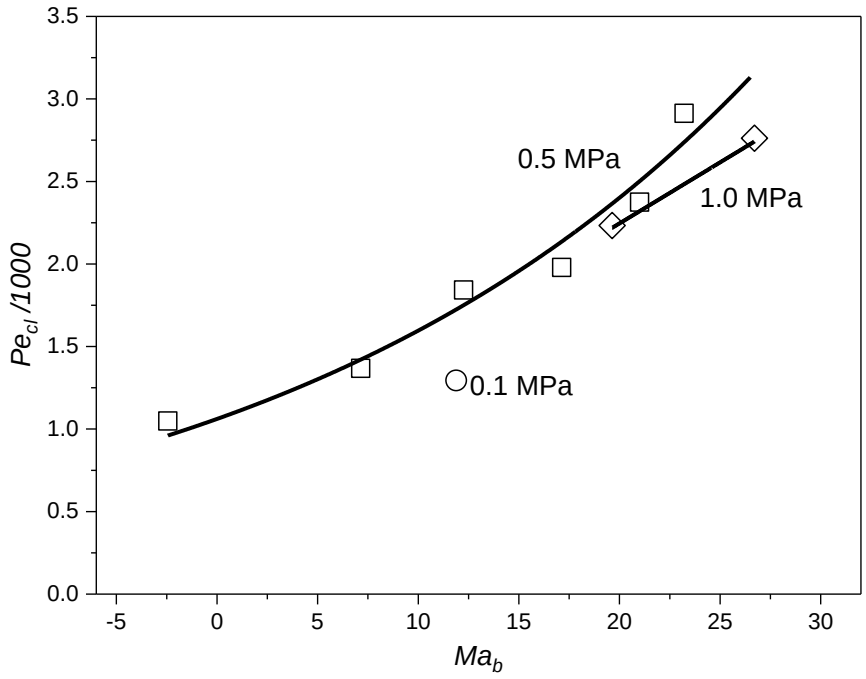


**Figure 4.8** Variations of $Pe_{cl}$ with $Ma_b$ for *n*-butanol/air mixtures at 360 K.

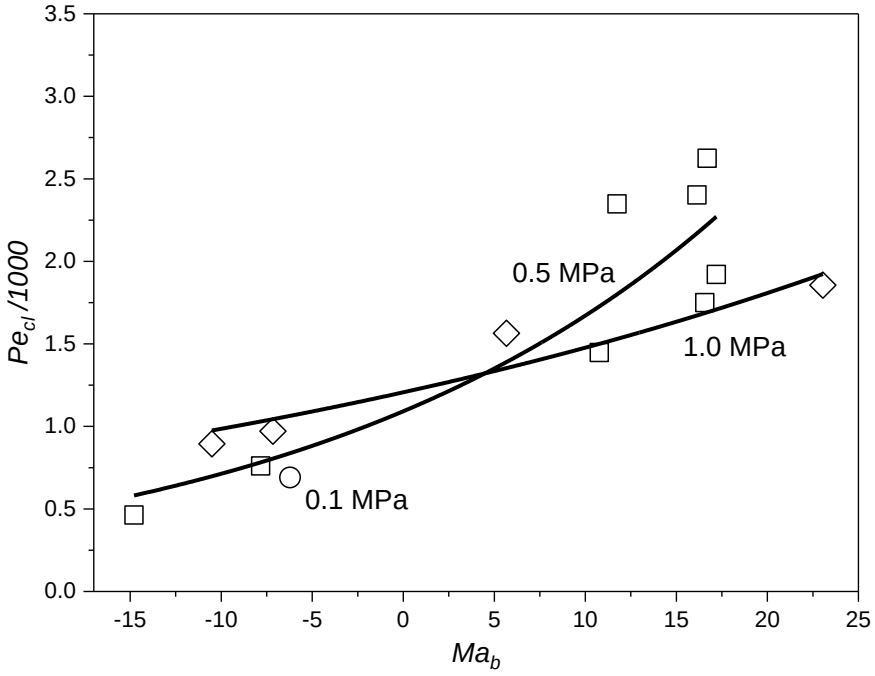


**Figure 4.9** Variations of $Pe_{cl}$ variations with $Ma_b$ for propane/air mixtures at 360 K.

### 4.3.3 Onset of cellularity in terms of Critical Karlovitz number

Theoretical [42, 48] and experimental [24, 169] studies have revealed the strong dependency of $Pe_{cl}$ upon $Ma_{sr}$. However, Bradley et al. [56] suggested that a more fundamental parameter than $Pe_{cl}$ for correlating the onset of instability is the critical Karlovitz number, $K_{cl}$, in that it is the stretch rate maintains flame stability (it smoothes out any wrinkles). The relationship between $K_{cl}$ , $Pe_{cl}$ and $Ma_b$ is given by Eq. (1.20) [56].

Values of $K_{cl}$ as a function of $Ma_{sr}$ were obtained from all the data presented in Figs. 4.8 and 4.9, using Eq. (1.20). These are shown in Figs. 4.10 and 4.11. Best fit curves are indicated by the solid lines. These exhibited similar trends of more rapid increases in $K_{cl}$ as $Ma_{sr}$ is reduced. There is also a decrease in $K_{cl}$ as the pressure is increased, indicative of generally improved flame stability. Because, the curves in Figs. 4.8 and 4.9 represent the boundary between stable and unstable regimes, any measurement that falls below the curve is unstable.

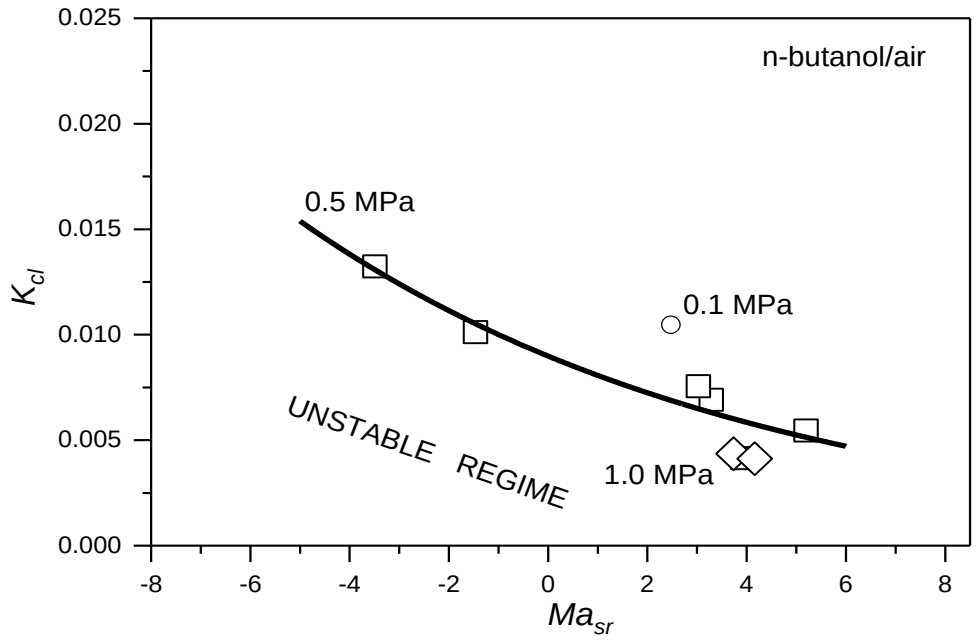


**Figure 4.10** Variations of $K_{cl}$ with $Ma_{sr}$ for *n*-butanol/air mixtures at 360 K.

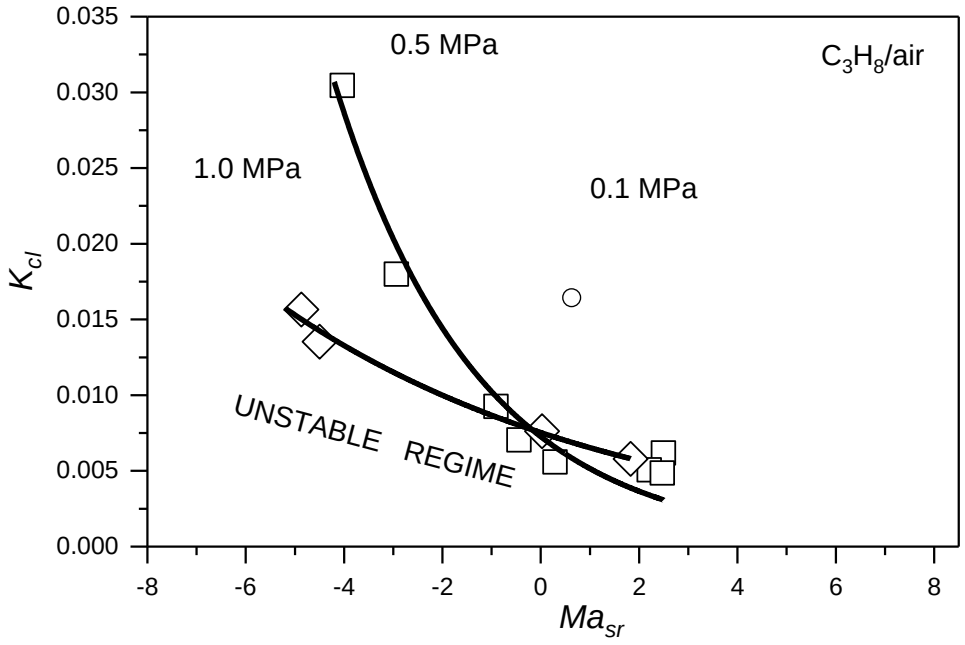


**Figure 4.11** Variations of $K_{cl}$ with $Ma_{sr}$ for propane/air mixtures at 360 K.

## 4.4 Turbulent burning velocities

Turbulent burning characteristics of $n$-butanol/air, $CH_4$/air and $H_2$/air mixtures during spherical explosions are now presented. The choice of conditions used in this thesis gives an extensive range of conditions presented in terms of the fundamental parameters. The author is unaware of any previous turbulent burning data for $n$-butanol/air mixtures, therefore these were sought in the present study. With regard to the $CH_4$/air and $H_2$/air data, turbulent burning velocities of these fuels are available in the literature. However, for the present conditions (of slow burning mixtures) these are scarce. The measurements of turbulent burning velocities of $n$-butanol/air were made using schlieren imaging technique, as described in Section 2.3.2, in a similar manner to those for laminar flames, except for the introduction of turbulence via the fans. Pressure measurement technique, as described in Section 2.3.1, was used to measure turbulent burning rates of $CH_4$/air and $H_2$/air mixtures. These were acquired simultaneously with the 3D swinging sheet technique, described in Section 2.3.3. Section 4.4.1 presents the turbulent burning rates of $n$-butanol/air mixtures, while those of $CH_4$/air and $H_2$/air are presented in Section 4.4.2.

### 4.4.1 *n*-butanol/air mixtures

To measure turbulent burning velocities of $n$-butanol/air mixtures, five explosions were conducted at each experimental condition. The extent of the measurements is summarised in Table 4.2 and the '$q$' after a given value of $u'$ indicates a flame quenching condition. A relatively large spark is required under turbulent compared with laminar conditions to overcome the effects of flame straining [170]. Therefore, a high energy spark ignition system, described in Section 2.2, was used. Spark energy initially produces a reacting plasma that assists the initial flame kernel to overcome the high strain rate [170]. Bradley et al. [24] conducted laminar experiments on flames in the current vessel and found that the flame becomes independent of spark assisted propagation as it reaches a radius of 8-10 mm. Beyond this radius

the flame is influenced by local stretch rate and increasing flame wrinkling [154]. They did not report the likely effect of ignition on turbulent flames. However, in a different work [10] they suggested that turbulent flames attain developed linear regime at a radius of 20 mm.

**Table 4.2** Summary of experimental conditions at *T*= 360 K, *q* indicates flame quenching

| P | 0.1 MPa | | | | | 0.5 MPa | | | | | 1.0 MPa | | | | |
|---|---|---|---|---|---|---|---|---|---|---|---|---|---|---|---|
| $\phi$ | $u'\ (m/s)$ | | | | | $u'\ (m/s)$ | | | | | $u'\ (m/s)$ | | | | |
| 0.7 | 0.5 | 1 | 2$q$ | - | - | 0.5 | 1 | 2$q$ | - | - | 0.5 | 1$q$ | - | - | - |
| 0.8 | 0.5 | 1 | 2 | 4$q$ | 6$q$ | 0.5 | 1 | 2 | 4 | 6 | 0.5 | 1 | 2 | 4 | 6 |
| 1.0 | 0.5 | 1 | 2 | 4 | 6 | 0.5 | 1 | 2 | 4 | 6 | - | 1 | 2 | 4 | 6 |
| 1.2 | 0.5 | 1 | 2 | 4 | 6 | 0.5 | 1 | 2 | 4 | 6 | - | - | - | - | - |
| 1.4 | 0.5 | 1 | 2 | 4 | 6 | 0.5 | 1 | 2 | 4 | 6 | - | - | - | - | - |

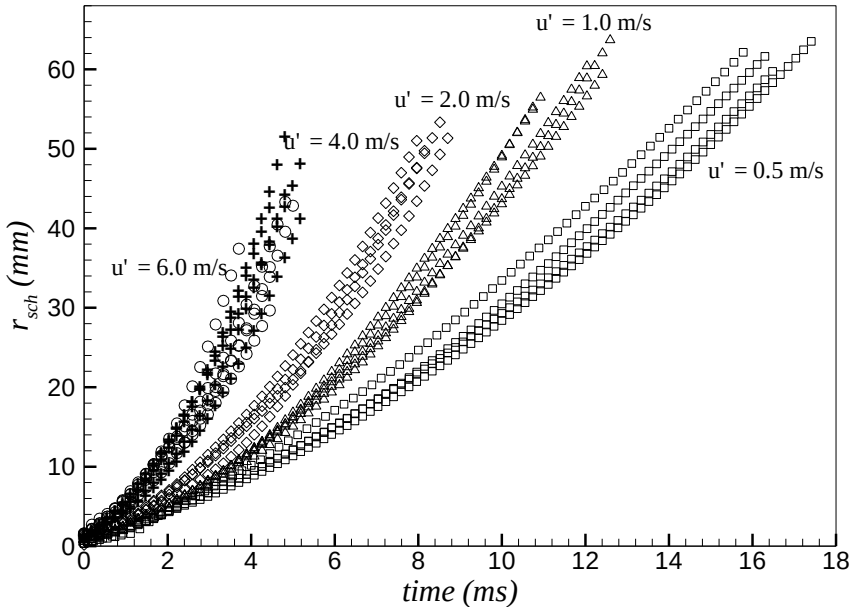


**Figure 4.12** Flame radius with increasing time from ignition for different $u'$, at $\phi$ = 1 and 0.5 MPa, 360 K.

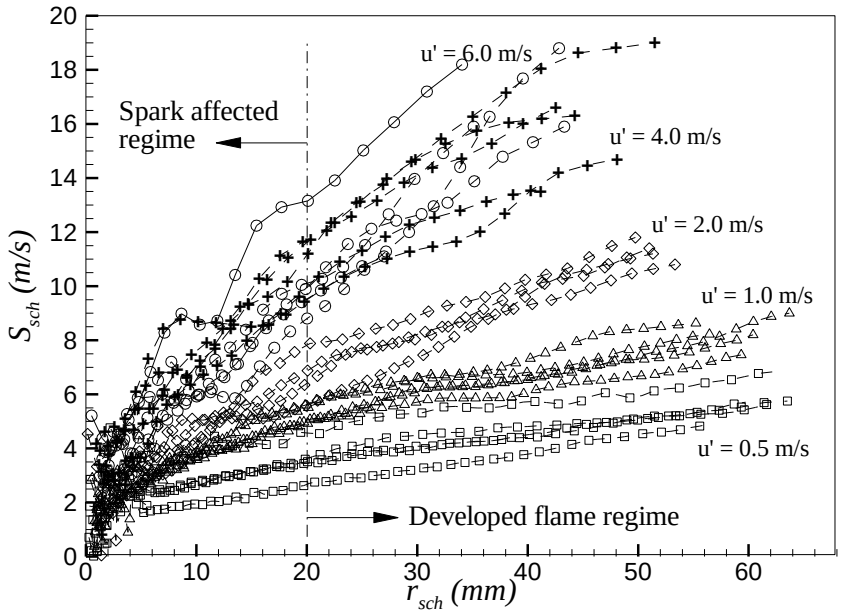


**Figure 4.13** Variations of $S_{sch}$ with increasing radii from ignition for different $u'$ at $\phi$ = 1 and 0.5 MPa, 360 K.

Shown in Fig. 4.12 are the mean flame schlieren radii, $r_{sch}$, obtained using the method described in Section 3.3, plotted against time from ignition at $\phi$=1 for $u'$ between 0.5 and 6.0 m/s at initial temperature and pressure of 360±5K and 0.5MPa. Turbulent flame speeds, $S_{sch}(=\frac{dr_{sch}}{dt})$, (the subscript, '*sch*' is used for historical reasons and will be retained here for consistency) were calculated. Shown in Fig. 4.13 are typical $S_{sch}$, against $r_{sch}$ curves for $\phi$ = 1 and for different $u'$. The inevitable stochastic nature of variation in turbulent burning is clearly seen. The vertical broken line at a radius of 20 mm indicated in Fig. 4.13 shows the beginning of developed linear regime with no spark influence.

Flame speeds $S_{sch}$ against mean radius $r_{sch}$ for different $\phi$, and $u'$ at pressures of 0.1, 0.5 and 1.0 MPa are shown in Fig. 4.14, Fig. 4.15 and Fig. 4.16 respectively. Again, each curve represents the mean of five explosions and the error bar indicates the standard deviation from the mean. Clearly an increase in $u'$ increases the flame speed. Cycle to cycle variations, in general, increase with turbulence but are relatively greater with the leanest mixture, as shown in Fig. 4.14(a). At the leanest $\phi$ value of 0.8, the change in $S_{sch}$ with increasing $u'$ is less distinguishable, with wide scatter in $S_{sch}$ as the flame develops. As $\phi$ is increased the increase in $S_{sch}$ is more clear. Maximum flame

speeds of approximately 27 m/s, are observed at rich mixtures i.e. at $\phi$ = 1.2 and 1.4 and at $u' = 6.0\ m/s$ for 0.5 MPa. Large scatter is also observed at the higher $u'$ values irrespective of $\phi$.

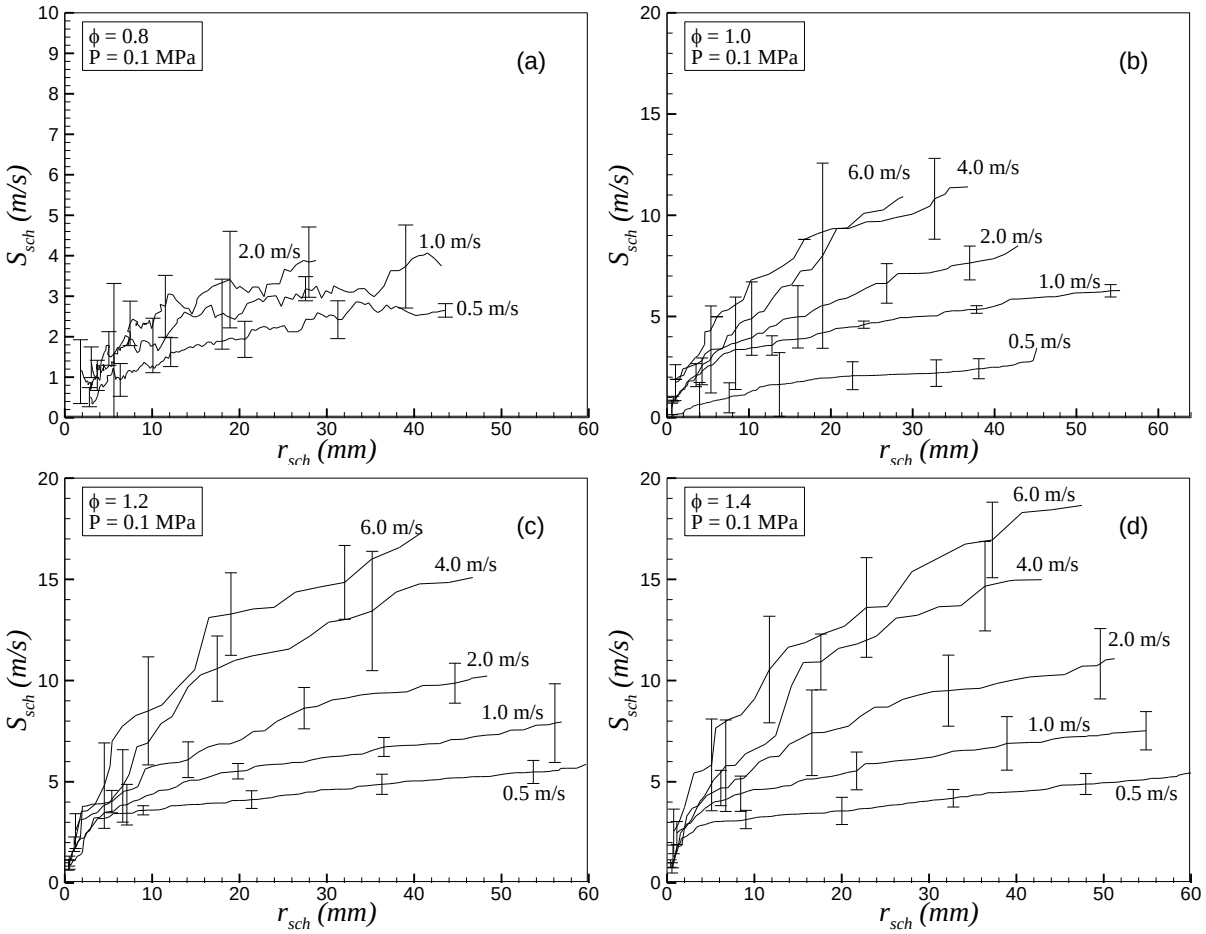


**Figure 4.14** Variations of $S_{sch}$ with increasing radius from ignition for different $u'$ at 360 K.

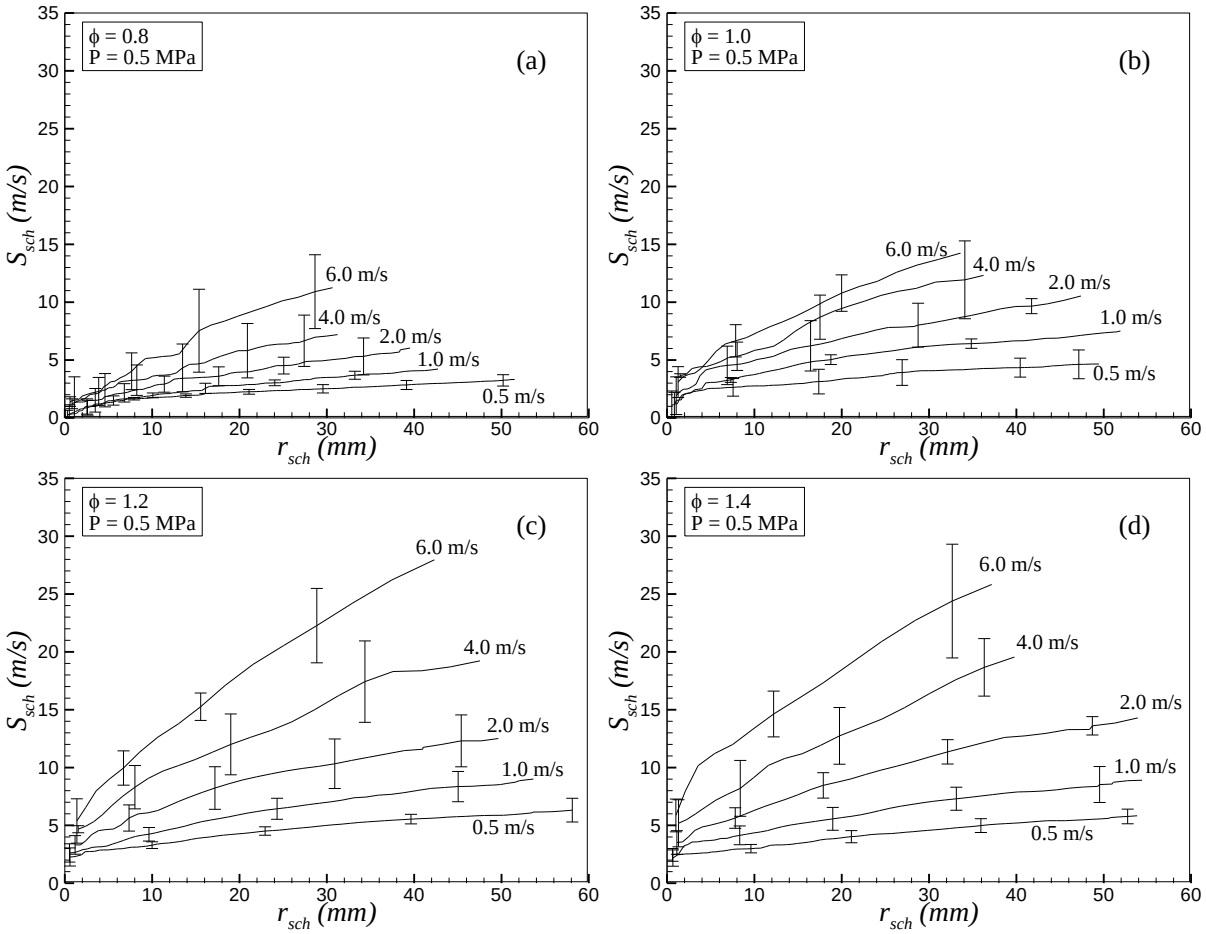


**Figure 4.15** Variations of $S_{sch}$ with increasing radii from ignition for different $u'$ at 360 K.

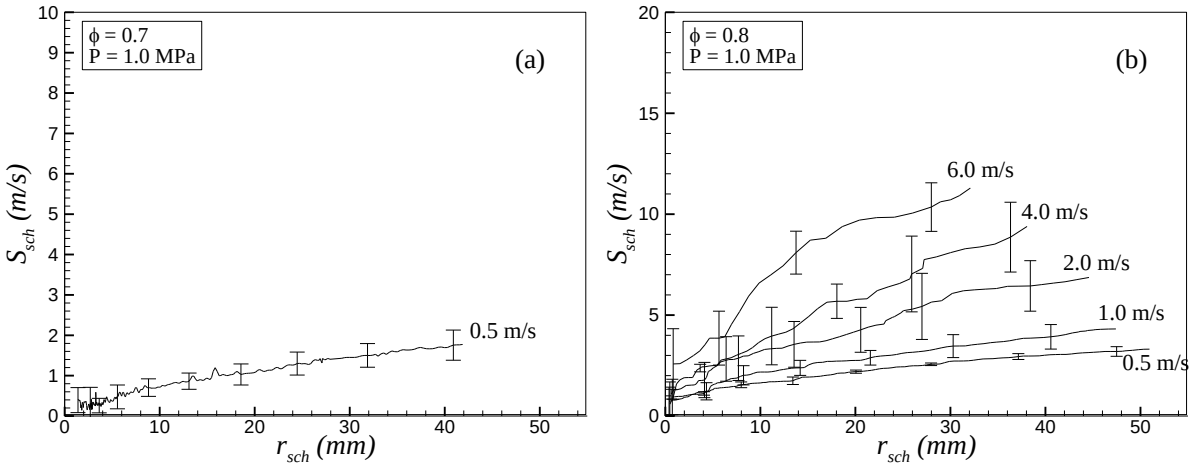


**Figure 4.16** Variations of $S_{sch}$ with increasing radii from ignition for different $u'$ at 360 K.

#### 4.4.1.1 Effect of *u'* on turbulent burning velocity

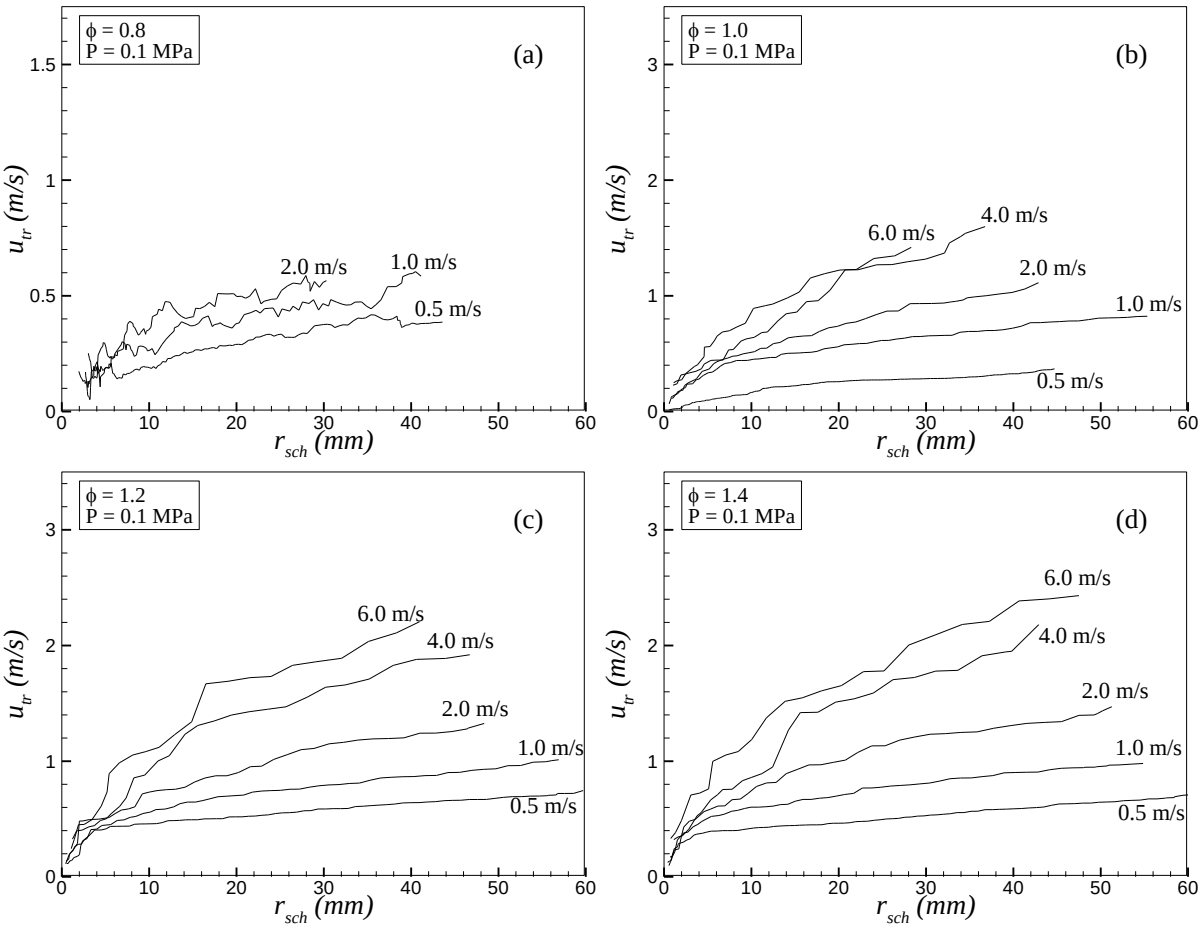


**Figure 4.17** Variations of $u_{tr}$ with increasing radii from ignition for different $\boldsymbol{u'}$ at 360 K.

Values of turbulent burning velocity, $u_{tr}$, were calculated from the data presented in Figs. 4.14 to 4.16 by the method discussed in Section 3.3. The density ratio, $\bar{\rho}_b/\rho_u$, is found from Gaseq software [57]. The corresponding values of $u_{tr}$ derived in this way, for different $\phi$ and$u'$,are plotted against $r_{sch}$ in Figs. 4.17 to Fig. 4.19 respectively. Trends for $u_{tr}$ are, in general, similar to those for $S_{sch}$ discussed above. $u_{tr}$ increases with increasing $u'$ with the trends being less pronounced at the lower $\phi$. As discussed for flame speeds, at lower values of $\phi$=0.8 and at 0.1 MPa, shown in Fig. 4.17(a), similar effects in $u_{tr}$ are observed i.e. the change in $u_{tr}$ with increasing $u'$ being less distinguishable. Moreover, for all experimental conditions, $u_{tr}$, at lowest $u'$ of 0.5 m/s, increase with radius at a decreasing rate. This suggests that there is

a limiting asymptotic value. Indeed at the lowest value of $u'$=0.5 m/s, irrespective of $\phi$ and $P$, a steady fully developed value of $u_{tr}$ has almost been attained at a radius of about 30 mm. For other conditions, a fully developed flame was not attained, even for the largest measured flames. Maximum turbulent burning velocities are observed at rich mixtures i.e. at $\phi$ = 1.4 and 6 m/s, at 0.5 MPa. However, a noticeable difference between trends for flame speed and burning velocity is the considerable increase in $u_{tr}$ between $\phi$ = 1.2 and 1.4, compared with the negligible increase of $S_{sch}$.

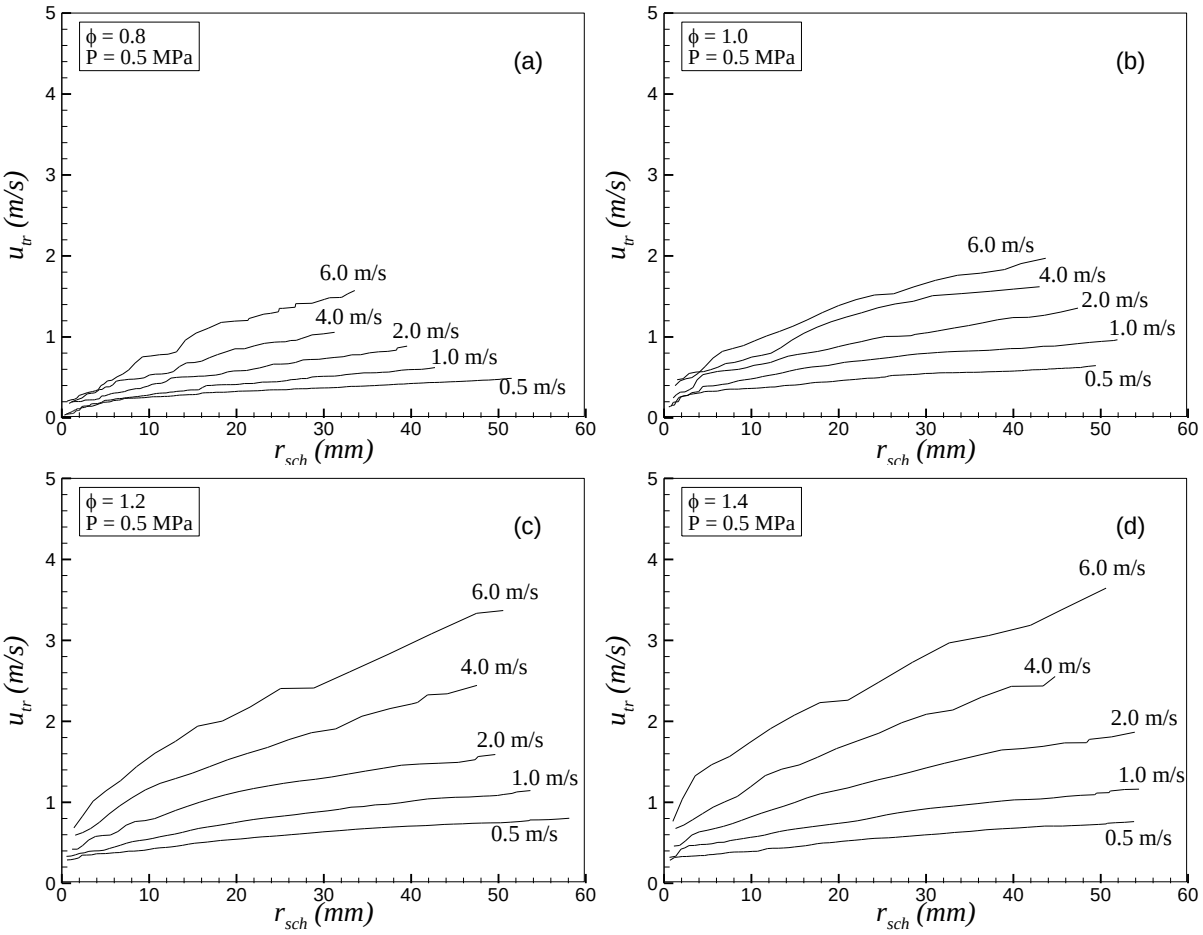


**Figure 4.18** Variations of $u_{tr}$ with increasing radii from ignition for different $u'$ at 360 K.

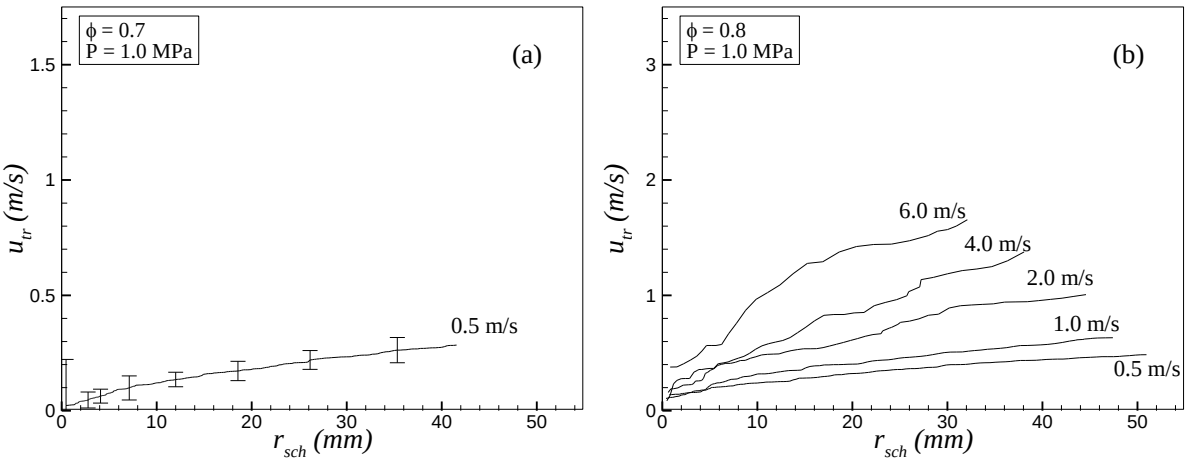


**Figure 4.19** Variations of $u_{tr}$ with increasing radii from ignition for different $u'$ at 360 K.

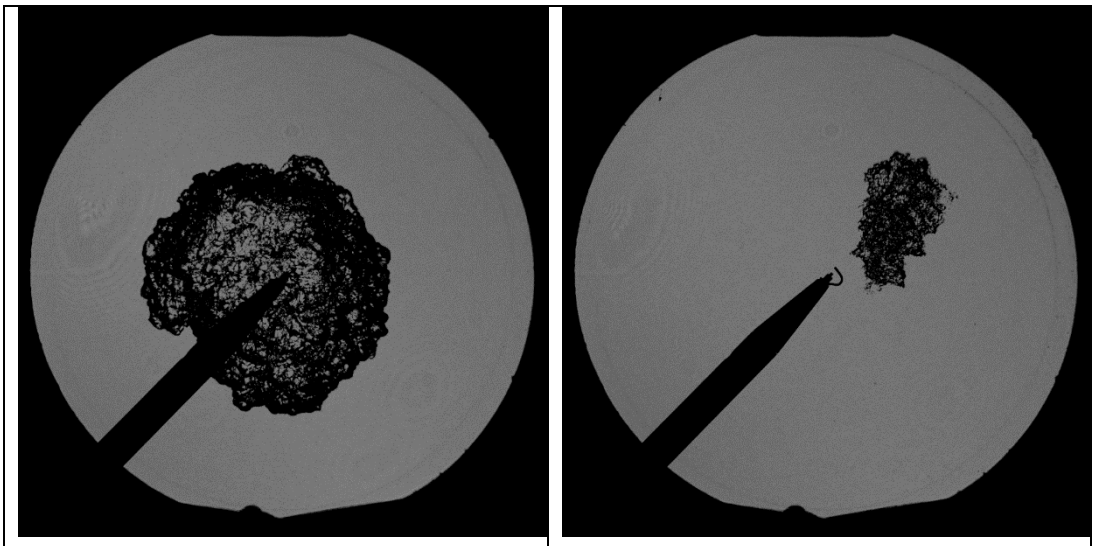

| (a) 90.7 ms after ignition | (b) 33 ms after ignition |
|---|---|

**Figure 4.20** Schlieren images of *n*-butanol/air mixtures at 0.5 MPa, 360 K $\phi$ =1.0 (a) $u'$ = 1.0 m/s (b) $u'$=6.0 m/s.

For a given value of $u'$, $S_{sch}$ and $u_{tr}$ increased with $r_{sch}$ and this has been attributed to the turbulent flame development [85]. There are considerably more variations in the flame speed data shown in Figs. 4.14 to 4.16 than for the laminar flames, discussed in Section 4.2. Lawes et al. [68] argued this to be due to the different instantaneous turbulent flow field at the time of ignition. They attributed these cyclic variations to the varying turbulent eddies encountered by the developing flame at different times and at different

positions. They [68] also suggested that these variations might not be due to ignition. No measurements of the effect of ignition were undertaken in the present work.

The randomised nature of turbulence inevitably introduces random variations in turbulent burning [10, 68]. In their work, Lipatnikov and Chomiak [11] suggested that, as the flame develops to eventually engulf the whole turbulent spectrum, a single characteristic value of burn rate might be attained. In practice, this may not be achievable. However, it might be expected that these variations will 'average out' over a long time and for large flames. However, measurements were possible in the present vessel up to 75 mm radius, due to the limited field of view by the window diameter, which is only about three times the integral length scale of turbulence. Perhaps, a single characteristic value of burn rate may not exist, as suggested in [61].

#### 4.4.1.2 Effect of pressure on turbulent burning velocity

Shown in Fig. 4.21 is the effect of pressure on $u_{tr}$ for $\phi$=0.8 and for two different $u'$. For lean mixtures, no significant influence of pressure on $u_{tr}$ is observed at low $u'$ and the scatter is large, as shown in Fig. 4.21(a). At high $u'$ values the differences are clear. In Fig. 4.21(b) $u_{tr}$ increases with pressure, and the effect is more pronounced under rich conditions and high $u'$ as shown in Fig. 4.22. In general, these figures show an increase of $u_{tr}$ with pressure, while laminar flames at the same conditions, presented in Section 4.2, exhibit an opposite trend.

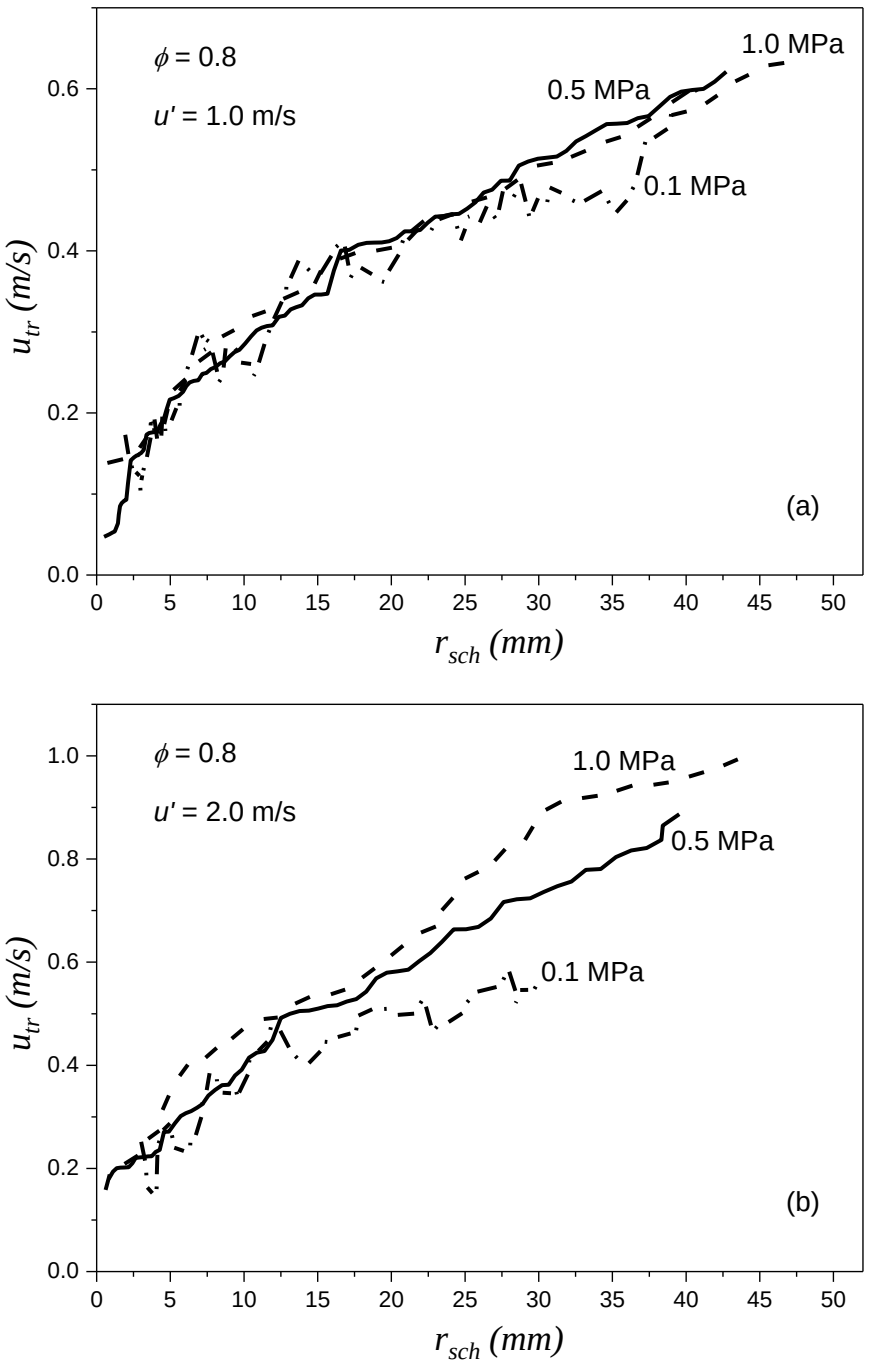


**Figure 4.21** Variations of $u_{tr}$ with increasing radii at 360 K $u'$=1.0 m/s (b) $u'$=2.0 m/s.

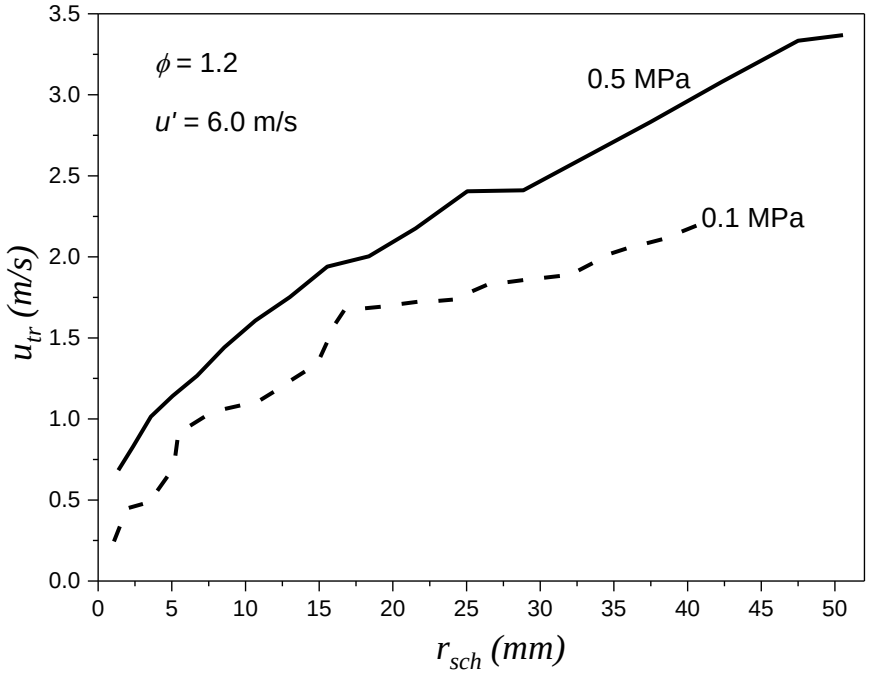


**Figure 4.22** Variations of $u_{tr}$ with increasing radii at 360 K.

#### 4.4.1.3 Effect of $\phi$ on turbulent burning velocity

In order to quantify the change in $u_{tr}$ with increasing $\phi$ and $u'$, shown in Fig. 4.23, values of turbulent burning velocities, $u_{tr}$, are plotted against $\phi$ at a flame radius of 30mm at pressures 0.1, 0.5 and 1.0 MPa. The ratio of effective rms turbulent velocity to rms turbulent velocity $u_k'/u'$varied between 0.62 and 0.7 for all $u'$ at 0.1, 0.5 and 1.0 MPa [68]. Symbols represent the mean value of five identical explosions and the standard deviations from the average values are shown by the error bars. Solid black lines show best fit curves through the data. As discussed for the $S_{sch}$ and $u_{tr}$ plots, increased scatter in the measurements of $u_{tr}$ are observed at higher $u'$ at all pressures. The $u_{tr}$ data on Fig. 4.23(c) for $\phi$ = 0.8 are slightly displaced to avoid overlap for better visualisation. Quench regions on the lean side of the mixtures are identified in each plot with the arrow pointing towards increasing $u'$.

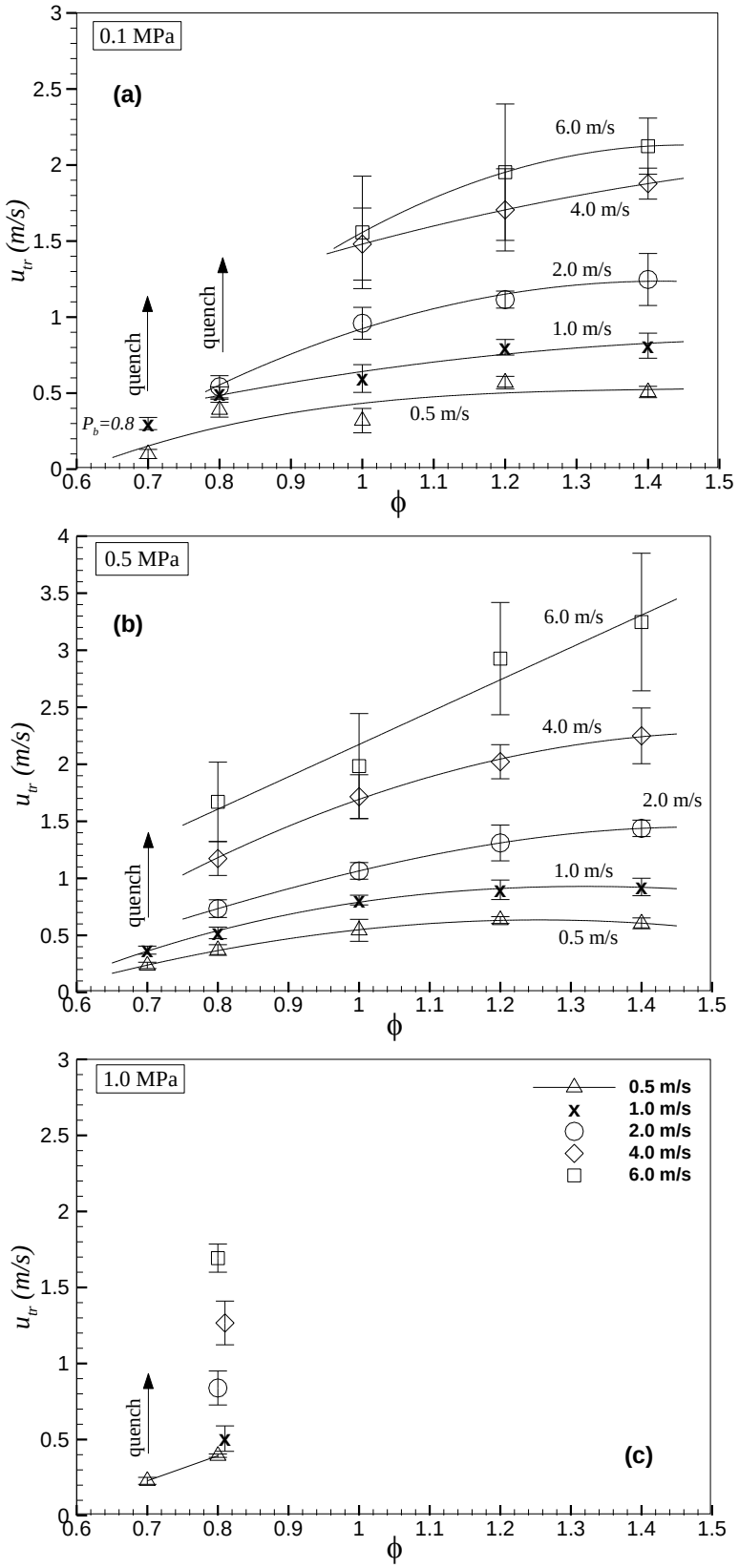


**Figure 4.23** Variation of $u_{tr}$ with $\phi$ for *n*-butanol/air at $r_{sch}$ $r_{sch}$= 30mm for different $u'$at 360 K (a) 0.1 MPa (b) 0.5 MPa (c) 1.0 MPa; solid line shows the best fit curve for the experimental data.

Generally, $u_{tr}$increased steadily from lean mixtures of $\phi$ = 0.8 to stoichiometric mixtures $\phi$ = 1.0. For flames at $u'$ = 0.5 m/s, the maximum value of $u_{tr}$ occurred on rich side at $\phi$ = 1.2. At $u'$ = 1.0 m/s values of $u_{tr}$ at $\phi$ = 1.4 reached similar values to $\phi$ = 1.2. and then exceeded them for $u'$ = 2 to 6 m/s. Similar behaviour was also observed by Lawes et al. [68] for $i$-octane/air mixtures. Flames quenched at $u' = 4m/s$ for $\phi$ = 0.8 at 0.1 MPa, while at 0.5 and 1.0 MPa 100% flame propagation was observed. Further lean mixtures e.g. $\phi$ = 0.7 resulted in flame quenching at lower $u'$ at all initial pressures. At 0.5MPa complete flame quenching was observed at $\phi$ = 0.7 and $u' = 2m/s$, whereas at 1.0 MPa flames quenched at a lower turbulence velocity of $u' = 1m/s$. On the other hand, at 0.1 MPa initial pressures and at $\phi$ = 0.7, 80% flame propagation, indicated by probability of burning, $p_b = 0.8$ in Fig. 4.23, was observed at $u' = 1m/s$. Further increase in $u'$ resulted in 20% flame propagation ($p_b = 0.2$) i.e. only 1 mixture exploded amongst five attempts made at $2m/s$.

#### 4.4.1.4 Effect of $u_k'$ on turbulent burning velocity

Abdel-Gayed et al. suggested [67] that in a turbulent explosion, initially a flame can only be wrinkled by turbulent eddies smaller than itself, while larger eddies in the flow field region merely convect it. As flame develops it experiences a greater proportion of turbulent spectrum, resulting in higher flame speeds and wrinkling. They defined a parameter, $u_k'$ to quantify the effect of rms contribution from different sized eddies and to show how flame straining rate develop in an explosion. It is calculated using the Eqs. (1.34) to (1.36).

Variations of $u_{tr}$ for the data presented in Figs. 4.17 to 4.19 are plotted against increasing $u_k'$ in Figs. 4.24 to Fig. 4.26, respectively. Values of $u_{tr}$ increase with increasing $u_k'$ and $u'$. Maximum values of $u_{tr}$ are observed for $u' = 6\ m/s$. Unlike the $S_{sch}$vs $r_{sch}$ and $u_{tr}$vs $r_{sch}$ plots, $u_{tr}$vs $u_k'$ reveals considerable change in $u_{tr}$ for different $u'$. Even at low $\phi$. $u_{tr}$ values plotted against $u_k'$ at $\phi$=0.8 and at 0.1 MPa in Fig. 4.24(a) show a significant variation and exhibit an oscillatory development, particularly at high $u$', as the flame experiences increasing $u_k'$. Such an oscillatory behaviour might be due to the deviation of

flame propagation from sphericality at high $u'$, as demonstrated in Fig. 4.20. This variation is reduced notably from leaner to richer flames.

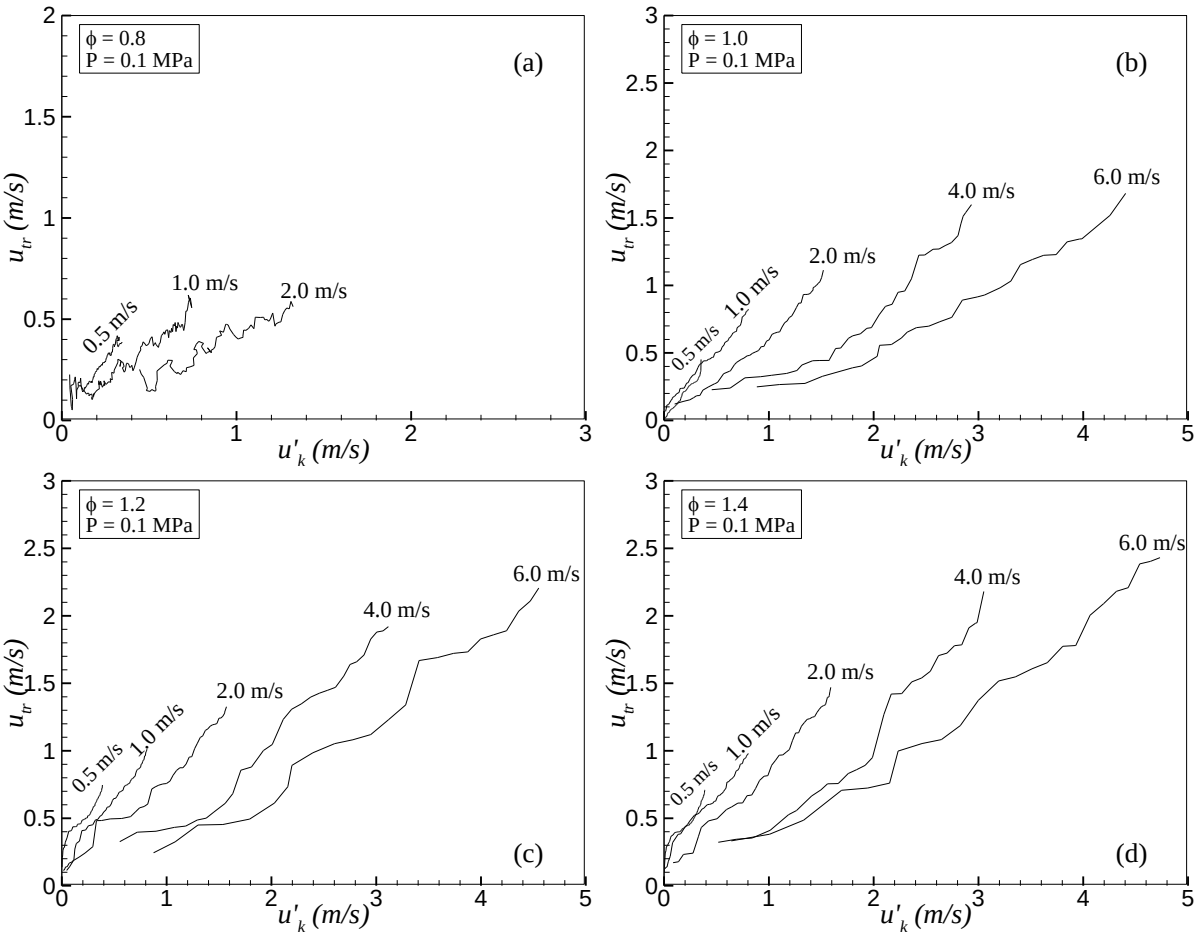


**Figure 4.24** Variations of $u_{tr}$ with $u'_k$ for different $u'$ at 360 K.

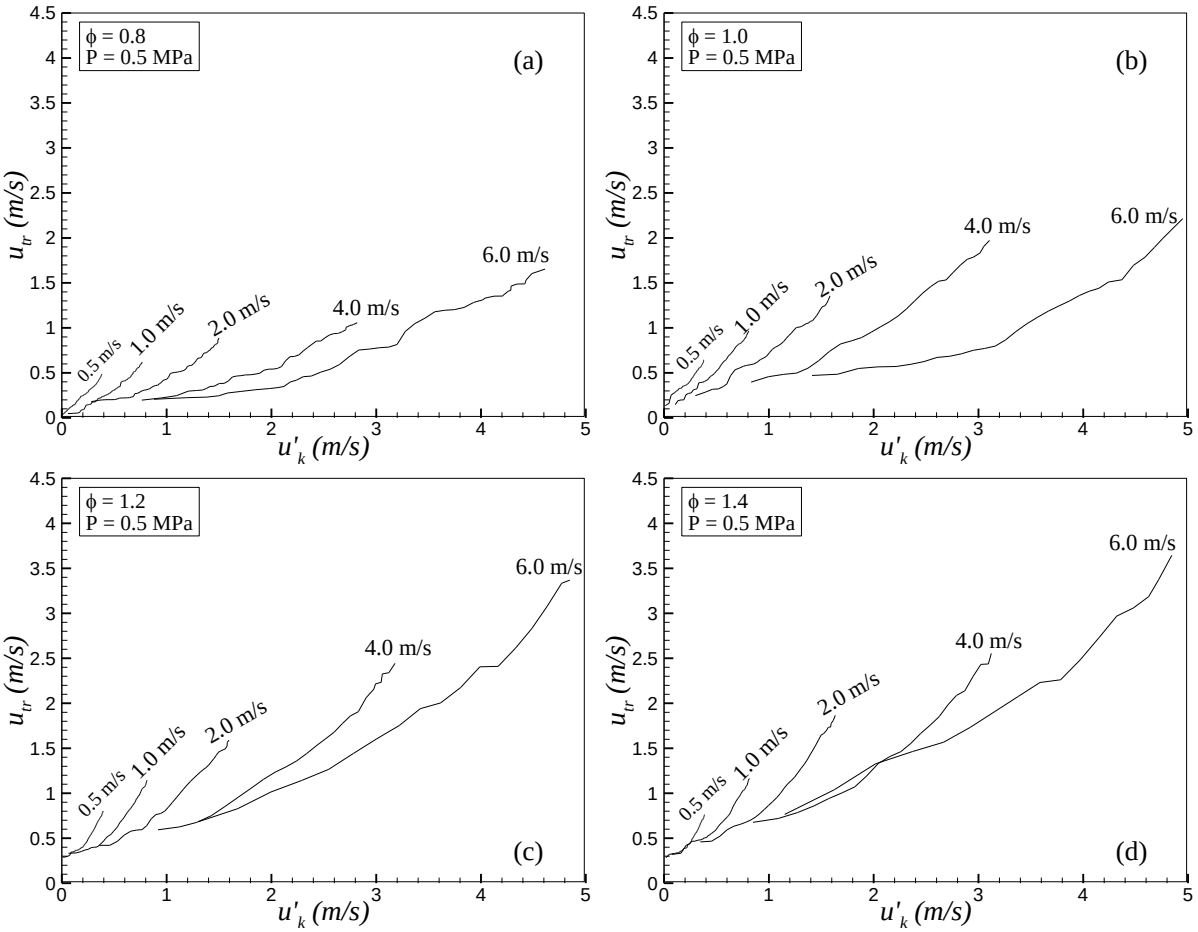


**Figure 4.25** Variations of $u_{tr}$ with $u'_k$ for different $u'$ at $\phi$ = 0.8, 1.0, 1.2 and 1.4 at 0.5 MPa, 360 K.

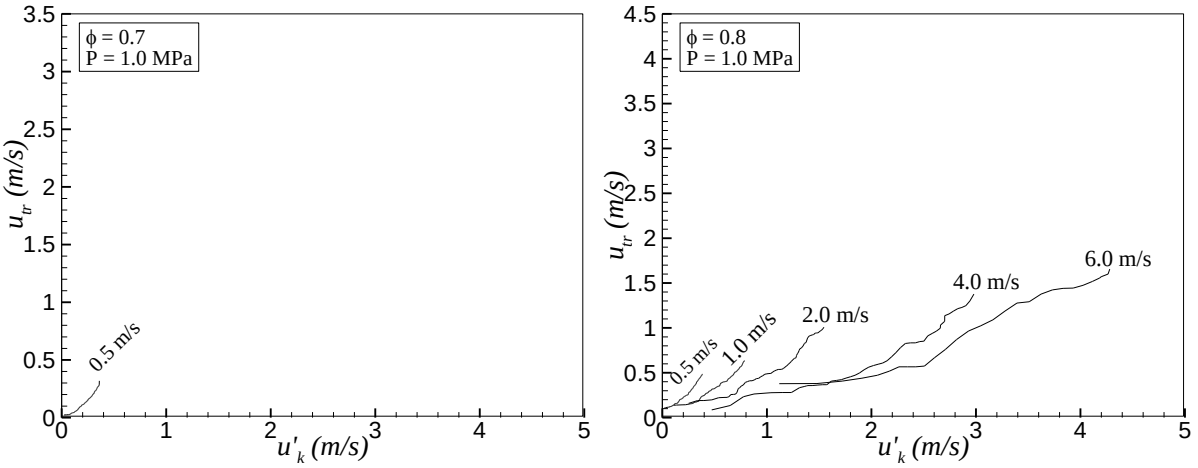


**Figure 4.26** Variations of $u_{tr}$ with $u'_k$ for different $u'$ at $\phi$ = 0.7, 0.8 at 1.0 MPa, 360 K.

#### 4.4.1.5 Enhancement of turbulent burning velocity ratio

Turbulent mass burning rates, $u_{tm}$, described in Section 1.4.4.1, are derived for the data presented in Figs. 4.24 to 4.26 using Eq. (1.42). The necessary data of $r_v/r_m$ are taken from [10] with a reported value of 1.32. These $u_{tm}$ values are normalised by the respective $u_l$, using results from Section 4.2.

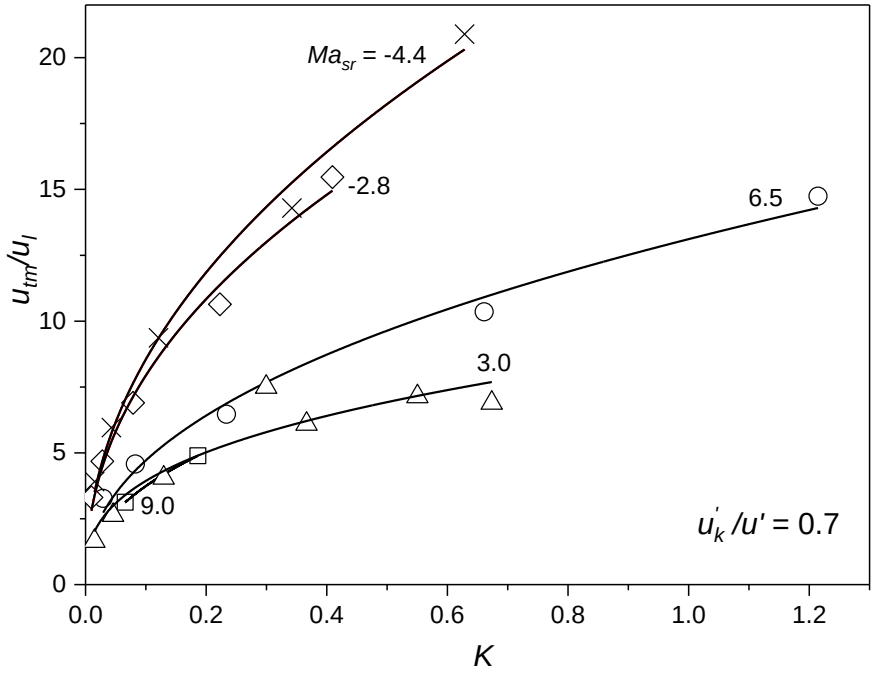


**Figure 4.27** Variations of $u_{tm}/u_l$ with $K$ for different $Ma_{sr}$ for *n*-butanol/air mixtures.

Shown in Fig. 4.27 are the turbulent burning enhancement ratios, $u_{tm}/u_l$ for $n$-butanol air mixtures plotted against $K$. These were calculated at a flame radius of 30 mm where $u_k'/u'$ is 0.7. Each symbol represents the mean from five identical explosions. Solid lines show the best fit curves through the data. These normalised data are grouped in terms of $Ma_{sr}$. Data for the conditions with close $Ma_{sr}$ values are omitted from the figure for clarity. $u_{tm}/u_l$ ratio increases with increasing $K$ and also with decreasing $Ma_{sr}$. This is further discussed in Section 5.4.

### 4.4.2 $CH_4$/air and $H_2$ mixtures

The turbulent mass burning rates, $u_{tm}$, for $CH_4$/air and $H_2$/air mixtures were measured for the experimental conditions presented in Table 4.3. These were obtained directly from the pressure measurement technique described in Section 2.3.1. These measurements were carried out simultaneously along with the 3D swinging laser sheet experiments that are presented in Section 4.5. As discussed in Section 2.3.3.2, $CH_4$/air and $H_2$/air mixtures were selected due to their low $u_l$ values so that they do not grow significantly during the time of swinging laser sheet sweep and allow more flame images to be captured before they grow beyond the volume of interest.

**Table 4.3** Experimental conditions for the present study, (+) represents the estimated value. (*) represents values from references for $u_l$ and $Ma_{sr}$.

| Fuel | $\Phi$ | T | P | $u'$ $(m/s)$ | $u_l$ (m/s) | $Ma_{sr}$ | Ref |
|---|---|---|---|---|---|---|---|
| $CH_4$ | 1.35 | 365 | 0.5 | 0.3-1.5 | 0.16 | 6* | [101] |
| | 1.25 | 365 | 0.5 | 0.3-2.0 | 0.241 | 4.8~ 5* | [101] |
| | 1.3 | 300 | 0.1 | 0.3-1.5 | 0.16* | 3.9~ 4* | [21] |
| | 0.7 | 300 | 0.1 | 0.3-1.5 | 0.21* | 2.7~3* | [21] |
| | 0.6 | 365 | 0.1 | 0.3-1.5 | 0.13 | 2* | [101] |
| $H_2$ | 0.3 | 365 | 0.5 | 0.3-2.0 | 0.102* | $-5^+$ | [171] |
| | 0.4 | 365 | 0.5 | 0.3-1.5 | 0.286* | -6.34* | [171] |

Unlike the schlieren imaging technique, with measurements at flame radii between about 20 mm up to a value of 55 mm in the developed linear regime, reliable pressure records could only be obtained between radii of 35 mm and 105 mm. Values of $u'$ varied between 0.3 to 2.0 m/s, while $u_{tm}$ and $r_m$ were calculated from pressure records data using Eqs. (1.40) and (1.41). Figures. 4.28 to 4.31 show $u_{tm}$ plotted against mean radius, $r_m$, for increasing $u'$ at

different experimental conditions for both $CH_4$ and $H_2$. These were grouped in terms of $Ma_{sr}$. Solid and broken lines shows the best fit through the obtained data, and error bars show the variability from three identical explosions.

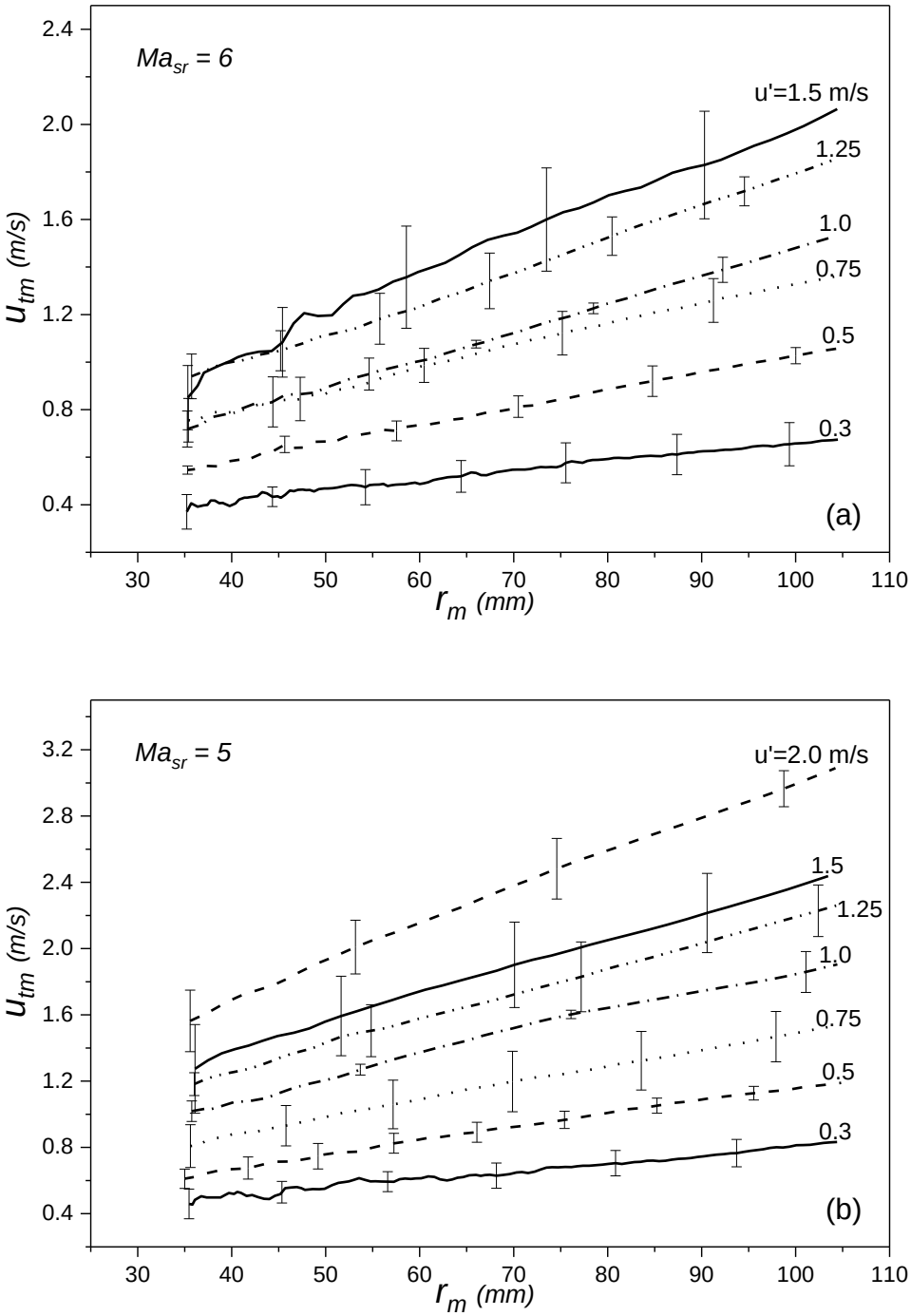


**Figure 4.28** Variations of $u_{tm}$ with $r_m$ for increasing $u'$ for $CH_4$/air at 365K, 0.5 MPa (a) $\phi$ =1.35 (b) $\phi$ =1.25.

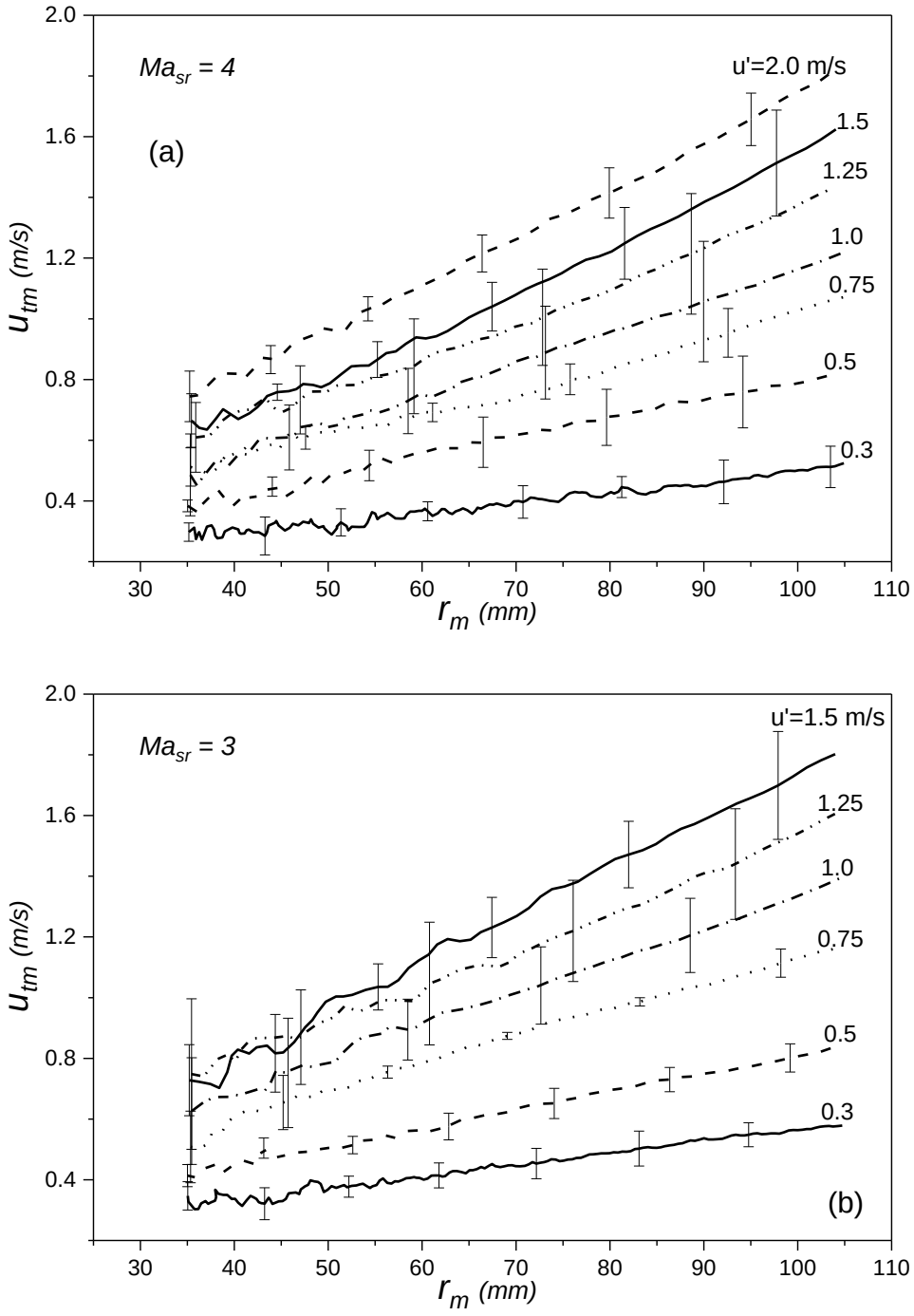


**Figure 4.29** Variations of $u_{tm}$ with $r_m$ for increasing $u'$ for $CH_4$/air at 300K, 0.1 MPa (a) $\phi$ =1.3 (b) $\phi$ =0.7.

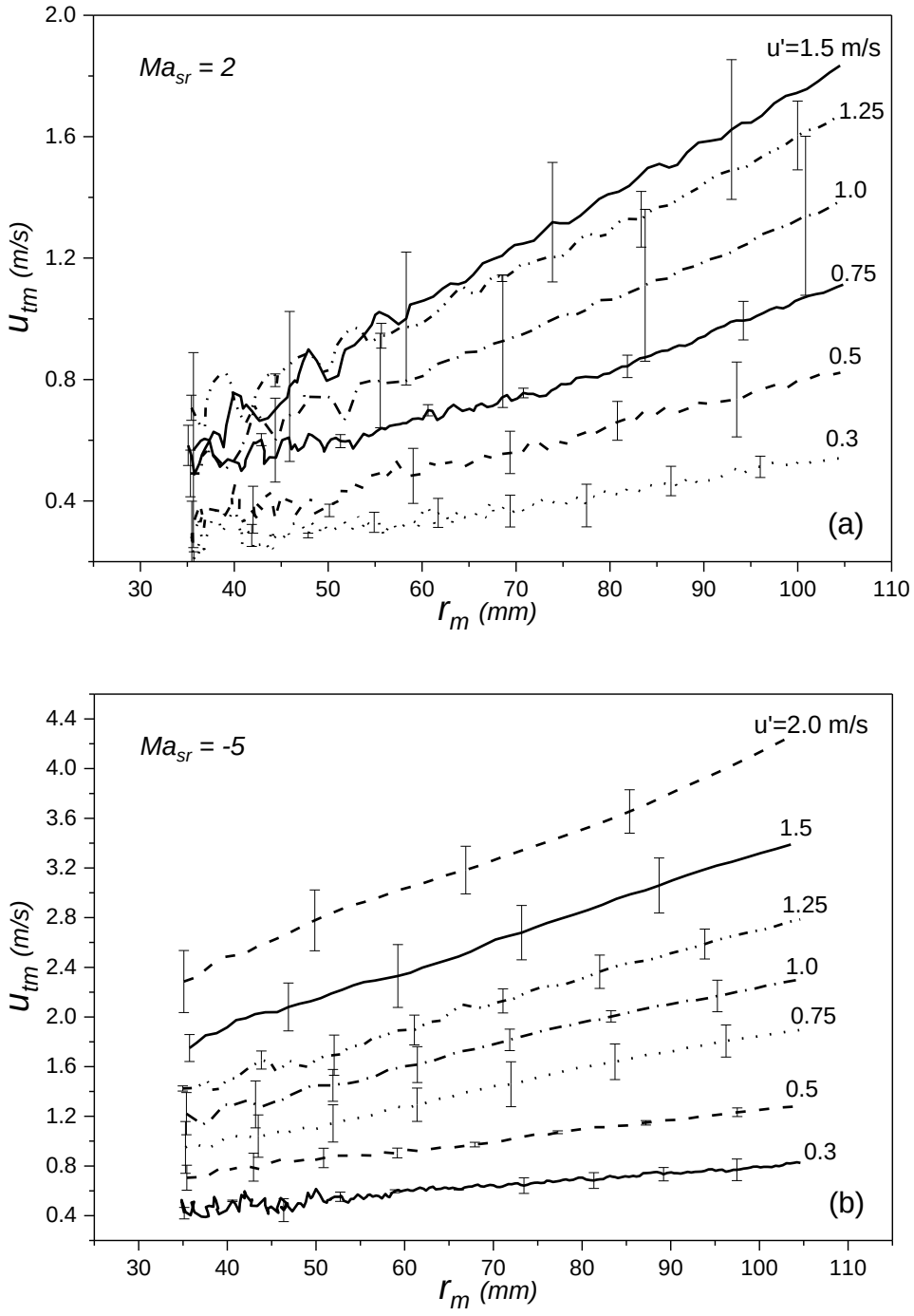


**Figure 4.30** Variations of $u_{tm}$ with $r_m$ for increasing $u'$ at 365K (a) $CH_4$/air $\phi$ =0.6, 0.1 MPa (b) $H_2$/air $\phi$ =0.3, 0.5MPa.

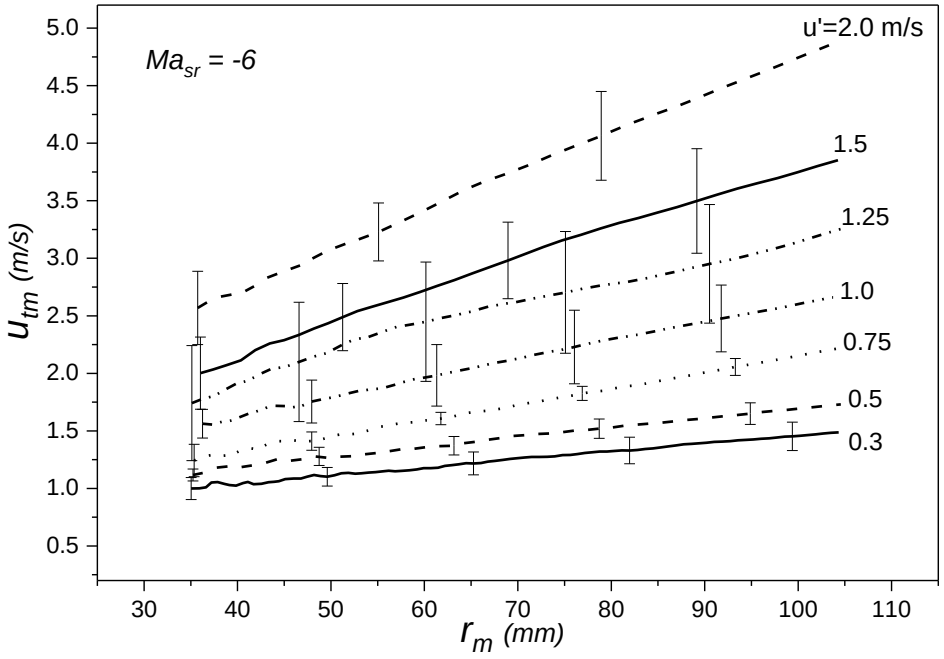


**Figure 4.31** Variations of $u_{tm}$ with $r_m$ for increasing $u'$ for $H_2$/air at $\phi$ =0.4, 0.5MPa, 365K.

Similar to the turbulent burning velocities of $n$-butanol/air mixtures presented in Section 4.4.1, $u_{tm}$ increased with increasing $r_m$ and $u'$, as a result of flame wrinkling due to the continual broadening of the effective turbulence spectrum, $u_k'$, described in Section 4.4.1. High scatter was observed in the $u_{tm}$ values during the initial stages of flame development for lean $CH_4$/air at =0.6, 365K and 0.1 MPa, as shown in Fig. 4.30(a). These are in line with the scatter for lean mixtures presented in $u_{tr}$ for $n$-butanol in Section 4.4.1.1 which supports the argument for the onset of flame quenching.

#### 4.4.2.1 Enhancement of turbulent burning velocity ratio

Values of $u_{tm}/u_l$ were found at a radius of 30 mm from the data in Figs. 4.28 to 4.31. These were obtained by slightly extrapolating to facilitate comparisons between the different techniques and with different fundamental parameters, such as the flame surface area ratio, presented in Section 4.5, where the maximum flame radius, in most cases, could only reach an approximate value of 30 mm. Values of $u_{tm}/u_l$ evaluated for $CH_4$ and $H_2$ mixtures are shown in Fig. 4.32 plotted against Karlovitz stretch factor, $K$, for different $Ma_{sr}$ values.

Solid lines are the best fit curves through the data. At lower $K$, values of $u_{tm}/u_l$ increase linearly followed by lesser fractional gains. These results are in line with the turbulent burning enhancement ratio for $n$-butanol/air mixtures presented in Section 4.4.1. Interestingly, the values of $u_{tm}/u_l$ from Fig. 4.27 and Fig. 4.32 for $Ma_{sr}$ values close to -5 and 6, were similar in magnitude over the range of $K$, while a slight difference was observed at low positive $Ma_{sr}$. This is discussed further in Section 5.4.

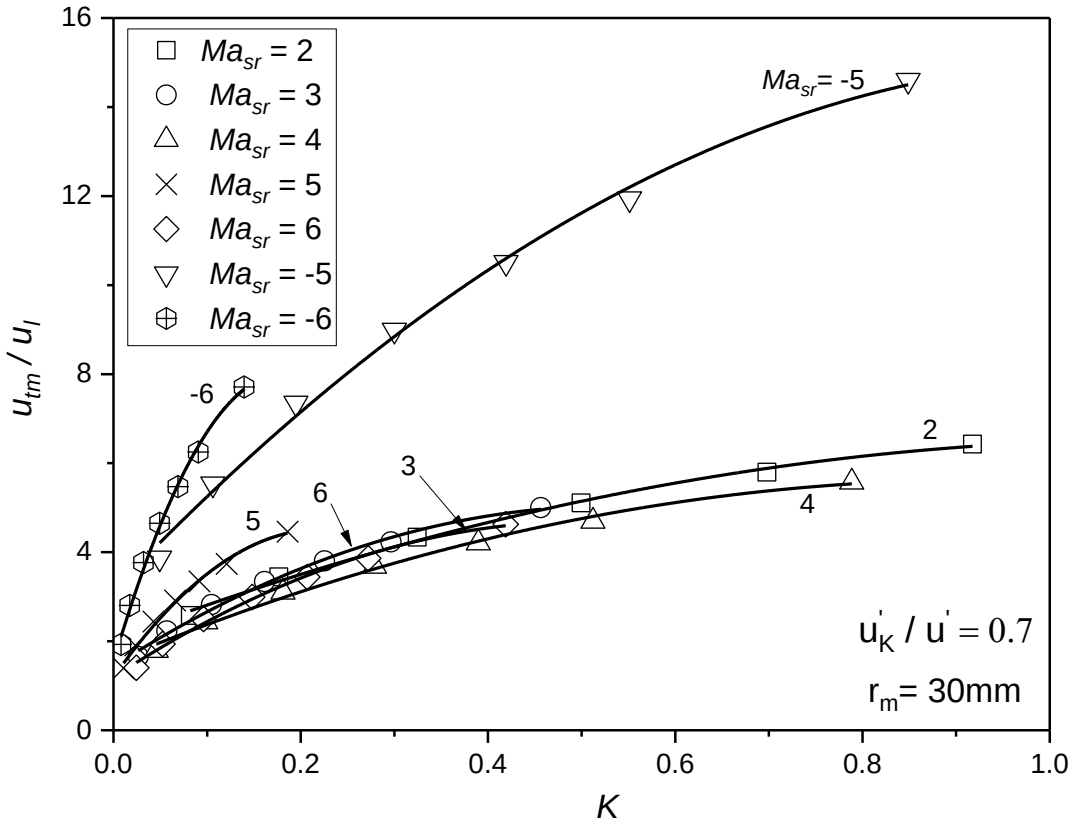


**Figure 4.32** Variations of $u_{tm}/u_l$ with Karlovitz stretch factor, $K$ for the experimental conditions in Table 4.3.

## 4.5 3D turbulent flame results

This section presents the work carried out on 3D turbulent flame structure using the 3D swinging sheet technique described in Section 2.3.3. As discussed in Section 1.6, this technique allows the flame analysis without the necessity for assumptions about the relationship between 2D flame structure and its extension into the third dimension. Limited by the laser repetition rate, this technique requires slow burning flames.

$CH_4$/air and $H_2$/air mixtures were employed for the study. Details of the different experimental conditions are presented in Table 4.3. The reference number in the Table shows the sources of $u_l$ and $Ma_{sr}$ data. To study the effects of $u'$, on turbulent flame structure, values ranging from 0.3 m/s to 2.0 m/s were employed. This led to Karlovitz stretch factor, $K$, values between 0.046 and 0.79.

### 4.5.1 2D Mie-scattered images

Shown in Fig. 4.33 is a set of 2D raw flame images obtained during a sweep at 21.5 ms after ignition for $CH_4$/air at $\phi$ =1.35, 365K and 0.5 MPa. The imaging laser was pulsed at 54 kHz and a total of 60 slices through the flame were captured at this 'instant'. The numbers indicate the order of sequential slicing. Every fourth image in Figs. 4.33 is dark. This is due to the limitation of the second IL laser cavity to pulse laser light at high frequencies. Nevertheless, this had no influence on the analysis or interpretation of results as the contrast between the flame and the background was reasonably well and the algorithms successfully detected the flame images by intensity gradient method.

Looking at these individual images it is difficult to predict the overall shape of the flame and its 3D structure. when the flame is analysed using a schlieren imaging technique, the flame appears almost spherical. The sequence of 2D slices reveal some limited information about the flame structure. For example, all slices exhibit considerable wrinkling and many of them (e.g. slices 14 to 17) show apparent fragmentations, or islands of burned gas that are unconnected to the main body of the flame. Further, other slices (e.g. slice 7 to 8) appear to show islands of unburned gas within the main flame. Better visualisation of the enlarged view of these (7 to 8) slices are presented in APPENDIX A (Fig. A.1). It is more informative to consider several adjacent flames rather than each one in isolation. For example, by comparing slices 6 to 9, shown in Fig. 4.33, it can be seen that the apparent island in frames 7 and 8 is more likely to be slice through a peninsular.

Shown in Fig. 4.34 is a similar sequence to that in Fig. 4.33 at the same conditions but at higher turbulence with $u'$ = 1.5 m/s. It can be seen that these images are much more fragmented and less sharp than those in Fig. 4.33. This makes analysis more problematic as discussed in Chapter 3. Images such as those in Figs 4.31 and 4.32 were used to provide quantitative data on parameters that include total surface areas and mean surface areas, results of which are presented in Section 4.5.4.

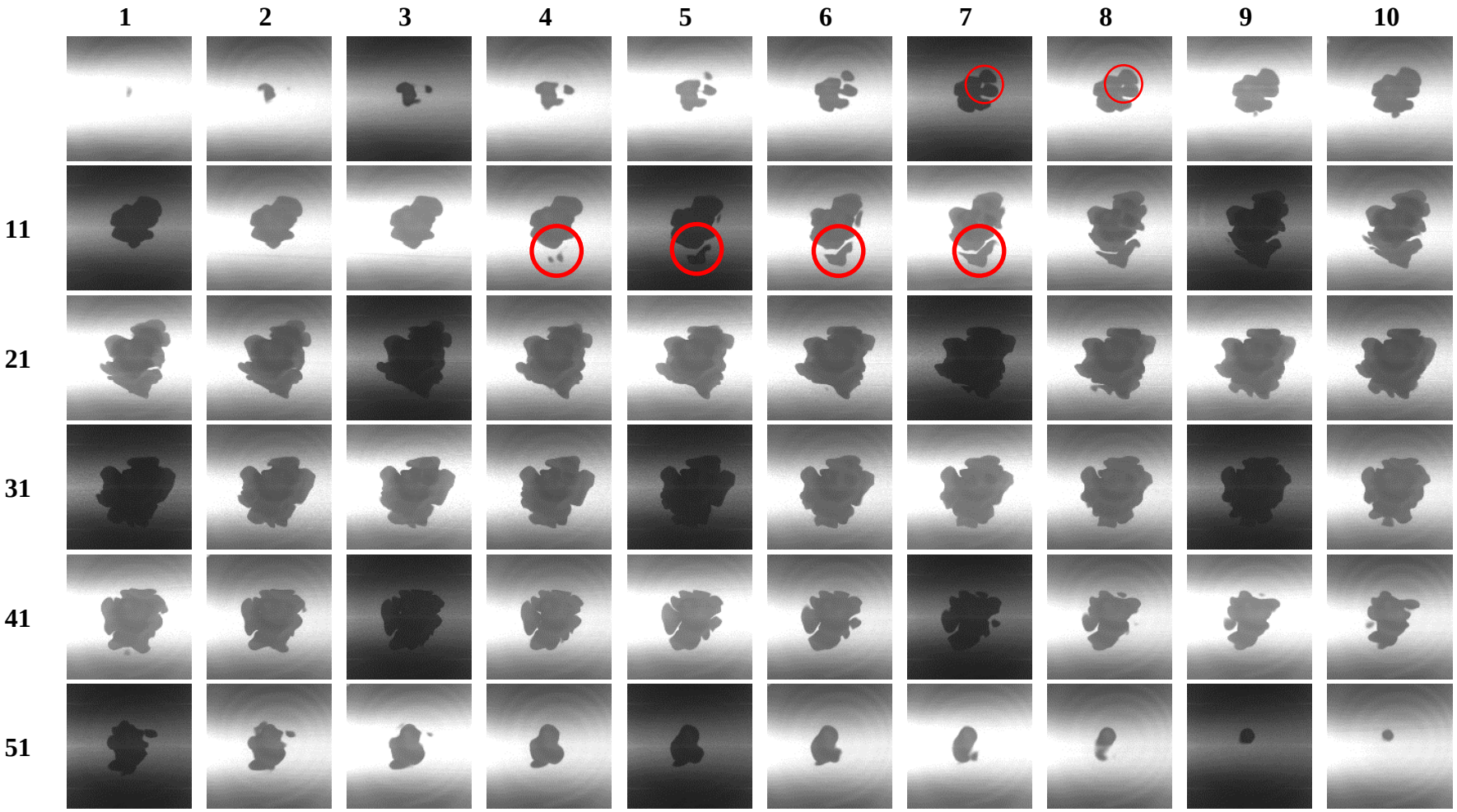


**Figure 4.33** Set of raw flame image data in one sweep at one instant for $CH_4$/air, 300K, 0.1MPa, $\phi$ = 0.7, $u'$=0.3 m/s.

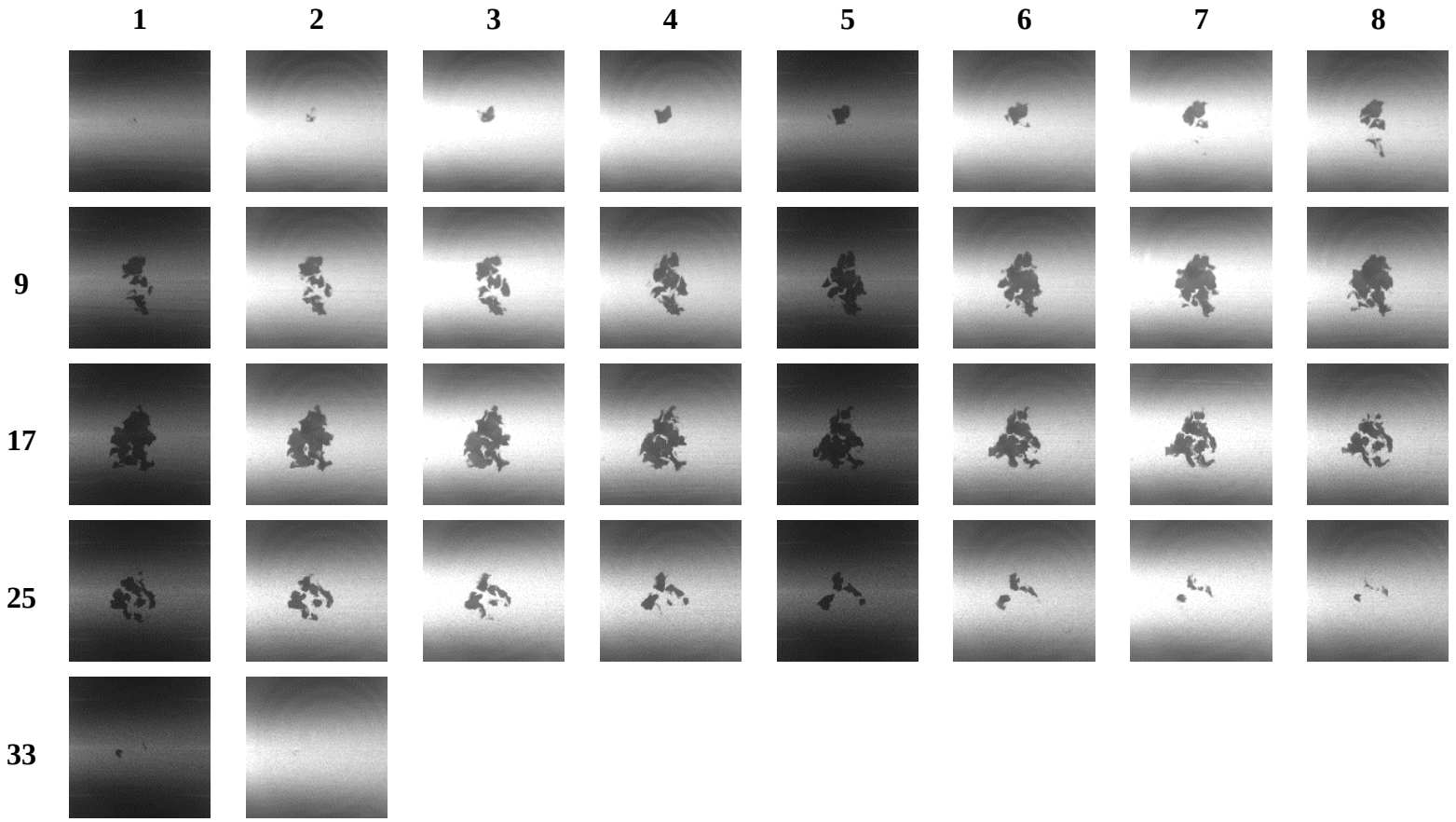


**Figure 4.34** Set of raw flame image data in one sweep at one instant for CH4/air, 300K, 0.1MPa, $\phi$ = 0.7, $u'$=1.5 m/s and 11.1 ms after ignition.

### 4.5.2 3D turbulent flame reconstructions

Figure 4.35 shows the 3D reconstructed flames for $CH_4$/air at $\phi$ =1.35, 365K and 0.5 MPa, at low turbulence of $u'$=0.3m/s and at different times during the same explosion. The image for 16.3 ms represents the reconstruction using the 2D images presented in Fig. 4.33. The raw images were binarised, as shown in Fig. 3.7, before reconstructions. As the flame grew, it tended to retain its overall approximately spherical shape formed during the ignition, while the surface became more wrinkled as the flame experienced increasing turbulent length scales.

The flame represented by the images in Fig. 4.36 at a higher $u'$=1.5m/s became progressively more distorted as it grew, with its surface becoming visibly highly wrinkled. These wrinkles increased the flame surface area and burning rate, as discussed in Sections 4.4. Because the flame represented in Fig. 4.36 was faster than that in Fig. 4.35, fewer images were captured.

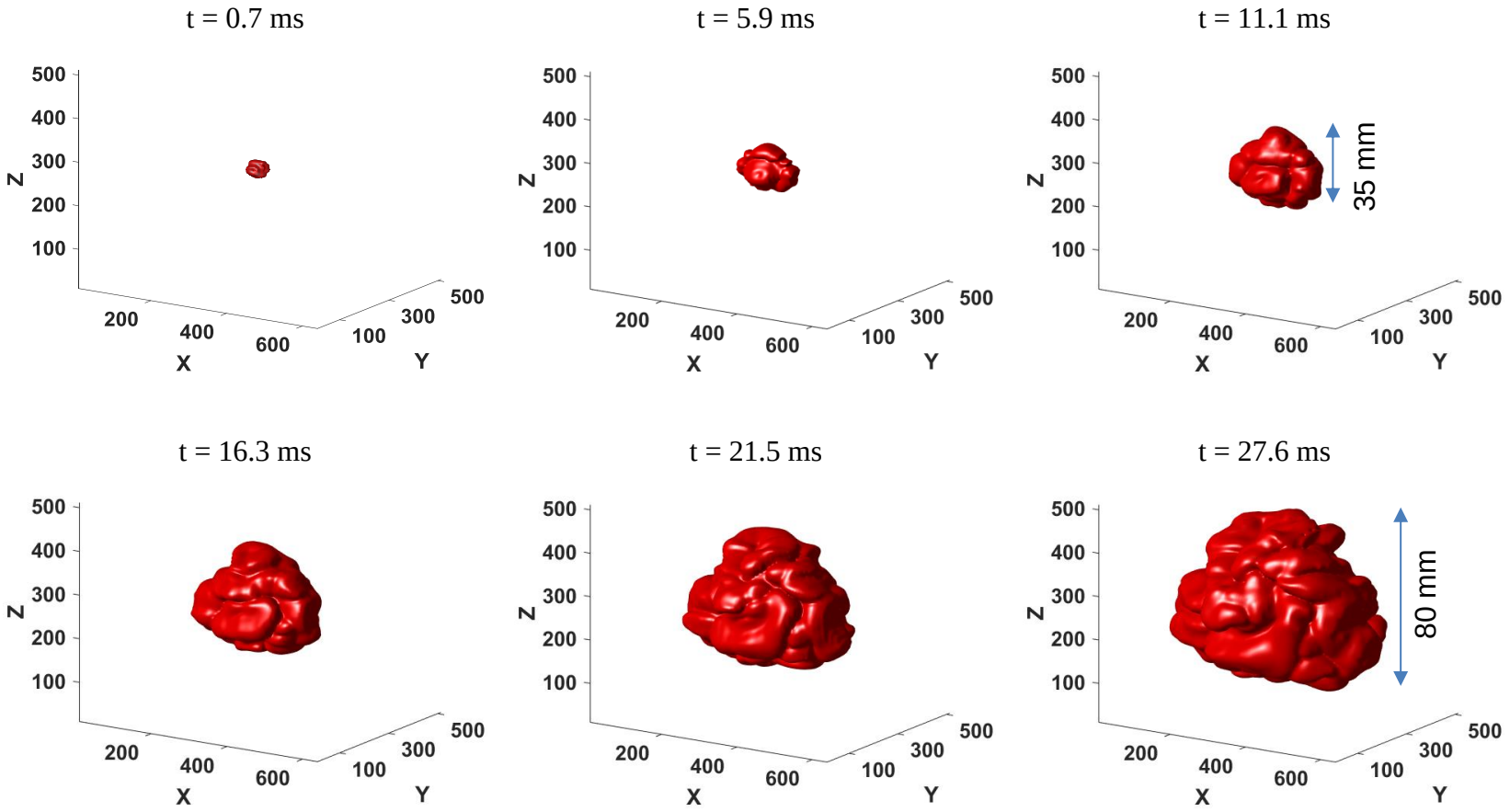


**Figure 4.35** 3D reconstructed $CH_4$/air flames, $\phi$=0.7, 300K, 0.1 MPa with increasing time during an explosion at $u'$=0.3m/s.

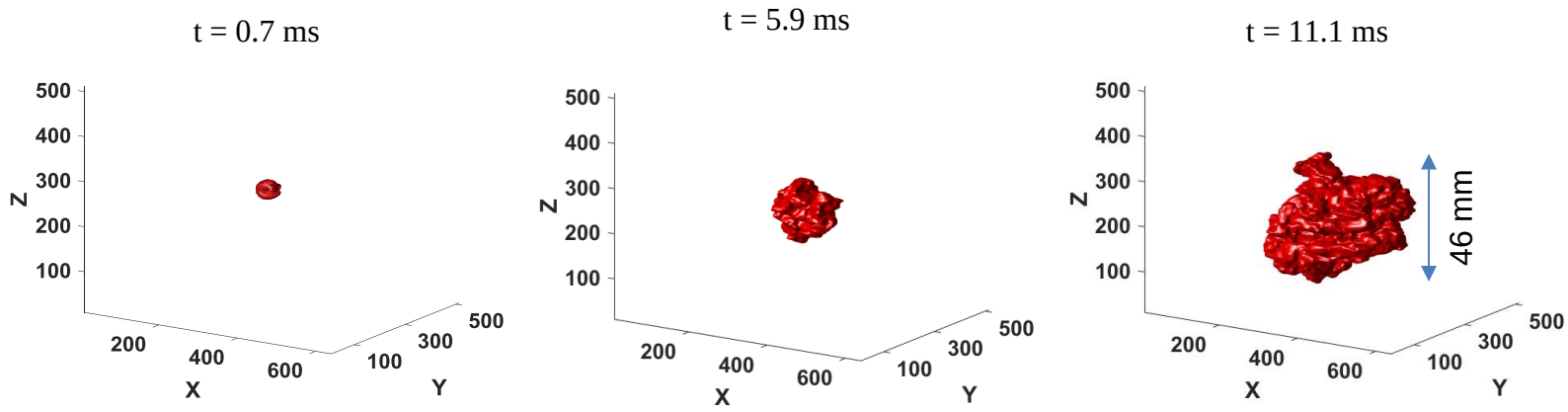


**Figure 4.36** 3D reconstructed $CH_4$/air flames, $\phi$=0.7, 300K, 0.1 MPa with increasing time during an explosion at $u'$=1.5m/s.

### 4.5.3 Flame radius

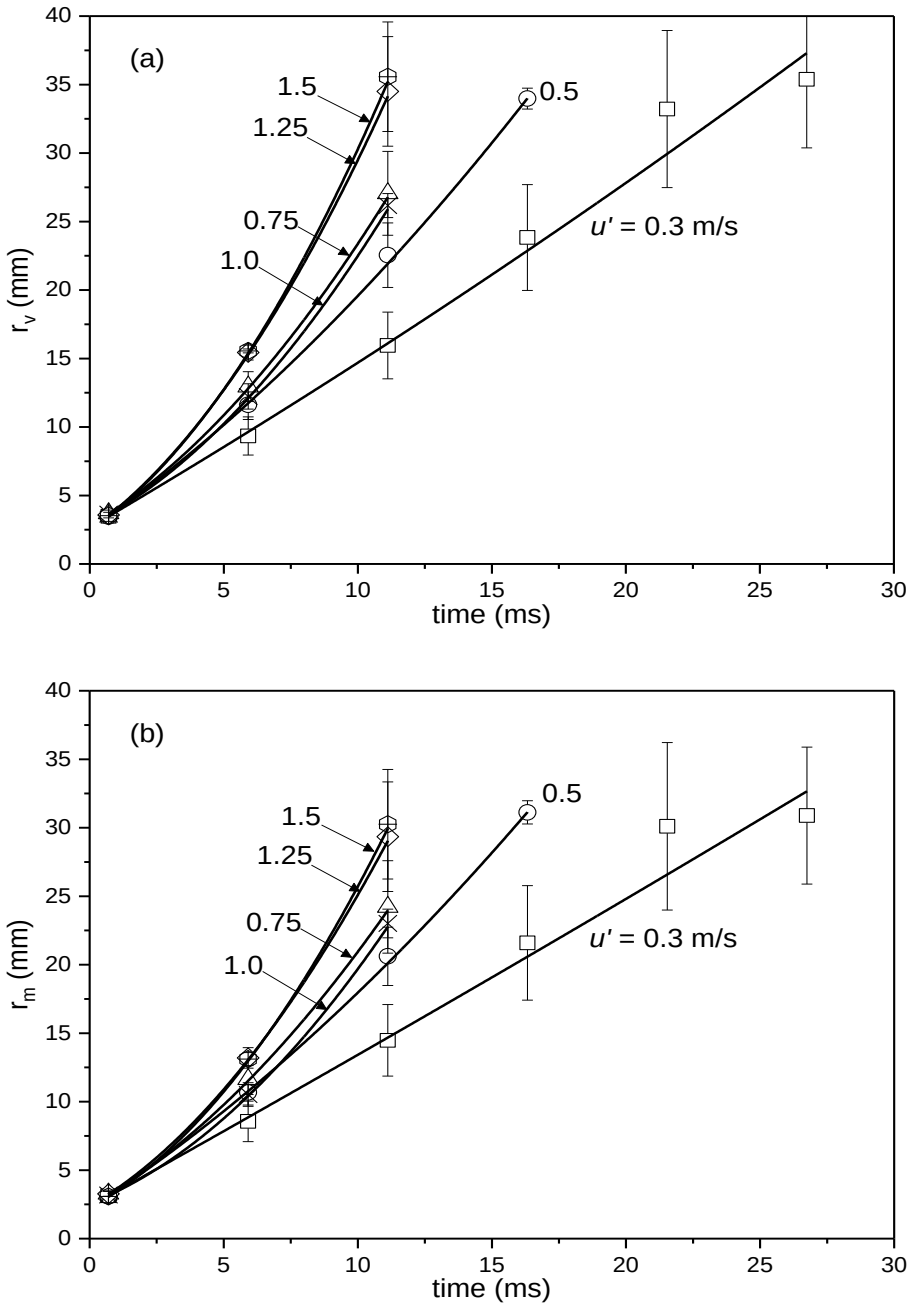


**Figure 4.37** $CH_4$/air flames at 0.5 MPa, 365K, $\phi$ = 1.35 (a) $r_v$ against time (b) $r_m$ against time for different $u'$.

Mean radii, $r_v$, based on volume balancing and $r_m$, based on mass balancing are obtained for $CH_4$/air flames at 0.5 MPa, 365K and $\phi$ = 1.35, using the method described in Section 3.3.3.3. Figs. 4.37(a) and 4.37(b) show $r_v$ and $r_m$ plotted against time for several values of $u'$. The symbols show the average of three explosions at the same condition, the error bar shows the standard deviation from the mean. Flame radii increases with time and $u'$.

As with the schlieren measurements of burning rate in Section 4.2, considerable variations between measurements were obtained, even under identical conditions. This was also reflected in the variability in the flame shape, as shown by the images of three flames under identical conditions in Fig. 4.38. The variability in the average flame diameter ranged between approximately 9% at low flame radii, up to 26% at higher flame radii. This gives an interesting measure of experimental variability under the well-controlled environment of the fan stirred vessel.

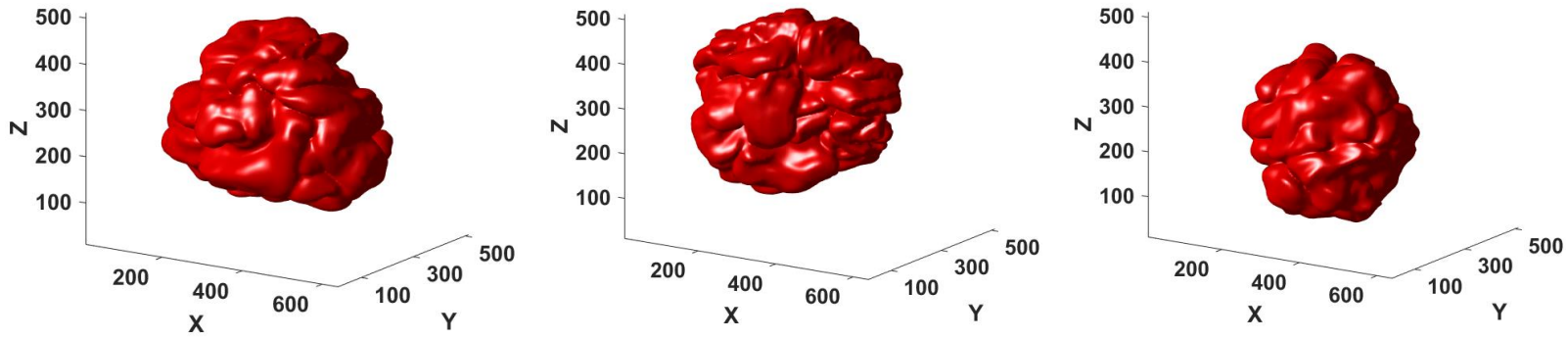


Explosion 1 Explosion 2 Explosion 3

**Figure 4.38** 3D reconstructed $CH_4$/air flames, 0.1 MPa, 300K, $\phi$=0.7, 16.3 ms after ignition for three identical explosions, at $u'$=0.3m/s.

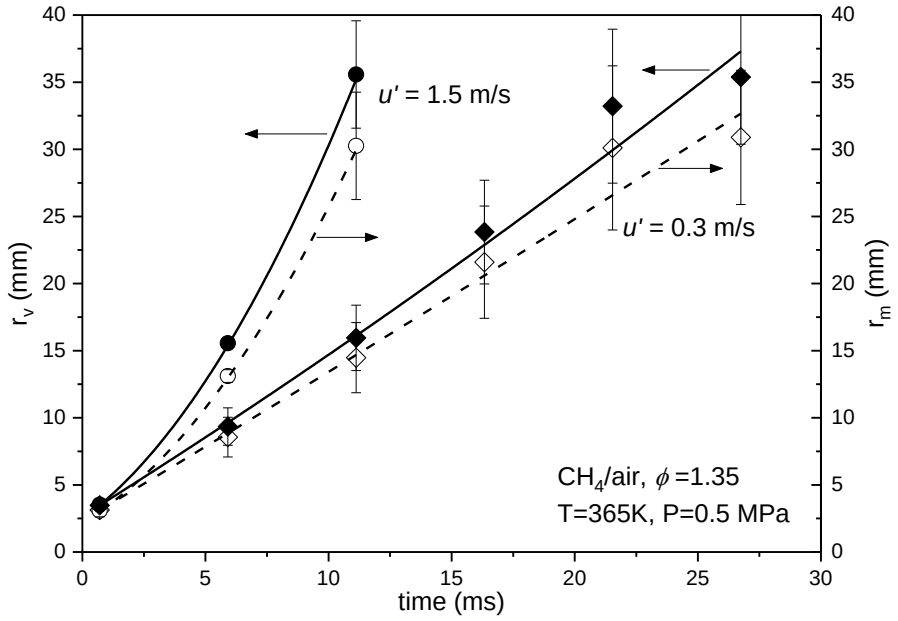


**Figure 4.39** Comparison of $r_v$ and $r_m$ against time.

Shown in Fig. 4.39 is a comparison of $r_v$ and $r_m$ for the data shown in Fig. 4.37 at different instances of time for $u'$ of 0.3 and 1.5 m/s. It is observed that the values of $r_m$ are always lower than $r_v$. The difference increase with increase in time from ignition. The maximum difference observed was 13 %.

Shown in Figs. 4.40 to 4.43 are the mean radii $r_m$ for increasing $u'$ for all the experimental conditions presented in Table 4.3. Solid lines are the best fit through the data. Again, the error bar shows the variability from three identical explosions. The relevant $Ma_{sr}$ values for each experimental condition is shown on the respective plot. Similar to the burning velocity data shown in Fig. 4.12, the trends of $r_m$ increase with time. For negative $Ma_{sr}$ conditions, the number of flames captured were limited and this is further discussed in Section 5.5.

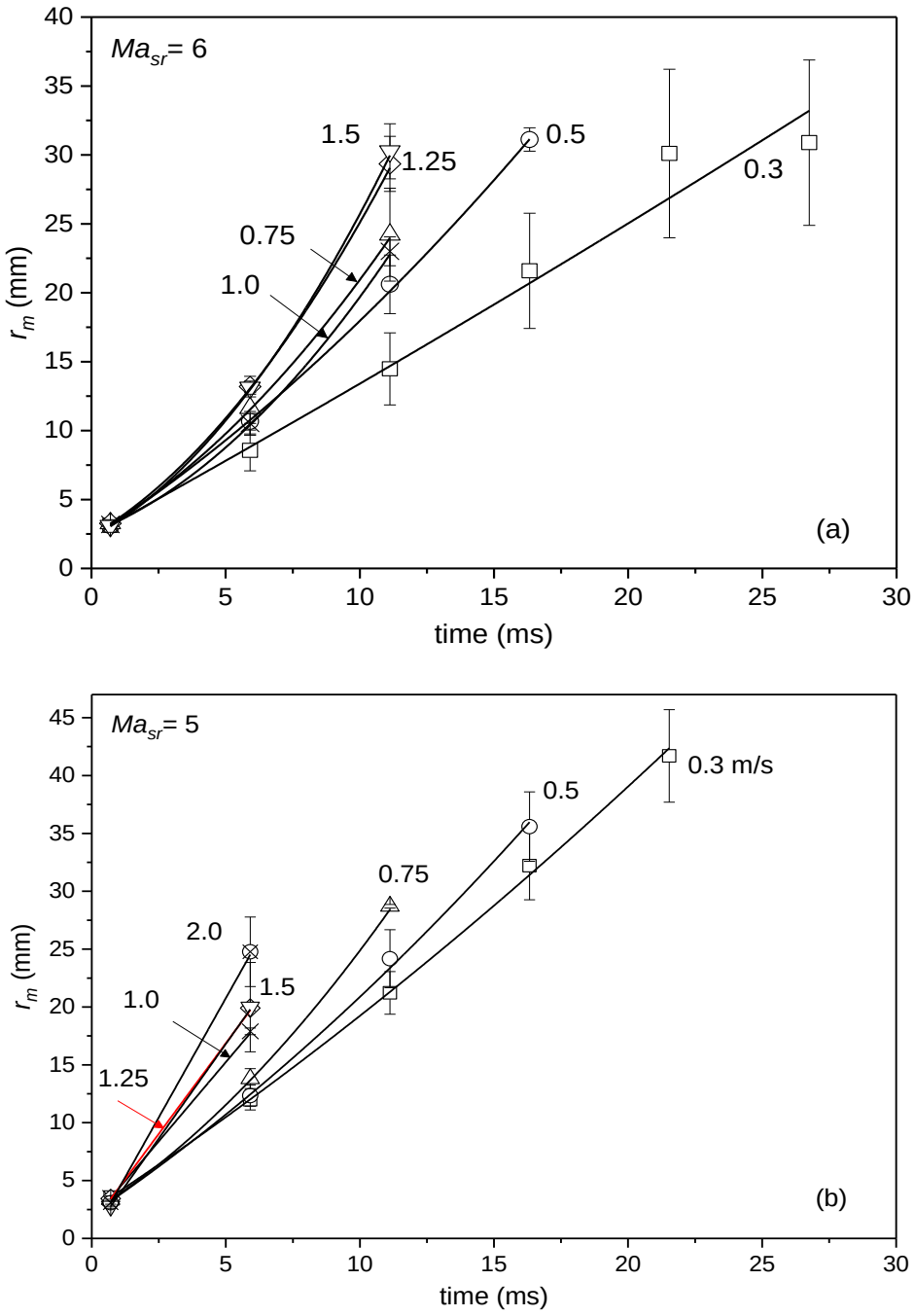


**Figure 4.40** Variations of $r_m$ against time for increasing $u'$ for $CH_4$/air at 365K, 0.5 MPa (a) $\phi$ =1.35, (b) $\phi$ =1.25.

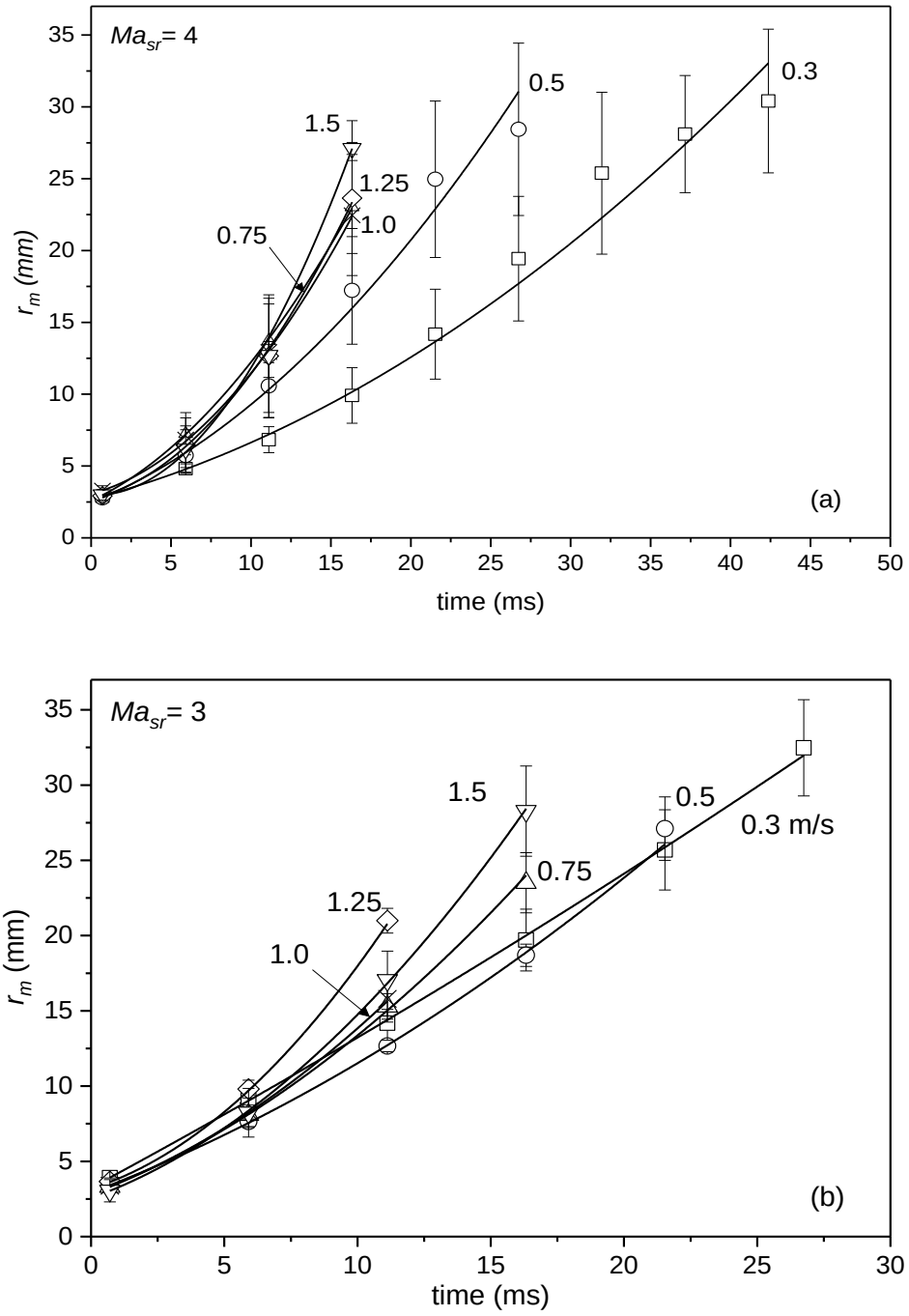


**Figure 4.41** Variations of $r_m$ against time for increasing $u'$ at for $CH_4$/air at 300K, 0.1 MPa (a) $\phi$ =1.3 (b) $\phi$ =0.7.

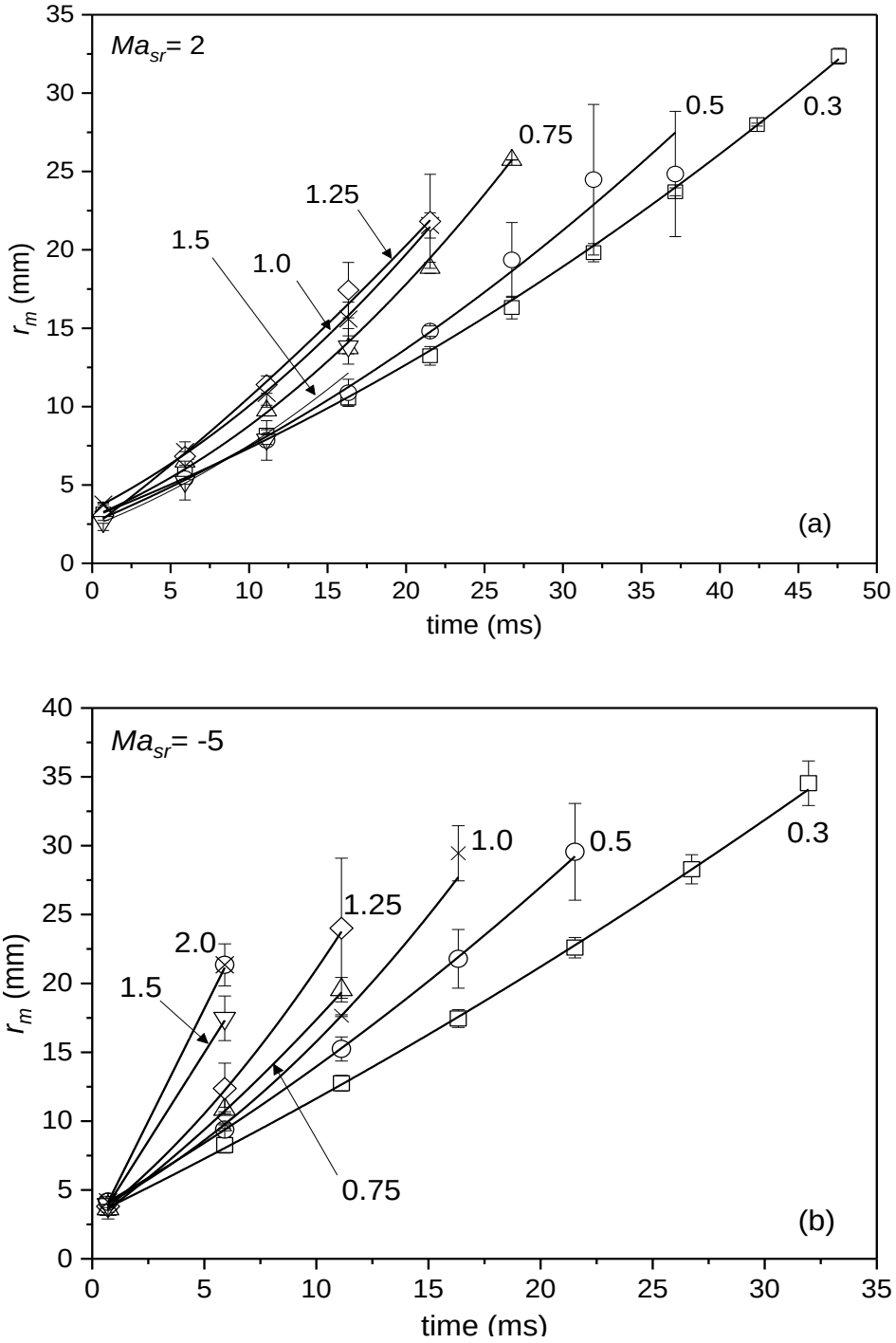


**Figure 4.42** Variations of $r_m$ against time for increasing $u'$ at 365K (a) $CH_4$/air $\phi$ =0.6, 0.1 MPa (b) $H_2$/air $\phi$ =0.3, 0.5MPa.

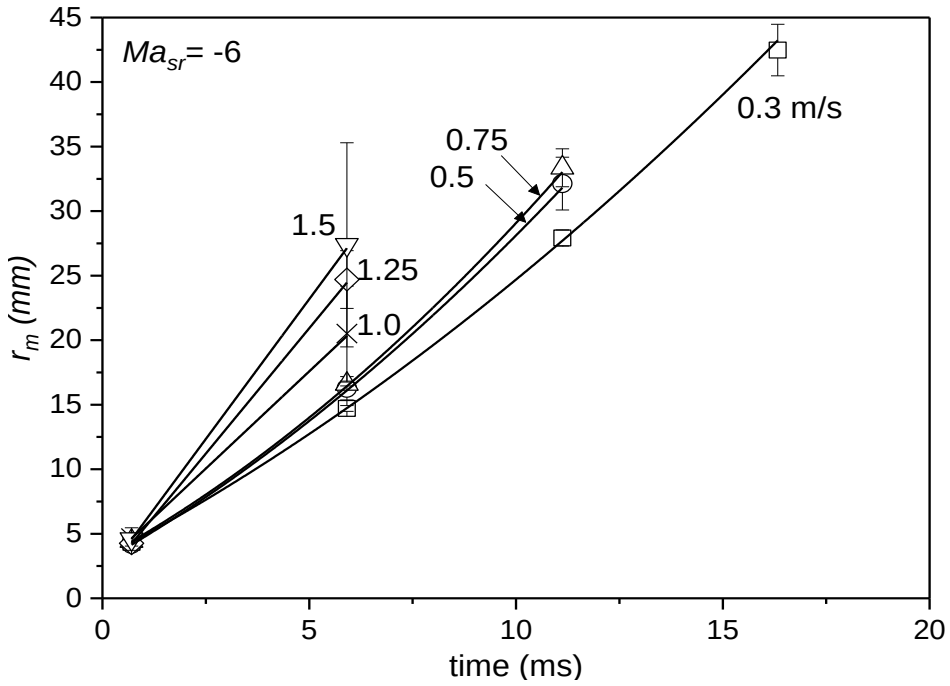


**Figure 4.43** Variations of $r_m$ against time for increasing $u'$ for $H_2$/air, $\phi$ =0.4, 0.5 MPa, 365 K.

### 4.5.4 Flame Surface Area ratio

Shown in Figs. 4.44 to 4.47 are surface area ratios, $A/a_m$, with increasing $u'$ for all the experimental conditions in Table 4.3. These represent the increase in flame area due to turbulence, compared with a laminar flame. Values of total flame surface area $A$, were obtained, as described in Section 3.3.3.1, using Eqs. (3.2) and (3.3). Values of mean spherical flame area, $a_m$, described in Section 3.3.3.3, were obtained using an algorithm developed by the present author. The symbols represent the average of three identical explosions under identical conditions. Solid lines are best fits through the data.

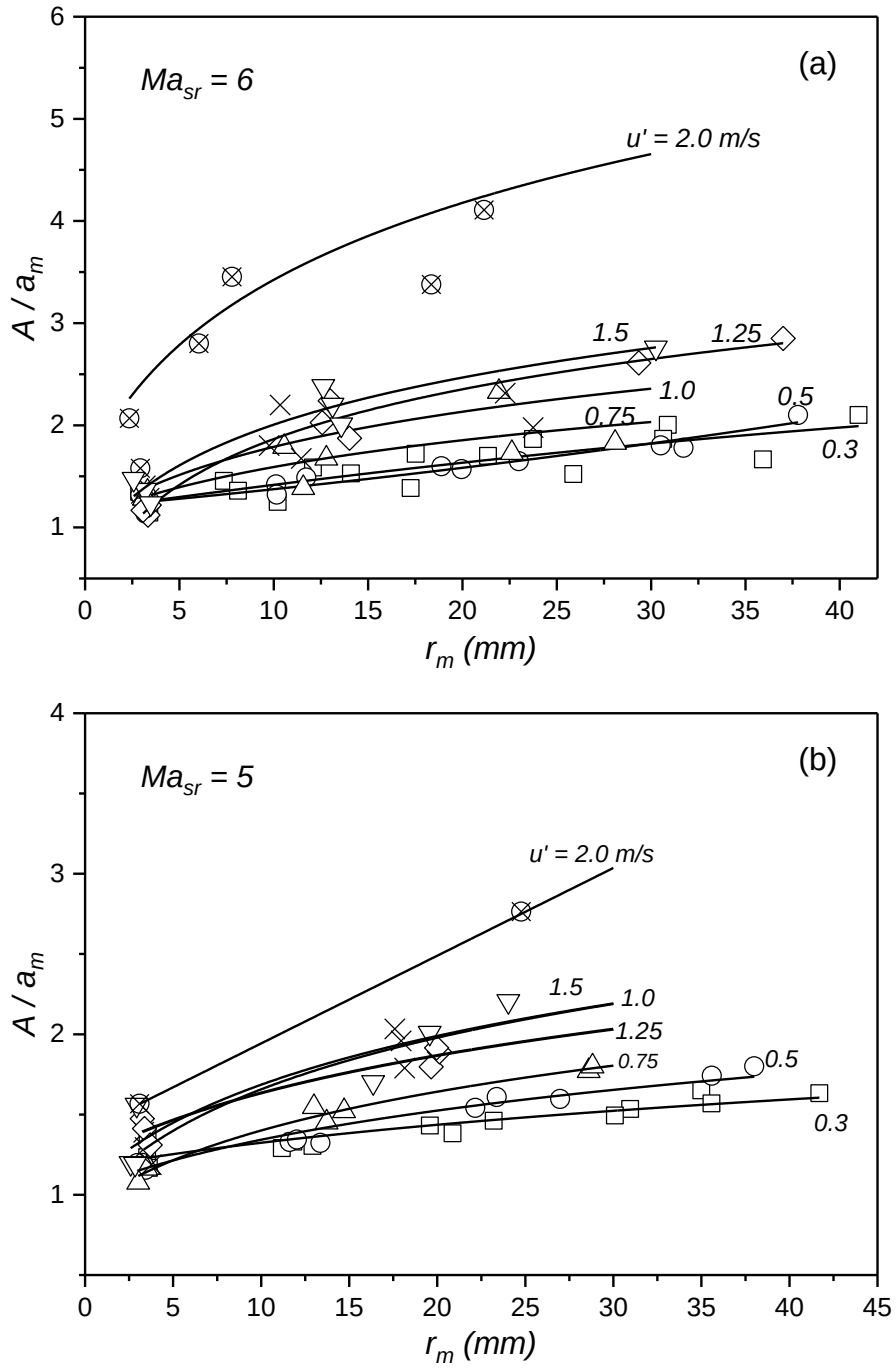


**Figure 4.44** Variations of $A/a_m$ with $r_m$ for increasing $u'$ for $CH_4$/air at 365K, 0.5 MPa (a) $\phi$ =1.35 (b) $\phi$ =1.25.

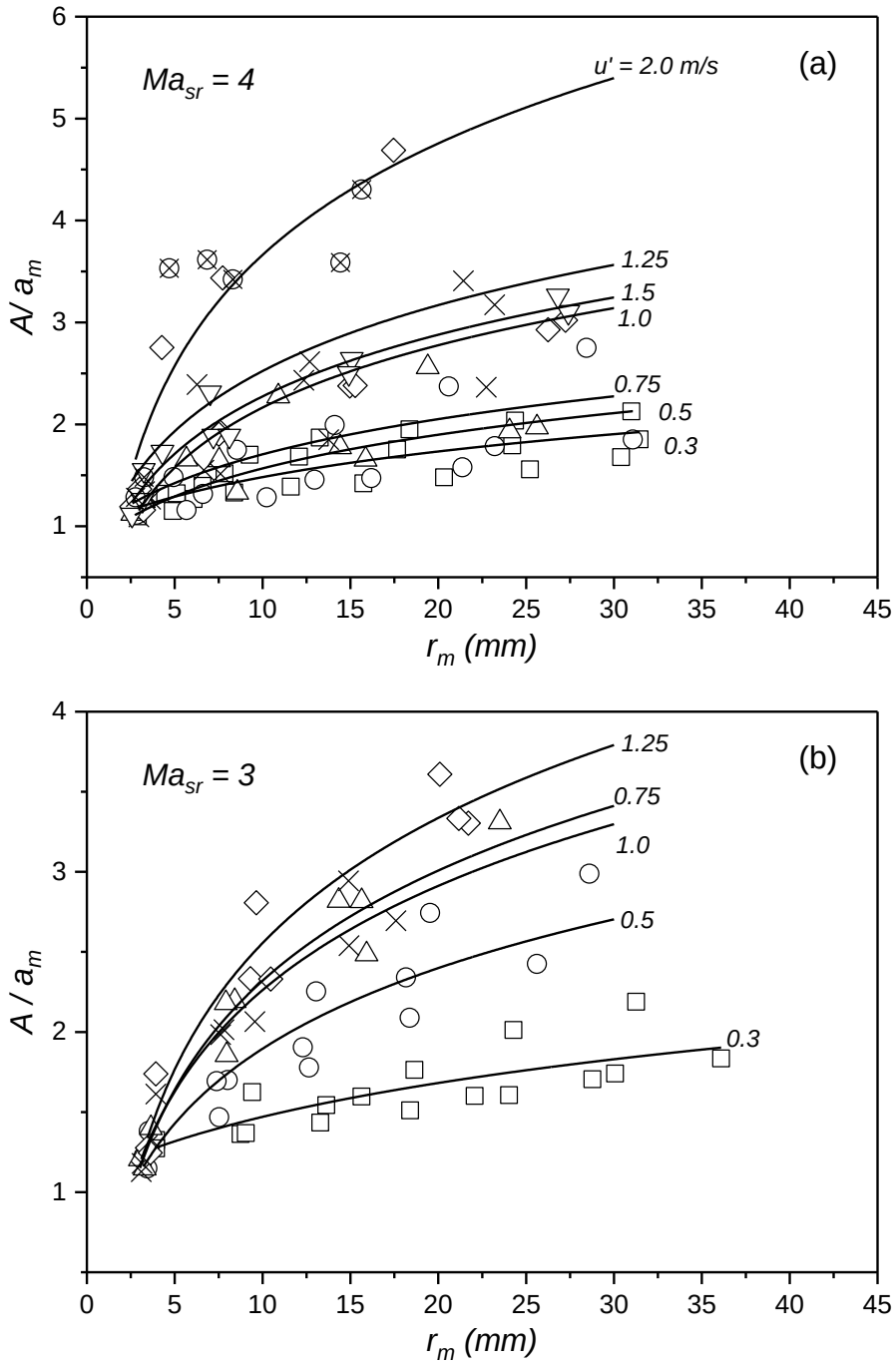


**Figure 4.45** Variations of $A/a_m$ with $r_m$ for $u'$ for $CH_4$/air at 300K, 0.1 MPa (a) $\phi$ =1.3 (b) $\phi$ =0.7.

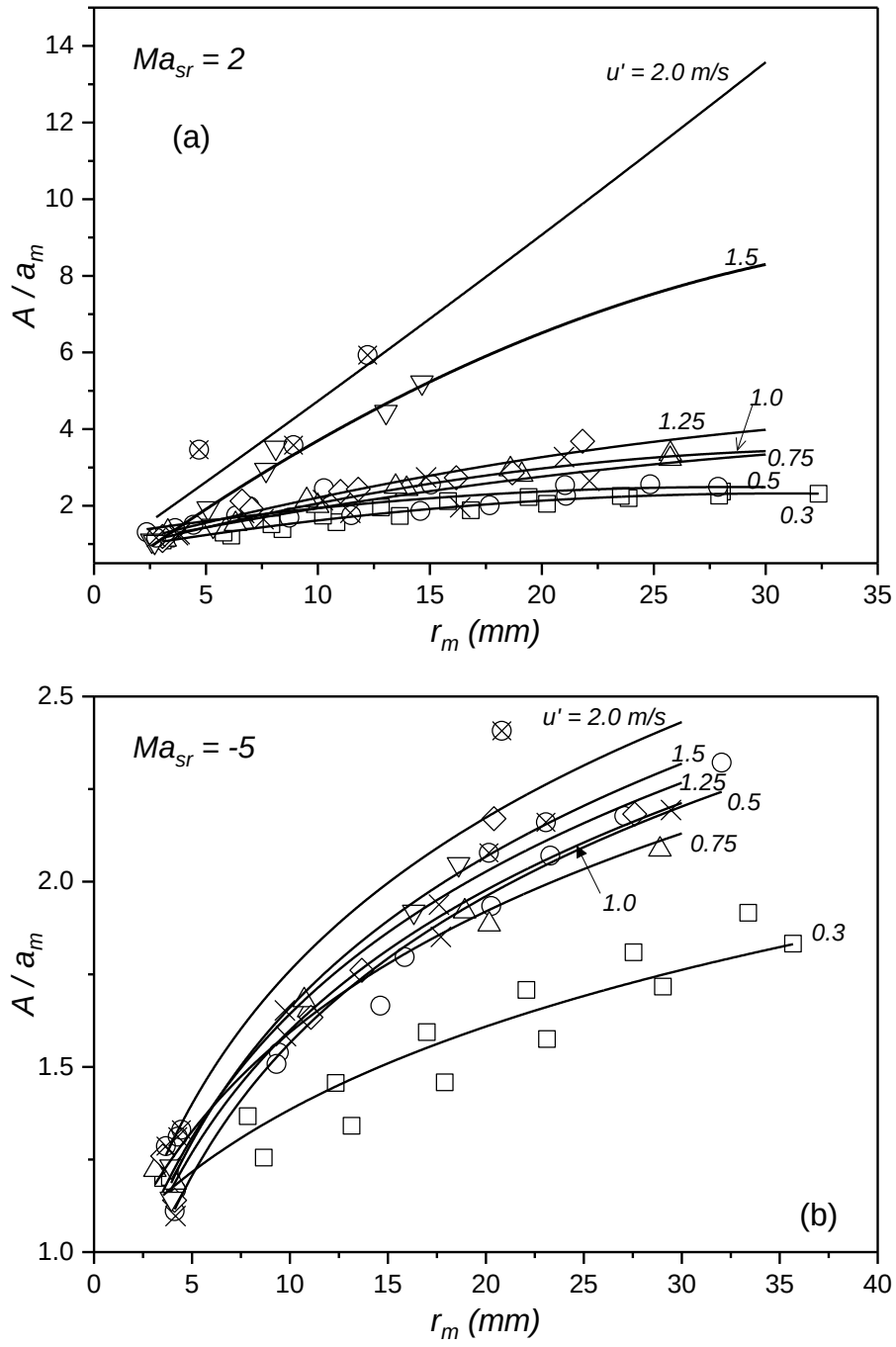


**Figure 4.46** Variations of $A/a_m$ with $r_m$ for increasing $u'$ at 365K (a) $CH_4$/air $\phi$ =0.6, 0.1 MPa (b) $H_2$/air $\phi$ =0.3, 0.5MPa.

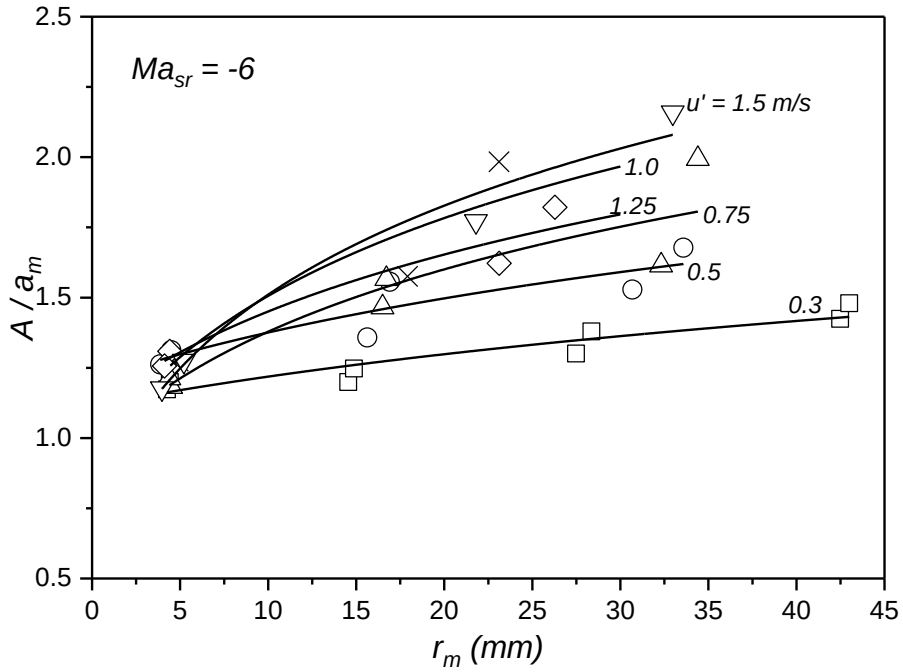


**Figure 4.47** Variations of $A/a_m$ with $r_m$ for increasing $u'$ for $H_2$/air at $\phi$ =0.4, 0.5MPa, 365K.

Figures 4.44 to 4.47, show the surface area ratio increasing with $r_m$ and $u'$. This is qualitatively in agreement with the trends for burning velocity (Section 4.4). A general trend of sharper rise in $A/a_m$ values with increasing $u'$ was observed. However, some scatter was evident in some cases, which is typical of turbulent flames. For high $u'$, only two successful explosions were conducted as the flame drifted out of the field of view quickly, demonstrated by schlieren images in Fig. 4.20. These effects were less pronounced at $u'$ values less than 1.5 m/s. For the initial flame kernels the $A/a_m$ values were nearly the same, but at $u'$ = 2.0 m/s had relatively higher $A/a_m$ values immediately after ignition, as flames developed and were distorted quickly with increasing $u'$. At the higher $u'$ value of 2.0 m/s, the number of images captured was limited due to higher burning rates, caused by the increasing turbulence. This lead to flames rapidly growing beyond the field of view. Best fit curves through these data were extended until $r_m$ = 30 mm to obtain generality at a large effective rms turbulence velocity, $u_k'$.

### 4.5.4.1 Enhancement of flame surface area ratio

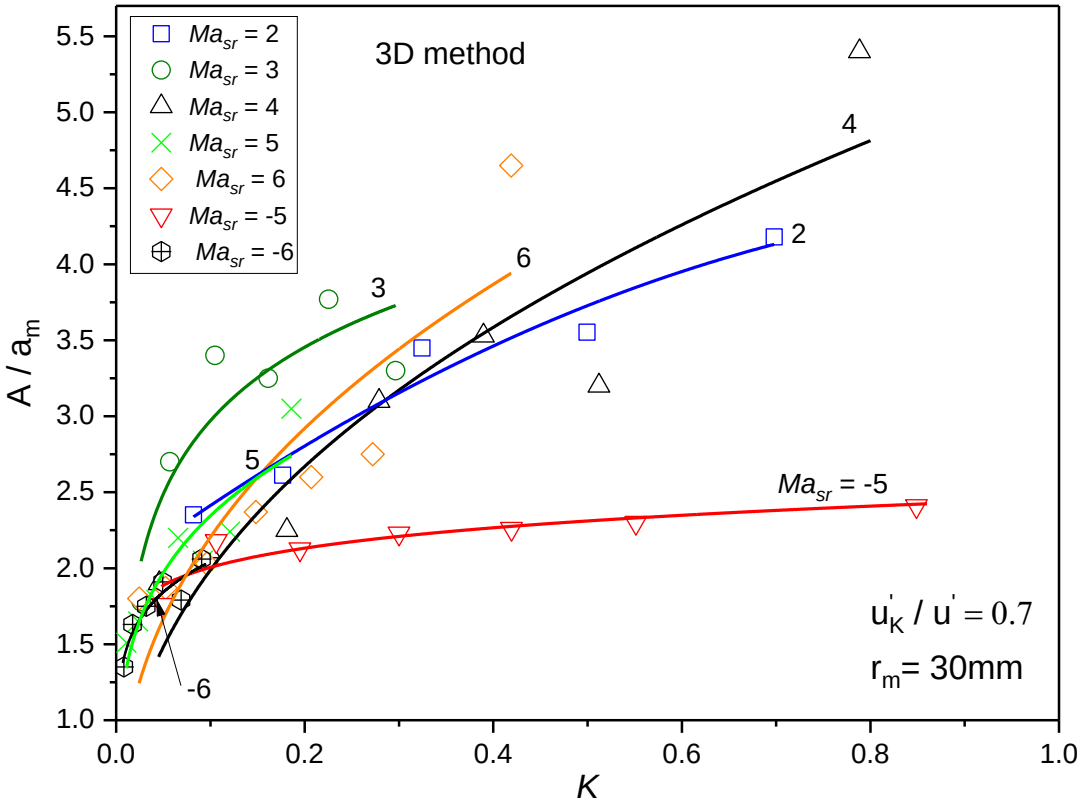


**Figure 4.48** Variations of $A/a_m$ with $K$ for the experimental conditions in Table 4.3.

Shown in Fig. 4.48 are the measured profiles of flame surface area enhancement ratio, $A/a_m$, indicated by open symbols, plotted against Karlovitz stretch factor, $K$, for different $Ma_{sr}$ values. These are evaluated at the same radius, as presented in Section 4.4, i.e. 30 mm, using Figs. 4.44 to 4.47, where $u'_k/u'$ is 0.7. Moreover, as discussed in Section 4.4, the flames at this radius were well into the developed linear regime, indicated on Fig. 4.13, independent of spark effect [154] and the turbulent flow field was well characterised [15]. With $u'$ = 0.75 and 1.0 m/s, where the maximum obtained mean flame radii fell short of 30mm, $A/a_m$ values were obtained by slightly extrapolating the trends. Solid lines are the best fits through the data. The effects of $Ma_{sr}$ on $A/a_m$ curves are quantified in this figure. It shows the increase in $A/a_m$ with decreasing positive $Ma_{sr}$, and increasing $K$ values. For

negative $Ma_{sr}$, the curves of $A/a_m$ are lower than the positive ones, while with $Ma_{sr}$ = -5 the curves flatten out as $K$ increases.

## 4.6 Quenching of turbulent flames

This Section describes the study of turbulent flame quenching using the schlieren and swinging laser sheet techniques. Quench flame data were obtained using the schlieren technique, described in Section 2.3.2, from [172]. Near quench 3D flame data were obtained using the swinging laser sheet technique, described in Section 2.3.3. The purpose of the swinging laser sheet 3D flame kernel measurements was to reveal any transition from a laminar to a turbulent flame kernel, ascertain, the volume of each kernel and whether an assumed mean spherical diameter at criticality was valid. The swinging laser sheet imaging repetition frequency was a maximum of 60 kHz, too low to record fully a detailed temporal quenching sequence. The other major aspects of this study were to correlate normalised kernel quenching diameters with Karlovitz stretch factor and to develop a unified approach to both premixed and non-premixed jet extinctions that are presented in Section 5.6.

### 4.6.1 Flame quenching

Figure 4.49 shows the radius for $CH_4$/air flame at 0.5 MPa, 365 K and $\phi$=0.6, revealed by 2D schlieren images, as a function of time until the flame kernel quenched. From these, values of $d$ were calculated. The flame images showed a struggle to survive and eventually quenching after 2.1 ms at a maximum radius of approximately 6 mm. This flame resides in a regime located at the edge of the new quench regime that is proposed in Fig. 5.23.

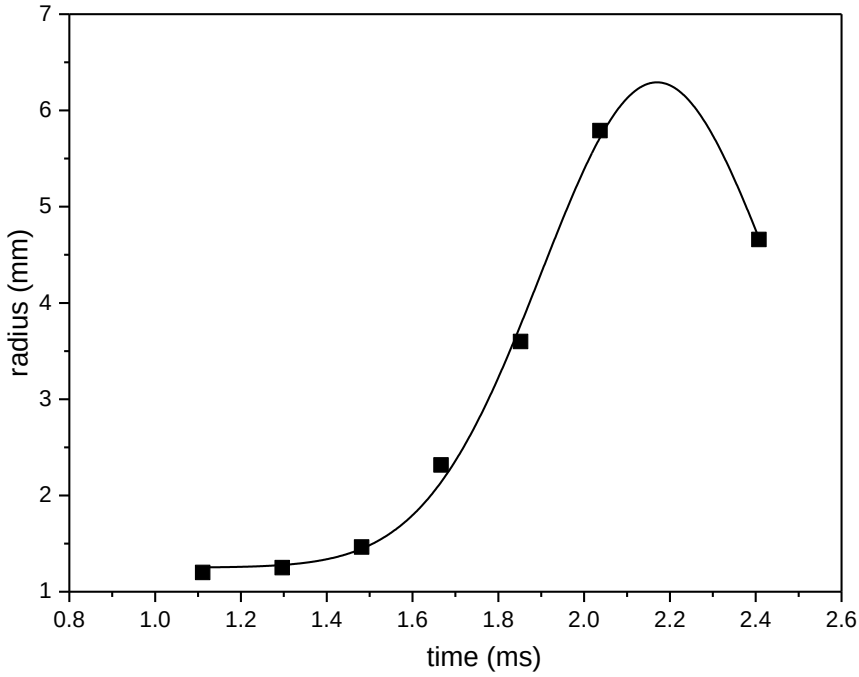


**Figure 4.49** Radius against time for quenching of a $CH_4$/air kernel at 0.5 MPa and 365 K at $\phi$ =0.6.

An example of the evolution of quenching kernels, in terms of $d/\delta_k$, is shown by the continuous curve in Fig. 4.50. Values of $d$, normalised by $\delta_k$, obtained using Eq. (1.18) with $k$ and $C_p$ evaluated at $T_0$ taken from [41], for the data in Fig. 4.49 are plotted against time. Two images are shown, binarised as described in Section 3.4, one just after kernel generation, the other of the quenching kernel at maximum $d/\delta_k$. After ignition the flame develops until it reaches a maximum value of $d$, the critical value, $d_k$, after which the flame starts to disintegrate and ultimately quench. The broken curve is of $u'_k$, obtained from the measured $u'$ and Eqs. (1.34) to (1.36).

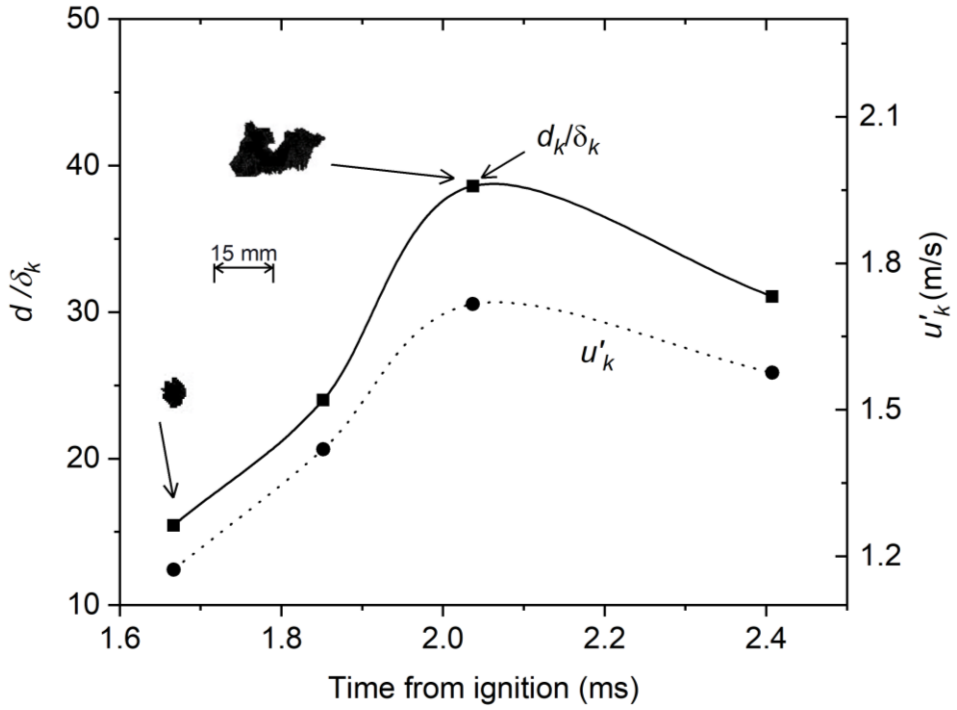


**Figure 4.50** Temporal variation of $d/\delta_k$ and $u'_k$ from ignition for quenching of a $CH_4$/air kernel at 0.5 MPa and 365 K at $\phi$=0.6, $K$= 11.6 [172].

Figure 4.51 compares the changing values of $d/\delta_k$ from both 2D schlieren, and 3D swinging sheet with images for $CH_4$/air, $\phi$ = 1.35 at 365 K and 0.5 MP, for $u'$ = 3 m/s in (a), and 2 m/s in (b). Values of $d/\delta_k$ from the two techniques were compared at different $u$' because of the more interesting evolution of the kernels and also to show how close the two techniques could predict the flame diameters close to quench. Moreover, the condition at ($u$'=3.0 m/s), captured by the schlieren technique, could not be captured by the 3D swinging laser sheet technique due to its limitations, discussed in Section 2.4. In Fig. 4.51(a) the earlier images reflect their origin around an electric spark. The five images show the initial establishment of a predominantly laminar flame that makes a transition to a turbulent flame. A near-spherical core of burned and burning gas supports the propagating flame. The flame is close to quench, but survives. However, it resides in a regime located at the edge of the new quench regime that will be proposed in Fig. 5.23. In Fig. 4.51(b) are two sets of 3D swinging sheet images. These give more spatial information on flame structure, although the schlieren images give a more continuous record, on

account of the shorter time interval between the adjacent sheets. The 3D images clearly show, for both flames, a struggle for survival against the increasing turbulence. The lower flame kernels with a broken cusp/like shape at 6 ms, reflect this more acutely, but both of the marginal flames in Fig. 4.51(a) and (b) survived unquenched.

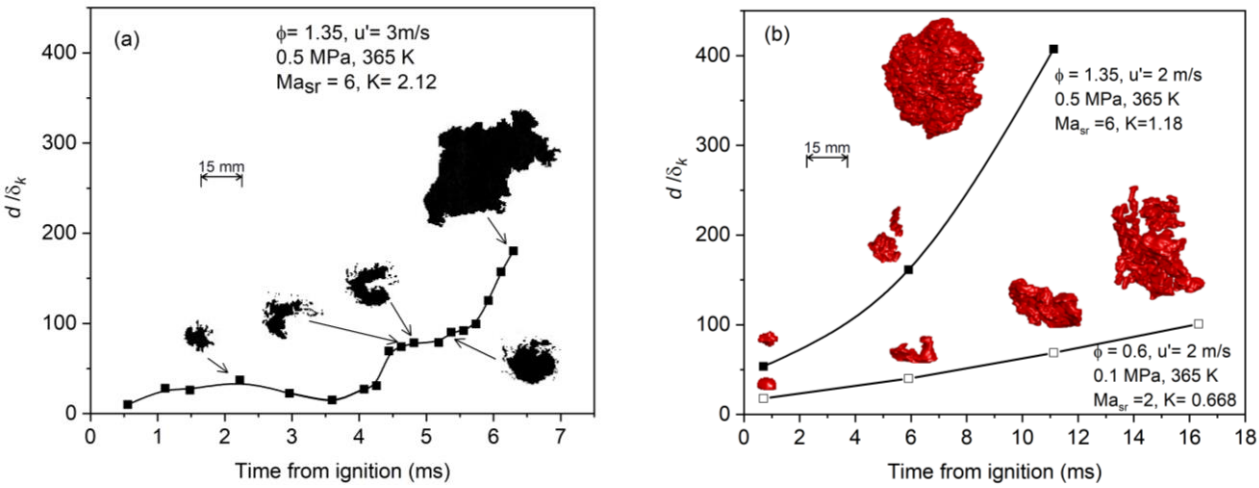


(a) Schlieren 2D images, *u′* = 3m/s. (b) Swinging sheet 3D images, *u′* = 2m/s.

**Figure 4.51** Temporal variations of $d/\delta_k$ from ignition for $CH_4$-air at 365 K from (a) schlieren [172], and (b) laser swinging sheets. Complete mixture details on the figures.

In contrast, the flame in Fig. 4.52 is remote from the quench regime on Fig. 1.6. It has a much less fragmentary, and more robust, structure than the flames in Fig. 51(a) and (b). The flame speed is significantly higher. In Fig. 4.53, the *n*-butanol/air, $\varphi$ = 0.7, schlieren images at 360 K and 0.5 MPa are of interest, in that the kernel is about to extinguish at $d/\delta_k$ = 55. Then propagation revives, with extinction finally occurring at $d_k/\delta_k$ = 77. All the experimental data collected on quench flames in terms of $d_k/\delta_k$ are listed in Table 4.4[172].

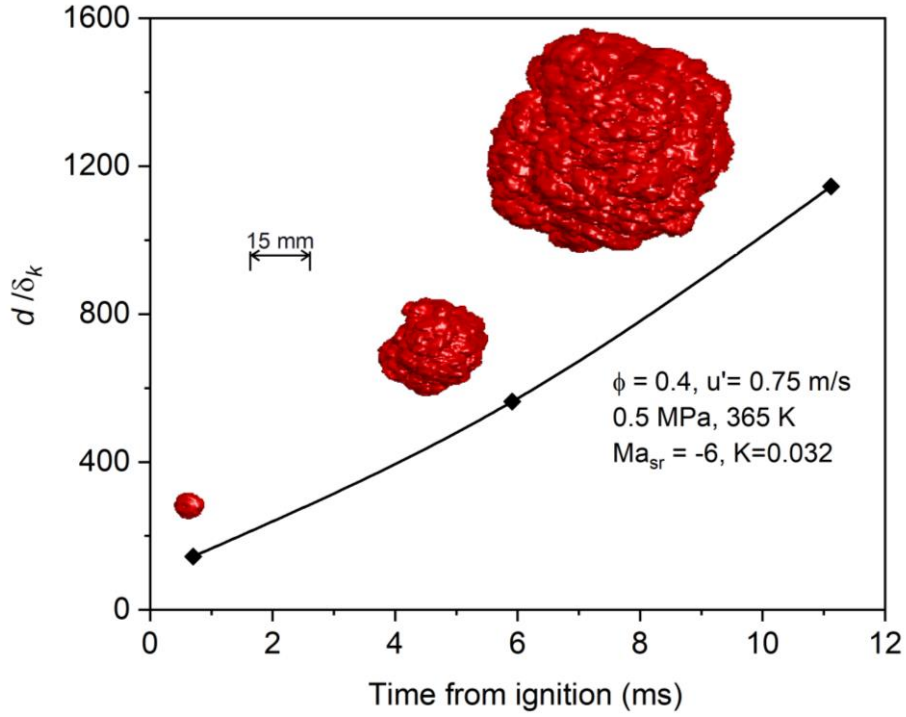


**Figure 4.52** Temporal variations of $d/\delta_k$ from ignition for $H_2$/air at 365 K from laser swinging sheet 3D images, $u'$ = 0.75 m/s. Complete mixture details on the figures.

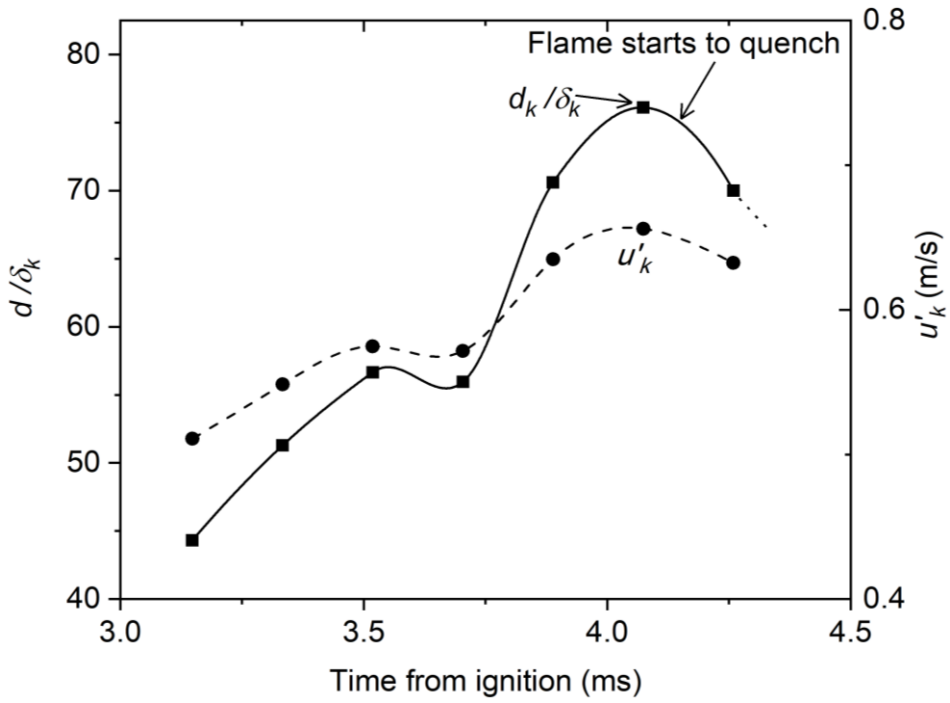


**Figure 4.53** Temporal variations of $d/\delta_k$ and $u'_k$ with time from ignition for *n*-butanol/air at 360 K, 0.5 MPa, $\phi$=0.7 and $u'$ = 2 m/s, $K$= 0.478, $p_{0.4}$.

**Table 4.4** Experimental Quench Data [172].

| Fuel/air mixture | Method | $T$ (K) | $P$ (MPa) | $\varphi$ | $u'$ (m/s) | $u'_k$ (m/s) | $\frac{d_k}{\delta_k}$ | $T^o$ (K) | $u_l$ (m/s) | $\nu$ (m²/s) | $K$ | $Ma_{sr}$ | $Ka$ | $p_b$ |
|---|---|---|---|---|---|---|---|---|---|---|---|---|---|---|
| $H_2$/0.11 $O_2$/0.89 $N_2$ | Schlieren technique | 300 | 0.1 | 0.5 | 6 | 2.14 | 16 | 1003 | 0.0975 | 1.76E-05 | 11.46 | 0.03 | 48 | 0.8 |
| $H_2$/0.115 $O_2$/0.885 $N_2$ | | 300 | 0.1 | 0.5 | 7 | 3.062 | 17 | 1003 | 0.111 | 1.77E-05 | 11.284 | -0.1 | 46 | 0.8 |
| $H_2$/0.11 $O_2$/0.89 $N_2$ | | 300 | 0.1 | 0.5 | 7 | 2.8 | 21 | 1003 | 0.0975 | 1.76E-05 | 14.445 | 0.03 | 58.6 | 0.6 |
| $H_2$/0.118 $O_2$/0.882$N_2$ | | 300 | 0.1 | 0.5 | 9 | 3.38 | 23 | 1003 | 0.124 | 1.77E-05 | 13.14 | -0.4 | 53.28 | 0.8 |
| $H_2$/air | | 365 | 0.5 | 0.15 | 2.25 | 0.82 | 24 | 1172 | 0.036 [101] | 4.79E-06 | 10.075 | -2 [101] | 39.71 | 0.8 |
| *n*-$C_4H_{10}O$/air | | 360 | 1 | 0.7 | 0.6 | 0.121 | 62 | 1500 | 0.095 | 2.14E-6 | 0.1215 | 6 | 0.388 | 0.8 |
| *n*-$C_4H_{10}O$/air | | 360 | 0.5 | 0.7 | 2 | 0.66 | 76 | 1400 | 0.147 | 4.27E-06 | 0.4785 | 9 | 1.89 | 0.4 |
| *n*-$C_4H_{10}O$/air | | 360 | 0.5 | 0.7 | 2 | 0.61 | 80 | 1400 | 0.147 | 4.27E-06 | 0.4785 | 9 | 1.89 | 0.4 |
| *i*-$C_8H_{18}$/air | | 365 | 0.5 | 0.8 | 6 | 2.3 | 125 | 1320 | 0.201[101] | 4.37E-06 | 1.344 | 5 [101] | 5.47 | 0.6 |
| *i*-$C_8H_{18}$/air | | 365 | 0.5 | 0.8 | 6 | 2.34 | 127 | 1320 | 0.201 [101] | 4.37E-06 | 1.344 | 5 [101] | 5.47 | 0.6 |
| *i*-$C_8H_{18}$/air | | 365 | 0.5 | 0.8 | 6.5 | 2.57 | 131 | 1320 | 0.201[101] | 4.37E-06 | 1.516 | 5 [101] | 6.51 | 0.4 |
| $CH_4$/air | | 365 | 0.5 | 1.35 | 3 | 0.83 | 37 | 1328 | 0.095 [101] | 4.60E-06 | 2.183 | 6 [101] | 8.54 | 0.8 |
| $CH_4$/air | Swinging sheet technique | 365 | 0.1 | 0.6 | 2 | 0.588 | 22 | 1220 | 0.189 [101] | 2.28E-5 | 0.668 | 2 [101] | 2.65 | 0.9 |
| $CH_4$/air | | 365 | 0.1 | 0.6 | 2 | 0.6 | 24 | 1220 | 0.189 [101] | 2.28E-5 | 0.668 | 2 [101] | 2.65 | 0.9 |
| $CH_4$/air | | 300 | 0.1 | 1.3 | 2 | 0.64 | 25 | 1220 | 0.16 [21] | 1.63E-05 | 0.788 | 4 [21] | 3.068 | 0.8 |
| $CH_4$/air | | 300 | 0.1 | 1.3 | 2 | 0.69 | 32 | 1220 | 0.16 [21] | 1.63E-05 | 0.788 | 4 [21] | 3.068 | 0.8 |
| $CH_4$/air | | 365 | 0.5 | 1.35 | 2 | 0.728 | 68 | 1328 | 0.095 [101] | 4.60E-06 | 1.1882 | 6 [101] | 5.06 | 0.8 |
| $CH_4$/air | | 365 | 0.5 | 1.35 | 2 | 0.74 | 77 | 1328 | 0.095 [101] | 4.60E-06 | 1.1882 | 6 [101] | 5.06 | 0.8 |

# Chapter 5

# Discussions

## 5.1 Introduction

This chapter discusses the laminar burning velocities of $n$-butanol/air mixtures in Section 5.2 followed by the laminar flame instabilities in Section 5.3. The turbulent burning characteristics of fuel/air mixtures and correlations with Karlovitz stretch factor are discussed in Section 5.4, flame structure analysis from 3D reconstructions and probabilities of burning in Section 5.5 and finally the quenching of turbulent flames in Section 5.6. The extended correlations on the *U-K* diagram also are presented.

## 5.2 Discussion of laminar burning velocities

The highest values of $u_l$ for *n*-butanol/air mixtures, presented in Fig. 4.3, occur for slightly rich mixtures, $\phi$ = 1.1. These drop significantly on the lean and rich sides with the lowest values at $\phi$ = 0.7. Both $L_b$ and $Ma_{sr}$, see Figs. 4.5 and 4.6, decrease with increasing $\phi$. These are associated with decreasing $Le$. Lean flames are more stable with positive values of $L_b$ becoming negative for rich flames and unstable due to the onset of cellularity. This also affects the evaluation of $Ma_{sr}$ increasing its variability, as shown in Fig. 4.6. For the higher pressure and richer mixtures, $S_n$ is enhanced by negative values of $Ma_{sr}$.

### 5.2.1 Comparison of $u_l$ with other studies

Unstretched laminar burning velocities from the present study are reproduced from Fig. 4.3, and compared with those from other studies [5, 112-114] in Fig. 5.1. The initial temperature for some of the $u_l$ measurements reported in [112,

173] are similar to those in the present work, but others were slightly lower and some higher.

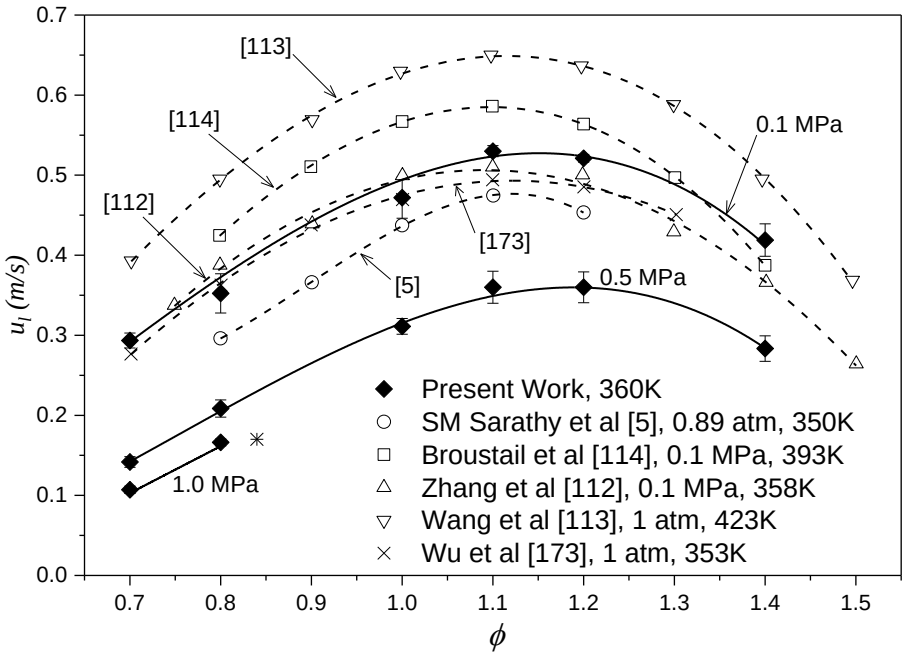


**Figure 5.1** $u_l$, of *n*-butanol/air mixtures at 0.1, 0.5 and 1.0 MPa at 360 K.

All $u_l$ data showed trends consistent with the present results at 0.1 MPa. The data of Zhang et al. [112] and Wu et al. [173] were at similar conditions to those in the present experiments. Values are similar on the lean side, while on the rich side the present values are noticeable higher. The effect of strain rate corrections [18, 32] on present data were scrutinized, as shown in APPENDIX A (Fig. A.2), by using Eqs. (1.15) and (1.16), however no significant change in $u_l$ were observed. In [18], it was shown that the strain rate corrections affected $u_l$ on the rich side at 0.1 MPa, however, the present results reveal no such influence. This is probably due to $Le$, shown in Fig. 4.4, are close to 1 on the rich side. The difference in $u_l$ between different studies on the rich side may likely be due to the errors in accurately evaluating flame speed at zero stretch imposed by the limited stable flame regime. Experimental data at higher pressure conditions reported in Fig. 5.1, are scarce. Only Wang et al. [113] have reported, recently, high pressure experimental data up to 20 atm. However, their initial temperature was 423 K which was much higher compared with the present work. Computed data have been reported at 1 atm and 343-373 K in [1, 5, 110, 111, 173-175]. In Fig. 5.2,

the present experimental data from Fig. 4.3 are compared with the predicted computations using CHEMKIN [176], employing the GRI MECH 3.0 mechanism [174]. This mechanism is validated for high temperature conditions, however, at high pressures its predicting accuracy still needs to be verified. Reasonable agreement was observed at 0.1 MPa at all $\phi$ and for lean mixtures at the higher pressures. However, at high pressures and for rich mixtures a considerable differences in $u_l$ are observed. Further research in terms of heat release rate computations is required to explain the discrepancies.

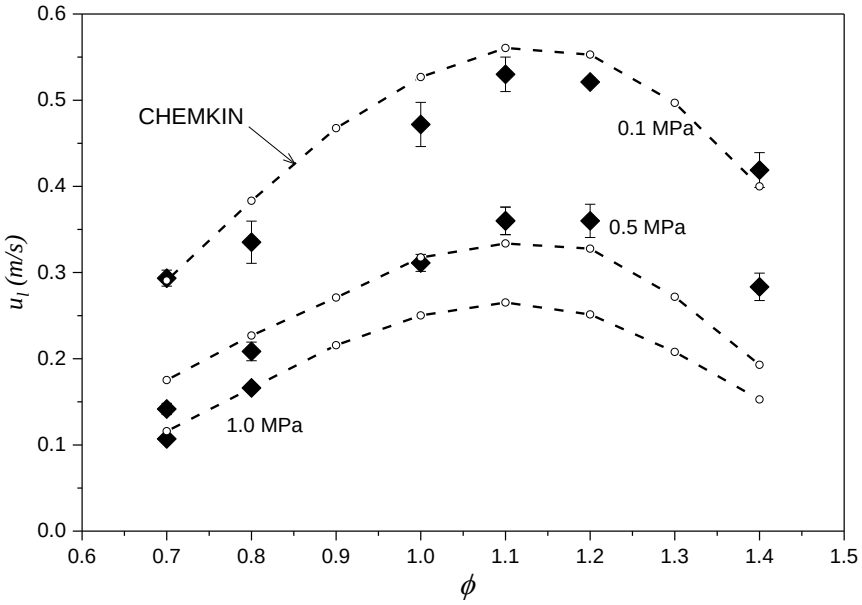


**Figure 5.2** Variation of $u_l$ with $\phi$ and $P$ for *n*-butanol/air mixtures at 360 K. Symbols are experimental measurements, broken lines are the computed values using CHEMKIN [176]

## 5.3 Laminar flame instabilities

The threshold Peclet number, $Pe_{cl}$, described in Section 1.3.4.1, marks the onset of instabilities [172] and it is of rational thought to expect their onset to be dependent upon $Ma_b$. Pressure dependencies are sought to exploit the leading role of $Pe_{cl}$ in this phenomena. Furthermore, such relationships suggest that high pressure laboratory explosions might be used to predict the effects of large-scale atmospheric explosions [168]. Consequently, large-scale atmospheric explosion data are compared with those from the present laboratory explosions at elevated pressures. Experimental results are first

presented by $Pe_{cl}$ as a function of $Ma_b$ then, because of the fundamental importance of the strain rate, $K_{cl}$ is expressed as a function of the strain rate Markstein number, $Ma_{sr}$ as in [56].

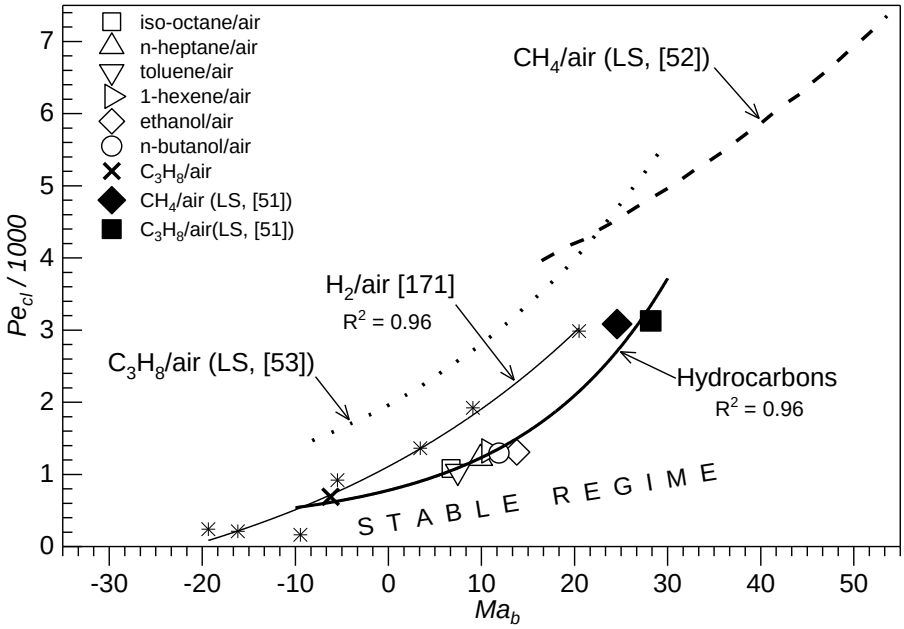


**Figure 5.3** $Pe_{cl}$ variations with $Ma_b$ for different hydrocarbons and $H_2$ [171] at 0.1 MPa in the explosion vessel with data from large scale explosions [51-53]. Bold black symbols are Shell atmospheric explosions.

Measured values of $Pe_{cl}$, reported in Fig. 4.8 and Fig. 4.9, are reproduced on Fig. 5.3 and Fig 5.4 and data for hydrocarbons from previous work are also presented. Table 5.1 lists all the fuels, and $\phi$, employed in the present work and also the references for the data from previous work. These are compared at pressures upto 1.0 MPa. Each experimental point is a mean value from three explosions. Figure 5.3 shows $Pe_{cl}$ plotted against $Ma_b$ for all different hydrocarbons at 0.1 MPa. Values of $\phi$ ranged from 0.7 to 1.4 for propane-air mixtures, and from 0.8 to 1.2 for methane. For other hydrocarbons, fuels were limited to $\phi$ values between 0.8-1.3, due to limitations imposed by liquid vapour pressures. Open symbols and cross represent measurements in the present combustion vessel, while filled symbols and broken lines are data from much larger scale atmospheric explosions [51-53]. Asterisk symbols show values for hydrogen from [171]. To obtain $Ma_b$ for these $H_2$ data, values of $L_b$ were taken from [177], as these were not reported in [171]. The thin line

curve shows the best fit. Maximum generality is sought for these measurements, on the basis of theoretical studies.

Comparisons are made with three groups of experiments, with measurements in large scale (LS) spherical, atmospheric vented explosions. The first two involved $C_3H_8$ [51, 53] and the second $CH_4$ [51, 52]. To emphasize the generality of the approach, these results, are presented in the form of $Pe_{cl}$, plotted against the $Ma_b$ from [169], alongside the results from the explosion vessel in Fig. 5.3. Unfortunately, there is a degree of ambiguity in the definitions of Markstein numbers, taken from [169] in [53] and [52], but the evidence in [21] suggested they were close to $Ma_{sr}$ and this has been assumed in these plots. These values were converted to $Ma_b$ using the Markstein number data in [23] for $CH_4$, and in [178] for $C_3H_8$. The dotted curve in Fig. 5.3 shows the $C_3H_8$ data and the dashed curve those for $CH_4$.

The Shell Research explosions [51] were within a large steel box structure, 10 m x 8.75 m x 6.25 m high [51]. Flame diameters reached 7 m. For the $CH_4$/air explosion, $\phi$ = 1.1, and for the $C_3H_8$/air explosion, $\phi$ = 1.06. The two bold black symbols in Fig. 5.3 and Fig. 5.4 show these data. The Factory Mutual LS experiments, with $C_3H_8$ [53] and $CH_4$, [52] covered a greater variety of mixtures, with flames of up to 2 m diameter, over a range of $\phi$ between 0.81-1.22.

Differences between the Shell and Factory Mutual LS data are attributed to different interpretations of Markstein number, not only between $Ma_b$ and $Ma_{sr}$, but also between different expressions for the latter [21, 169]. Errors in the measurement of $Ma_b$ are also important [169]. Other errors might arise from different ways in measuring $r_{cl}$. This is particularly so at negative values of $Ma_b$, where stable combustion is of short duration [179], and a fractal expression might be required for the extrapolation to zero stretch rate [171]. Figure 5.4(a) and (b) show plots of $Pe_{cl}$ against $Ma_b$ for different hydrocarbons, measured at 0.5 and 1.0 MPa, respectively. At both pressures a best fit curve, shown by a solid line, was obtained through the data from the explosion vessel.

Similar Peclet numbers were achieved in large scale atmospheric explosions, and, on a smaller scale, in laboratory explosions in the present work. However, in atmospheric explosions large Peclet numbers were achieved by large fireballs, whereas in closed vessel explosions it was achieved at a higher pressure by a much smaller flame, but because of the higher pressure, one endowed with a small laminar flame thickness. The discussion in this Section relates to wide ranges of fuels and pressures. The dependencies of the instability phenomena on small and large scales were carefully studied, although, for the large scale atmospheric explosions, the data only covered propane and methane.

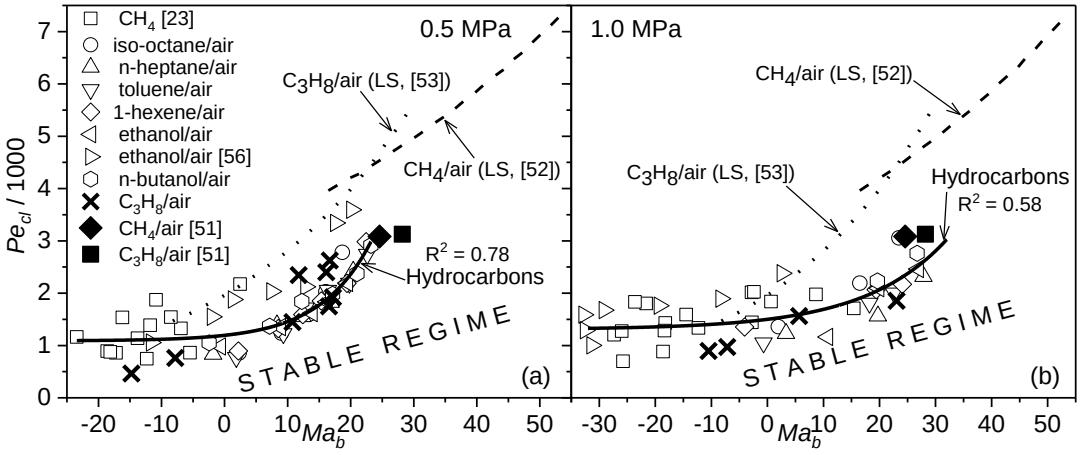


**Figure 5.4** $Pe_{cl}$ variations with $Ma_b$ for different hydrocarbon/air explosion vessel data.

The roles of both Markstein and Peclet numbers become clear and as reasoned in Section 4.3.3, give rise to a more fundamental correlating parameter $K_{cl}$, given by Eq. (1.20), for flame stability. For the $Pe_{cl}$ shown in Fig. 4.7, values of $K_{cl}$ for $n$-butanol/air mixtures at 0.5 and 1.0 MPa are presented against the corresponding $Ma_{sr}$ in Fig. 5.5. The solid line shows the best fit exponential curve through these data points.

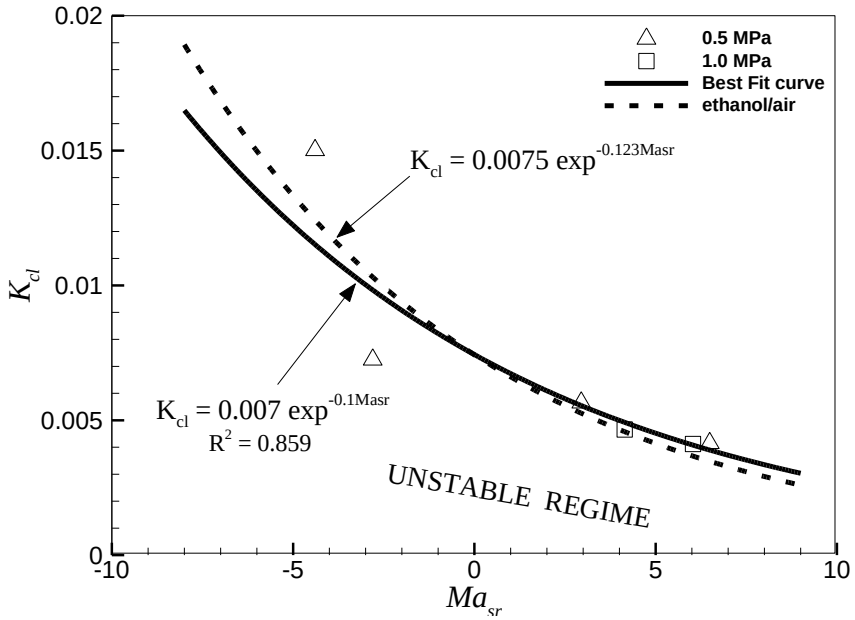


**Figure 5.5** $K_{cl}$, expressed in terms of $Ma_{sr}$ for *n*-butanol/air (solid line) and ethanol/air [56] (broken line) mixtures.

Bearing in mind the uncertainties shown by the error bars in Fig. 4.6 in deriving $Ma_{sr}$, a satisfactory correlation, irrespective of pressure, exists with an $R^2$ value of 0.859. For positive $Ma_{sr}$, smaller values of $K_{cl}$ are sufficient to keep the flames stable. As $Ma_{sr}$ values become increasingly negative higher $K_{cl}$ values are required for stable flame propagation, narrowing the critical stretch regime. The exponential correlation of $K_{cl} - Ma_{sr}$ for $n$-butanol/air mixtures at 360 K in Fig. 5.5 closely follows the correlation in [56] for high pressure ethanol/air explosions at 358K. These are shown as a dotted line in Fig. 5.5, indicating a more rational expression for instabilities in terms of $K_{cl}$ rather than $Pe_{cl}$ alone. Moreover, the similarities in the two $K_{cl} - Ma_{sr}$ correlations suggest that it could be more reasonable to present a general correlation of $K_{cl}$ in terms of $Ma_{sr}$ independent of fuel and initial conditions.

The experimentally measured dependencies of $K_{cl}$ on pressure and $Ma_{sr}$ are reported for the first time for many different fuels. $K_{cl}$ data from present measurements, as well as from previously reported work are presented in Table 5.1 at different initial conditions, correlated in terms of $Ma_{sr}$. They are presented in Fig. 5.6. Best fit curves are sought to obtain a more generalised expression.

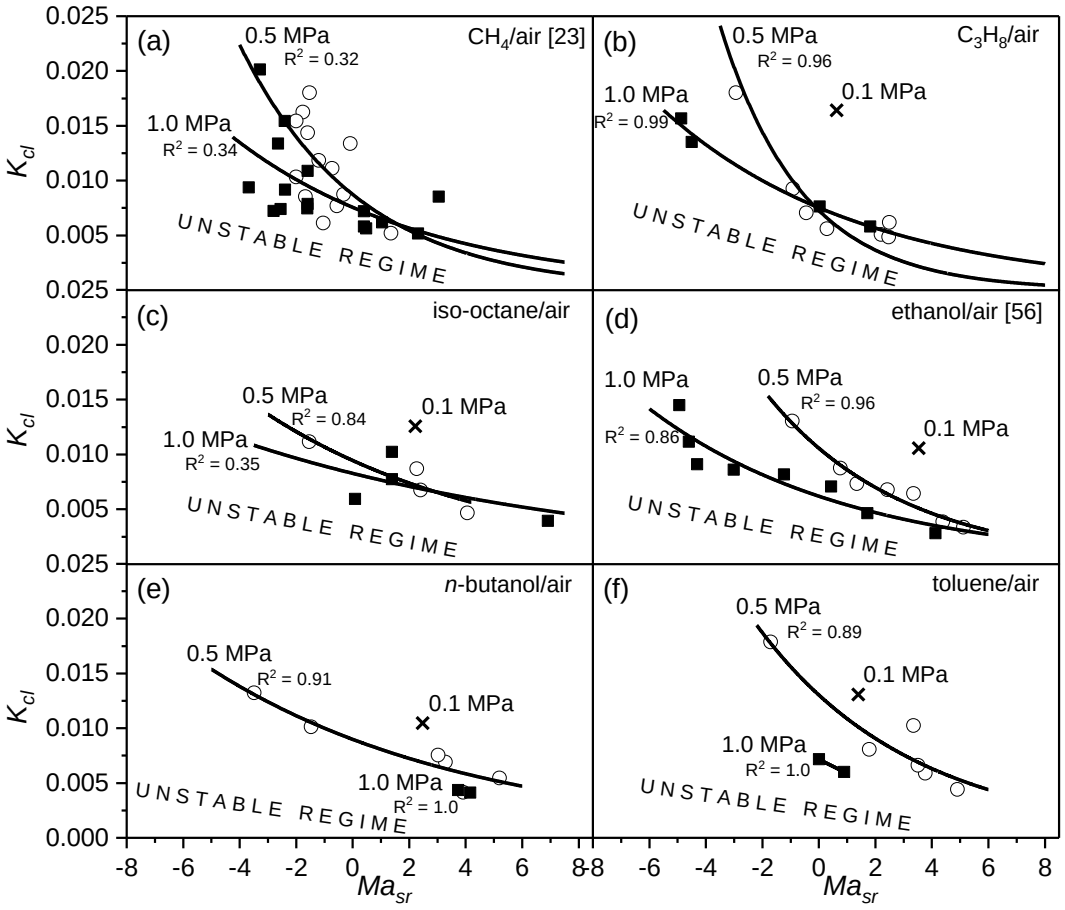


**Figure 5.6** Values of $K_{cl}$ plotted against $Ma_{sr}$ for all hydrocarbon/air explosion vessel data.

Clearly for flame stability $K_{cl}$ decreases with increase in $Ma_{sr}$. From Fig. 5.6, there is no clear tendency for any fuel or group of fuels to exhibit a correlational trend comparable to that of pressure. In addition, any possible influence of $\sigma$ was explored. It is significant, that the theory in [42] predicts it has a small influence on $Pe_{cl}$, particularly at the lower Markstein numbers. The present large data set was scrutinised and it revealed no such influence. This contrasts with other studies in which this variable was more successsfully isolated and controlled, such as the propane experiments in [180], and hydrogen experiments in [181].

Shown in Fig. 5.7 are all the hydrocarbon fuel data, for the fuels presented in Table 5.1, plotted in terms of $K_{cl}$ against $Ma_{sr}$ for pressures of 0.1, 0.5 and 1.0 MPa. Best fit expressions for these pressures are:

$$K_{cl} = 0.015 \exp(-0.11 Ma_{sr}) \quad \text{at 0.1 MPa, } R^2 = 0.95. \tag{5.1}$$

$$K_{cl} = 0.009 \exp(-0.11 Ma_{sr}) \quad \text{at 0.5 MPa, } R^2 = 0.58. \tag{5.2}$$

$$K_{cl} = 0.007 \exp(0.11 Ma_{sr}) \quad \text{at 1.0 MPa, } R^2 = 0.67. \tag{5.3}$$

Notwithstanding the scatter, there is a clear tendency for $K_{cl}$ to decrease, and flames to become more stable, with increasing pressure and $Ma_{sr}$. As a result, it is possible to predict the extent of the unstable regime for laminar flames as a function of $Ma_{sr}$ and pressure.

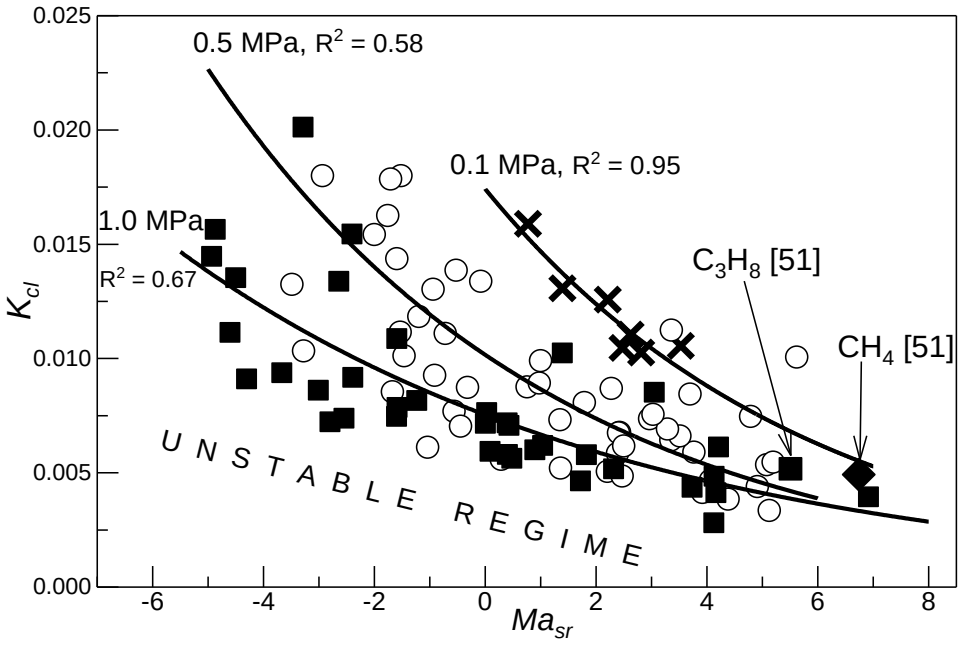


**Figure 5.7** $K_{cl}$ variations with $Ma_{sr}$. Explosion vessel data for different hydrocarbon/air mixtures at different pressures. Crosses (0.1 MPa), open circles (0.5 MPa), filled squares (1.0 MPa). Solid curves shows best fits through these data.

Because of the key role of $Pe_{cl}$, the low values of both $\delta_l$ and flame radius in high pressure explosion vessels make it possible to predict the onset of instabilities in much larger explosions, at atmospheric pressure, $P_a$, from high pressure laboratory explosions, $P$. Figure 5.6 and 5.7 clearly show the diverse influences of fuel, through values of $Ma_{sr}$, and pressure upon $K_{cl}$, and hence $Pe_{cl}$ . These influences can be generalised to yield an expression for $K_{cl}$ in terms of different values of $P/P_a$ and $Ma_{sr}$. For all the hydrocarbons studied in the explosion vessel:

$$K_{cl} = 0.017.\exp(-0.165.Ma_{sr}).(P/P_a)^{-0.39}, \qquad R^2 = 0.66. \qquad (5.4)$$

This relationship is shown by the bold curve in plot of $K_{cl}.(P/P_a)^{0.39}$ against $Ma_{sr}$ in Fig. 5.8. The optimal relationships are also shown for 0.1, 0.5 and 1.0 MPa.

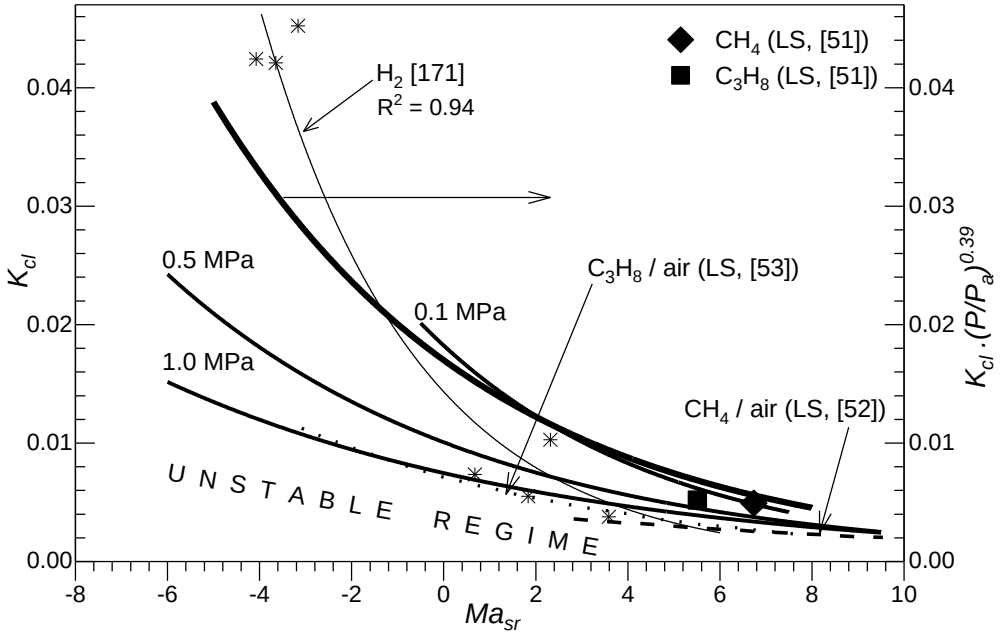


**Figure 5.8** Solid curves show $K_{cl}$ variations with $Ma_{sr}$ from explosion vessel data at 0.1, 0.5 and 1.0 MPa alongside data for LS atmospheric explosions [51-53].

Solid curves show $K_{cl}$ variations with $Ma_{sr}$ from explosion vessel data at 0.1, 0.5 and 1.0 MPa alongside data for LS atmospheric explosions [51-53]. The large scale explosion data from LS [51] lie on the 0.1 MPa hydrocarbon curve. The LS $C_3H_8$ [53] and LS $CH_4$ [52] broken data curves are located somewhat further from the 0.1 MPa isobar. The asterisked points represent explosion vessel data for $H_2$/air at 0.1 MPa, and exhibit higher values of $K_{cl}$. The best curve fit through these data is shown by a thin solid line, which yields the expression:

$$K_{cl} = 0.0128.\exp(-0.32.Ma_{sr}). \qquad (5.5)$$

These $H_2$ data are excluded from Fig. 5.6 and Fig. 5.7 because of their wide divergence from the hydrocarbon data. The differences lie in the nature of correlations based on $\delta_l$. Because H atoms diffuse rapidly in laminar flames

towards the leading edge, and initiate reaction to a greater extent than in hydrocarbon flames, the preheat zone is consequently much reduced [41] [182]. When hydrogen flame parameters are normalised by $\delta_l$, as distinct from $\delta_k$, there is a diminished comparability with other flames. An example is the normalising of jet flame diameters at blow-off with $\delta_l$ [183].

The large scale laminar atmospheric flames become unstable, at flame speeds that are predictable, using fractal approaches [47, 48, 51]. An important aspect of this is the pressure pulse generated by the accelerating flame and the associated increasing rate of change of heat release rate [46]. In the large scale propane explosions of [51] the flame rapidly accelerated, with the flame speed more than tripling in 0.56 sec. Using the monopole assumption for the flame, it was estimated in [46] that, at a flame radius of 100 m, the maximum over-pressure one km from the propane fireball centre would be 0.3 kPa. A comparable atmospheric faster burning hydrogen flame, with $\phi$ = 0.5, would generate a significantly greater maximum over-pressure of 2 kPa. The reflection of such pressure pulses and their interactions with the flame can create Rayleigh-Taylor instabilities, additional to the existing instabilities, generating even stronger oscillatory pressure pulses [184].

An interesting aspect of flame instability is the practice of extrapolating a stable flame speed, or burning velocity, to zero stretch rate, using the observed stable relationship with stretch rate, to obtain a stretch free laminar burning velocity, notwithstanding such a value would reside in a regime of flame instability. Nevertheless, such values provide datums from which actual burning velocities can be derived, for given strain rates and curvatures, with the aid of the appropriate Markstein numbers.

Interestingly, in flames with only mild turbulence, there is a regime of enhanced turbulent burning velocity due to similar instabilities [74] and is further discussed in Section 5.4. The maximum enhancement, shown in Fig. 1.6, occurs at a turbulent Karlovitz stretch factor, $K$, of about 0.02, with negative $Ma_{sr}$.

**Table 5.1** Experimental data sources for all the fuels used for laminar flame instabilities study

| Apparatus | Mixture properties | | | | Ref |
|---|---|---|---|---|---|
| | Fuel | *T* (K) | *P* (MPa) | $\phi$ | |
| Explosion vessel | $H_2$ | 365 | 0.1 | 0.3-1.0 | [171] |
| Explosion vessel | $CH_4$ | 300-400 | 0.5-1.0 | 0.8-1.2 | [23] |
| Explosion vessel | ethanol | 358 | 0.5-1.4 | 0.8-1.4 | [56] |
| Large Scale (LS) | $CH_4$, $C_3H_8$ | | 0.1 | 0.81-1.22 | [52, 53] |
| Large vented box | $CH_4$, $C_3H_8$ | | 0.1 | 1.1, 1.06 | [51] |
| Explosion vessel | $i$-octane, ethanol, $n$-heptane, toluene, 1-hexene | 360 | 0.1-1.0 | 0.8-1.3 | [152] |
| Explosion vessel | $C_3H_8$, $n$-butanol | 360 | 0.1-1.0 | 0.8-1.3 | Present work |

## 5.4 Turbulent burning velocities: Comparisons and correlations

Here turbulent burning characteristics of *n*-butanol/air mixtures are compared with those of other fuels reported in the literature. The dimensionless correlations of $u_{tm}$ with Karlovitz stretch factor are presented for the full range of the experimental conditions for *n*-butanol/air mixtures. A comparison is made between the present and previous correlations.

### 5.4.1 Comparison of turbulent burning velocity of *n*-butanol with other hydrocarbons

Values of $u_{tm}$ for $n$-butanol/air mixtures, are compared with those of $i$-octane/air mixtures reported in [68, 123] under the same conditions, of 0.5 MPa and 360 K at different $u'$, in Fig. 5.9. Also presented are ethanol air $u_{tm}$ data at 0.5 MPa and 358K from [10]. These $u_{tm}$ are plotted for a flame radius of 30mm, against $\phi$ for different $u'$. Five experimental data point of $u_{tm}$ at each $\phi$ are presented for $n$-butanol and $i$-octane and best fit curves drawn. For ethanol, only the average from five explosions were available in [10]. Values of $u_{tm}$ increase with $\phi$ and, for a given $\phi$, increase with $u'$. For a given $u'$, between $\phi$ = 0.8 and 1.4, ethanol air mixtures yielded higher $u_{tm}$ compared to $n$-butanol followed by $i$-octane air mixtures. They dropped significantly at the richest mixture of $\phi$=1.5. These results are in line with results in [2, 121], comparing $n$-butanol and $i$-octane as an engine fuel. At low $u'$, lean ethanol and $n$-butanol have similar $u_{tm}$ values, while at higher $u'$, they are considerably higher than those of $n$-butanol. The higher $u_{tm}$ values for ethanol/air mixtures can be attributed to the lower $Ma_{sr}$, shown in Fig. 5.10, compared to $n$ -butanol and $i$-octane/air mixtures. As discussed for laminar flames in Section 5.2, positive $Ma_{sr}$ decreases the burning velocity with stretch while mixtures with negative $Ma_{sr}$ tend to burn faster and turbulent conditions also enhances it [24]. $i$-octane flames are found to quench at $u' =$

$4\ m/s$ and $\phi$ = 0.8. On the other hand for the same values of $\phi$, $n$-butanol and ethanol flames burned efficiently even at $u' = 6\ m/s$.

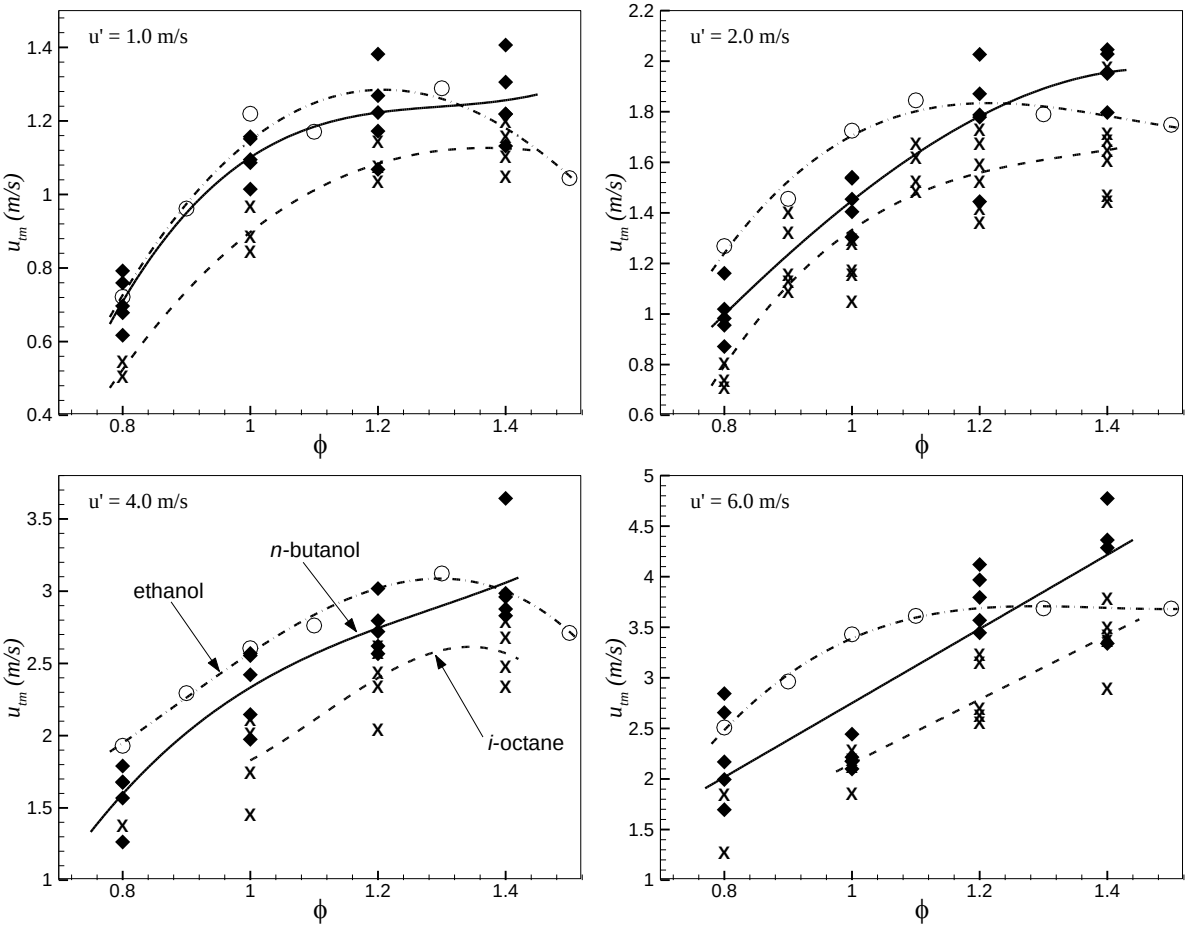


**Figure 5.9** Comparison of $u_{tm}$, for ethanol (circles) at 358K, *n*-butanol/air (filled diamonds) [10] and $i$-octane/air (crosses) [68] at 360 *K* at $r_{sch}$ = 30mm against $\phi$ for different $u'$at 0.5 MPa.

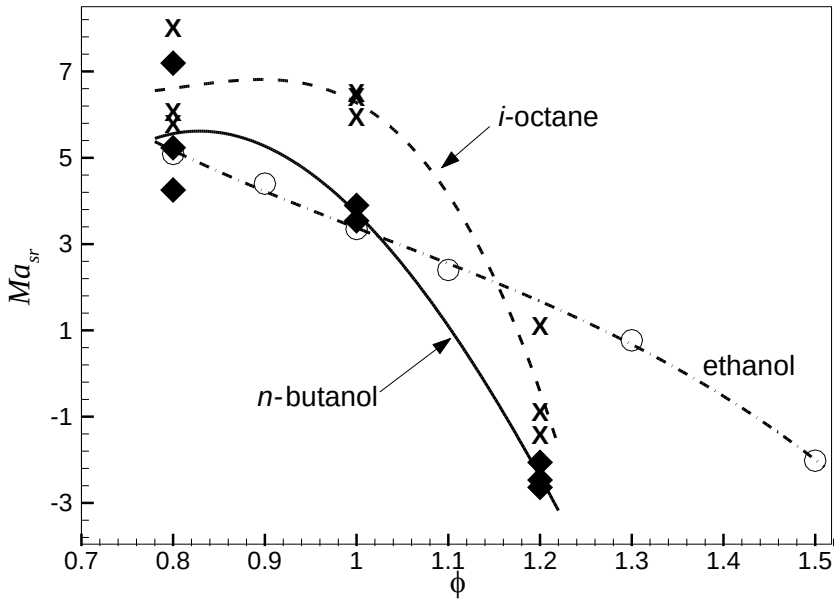


**Figure 5.10** Strain rate Markstein numbers, $Ma_{sr}$ for ethanol (circles) at 358K, *n*-butanol [10] (filled diamonds) and *i*-octane/air (crosses, [68, 123]) flames at 360 K against $\phi$ at 0.5 MPa.

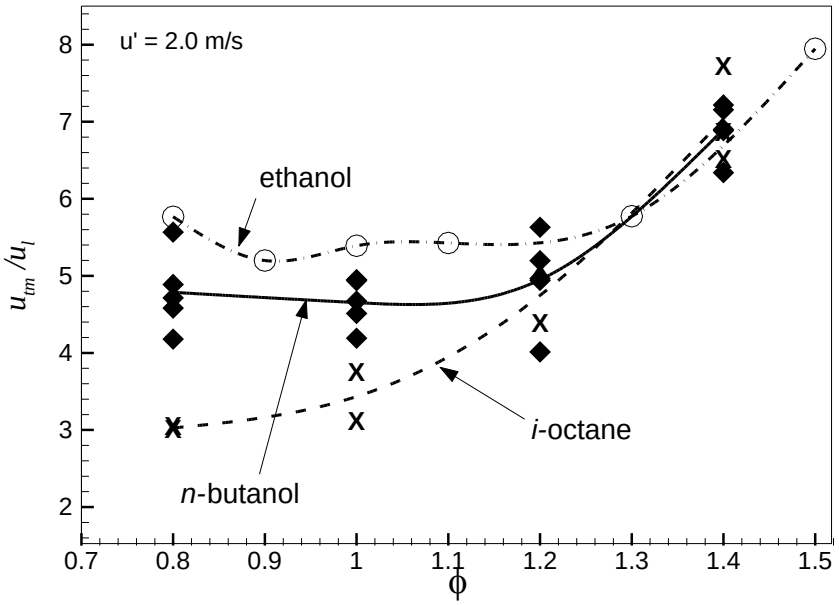


**Figure 5.11** $u_{tm}/u_l$ for ethanol (circles) at 358K, *n*-butanol [10] (filled diamonds) and *i*-octane/air (crosses, [68, 123]) flames at 360 K against $\phi$ at 0.5 MPa.

Compared in Fig. 5.11, for $u'$=2.0 m/s is the ratio of $u_{tm}/u_l$, plotted against $\phi$ for ethanol, $n$-butanol and $i$-octane flames at 0.5 MPa and at a flame radius of 30 mm. Values of $u_{tm}/u_l$ are relatively higher for ethanol flames compared to $n$-butanol/air and $i$-octane over the range of $\phi$ = 0.8 to 1.2. The magnitude of $u_{tm}$ is approximately 5 for $n$-butanol flames from $\phi$ = 0.8 to 1.2 and 5.5 for ethanol. Lean $i$-octane flames exhibit the lowest $u_{tm}/u_l$ of 3 at $\phi$ = 0.8, increasing gradually to 4.2 at $\phi$ =1.2. However, beyond this value all exhibit a similar trend, with $u_{tm}/u_l$ values increasing further to almost 8 at $\phi$ = 1.5 for ethanol flames. This behaviour is in line with the results of $Ma_{sr}$, shown in Fig. 5.10. Unlike $i$-octane, that quenches at $\phi$ = 0.8 and $u'$≥4m/s, quenching was not observed for $n$-butanol and ethanol flames at any value of $u'$ indicating appreciable burning rates over a wide range of $\phi$.

### 5.4.2 Correlations of $u_{tm}$ with $K$

It is widely accepted [8, 10, 64, 67, 68, 74, 92] that turbulent burning velocities are mainly affected by $u'$, $\phi$ , and P. The effect of $u'$ on $u_{tr}$ can be seen from Fig. 4.17 to Fig. 4.19, and that on $u_{tm}$ is seen from Fig. 4.28 to Fig. 4.31. The dependency of $u_{tr}$ and $u_{tm}$ upon $r_{sch}$ and $r_m$, respectively, is significantly influenced by $u'$. It is suggested in [59] that this is due to the flames experiencing more flame wrinkling at high $u'$ values thereby increasing the flame surface area. In contrast, the flames at the onset of quenching for lean mixtures do not follow the same tendency. For example, in Fig. 4.17(a), $u_{tr}$ for $n$-butanol/air mixtures, $\phi$ = 0.8, 0.1 MPa, increased with $u'$ due to flame wrinkling, but at a decreasing rate and with large scatter, as a consequence of observable evidence of quenching, particularly for flames of $u'$ ≥ 1 m/s. The scatter was also evident from Fig. 4.30(a) for $CH_4$/air, 0.6, 0.1 MPa where large scatter is seen in $u_{tm}$ before the flame radius reached a value of 60mm. It was difficult to initiate these lean mixtures above $u'$ = 2 m/s. While scatter in the lean mixtures was attributed to the onset of flame quenching [10], that in the rich mixtures at higher $u'$ values was due to flames being convected away from ignition point due to higher turbulence, as demonstrated in Fig. 4.20.

Bradley and co-workers [62, 67, 85] have expressed these turbulent burning velocities in terms of several dimensionless groups. The $u_{tm}$ measurements for all the fuels, in Section 4.4, are expressed by $u_{tm}/u_l$ and correlated with the dimensionless stretch factor $K$ in Fig. 4.27 for $n$-butanol/air and in Fig. 4.32 for $CH_4$ and $H_2$/air mixtures. $u_{tm}/u_l$ ratio increased with increasing $K$. For a given $K$ value it increased with decreasing $Ma_{sr}$. The $u_{tm}/u_l$ data for similar values of $Ma_{sr}$ are omitted from Fig. 4.27, as the uncertainty in $Ma_{sr}$ values can be as much as ±1. It is suggested in [77] that for high values of $Ma_{sr}$, $u_{tm}/u_l$ values are lower, which might be due to the lower resistance of flame to quenching. The maximum $u_{tm}/u_l$ values for the range of $K$ values obtained during the present work are in line with the maximum values ~ 15 obtained in [65, 185]. The curves show a deviation from the linear relationship which is called the bending effect [11, 19, 61]. It marks a departure from the local flamelet structure due to flamelet quenching and has been reviewed in depth in [93, 94]. This bending effect, in Figs. 4.27 and 4.32, was observed for $K$≥0.5, where the laminar flame thickness, $\delta_l$, attains a value greater than the Kolmogorov length scales, $\eta$. This phenomenon is most visible for $Ma_{sr}$=2,4 and -5 curves in Fig. 4.32. For positive $Ma_{sr}$ values, the curves are closer to each other and exhibit stronger saturation of burning velocity enhancement, rising only up to $u_{tm}/u_l$ ~ 6 for $Ma_{sr}$ = 2 at the maximum $K$ reported. Whereas for the negative $Ma_{sr}$ curves the values are considerably higher, and up to a $u_{tm}/u_l$ ~ 15 at $K$ =1 for $Ma_{sr}$= -5.

Interestingly, values of $u_{tm}/u_l$ from both Fig. 4.27 and Fig. 4.32, for $n$-butanol and $CH_4$/air mixtures respectively, close to $Ma_{sr}$= -5 and 3 were similar in magnitude over the range of $K$ while a reasonable difference was observed at positive $Ma_{sr}$ of 6, which could be attributed to errors in evaluating $Ma_{sr}$. Interestingly, for negative $Ma_{sr}$, values of $u_{tm}/u_l$ are high even at low $K$ compared to positive $Ma_{sr}$ curves. It is suggested that this could be due to instabilities arising from thermos-diffusive effects as discussed in Section 5.3.

It is suggested in [62] that the increase in flame surface area, associated with flame wrinkling, leads to an increase in $u_{tm}$ with $u_k'$. Bradley and co-workers [10, 74, 92] measured $u_{tm}$ for different fuels over a range of temperatures and

pressures and correlated non-dimensionalised $u_{tm}/u_k'$ with $K$ in terms of different $Ma_{sr}$. It is suggested in [64] that the influence of $Ma_{sr}$, which is associated with flame straining, dominates over curvature, $Ma_{cr}$, in its effect on increasing turbulent burning velocities. The expression obtained for $u_{tm}/u_k'$ in terms of $K$ is given by Eqs. (1.48)-(1.52) [10].

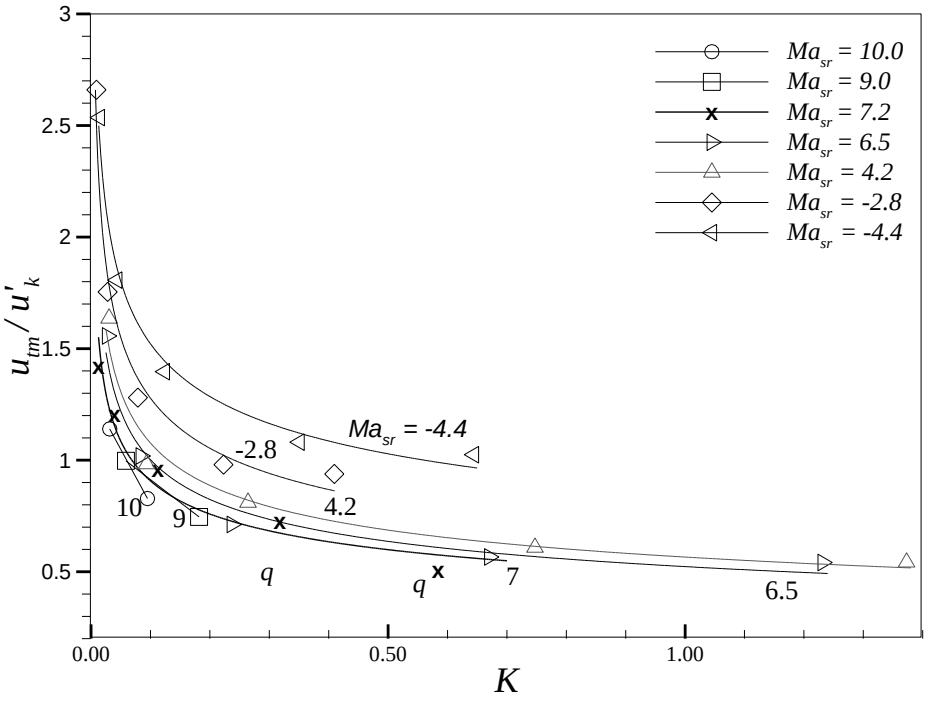


**Figure 5.12** Correlation of $u_{tm}/u'_k$ with $K$ using schlieren experiments

The present experimental data of $u_{tm}$ for $n$-butanol/air mixtures are correlated in terms of $u_{tm}/u_k'$ with $K$ for a flame radius of 30 mm and positive and negative values of $Ma_{sr}$ in Fig. 5.12. Values of $u_l$, ν, $Ma_{sr}$ used in these correlations are presented in Table 4.1. Solid lines are the best fit curve for the data at a single $Ma_{sr}$. For a given $Ma_{sr}$, $u_{tm}/u_k'$ has higher values at lower $K$ and this reduces with increase in $K$. For a given $K$, the more negative the $Ma_{sr}$ the greater is the $u_{tm}/u_k'$.

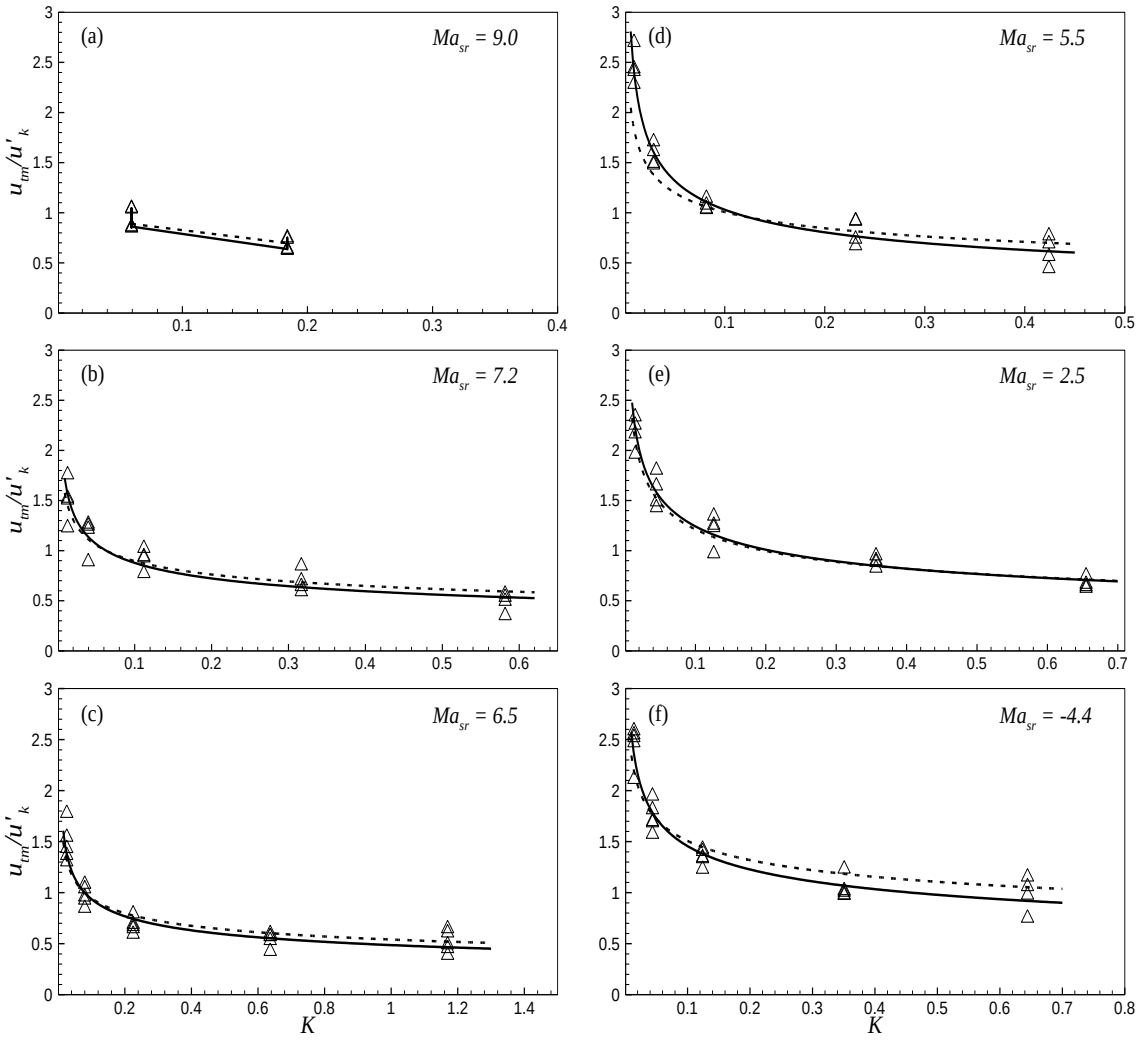


**Figure 5.13** Correlation of $u_{tm}/u'_k$ with $K$ using schlieren experiments (open triangles); and broken curve using the Eq.(1.48); solid curve shows the best fit for data from present schlieren experiments.

Shown in Fig. 5.13 are the correlated curves of $u_{tm}/u'_k$, obtained in the present measurements, compared with the $u_{tm}/u'_k$ values, calculated using Eq. (1.48), for different $Ma_{sr}$. The open triangles are the experimental values best fitted with the solid curve, whereas, the broken curve represent the values of $u_{tm}/u'_k$ obtained using the correlation of Eq. (1.48). The coefficient of determination, $R^2$, for the experimental data in Fig. 5.13 ranged from 0.85 to 0.92. The general trend for both the curves decrease with $K$ for a constant $Ma_{sr}$. For $K < 0.1$, rapid increases in both $u_{tm}/u'_k$ values were observed. It was suggested in [72, 171] that flames in the region $K \leq 0.05$ are subjected to instabilities, discussed in Section 5.3, resulting in increased burning

velocities due to high flame stretch rate and this is evident from the present experimental values of $u_{tm}/u_k'$ in Fig. 5.13. Bearing in mind the inevitable scatter in measured turbulent burning velocities, the agreement between both the curves is satisfactory, except for negative $Ma_{sr}$, shown in Fig. 5.13(f), where the measured values of $Ma_{sr}$ are subjected to increased scatter. For very positive $Ma_{sr}$ the two curves agree well. As $K$ increases flamelet merging and localised flame extinctions occur that contribute to decreasing $u_{tm}/u_k'$ [72].

The curves in Fig. 5.13 are reproduced on Figs. 5.14 and Fig. 5.15 for positive and negative $Ma_{sr}$ respectively along with the experimentally derived values of $u_{tm}/u_k'$ against $Ma_{sr}$ from previous work [10, 74, 92, 186-188]. Each curve is represented by an $Ma_{sr}$ value with the appropriate reference. The solid thick curves are the present work and its $Ma_{sr}$. The agreement between the different correlations is quite satisfactory for combustion vessel work study but less for the burner work [186], shown by broken curve in Fig. 5.14. However, a noticeable discrepancy among the curves at negative $Ma_{sr}$, shown in Fig. 5.15, is observed which could be attributed to increased scatter in evaluating $Ma_{sr}$. Nevertheless, the curves, presented for both positive and negative $Ma_{sr}$ are in good agreement with the previous data obtained in the present combustion vessel indicating that the correlation, given by Eq. (1.48) holds well for the present experimental results.

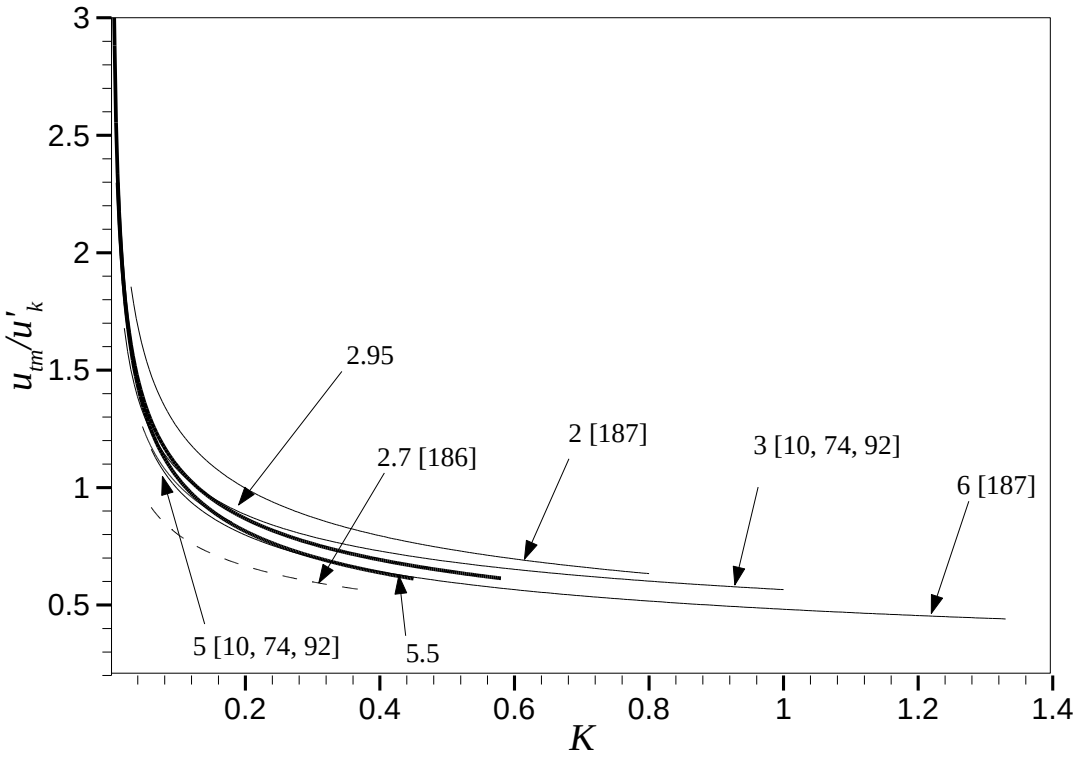


**Figure 5.14** $u_{tm}/u'_k$ plotted against $K$ for positive $Ma_{sr}$.

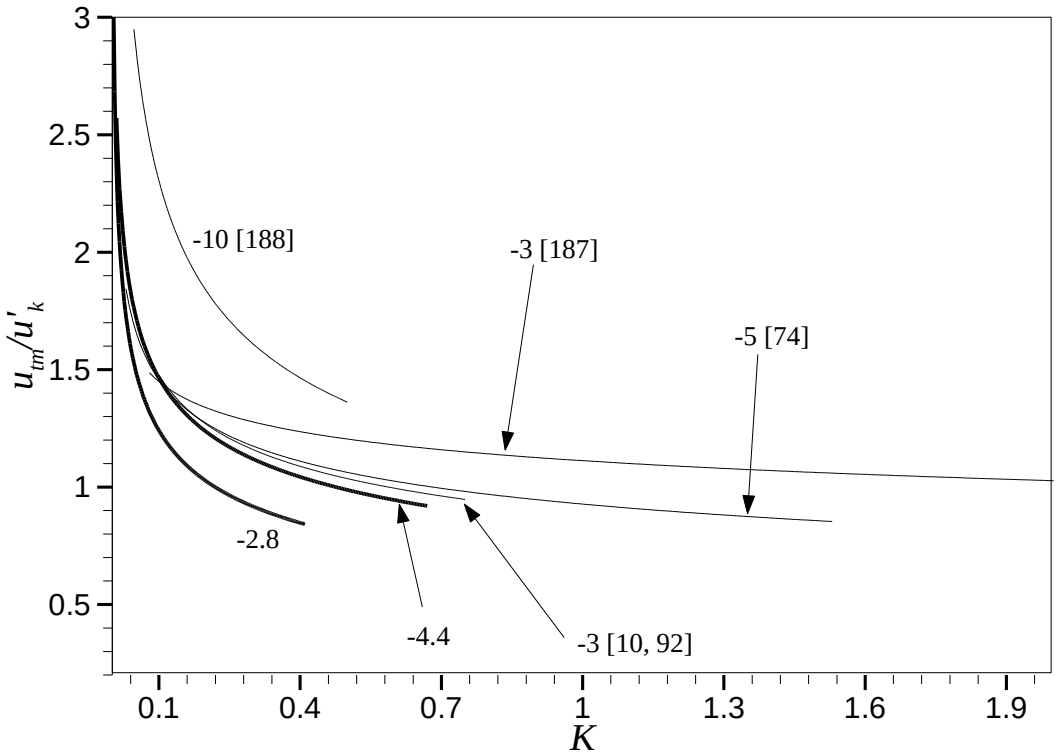


**Figure 5.15** $u_{tm}/u'_k$ plotted against $K$ for negative $Ma_{sr}$.

## 5.5 3D turbulent flame structure analysis

The 3D measurements of flame surface area enhancement by the swinging sheet technique described in Section 2.5 and reported in Section 4.5.4 are now discussed in Section 5.5.2. Using the enhancement of turbulent burning velocity ratio, presented in Section 4.4.2.1, and the enhancement of flame surface area ratio, presented in Section 4.5.4.1 for the conditions in Table 4.3, values of $P_b^{0.5}$ are obtained. These are presented in Section 5.5.3 and discussed in comparison with 2D estimates of the same in Section 5.5.4. The disparity in the two enhancement ratios obtained using 3D and 2D methods are discussed in Section 5.5.5.

### 5.5.1 Analysis of raw flame images

Apparently, the frames 14 to 17, in Fig. 4.33, for $CH_4$/air flames have islands of flames detached from the main flame giving an appearance of two separate flames, although these were, in fact, found to be interconnected with the main flame from frame 18. Thus, a 2D analysis with a fixed sheet position, would have incorrectly implied that the flame existed in multiple, fragmented parts. In addition, frames 7 to 8 reveal a pocket of unburned mixture within the main flame, further complicating the study. Again, analysis of this single sheet would imply that this region is isolated, but analyzing the frames either side of this flame image reveal this region to be part of a deep wrinkle in the flame surface. Particularly at low turbulence, these apparent islands and pockets are in fact fingers of burned and unburned mixture interconnected to other gas regions on different planes [79, 132, 189]. It is important as to which slice of flame is considered for analysis when using 2D techniques as this could increase the uncertainty, if the captured slice does not pass through the centre of the flame. Flames close to quench tend to move from the centre of the vessel, as demonstrated in schlieren flame images of Fig. 4.20, increasing the uncertainty of slicing the flame through the centre.

### 5.5.2 Flame surface area ratio

As discussed in Sections 5.4, wrinkling increases the flame surface area and burning rate in turbulent flames. This is evident from Fig. 4.32 and Fig. 4.48 for turbulent burning enhancement and flame surface area enhancement respectively. Figure 4.48 shows the increase in $A/a_m$ with increasing $K$. For a given $K$, it decreases from positive to negative $Ma_{sr}$. For negative $Ma_{sr}$, the curves of $A/a_m$ are lower than the positive ones with the $Ma_{sr}$ = -5 curve flattening out as $K$ increases. Shown in Fig. 5.16 are the area enhancement ratio, reproduced from Fig. 4.48 plotted against $u'/u_l$ for different $Ma_{sr}$. The Direct Numerical Simulations, DNS results from Nivarti et al. [93], obtained for statistically-planar flames of unity $Le$, are compared. Since, integral length scales were different in the DNS work (1 mm), $u'/u_l$ were chosen instead of *K* for comparison. In their work [93] they argued that the growth of flame surface area is inhibited with increasing $u'/u_l$ as smaller length scales, though efficient at creating curvatures, do not strain the flame effectively. Moreover, they found the generated curvatures to be mostly negative, contributing to negative stretch rate that decreases the flame surface area. The present 3D $A/a_m$ ratios are in line with the DNS in [93] for the range of $u'/u_l$ values. In addition, the maximum area enhancement measured, $A/a_m$ ~ 5, is in line with the maximum values measured in the piloted burners by Wabel et al. [185] and Yuen et al. [65].

For positive $Ma_{sr}$, similar values ~ 5 for $u_{tm}/u_l$, shown in Fig. 4.32, and $A/a_m$, shown in Fig. 4.48, are observed. This shows that the increase in burning is accounted almost entirely by flame wrinkling, caused by $u'$, and flame stretch, expressed in terms of $P_b^{0.5}$. However, a contrary effect was observed in the curves, with negative $Ma_{sr}$ values. In that values of $A/a_m$, shown in Fig. 4.48 are much lower than their corresponding values of $u_{tm}/u_l$, shown in Fig. 4.32. It is tentatively suggested that the high $u_{tm}/u_l$ values for the negative $Ma_{sr}$ curves could be due to the instability created in lean $H_2$ flames enhancing the burning rate. PLIF images of OH fluorescence from a lean hydrogen laminar explosion flame, with negative $Ma_{sr}$, in [78] revealed that the flames in the

negative curvature regimes around an unstable flame cell quenches and the flame front is locally fractured. This could also be a reason for the negative $Ma_{sr}$ turbulent flames to exhibit low $A/a_m$, however, this has not been quantified in the present study. On the other hand, the explosion flames with positive $Ma_{sr}$ are solely affected by $u$' thereby increasing the flame curvatures, the effect of which is seen as high $A/a_m$ (see Fig. 4.48 for positive $Ma_{sr}$).

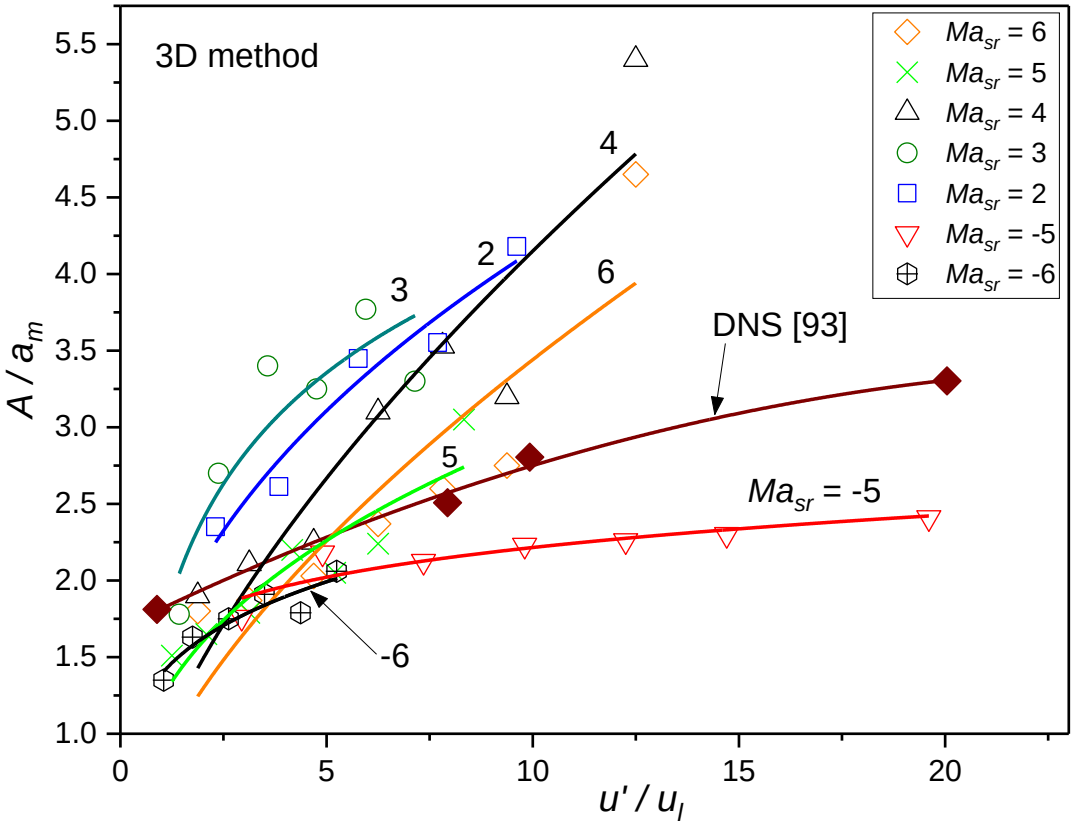


**Figure 5.16** Variations of *A/a*$_m$ with *K* for the experimental conditions in Table 4.3.

### 5.5.3 Evaluation of probability of burning from 3D flame data

The enhancement in the turbulent burning velocity, $u_{tm}/u_l$, discussed in Section 5.4, was expressed in terms of flame area ratios by Damköhler's first hypothesis [59] and is presented in [13] as given by Eq. (1.53). In a weak turbulent regime [59], the turbulent burning velocity enhancement ratio, $u_t/u_l$, is accounted entirely by the enhancement in the flame surface area ratio, $A/a$ as given by Eq. (1.53) due to the flame surface wrinkling by turbulent eddies. The balancing of these two expressions in Eq. (1.53) was confirmed by 2D

experimental measurements and DNS studies of several researchers [93, 186, 190, 191] where the Markstein numbers were close to zero and $P_b^{0.5}$ close to 1. This is consistent with Damköhlers first hypothesis [59] of increased $u_t$ due to increase in flame surface area in the weak regime. However, as laminar flames are affected by non-unity Lewis numbers and non-zero Markstein numbers, turbulent flames with non-zero Markstein numbers and non-unity $P_b^{0.5}$ values are also affected by thermo-diffusive effects [11].

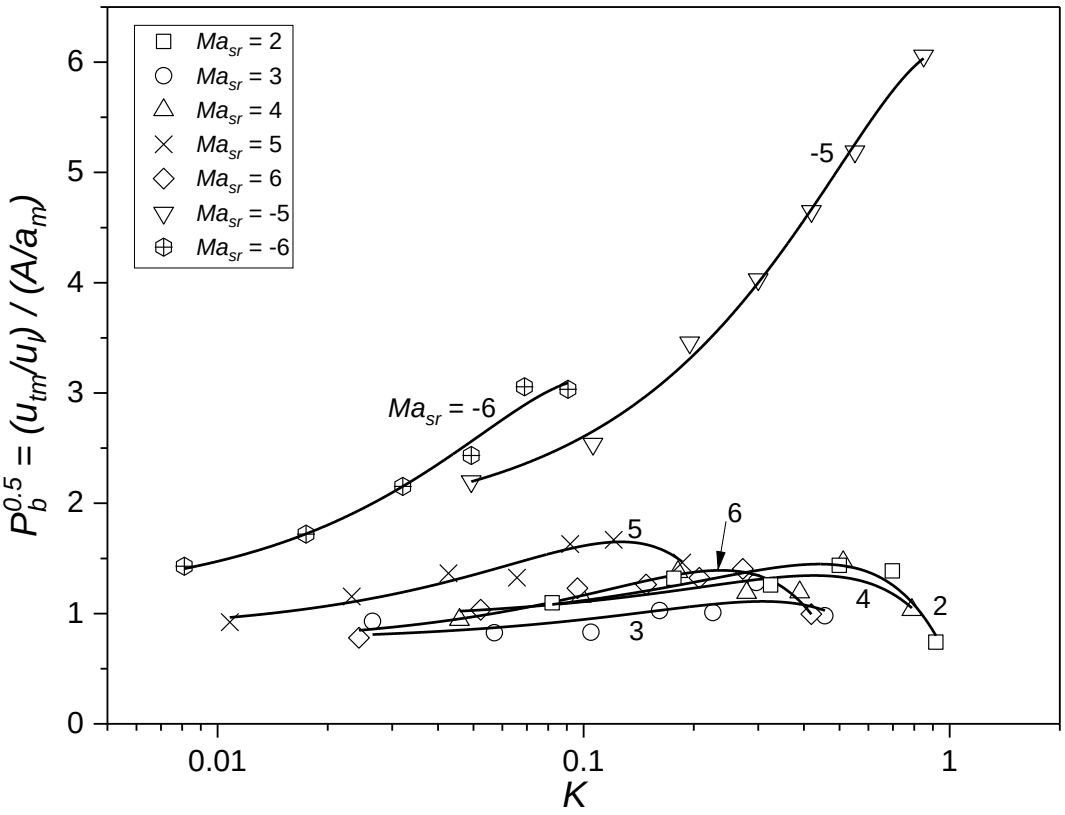


**Figure 5.17** Probability of burning, $P_b^{0.5}$, as a function of Karlovitz stretch factor, *K*.

Theoretical values of $P_b^{0.5}$ were computed in [72] and experimental values were presented in [13], as shown in Fig. 1. 7. The experimental values of $P_b^{0.5}$ were based on the inferred $A/a$ ratios from spatial contours of mean reaction progress variable, $\bar{c}$, obtained using 2D measurement techniques. The effects of flame stretch were quantified through derived $P_b^{0.5}$ over a range of non-zero $Ma_{sr}$ and $K$ values and this was found close to 1. In the present work, a direct comparison between measured 3D flame surface areas, presented in Section

4.5.4 and measured $u_{tm}/u_l$, presented in Section 4.4.2, has been obtained. These were used to evaluate values of $P_b^{0.5}$ for non-zero Markstein number mixtures, presented in Table 4.3, to understand the limits of validity of Eq. (1.53). All the necessary data in calculating and analysing the obtained results are presented in Table 5.2.

Using the measured values of $u_{tm}/u_l$ and $A/a_m$ from Fig. 4.32 and Fig. 4.48 respectively, the values of $P_b^{0.5}$ are calculated using the Eq. (1.53). These are plotted against $K$, in Fig. 5.17 for different $Ma_{sr}$. Solid lines are the best fit curves through the data. For positive $Ma_{sr}$, the $P_b^{0.5}$ is more or less close to unity yet increasing monotonically until the highest $K$ values are reached. The decrease in the $P_b^{0.5}$ values close to the maximum $K$ for each $Ma_{sr}$ is suggested to be due to the global quenching [13]. For $Ma_{sr}$ =5, the $P_b^{0.5}$ values vary from close to unity to a maximum value of 1.5 over the range of $K$ employed, while for negative $Ma_{sr}$ cases, it varies from 1.5 (for $Ma_{sr}$=-6) to a maximum of 6 (for $Ma_{sr}$=-5) for a $K$ value close to unity. For positive $Ma_{sr}$ fairly good agreement was found in $P_b^{0.5}$ values, evaluated from the present 3D measurements and that of those presented in Fig. 1.7 using 2D measurement techniques, which were close to unity. $P_b^{0.5}$ values were close yet no consistency was found in terms of $Ma_{sr}$. However, for negative $Ma_{sr}$ conditions, the present 3D results reveal that $P_b^{0.5}$ are far from unity, even at low $K$ and can reach values as high as 6 at higher $K$ values.

### 5.5.4 Evaluation of probability of burning from 2D flame sheets

Using the centre line image of the captured swinging laser sheet data, 2D estimates of surface area enhancement, $A_{2D}/a_{m,2D}$, were also evaluated, based on the assumption of isotropy [64]. For each centre line image the perimeter, $P$, of the 2D contour is equated to that of a circle to evaluate the equivalent radius, $r$. This radius, $r$, was used to estimate the total flame surface area, $A_{2D} = 4\pi r^2$, from an equivalent sphere. The mean flame surface area for these 2D contours follow the method presented in [64] of evaluating a mean radii, $r_j$, based on unburned and burned gas mass balance as shown in Fig. 1.5. It is important to mention that the propensity of the flames to drift

away from the centre of the vessel at high $u'$ increase and the slicing of the laser sheet, when fixed in case of a 2D measurement technique, through the centre of developing flame cannot be ascertained.

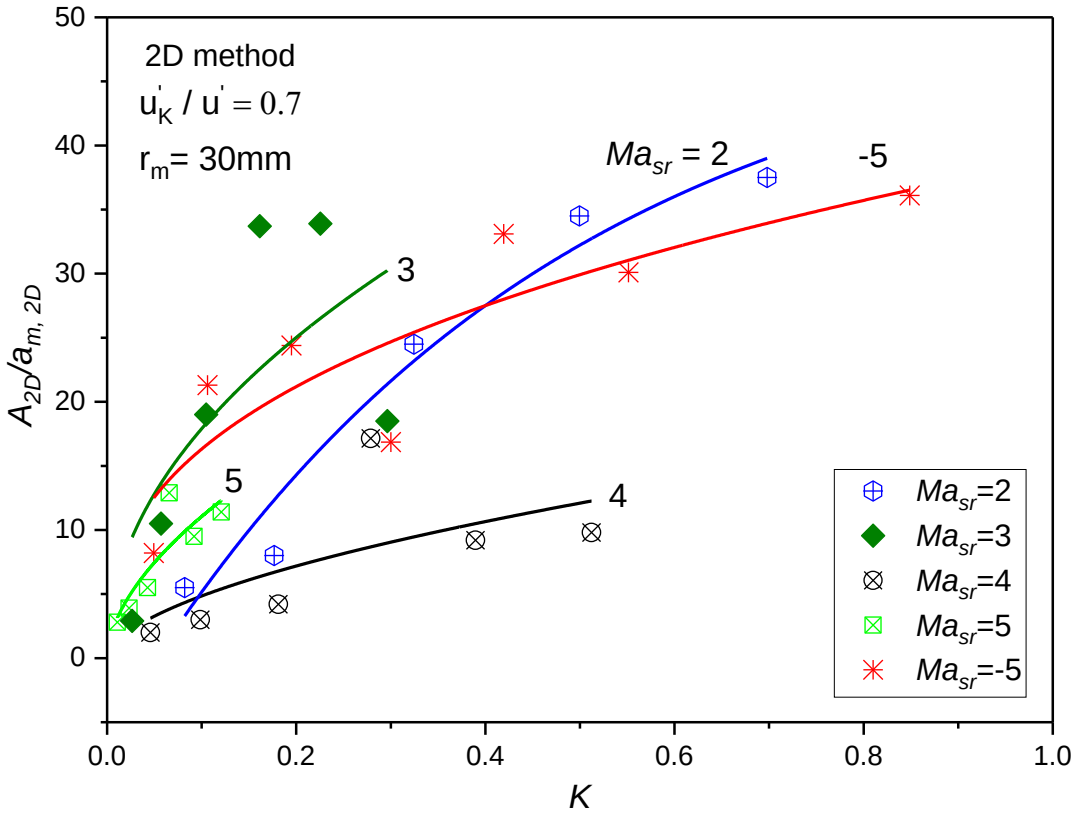


**Figure 5.18** Flame surface area enhancement ratio, $A/a_m$ against, $K$ using 2D flame data.

Shown in Fig. 5.18 are the 2D estimates of $A_{2D}/a_{m,2D}$, for the mixture conditions presented in Table 4.3, against $K$. Solid lines are the best fit curves through the data. Apparently, for positive $Ma_{sr}$, the trend is similar to that of the 3D estimates, shown in Fig. 4.48, except for $Ma_{sr}$ = −5 (red curve). More importantly, a striking difference in the area enhancement magnitudes, of an order of 1, are noticed from the 2D estimates. These $A_{2D}/a_{m,2D}$, compare reasonably well with values inferred previously in [13] upon assuming Eq. (1.53) to hold.

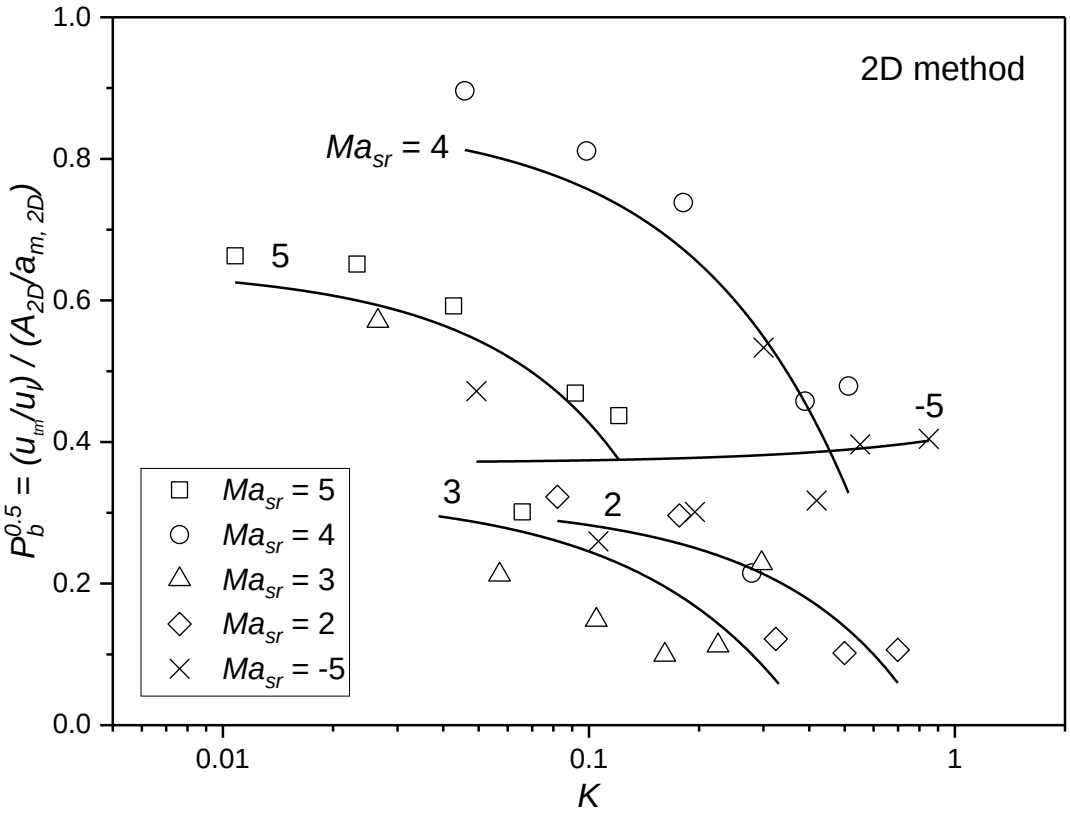


**Figure 5.19** Probability of burning, $P_b^{0.5}$, evaluated from 2D method, as a function of $K$

Shown in Fig. 5.19 are the $P_b^{0.5}$ profiles obtained from the 2D estimates of the area enhancement ratio, $A_{2D}/a_{m,2D}$, presented in Fig. 5.18, and the turbulent burning enhancement ratio, $u_{tm}/u_l$ from Fig. 4.32. Solid lines are the best fit curves through the data. Unlike $P_b^{0.5}$ profiles obtained from 3D measurements, the 2D estimates of $P_b^{0.5}$ apparently decrease with increasing $K$, except for $Ma_{sr}$ = -5. For any given $Ma_{sr}$, the $P_b^{0.5}$ values are <1 and again no consistency is found in terms of $Ma_{sr}$. However, these values are close in proximity to the ones presented in [13], shown in Fig. 1.7, except for the $Ma_{sr}$ = -5 case. This suggests that Eq. (1.53) appears to be valid based on 2D estimates of the area enhancement ratio.

### 5.5.5 Proposed parameter $Z$

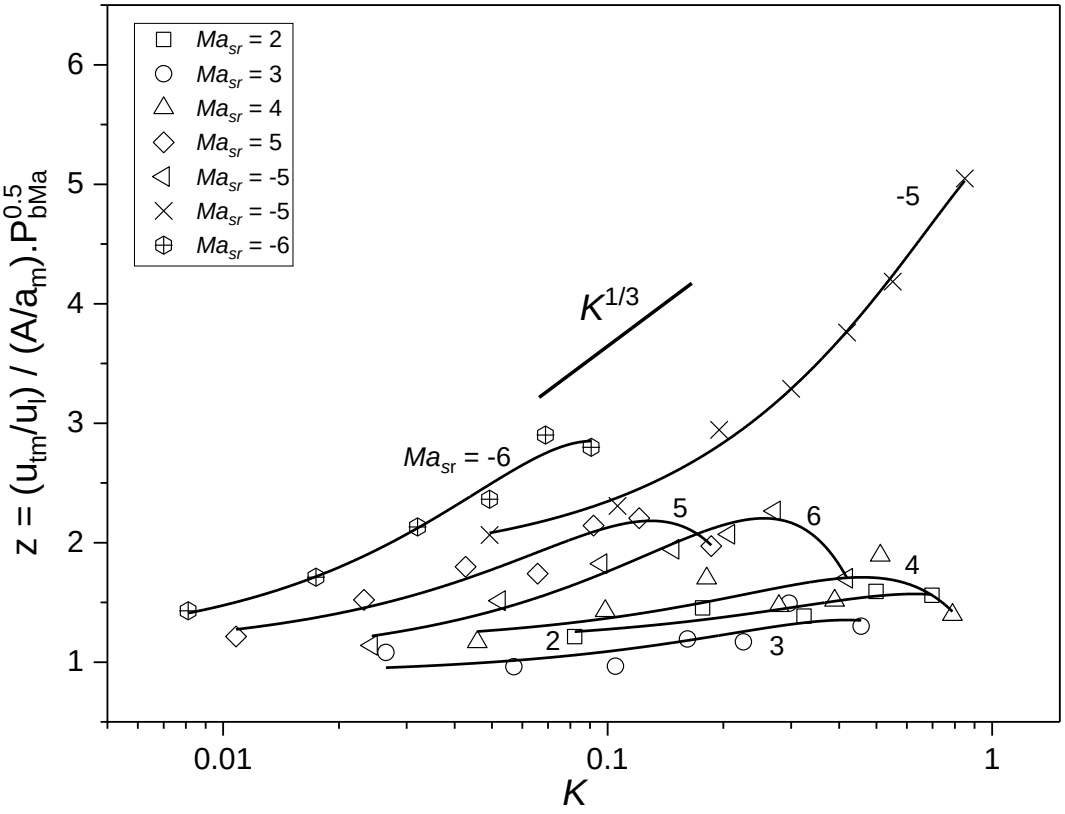


**Figure 5.20** $Z$ plotted against $K$ for different $Ma_{sr}$.

The disparity in turbulent burning enhancement and the flame surface area enhancement, from 3D measurements, over and above any stretch effects as quantified by $P_b^{0.5}$, which is argued to be closer to unity according to [13], as shown in Fig. 1.7, is expressed as $Z$ given by

$$Z = \frac{u_{tm}/u_l}{(A/a_m)P_b^{0.5}} \tag{5.6}$$

Figure 5.20 shows the parameter $Z$ plotted against increasing $K$ for different $Ma_{sr}$. Solid lines are the best fit curves through the data.

In their work, Nivarti et al. [192] suggested a scaling law, shown as $K^{1/3}$ in Fig. 5.20, that estimated the contribution of diffusivity enhancement from small scale turbulence in addition to the contribution of area enhancement due to flame wrinkling by large scale turbulence. In a collaboration with University of Cambridge, it is being argued that this term $Z$ can be interpreted as the

diffusivity enhancement contribution which is given by Damköhlers second hypothesis, $\sqrt{D_t/D_l}$, discussed in [94]. It states that turbulent length scales smaller than the turbulent flame brush thickness amplify diffusive transport processes. The slope of $Z$ for negative $Ma_{sr}$ curves, in Fig. 5.20, agree well with the scaling law $K^{1/3}$. This suggests that the diffusivity enhancement play a significant role in burning velocity enhancement, at least for negative $Ma_{sr}$ flames. The high values of $Z$ ($P_b^{0.5}$ in Fig. 5.17) at low $K$<0.05, for these negative $Ma_{sr}$ mixtures, could be due to instabilities playing a significant role and this is also evident from Fig. 1.6, while at high $K$ it could possibly be the diffusivity enhancement more dominant. For positive $Ma_{sr}$, the diffusivity enhancement may not be negligible at high $K$.

Wabel et al. [185] (Driscoll and workers) also suggested a possible explanation for the difference in these two enhancement ratios that could be attributed to the broadening of the preheat zone that may cause thermal diffusivity to dominate over the flame wrinkling mechanism. They argued that the smallest eddies decay while traversing through the broadened preheat zone and do not contribute to flame surface wrinkling. However, their reported values were at much higher $K$ compared to the present work. Similar conclusions were also reported by Yuen et al. [65] (Gülder and co-workers). They concluded that at high $K$, the small scale turbulence destroys the scalar gradients within the flame front and inhibits its growth. Moreover, the DNS work from Nivarti et al. [94, 192], also reinforces the argument of diffusivity enhancement ratio playing a significant role at high $K$.

**Table 5.2** Data required for the analysis of present experimental study.

| | | | $u'\ (m/s)$ | $R_L^{-0.5}$ | $u'/u_l$ | $K$ |
|---|---|---|---|---|---|---|
| $CH_4$ | $Ma_{sr}$ | 6 | 0.3 | 0.0277 | 3.158 | 0.069 |
| | $\rho_u\ (Kg/m^3)$ | 4.4918 | 0.5 | 0.0214 | 5.263 | 0.149 |
| | $\rho_b\ (Kg/m^3)$ | 0.7457 | 0.75 | 0.0175 | 7.895 | 0.273 |
| | $\vartheta\ (m^2/s)$ | 4.6e-6 | 1.0 | 0.0152 | 10.526 | 0.420 |
| | $\delta_l\ (m)$ | 4.84e-5 | 1.25 | 0.0136 | 13.158 | 0.587 |
| | | | 1.5 | 0.0124 | 15.79 | 0.772 |
| | | | 2.0 | 0.0107 | 21.053 | 1.188 |
| $CH_4$ | $Ma_{sr}$ | 5 | 0.3 | 0.0277 | 1.6667 | 0.0192 |
| | $\rho_u\ (Kg/m^3)$ | 4.509 | 0.5 | 0.0214 | 2.7778 | 0.0413 |
| | $\rho_b\ (Kg/m^3)$ | 0.7328 | 0.75 | 0.0175 | 4.1667 | 0.0759 |
| | $\vartheta\ (m^2/s)$ | 4.59e-6 | 1.0 | 0.0151 | 5.5556 | 0.1169 |
| | $\delta_l\ (m)$ | 2.55e-5 | 1.25 | 0.0135 | 6.9444 | 0.1634 |
| | | | 1.5 | 0.0124 | 8.3333 | 0.2147 |
| | | | 2.0 | 0.0107 | 11.1111 | 0.3306 |
| $CH_4$ | $Ma_{sr}$ | 4 | 0.3 | 0.0521 | 1.8750 | 0.0458 |
| | $\rho_u\ (Kg/m^3)$ | 1.0951 | 0.5 | 0.0404 | 3.1250 | 0.0986 |
| | $\rho_b\ (Kg/m^3)$ | 0.1512 | 0.75 | 0.0330 | 4.6875 | 0.1811 |
| | $\vartheta\ (m^2/s)$ | 1.63e-5 | 1.0 | 0.0285 | 6.2500 | 0.2788 |
| | $\delta_l\ (m)$ | 1.02e-4 | 1.25 | 0.0255 | 7.8125 | 0.3896 |
| | | | 1.5 | 0.0233 | 9.3750 | 0.5122 |
| | | | 2.0 | 0.0202 | 12.5000 | 0.7885 |
| $CH_4$ | $Ma_{sr}$ | 3 | 0.3 | 0.0520 | 1.4286 | 0.0265 |
| | $\rho_u\ (Kg/m^3)$ | 1.1216 | 0.5 | 0.0402 | 2.3810 | 0.0570 |
| | $\rho_b\ (Kg/m^3)$ | 0.183 | 0.75 | 0.0329 | 3.5714 | 0.1048 |
| | $\vartheta\ (m^2/s)$ | 1.62e-5 | 1.0 | 0.0285 | 4.7619 | 0.1613 |
| | $\delta_l\ (m)$ | 7.71e-5 | 1.25 | 0.0255 | 5.9524 | 0.2255 |
| | | | 1.5 | 0.0232 | 7.1429 | 0.2964 |
| $CH_4$ | $Ma_{sr}$ | 2 | 0.3 | 0.0616 | 1.5873 | 0.0388 |
| | $\rho_u\ (Kg/m^3)$ | 0.9258 | 0.5 | 0.0477 | 2.6455 | 0.0835 |
| | $\rho_b\ (Kg/m^3)$ | 0.1971 | 0.75 | 0.0390 | 3.9683 | 0.1535 |
| | $\vartheta\ (m^2/s)$ | 2.28e-5 | 1.0 | 0.0338 | 5.2910 | 0.2363 |
| | $\delta_l\ (m)$ | 1.2e-4 | 1.25 | 0.0302 | 6.6138 | 0.3302 |
| | | | 1.5 | 0.0276 | 7.9365 | 0.4341 |
| | | | 2.0 | 0.0239 | 10.5820 | 0.6684 |

| | | | | | | |
|---|---|---|---|---|---|---|
| $H_2$ | $Ma_{sr}$ | -5 | 0.3 | 0.0290 | 2.9412 | 0.0627 |
| | $\rho_u\ (Kg/m^3)$ | 4.2591 | 0.5 | 0.0225 | 4.9020 | 0.1349 |
| | $\rho_b\ (Kg/m^3)$ | 1.3214 | 0.75 | 0.0183 | 7.3529 | 0.2478 |
| | $\vartheta\ (m^2/s)$ | 5.04e-6 | 1.0 | 0.0159 | 9.8039 | 0.3815 |
| | $\delta_l\ (m)$ | 4.38e-5 | 1.25 | 0.0142 | 12.2549 | 0.5331 |
| | | | 1.5 | 0.0130 | 14.7059 | 0.7008 |
| | | | 2.0 | 0.0112 | 19.6078 | 1.0789 |
| $H_2$ | $Ma_{sr}$ | -6 | 0.3 | 0.0295 | 1.0490 | 0.0081 |
| | $\rho_u\ (Kg/m^3)$ | 4.1179 | 0.5 | 0.0228 | 1.7483 | 0.0174 |
| | $\rho_b\ (Kg/m^3)$ | 1.0914 | 0.75 | 0.0186 | 2.6224 | 0.0320 |
| | $\vartheta\ (m^2/s)$ | 5.21e-6 | 1.0 | 0.0161 | 3.4965 | 0.0493 |
| | $\delta_l\ (m)$ | 1.82e-5 | 1.25 | 0.0144 | 4.3706 | 0.0689 |
| | | | 1.5 | 0.0132 | 5.2448 | 0.0906 |
| | | | 2.0 | 0.0114 | 6.9930 | 0.1395 |

## 5.6 Quenching of turbulent flame kernels

The data, presented in Section 4.6, for quench and near quench flame kernels were explored in terms of studying the influence of $K$. The relevant experimental data on the critical dimensionless flame diameters, $d_k/\delta_k$, are listed in Table 4.4 [172], whilst Fig. 5.21 shows the interrelationships of this and other key parameters. Because of the importance of the smaller length scales in quenching, it might be thought advantageous to plot these values against a Karlovitz factor, $Ka$, based on the smaller Kolmogorov eddy time scale, $\tau_\eta = \eta/u_\eta$. This anticipation holds no advantage because it can be shown that $Ka/K \approx 15^{0.5}$. Values of $Ka$ are given in the Table 4.4. Figure 5.21 shows the $d_k/\delta_k$ data points and the bold curves are plots of these against $K$ for $H_2$, $CH_4$, and the grouping of the higher hydrocarbons i.e. n-butanol, listed in Table 4.4. The hydrocarbons display similar values of $d_k/\delta_k$, although they are more conveniently correlated in terms of $p_{0.4}$. The regime of flame quenching lies beneath these plotted curves for all the different fuels.

The hydrocarbons are the most easily quenched, at the lowest values of $K$, and are associated with the highest values of $Ma_{sr}$. Hydrogen mixtures are the most difficult to quench, at the highest values of $K$, and these are

associated with the lowest and negative values of $Ma_{sr}$ Methane mixtures have intermediate $Ma_{sr}$ values.

### 5.6.1 Quenching of lifted jet flames

Turbulent fuel jets of lifted jet flames entrain air, and the leading reaction zone is the most reactive region, where the local mixture attains the maximum laminar burning velocity, $u_{lm}$, [193]. Thereafter, with increasing fuel jet velocity more air is entrained and its reaction with the fuel is aided by the mixing with the hot gases created in the initial most reactive zone. Eventually the jet entrains more than sufficient air for reaction, the flame quenches, and blows off the burner. For a given fuel jet velocity, pipe diameters, $D$, that are less than a critical size, cannot maintain a flame. This size represents the critical jet flame diameters, $D_b$, before blow-off for the given conditions. It is normalised by the jet flame laminar flamelet thickness, $\delta_k$, of the most reactive mixture, to give $(D_b/\delta_k)$. The fuel jet flow rate is characterised by a dimensionless Flow number, $U^*$, $= (u/u_{lm})(\delta_k/D)^{0.4}(P_i/P_a)$. Values of $U^*$ at blow-off are $U_b^*$. Values of $D_b/\delta_k$, are plotted against $U_b^*$ in Fig. 5.21, with values taken from [183]. From its derivation, it is apparent that the flow number has a similarity with the Karlovitz stretch factor, $K$ [26, 183]. $U_b$* therefore appears as the secondary *x*-axis, against which the present experimental values of $D_b/\delta_k$, on the secondary y-axis, are plotted by the dotted curves, for different values of $p_b$. For both $CH_4$ and hydrocarbons, choked jet flow, develops above about $U_b^*$= 200.

Although the limiting values of $d_k/\delta_k$ and $D_b/\delta_k$ in the two sets of diverse results are rather different, they reflect the underlying similarity between premixed and jet flamelet structures, and are similarly influenced by $Ma_{sr}$. A striking aspect of both sets of curves is the sharp increases in $d_k/\delta_k$ and $D_b/\delta_k$ with $K$ and $U_b^*$, respectively. This implies that large increases in *u'* and *u* can create high burning rates, only if they are accompanied by large commensurate increases in, respectively, explosion vessel sizes and burner diameters.

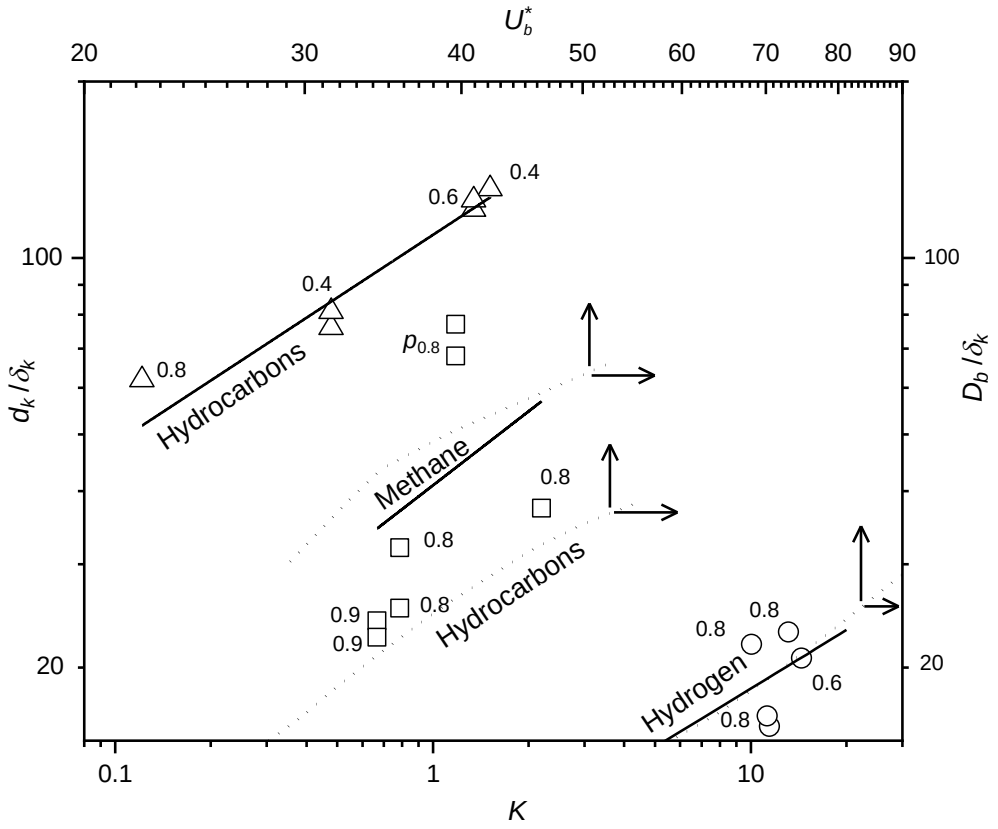


**Figure 5.21** Symbols show probabilities of flame propagation for $d/\delta_k$ and $K$. Dotted curves show jet flame $D_b/\delta_k$ values at $U_b$* from [183]. Numbers adjacent to symbols are $p_b$ values. Flame quenching occurs beneath the curves. Symbols: △, for hydrocarbons, □, for $CH_4$, and, ○, for $H_2$, throughout the paper.

### 5.6.2 Flame quenching on the *U/K* diagram

The flame quenching regime, indicated by C in Fig. 1.6 was re-examined in the light of the data in [101], along with the data in the present study for the mixtures presented in Table 4.2 and Table 4.3. The procedure adopted was, initially, to plot all the $p_{0.8}$ data from these sources in Fig. 5.22, and then derive, the best fit curve of $Ma_{sr}$ against $K$. Figure 5.22shows values of $Ma_{sr}$, for $p_{0.8}$, plotted against $K$, for the different mixtures. The open symbols show the data taken from [101], whilst solid symbols are from the present study. The dotted curve shows the best fit curve through the data from [101], given by the Eq. (1.55), and the solid curve is the best fit through all the data points, including the present ones. This gives,

$$Ma_{sr} = -2.24\ln(K) + 3.8. \quad (5.7)$$

Not surprisingly, the quenching tendency is increased with an increase in $K$, whilst at the larger values of $K$, negative values of $Ma_{sr}$ become necessary for flame survival. No flame quenching was observed for $H_2$/air at $Ma_{sr}$ = -2.8 [101], even when $u'$ was increased to 10 m/s, the maximum attainable value with the present fan-stirred vessel.

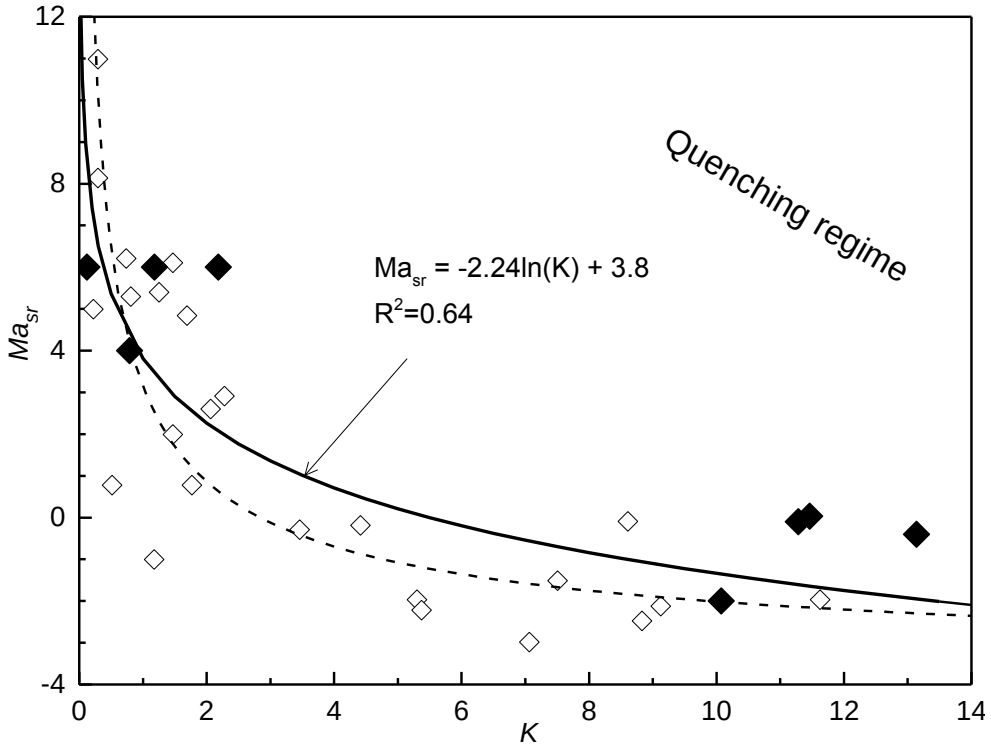


**Figure 5.22** Measured *K* values at $p_{0.8}$ as a function of $Ma_{sr}$. Open symbols from [11], and solid symbols from the present study.

These correlations contribute to the revised form of Fig. 1.6, with the plot of $U$ against $K$ for different $Ma_{sr}$ in Fig. 5.23. Mindful that values of $Ma_{sr}$ are not known with high accuracy, the plots of $U$ against $K$ for different $Ma_{sr}$ were optimised further, making allowance for this.

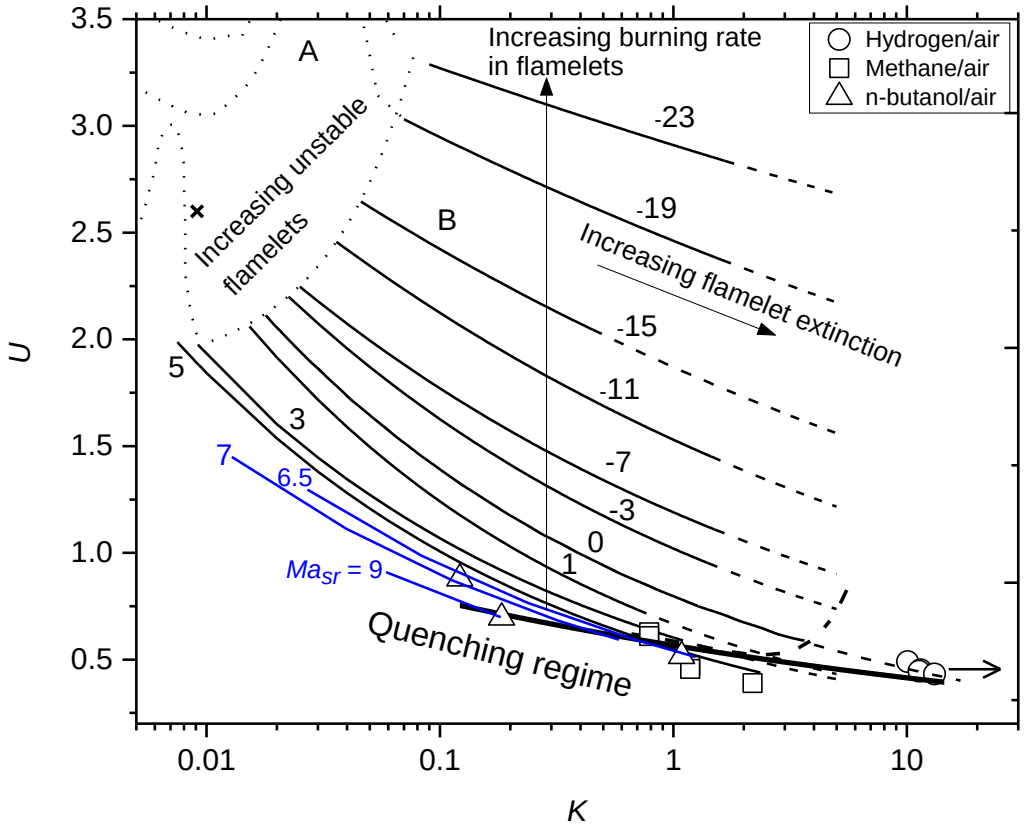


**Figure 5.23** *U/K* diagram of showing regimes of turbulent combustion over a range of $Ma_{sr}$, including the new limits of quenching for $p_{0.8}$. Dashed curve is the limit reported in [74]. Symbols show the current experimental points.

Shown in Fig. 5.23 are the $U$ values plotted against $K$ for different $Ma_{sr}$ indicating different turbulent combustion regimes. These are discussed in detail in [13, 74]. The figure shows work reproduced from [74] including data presented in Section 4.6 and Section 5.4. The general trend is a decrease in $U$ with increasing $K$, while it increases with a decrease in $Ma_{sr}$ for a constant $K$ value. The figure is divided into three regimes namely A, B and C. Regime A is the low $K$ region that features increasingly unstable flamelets, due to the interaction of flame with laminar flame instabilities and the onset of very mild turbulence at values of $u'$. Interestingly, for a rich $n$-butanol/air mixture, $\phi$ =1.2, and at low turbulence of $u'$ = 0.3 m/s, presented in Section 5.4, the obtained $K$ and $U$ was 0.091 and 2.6 respectively, shown as cross in Fig. 5.23, and falls in the unstable regime. This increase in $U$ was due to the laminar flame instabilities, as discussed in Section 5.3.

Regime B consists of stable flames where wrinkling increases turbulent burning velocity, $u_t$. The data presented in Section 4.6 and Section 5.4, extend the $U$ values from $Ma_{sr}$ = 5 to more positive $Ma_{sr}$= 9, shown as blue lines. It is striking to see the relationship of $U$ against $K$ holds true for the extended positive $Ma_{sr}$.

Regime C includes increasing flame extinction and ultimate flame quench at high values of *K*. The quenching limits of Fig. 1.6 extend beyond the previous limit, shown by the dashed curve, and $p_{0.8}$ is expressed by the bold curve in Fig. 5.23 as a new quenching regime boundary that extends through the more positive $Ma_{sr}$ curves presented in Regime B. The onset of flame quenching for these quench flames is defined by $p_{0.8}$. In addition to the influences of the correlations in Fig. 5.22, due regard was paid to the observed sustainability of near-marginal flames, such as those in Fig. 4.51, in constructing the curve for the onset of quenching. This curve is obtained by using a best fit curve through the experimental quench points shown by solid symbols and an empirical correlation is evaluated. Since $U$ is a function of $Ma_{sr}$ and $K$, the best fit curve presented in Fig. 5.22 should also hold good for the quench limit shown by the solid line in Fig. 5.23. The new quench regime covers higher values of $K$ and $Ma_{sr}$.

# Chapter 6

# Conclusions and Recommendations for Future Research

Fundamental studies of laminar and turbulent burning rates of $n$-butanol/ air mixtures at high temperatures are presented for a wide range of pressures and equivalence ratios, $\phi$. The associated instabilities are also explored. Furthermore, the development of 3D swinging sheet technique has been presented, that revealed important information on surface areas of propagating and near quench flames in three dimensions for a variety of fuel/air mixtures characterised in terms of their strain rate Markstein numbers. The following subsections outline the conclusions from the present work.

## 6.1 Laminar burning characteristics

Laminar burning characteristics and the associated instabilities of $n$-butanol air mixtures at 360K for pressures ranging from 0.1 – 1.0 MPa and $\phi$ between 0.7 and 1.4 are studied. The conclusions from this study are summarised:

1. Laminar burning velocities and the associated Markstein lengths, strain rate Markstein numbers, critical Peclet numbers, and the corresponding critical Karlovitz numbers, associated with the onset of instabilities are presented.
2. Laminar burning velocities decreased with increasing pressure. The lowest values of $u_l$ were found for lean mixtures i.e. at $\phi$ = 0.7 and increased with increase in $\phi$. The maximum values of $u_l$ at a given pressure are found to be on the richer side of the mixtures at $\phi$ = 1.1.
3. Burned gas Markstein lengths, $L_b$, decreased with increasing pressure and $\phi$. At 0.5 MPa, $L_b$ reached negative values at rich mixtures resulting in an increase in burning rate with stretch.

1) Strain rate Markstein numbers, $Ma_{sr}$ decreased with increasing pressure and $\phi$, with values eventually becoming negative at high pressures, with rich mixtures.

### 6.1.1 Flame Instabilities

1. Analyses from experimental data, have identified the transition to the low strain rate regime in which laminar flames become unstable. The instabilities result in increasing flame wrinkling and burning velocities. For the present data, a satisfactory correlation exists between $K_{cl}$, and $Ma_{sr}$ and is found to be dependent on initial pressure.
2. The $K_{cl} - Ma_{sr}$ approach demonstrates how small laboratory explosions can be predictors of large atmospheric flame speeds. It has been shown that large hydrogen atmospheric flame speeds deviate from the generalised expressions for hydrocarbons, and why this is so.
3. The predictable atmospheric flame speed accelerations, due to increasing flame wrinkling, yield a rate of change of the heat release rate that creates a calculable overpressure. Such pressure pulses can further accelerate the flame due to the development of Rayleigh-Taylor instabilities.
4. The increasing flame instabilities that occur as the $K_{cl}$ increases with decreasing $Ma_{sr}$ is paralleled by a similar phenomenon in mildly turbulent flames.

## 6.2 Turbulent burning characteristics

Turbulent burning characteristics of $n$-butanol air mixtures at 360K for pressures ranging from 0.1 – 1.0 MPa and $\phi$ between 0.7 and 1.4 are studied. The main conclusions of this study are summarized as follows:

1. Turbulent burning velocities values are enhanced with the increase in both $\phi$, and turbulent velocity, $u'$. However, at the lower $u'$ of 0.5 m/s, $u_t$ was observed to level off beyond $\phi$=1.1.

2. Values of $u_{tm}$, $Ma_{sr}$, and $u_{tr}/u_l$ of $n$-butanol/air mixtures are compared with that of $i$-octane/air and ethanol/air mixtures, under the same conditions. Values of $u_{tm}$ of $n$-butanol/air mixtures are higher than $i$-octane/air mixtures for all $u'$. This is attributed to lower $Ma_{sr}$. These are similar to ethanol/air mixtures at low $u'$, however, slightly lower than ethanol at higher $u'$. Moreover, $n$-butanol/air flames are found to have appreciable burning rates over a range of $\phi$.
3. Experimental values of turbulent mass burning velocity normalized by the effective rms turbulent velocity, $u_{tm}/u'_k$, for $n$-butanol/air mixtures are correlated in terms of Karlovitz stretch factor, $K$ and $Ma_{sr}$. $u_{tm}/u'_k$ decreased with increasing $K$ for a constant $Ma_{sr}$. However, for a given $K$, decrease in $Ma_{sr}$ increased $u_{tm}/u'_k$.
4. The derived experimental values of $u_{tm}/u'_k$ using present schlieren measurements are compared with the values of $u_{tm}/u'_k$obtained from previous correlations and a good agreement was found.
5. The $u_{tm}/u'_k$ curves from previous studies, see Fig. 5.23, are extended to a positive $Ma_{sr}$ of 9.
6. The present results of $u_{tm}/u_l$ demonstrate the well-known bending effect at high *K*, see Figs. 4.27 and 4.32.

## 6.3 3D flame surface area ratios

Measurements of 3D flame surface areas of $CH_4$ and $H_2$ flames are made using swinging laser sheet technique. Time resolved 3D turbulent flame front structures were characterized successfully. High speed Nd:YAG laser; capable of pulsing up to 60 kHz in conjunction with a high speed camera and a rotating mirror; were used. The initial temperatures and pressure varied between 0.1 -0.5 MPa and 300 – 365K respectively. Algorithms were developed to reconstruct the 3D flame surface and determine various flame parameters. The conclusion from 3D flame study are summarised below:

1. The explosion flames were resolved at a reasonable spatial resolution of 0.196 mm over an interrogation volume of ~ 100 x 100 x 102 mm.

Unlike other 3D techniques reported in the literature, the present technique requires one camera and is less expensive.

2. The 3D technique allowed measurements of flame parameters, such as total flame surface area, $A$, mean flame surface areas, $a_m$, $a_v$ for the first time for explosion flames. Mean flame radii based on mass balancing, $r_m$, were found to be lower than the mean radii from volume balancing, $a_v$.
3. The 3D experimental values of $A/a_m$ are comparable with DNS results and motivate further investigation at different experimental conditions.
4. Values of $A/a_m$ obtained using 2D and 3D techniques are found to have discrepancies approximately of an order of 1.
5. Damköhler's hypothesis was re-examined and the enhancement of turbulent burning velocity $u_{tm}/u_l$ is compared with the enhancement in flame surface area ($A/a_m$) both in 2D and 3D for different explosion flames, characterised by their $Ma_{sr}$, as a function of *K*.
6. Measurements obtained using the 3D measurements indicate a shortfall in the 3D surface area enhancement ($A/a_m$) compared to turbulent burning enhancement, while 2D $A/a_m$ measurements, that assume isotropy, appear to account for it.
7. In a collaboration with University of Cambridge, a new diffusivity parameter, $Z$, is proposed to nullify the disparity in the $u_{tm}/u_l$ and 3D $A/a_m$ enhancements while including stretch effects through the burning probability, $P_b^{0.5}$. The parameter $Z$ could be interpreted as turbulent diffusivity enhancement that amplifies the turbulent burning at microscopic length scales. Further research is encouraged to confirm the diffusivity enhancement interpretation.

## 6.4 Quenching of turbulent flames and extension of its limit on *U/K* diagram

Generalised quench data, acquired in the present study covered $n$-butanol, $CH_4$, $H_2$, and other fuels. The conclusions from this study are presented below:

1. Structures of explosion quenching kernels, have been revealed by the swinging laser sheet technique. These supported the use of normalised mean diameters, $d_k/\delta_k$, of these kernels to be correlated with $K$ and $Ma_{sr}$. Such diameters increased with *K*, and decreased with $Ma_{sr.}$, see Fig. 5.23.
2. Analyses of turbulent flame quenching are extended to non-premixed jet flames sustained by the entrainment of air by the fuel jet. Here quenching occurs at high jet velocities and small pipe diameters, $D_b$.
3. There are informative parallels between $d_k/\delta_{k,}$ and $D_b/\delta_k$, the normalised fuel jet pipe diameter with flame extinction, at blow -off. Similar to explosion quench kernels, the quenching normalised diameters, $D_b/\delta_k$, of lifted jet flames, increased with $U^*$, a parameter related to $K$, and decreased with $Ma_{sr}$, see Fig. 5.23. The similar trends in the two sets of values of normalised diameters reflect the similarities of flamelet combustion in both premixed and jet flames.
4. The results also show that ever-larger explosions and burners are required to sustain flames at increasing Karlovitz stretch factors, $K$, and flow numbers, $U^*$. Conversely, to extend quenching in explosion flames requires smaller flame kernels, and, to extend quench in flame traps, comprised of small diameter quenching tubes, quenching, requires ever-smaller tubes.
5. For hydrogen, values of $d_k/\delta_{k,}$ and $D_b/\delta_k$, are possible over greater ranges of conditions than for other fuels indicating the resistance of $H_2$ flames to quench, even with high turbulence.
6. Experimental data, for quenching flames, have extended the boundary of the existing quench limit on the *U/K* diagram to higher values of both $K$ and $Ma_{sr}$. This is particularly marked above $K$ =1 where there is a marked reduction in the quench regime, C. However, the new data extend only to $Ma_{sr}$ = -3, due to the difficulty of quenching those mixtures with more negative values of $Ma_{sr}$, usually associated with the higher pressures and temperatures.

## 6.5 Recommendations for Future Research

1. Based on the obtained swinging laser sheet data, it is encouraged to determine other flame parameters like the flame surface density, $\sum$, and flame curvatures. Curvature measurements of the present 3D data could verify the findings in [93] regarding the formation of negative curvatures and destruction of surface areas at high $K$.
2. Limited by the camera resolution at high framing rates, the uncertainty in evaluating the flame surface area at Kolmogorov length scales i.e. less than 0.19 mm could not be reported. Concerning this, simultaneous Mie-scatter and PLIF can help determine the reaction zone front and appropriate iso-surface to verify the flame edge detection. This will enable to identify any surface area left unaccounted at small length scales.
3. Only mixtures having a low $u_l$ value and at low $u'$ could be investigated. Using higher frequency laser and camera, can help capture flames with faster burning rates and also at high $u'$.
4. Further research is encouraged to acquire more experimental data to verify the interpretation of diffusivity enhancement at high $K$ and negative $Ma_{sr}$ conditions. Furthermore, experiments are required to understand the role of instabilities at low turbulence, particularly, in the regime $K$<0.05 and negative $Ma_{sr}$. Moreover, the possibility of using fractal theory to explain the discrepancy between turbulent burning and flame surface area enhancements at high $K$ values also needs to be checked.
5. It was difficult to capture fully quenched flames as they tend to convect away from the volume of interest and become wispy, thereby increasing the uncertainty in their edge detection. Possibly higher framing rates and high melting point seed particles could aid the analysis of these quenched flames and understand its topology more accurately.

6. It is encouraged to acquire more experimental data for quenching kernels, in particular, for negative $Ma_{sr}$ mixtures to confirm the relationship between kernel quenching sizes and stretch rates.
7. It is also encouraged to conduct chemical kinetics simulations to understand the underlying effects of reaction rates, contributing to predicted differences in $u_l$ values of $n$-butanol at high pressures.

## 6.6 Summary of Conclusions

Laminar and turbulent burning characteristics of $n$-butanol/air explosion flames were studied using schlieren photography technique. The instabilities associated with laminar explosions and their significance on burning velocities at low turbulence are explored. Flames are characterised based on strain rate Markstein numbers, $Ma_{sr}$, and correlations are presented in terms of *U-K* relationships. Furthermore, a novel 3D swinging laser imaging technique was employed to visualize premixed explosion flames at low turbulence. Time resolved 3D turbulent flame structures were characterized successfully using this technique. It allowed the direct measurements of 3D flame surface areas without the assumption of isotropy. This gave useful insights in to the flame surface area enhancement of a variety of fuel air mixtures corresponding to different $Ma_{sr}$. For positive $Ma_{sr}$, the enhancement in flame area accounted for the turbulent burning enhancement while for negative $Ma_{sr}$ mixtures it fell short by a factor of 6. Finally, four major aspects of quench flames are covered: *(i)* Use of a swinging laser sheet to ascertain kernel shape and whether a mean quenching diameter is a valid parameter, *(ii)* Measurement and correlation of normalised kernel quenching diameters, *(iii)* Development of a unified approach to both premixed and non-premixed jet extinctions. (*iv*) Extension of quenching limit on the *U/K* diagram.

# References


1. Veloo, P.S. and F.N. Egolfopoulos, *Flame propagation of butanol isomers/air mixtures.* Proceedings of the Combustion Institute, 2011. **33**(1): p. 987-993.
2. Aleiferis, P., J. Serras-Pereira, and D. Richardson, *Characterisation of flame development with ethanol, butanol, iso-octane, gasoline and methane in a direct-injection spark-ignition engine.* Fuel, 2013. **109**: p. 256-278.
3. Global, S., *Net Carbon footprint.* 2019.
4. Outlook, B.E., *2019 edition.* London, United Kingdom2019.
5. Sarathy, S., M. Thomson, C. Togbé, P. Dagaut, F. Halter, and C. Mounaim-Rousselle, *An experimental and kinetic modeling study of n-butanol combustion.* Combustion and Flame, 2009. **156**(4): p. 852-864.
6. Yacoub, Y., R. Bata, and M. Gautam, *The performance and emission characteristics of C1-C5 alcohol-gasoline blends with matched oxygen content in a single-cylinder spark ignition engine.* Proceedings of the Institution of Mechanical Engineers, Part A: Journal of Power and Energy, 1998. **212**(5): p. 363-379.
7. Chen, Z., Z. Wu, J. Liu, and C. Lee, *Combustion and emissions characteristics of high n-butanol/diesel ratio blend in a heavy-duty diesel engine and EGR impact.* Energy Conversion and Management, 2014. **78**: p. 787-795.
8. Peters, N., *Turbulent combustion*. 2000: Cambridge university press.
9. Glassman, I., R.A. Yetter, and N.G. Glumac, *Combustion*. 2014: Academic press.
10. Bradley, D., M. Lawes, and M.S. Mansour, *Correlation of turbulent burning velocities of ethanol–air, measured in a fan-stirred bomb up to 1.2 MPa.* Combustion and Flame, 2011. **158**(1): p. 123-138.
11. Lipatnikov, A.N. and J. Chomiak, *Turbulent flame speed and thickness: phenomenology, evaluation, and application in multi-dimensional simulations.* Progress in Energy and Combustion Science, 2002. **28**(1): p. 1-74.
12. Harker, M., T. Hattrell, M. Lawes, C. Sheppard, N. Tripathi, and R. Woolley, *Measurements of the three-dimensional structure of flames at low turbulence.* Combustion Science and Technology, 2012. **184**(10-11): p. 1818-1837.
13. Bagdanavicius, A., P.J. Bowen, D. Bradley, M. Lawes, and M.S. Mansour, *Stretch rate effects and flame surface densities in premixed turbulent combustion up to 1.25 MPa.* Combustion and Flame, 2015. **162**(11): p. 4158-4166.
14. Kohse-Höinghaus, K., R.S. Barlow, M. Aldén, and J. Wolfrum, *Combustion at the focus: laser diagnostics and control.* Proceedings of the Combustion Institute, 2005. **30**(1): p. 89-123.

15. Nwagwe, I.K., H.G. Weller, G.R. Tabor, A.D. Gosman, M. Lawes, C.G.W. Sheppard, and R. Wooley, *Measurements and large eddy simulations of turbulent premixed flame kernel growth.* Proceedings of the Combustion Institute, 2000. **28**(1): p. 59-65.
16. Ma, L., Y. Wu, Q. Lei, W. Xu, and C.D. Carter, *3D flame topography and curvature measurements at 5 kHz on a premixed turbulent Bunsen flame.* Combustion and Flame, 2016. **166**: p. 66-75.
17. Lozano, A., B. Yip, and R. Hanson, *Acetone: a tracer for concentration measurements in gaseous flows by planar laser-induced fluorescence.* Experiments in fluids, 1992. **13**(6): p. 369-376.
18. Bradley, D., M. Lawes, and M. Morsy, *Flame speed and particle image velocimetry measurements of laminar burning velocities and Markstein numbers of some hydrocarbons.* Fuel, 2019. **243**: p. 423-432.
19. Bradley, D. *How fast can we burn?* in *Symposium (International) on Combustion*. 1992. Elsevier.
20. van Lipzig, J.P.J., E.J.K. Nilsson, L.P.H. de Goey, and A.A. Konnov, *Laminar burning velocities of n-heptane, iso-octane, ethanol and their binary and tertiary mixtures.* Fuel, 2011. **90**(8): p. 2773-2781.
21. Bradley, D., P. Gaskell, and X. Gu, *Burning velocities, Markstein lengths, and flame quenching for spherical methane-air flames: a computational study.* Combustion and Flame, 1996. **104**(1): p. 176-198.
22. Griffiths, J.F. and J.A. Barnard, *Flame and combustion*. 1995: CRC Press.
23. Gu, X.J., M.Z. Haq, M. Lawes, and R. Woolley, *Laminar burning velocity and Markstein lengths of methane–air mixtures.* Combustion and Flame, 2000. **121**(1–2): p. 41-58.
24. Bradley, D., R.A. Hicks, M. Lawes, C.G.W. Sheppard, and R. Woolley, *The Measurement of Laminar Burning Velocities and Markstein Numbers for Iso-octane–Air and Iso-octane–n-Heptane–Air Mixtures at Elevated Temperatures and Pressures in an Explosion Bomb.* Combustion and Flame, 1998. **115**(1–2): p. 126-144.
25. Karlovitz, B., D. Denniston Jr, D. Knapschaefer, and F. Wells. *Studies on Turbulent flames: A. Flame Propagation Across velocity gradients B. turbulence Measurement in flames*. in *Symposium (international) on combustion*. 1953. Elsevier.
26. Williams, F., *Combustion Theory 2nd Edition,(1985)*. The Benjamin/Cummings Publishing Company, Inc.
27. Markstein, G.H., *Experimental and theoretical studies of flame-front stability.* Journal of the Aeronautical Sciences, 1951. **18**(3): p. 199-209.
28. Clavin, P., *Dynamic behavior of premixed flame fronts in laminar and turbulent flows.* Progress in Energy and Combustion Science, 1985. **11**(1): p. 1-59.
29. Dowdy, D.R., D.B. Smith, S.C. Taylor, and A. Williams. *The use of expanding spherical flames to determine burning velocities and stretch effects in hydrogen/air mixtures*. in *Symposium (International) on Combustion*. 1991. Elsevier.
30. Steinberg, A.M. and J.F. Driscoll, *Straining and wrinkling processes during turbulence–premixed flame interaction measured using*

*temporally-resolved diagnostics.* Combustion and Flame, 2009. **156**(12): p. 2285-2306.
31. Bradley, D., P. Gaskell, A. Sedaghat, and X. Gu, *Generation of PDFS for flame curvature and for flame stretch rate in premixed turbulent combustion.* Combustion and flame, 2003. **135**(4): p. 503-523.
32. Bonhomme, A., L. Selle, and T. Poinsot, *Curvature and confinement effects for flame speed measurements in laminar spherical and cylindrical flames.* Combustion and Flame, 2013. **160**(7): p. 1208-1214.
33. P. Clavin, F.A.W., *Effects of molecular diffusion and of thermal expansion on the structure and dynamics of premixed flames in turbulent flows of large scale and low intensity.* J. Fluid Mech., 1982. **116**: p. 251-282.
34. Chung K. Law, P.C., M. Mizomoto, H. Yoshida, *Flame curvature and preferential diffusion in the burning intensity of bunsen flames.* Symp. (Int.) Combust., 1986. **21**: p. 1803-1809.
35. Ciccarelli, G. and S. Dorofeev, *Flame acceleration and transition to detonation in ducts.* Prog. Energy Combust. Sci., 2008. **34**(4): p. 499-550.
36. Matalon, M. and B. Matkowsky, *Flames as gasdynamic discontinuities.* J. Fluid Mech., 1982. **124**: p. 239-259.
37. Poinsot, T. and D. Veynante, *Theoretical and numerical combustion*. 2005: RT Edwards, Inc.
38. Abdel-Gayed, R., D. Bradley, and F.-K. Lung, *Combustion regimes and the straining of turbulent premixed flames.* Combust. Flame, 1989. **76**(2): p. 213-218.
39. Griffiths, J. and J. Barnard, *Flame and Combustion, ed.* BA Professional, 1995. **3**.
40. Turns, S.R., *An introduction to combustion: Concepts and Applications*. Vol. 287. 1996: McGraw-hill New York.
41. Göttgens, J., F. Mauss, and N. Peters, *Analytic approximations of burning velocities and flame thicknesses of lean hydrogen, methane, ethylene, ethane, acetylene, and propane flames.* Symp. (Int.) Combust., 1992. **24**(1): p. 129-135.
42. Bechtold, J. and M. Matalon, *Hydrodynamic and diffusion effects on the stability of spherically expanding flames.* Combustion and Flame, 1987. **67**(1): p. 77-90.
43. Darrieus, G., *Propagation d'un front de flamme: assai de theorie des vitesses anomales de deflagration par developpement spontane de la turbulence.* 6th Int. Cong. Appl. Mech., Paris., 1938.
44. Landau, L., *On the theory of slow combustion.* Acta Physicochim (USSR), 1944. **19**: p. 77-85.
45. Searby, G., *Experimental studies of instabilities of laminar premixed flames.* arXiv preprint physics/0606258, 2006.
46. Bradley, D., A. Dowling, and A. Morgans, *Combustion Instabilities*, in *Turbulent Premixed Flames*. 2011, Cambridge University Press UK. p. 151-243.
47. Gostintsev, Y.A., A.G. Istratov, and Y.V. Shulenin, *Self-similar propagation of a free turbulent flame in mixed gas mixtures.* Combustion, Explosion and Shock Waves, 1988. **24**(5): p. 563-569.

48. Bradley, D., *Instabilities and flame speeds in large-scale premixed gaseous explosions.* Philosophical Transactions of the Royal Society of London. Series A: Mathematical, Physical and Engineering Sciences, 1999. **357**(1764): p. 3567-3581.
49. Bradley, D. and C. Harper, *The development of instabilities in laminar explosion flames.* Combustion and Flame, 1994. **99**(3-4): p. 562-572.
50. Bradley, D., C. Sheppart, R. Woolley, D. Greenhalgh, and R. Lockett, *The development and structure of flame instabilities and cellularity at low Markstein numbers in explosions.* Combustion and Flame, 2000. **122**(1): p. 195-209.
51. Bradley, D., T. Cresswell, and J. Puttock, *Flame acceleration due to flame-induced instabilities in large-scale explosions.* Combustion and Flame, 2001. **124**(4): p. 551-559.
52. Bauwens, C., J. Bergthorson, and S. Dorofeev, *Critical peclet numbers for the onset of darrieus-landau instability in atmospheric-pressure methane-air flames.* Proceedings of the 25th ICDERS, Leeds, UK (August 2-7, 2015), 2015.
53. Bauwens, C.R., J.M. Bergthorson, and S.B. Dorofeev, *Experimental study of spherical-flame acceleration mechanisms in large-scale propane–air flames.* Proceedings of the Combustion Institute, 2015. **35**(2): p. 2059-2066.
54. Kagan, L. and G. Sivashinsky, *Parametric transition from deflagration to detonation: Runaway of fast flames.* Proceedings of the Combustion Institute, 2017. **36**(2): p. 2709-2715.
55. Kagan, L. and G. Sivashinsky, *Transition to detonation of an expanding spherical flame.* Combustion and Flame, 2017. **175**: p. 307-311.
56. Bradley, D., M. Lawes, and M. Mansour, *Explosion bomb measurements of ethanol–air laminar gaseous flame characteristics at pressures up to 1.4 MPa.* Combustion and Flame, 2009. **156**(7): p. 1462-1470.
57. Morley, C., "Gaseq: a chemical equilibrium program for Windows." http:// www. gaseq. co. uk. (2005).
58. Mallard, E. and H. Le Chatelier, *Combustion of explosive gas mixtures.* Ann. mines, 1883. **8**: p. 274.
59. Damköhler, G., *Der einfluss der turbulenz auf die flammengeschwindigkeit in gasgemischen.* Zeitschrift für Elektrochemie und angewandte physikalische Chemie, 1940. **46**(11): p. 601-626 (Translation: NACA (1947) 1112).
60. Peters, N., *The turbulent burning velocity for large-scale and small-scale turbulence.* Journal of Fluid mechanics, 1999. **384**: p. 107-132.
61. Driscoll, J.F., *Turbulent premixed combustion: Flamelet structure and its effect on turbulent burning velocities.* Progress in Energy and Combustion Science, 2008. **34**(1): p. 91-134.
62. Bradley, D., A. Lau, and M. Lawes, *Flame stretch rate as a determinant of turbulent burning velocity.* Philosophical Transactions of the Royal Society of London A: Mathematical, Physical and Engineering Sciences, 1992. **338**(1650): p. 359-387.

63. Kobayashi, H., Y. Kawabata, and K. Maruta. *Experimental study on general correlation of turbulent burning velocity at high pressure*. in *Symposium (International) on Combustion*. 1998. Elsevier.
64. Bradley, D., M. Haq, R. Hicks, T. Kitagawa, M. Lawes, C. Sheppard, and R. Woolley, *Turbulent burning velocity, burned gas distribution, and associated flame surface definition.* Combustion and Flame, 2003. **133**(4): p. 415-430.
65. Yuen, F.T. and Ö.L. Gülder, *Turbulent premixed flame front dynamics and implications for limits of flamelet hypothesis.* Proceedings of the Combustion Institute, 2013. **34**(1): p. 1393-1400.
66. Bray, K., *The challenge of turbulent combustion.* Symp. (Int.) Combust., 1996. **26**(1): p. 1-26.
67. Abdel-Gayed, R., D. Bradley, and M. Lawes, *Turbulent burning velocities: a general correlation in terms of straining rates.* Proc. R. Soc. Lond. A, 1987. **414**(1847): p. 389-413.
68. Lawes, M., M.P. Ormsby, C.G.W. Sheppard, and R. Woolley, *The turbulent burning velocity of iso-octane/air mixtures.* Combustion and Flame, 2012. **159**(5): p. 1949-1959.
69. Kolmogorov, A.N., *The local structure of turbulence in incompressible viscous fluid for very large Reynolds numbers.* Proceedings of the Royal Society of London. Series A: Mathematical and Physical Sciences, 1991. **434**(1890): p. 9-13.
70. McComb, W., *The Physics of Fluid Turbulence Oxford University Press*. 1990, Oxford.
71. Taylor, G.I., *Statistical theory of turbulence. IV. Diffusion in a turbulent air stream.* Proc. R. Soc. Lond. A, 1935.
72. Bradley, D., P. Gaskell, X. Gu, and A. Sedaghat, *Premixed flamelet modelling: Factors influencing the turbulent heat release rate source term and the turbulent burning velocity.* Combustion and flame, 2005. **143**(3): p. 227-245.
73. Bradley, D., M. Lawes, and M. Mansour, *Flame surface densities during spherical turbulent flame explosions.* Proceedings of the Combustion Institute, 2009. **32**(1): p. 1587-1593.
74. Bradley, D., M. Lawes, K. Liu, and M.S. Mansour, *Measurements and correlations of turbulent burning velocities over wide ranges of fuels and elevated pressures.* Proceedings of the Combustion Institute, 2013. **34**(1): p. 1519-1526.
75. Borghi, R., *On the structure and morphology of turbulent premixed flames*, in *Recent advances in the Aerospace Sciences*. 1985, Springer. p. 117-138.
76. Poinsot, T., D. Veynante, and S. Candel, *Quenching processes and premixed turbulent combustion diagrams.* Journal of Fluid Mechanics, 1991. **228**: p. 561-606.
77. Mansour, M.S., *Fundamental study of premixed combustion rates at elevated pressure and temperature*. 2010, University of Leeds.
78. Bradley, D., *Problems of predicting turbulent burning rates.* Combustion Theory and Modelling, 2002. **6**(2): p. 361-382.

79. Gillespie, L., M. Lawes, C. Sheppard, and R. Woolley, *Aspects of laminar and turbulent burning velocity relevant to SI engines.* SAE transactions, 2000: p. 13-33.
80. Filatyev, S.A., J.F. Driscoll, C.D. Carter, and J.M. Donbar, *Measured properties of turbulent premixed flames for model assessment, including burning velocities, stretch rates, and surface densities.* Combustion and Flame, 2005. **141**(1-2): p. 1-21.
81. Lawn, C. and R. Schefer, *Scaling of premixed turbulent flames in the corrugated regime.* Combustion and flame, 2006. **146**(1-2): p. 180-199.
82. Kobayashi, H., *Experimental study of high-pressure turbulent premixed flames.* Experimental thermal and fluid science, 2002. **26**(2-4): p. 375-387.
83. Bray, K.N.C. and R. Cant, *Some applications of Kolmogorov's turbulence research in the field of combustion.* Proceedings of the Royal Society of London. Series A: Mathematical and Physical Sciences, 1991. **434**(1890): p. 217-240.
84. Bray, K.N.C., *Studies of the turbulent burning velocity.* Proceedings of the Royal Society of London. Series A: Mathematical and Physical Sciences, 1990. **431**(1882): p. 315-335.
85. Abdel-Gayed, R., K. Al-Khishali, and D. Bradley, *Turbulent burning velocities and flame straining in explosions.* Proc. R. Soc. Lond. A, 1984. **391**(1801): p. 393-414.
86. Lewis, B. and G. Von Elbe, *Combustion, flames and explosions of gases*. 2012: Elsevier.
87. Bradley, D. and A. Mitcheson, *Mathematical solutions for explosions in spherical vessels.* Combustion and Flame, 1976. **26**: p. 201-217.
88. Clavin, P. and F. Williams, *Theory of premixed-flame propagation in large-scale turbulence.* Journal of fluid mechanics, 1979. **90**(3): p. 589-604.
89. Abdel-Gayed, R.G. and D. Bradley, *A two-eddy theory of premixed turbulent flame propagation.* Philosophical transactions of the royal society of London. Series A, Mathematical and physical sciences, 1981. **301**(1457): p. 1-25.
90. Gülder, Ö.L. *Turbulent premixed flame propagation models for different combustion regimes*. in *Symposium (International) on Combustion*. 1991. Elsevier.
91. Zimont, V.L., *Gas premixed combustion at high turbulence. Turbulent flame closure combustion model.* Experimental Thermal and Fluid Science, 2000. **21**(1): p. 179-186.
92. Bradley, D., M. Lawes, and M. Mansour, *Measurement of turbulent burning velocities in implosions at high pressures.* Proceedings of the Combustion Institute, 2011. **33**(1): p. 1269-1275.
93. Nivarti, G. and S. Cant, *Direct Numerical Simulation of the bending effect in turbulent premixed flames.* Proceedings of the Combustion Institute, 2017. **36**(2): p. 1903-1910.
94. Nivarti, G.V. and R.S. Cant, *Scalar transport and the validity of Damköhler's hypotheses for flame propagation in intense turbulence.* Physics of Fluids, 2017. **29**(8): p. 085107.

95. Bagdanavicius, A., P. Bowen, N. Syred, P. Kay, A. Crayford, G. Sims, and J. Wood, *Burning velocities of alternative gaseous fuels at elevated temperature and pressure.* AIAA journal, 2010. **48**(2): p. 317-329.
96. Law, C., D. Zhu, and G. Yu, *Propagation and extinction of stretched premixed flames.* Symp. (Int.) Combust., 1988. **21**(1): p. 1419-1426.
97. Yang, S. and S. Shy, *Global quenching of premixed $CH_4$/air flames: Effects of turbulent straining, equivalence ratio, and radiative heat loss.* Proc. Combust. Inst., 2002. **29**(2): p. 1841-1847.
98. Ji, C., E. Dames, Y.L. Wang, H. Wang, and F.N. Egolfopoulos, *Propagation and extinction of premixed $C_5$–$C_{12}$ n-alkane flames.* Combust. Flame, 2010. **157**(2): p. 277-287.
99. Chomiak, J. and J. Jarosiński, *Flame quenching by turbulence.* Combust. Flame, 1982. **48**: p. 241-249.
100. Thibault, P., Y. Liu, C. Chan, J. Lee, R. Knystautas, C. Gurap, B. Hjertager, and K. Fuhre, *Transmission of an explosion through an orifice.* NASA STI/Recon Technical Report N, 1982. **83**.
101. Bradley, D., M. Lawes, K. Liu, and R. Woolley, *The quenching of premixed turbulent flames of iso-octane, methane and hydrogen at high pressures.* Proc. Combust. Inst., 2007. **31**(1): p. 1393-1400.
102. Al-Khishali, K., D. Bradley, and S. Hall, *Turbulent combustion of near-limit hydrogen-air mixtures.* Combust. Flame, 1983. **54**(1-3): p. 61-70.
103. Abdel-Gayed, R.G., D. Bradley, and A.K.C. Lau, *The straining of premixed turbulent flames.* Symposium (International) on Combustion, 1989. **22**(1): p. 731-738.
104. Law, C., D. Zhu, and G. Yu. *Propagation and extinction of stretched premixed flames*. in *Symposium (International) on Combustion*. 1988. Elsevier.
105. Stahl, G.R., B. & Warnatz, J., *Dynamics of reactive systems. Part 1.* Flames. Prog. Astronaut. Aeronaut, 1988. **113**(195).
106. Klimov, A., *Zhournal Prikladnoi Mekchaniki i Tekhnicheskoi Fiziki 3* 1963: p. 49.
107. Williams, F., *A review of some theoretical considerations of turbulent flame structure.* AGARD Conference, 164, 1975.
108. Kuznetsov, V., *Limiting laws of propagation of a turbulent flame.* Combust. Explos. Shock Waves, 1982. **18**(2): p. 172-179.
109. Abdel-Gayed, R.G., D. Bradley, M.N. Hamid, and M. Lawes, *Lewis number effects on turbulent burning velocity.* Symposium (International) on Combustion, 1985. **20**(1): p. 505-512.
110. Gu, X., Z. Huang, Q. Li, and C. Tang, *Measurements of laminar burning velocities and Markstein lengths of n-butanol− air premixed mixtures at elevated temperatures and pressures.* Energy & Fuels, 2009. **23**(10): p. 4900-4907.
111. Gu, X., Z. Huang, S. Wu, and Q. Li, *Laminar burning velocities and flame instabilities of butanol isomers–air mixtures.* Combustion and Flame, 2010. **157**(12): p. 2318-2325.
112. Zhang, Z., S. Zhu, J. Liang, L. Tian, and G. Li, *Experimental and kinetic studies of premixed laminar flame of acetone-butanol-ethanol (ABE)/air.* Fuel, 2018. **211**: p. 95-101.

113. Wang, G., Y. Li, W. Yuan, Y. Wang, Z. Zhou, Y. Liu, and J. Cai, *Investigation on laminar flame propagation of n-butanol/air and n-butanol/O 2/He mixtures at pressures up to 20 atm.* Combustion and Flame, 2018. **191**: p. 368-380.
114. Broustail, G., P. Seers, F. Halter, G. Moréac, and C. Mounaïm-Rousselle, *Experimental determination of laminar burning velocity for butanol and ethanol iso-octane blends.* Fuel, 2011. **90**(1): p. 1-6.
115. Broustail, G., F. Halter, P. Seers, G. Moréac, and C. Mounaïm-Rousselle, *Experimental determination of laminar burning velocity for butanol/iso-octane and ethanol/iso-octane blends for different initial pressures.* Fuel, 2013. **106**: p. 310-317.
116. Zhang, X., C. Tang, H. Yu, Q. Li, J. Gong, and Z. Huang, *Laminar flame characteristics of iso-octane/n-butanol blend–air mixtures at elevated temperatures.* Energy & Fuels, 2013. **27**(4): p. 2327-2335.
117. Beeckmann, J., L. Cai, and H. Pitsch, *Experimental investigation of the laminar burning velocities of methanol, ethanol, n-propanol, and n-butanol at high pressure.* Fuel, 2014. **117**: p. 340-350.
118. Beeckmann, J., O. Röhl, and N. Peters, *Numerical and experimental investigation of laminar burning velocities of iso-octane, ethanol and n-butanol*. 2009, SAE Technical Paper.
119. Alasfour, F., *Butanol—a single-cylinder engine study: availability analysis.* Applied Thermal Engineering, 1997. **17**(6): p. 537-549.
120. Szwaja, S. and J. Naber, *Combustion of n-butanol in a spark-ignition IC engine.* Fuel, 2010. **89**(7): p. 1573-1582.
121. Serras-Pereira, J., P. Aleiferis, and D. Richardson, *An analysis of the combustion behavior of ethanol, butanol, iso-octane, gasoline, and methane in a direct-injection spark-ignition research engine.* Combustion Science and Technology, 2013. **185**(3): p. 484-513.
122. Yao, M., H. Wang, Z. Zheng, and Y. Yue, *Experimental study of n-butanol additive and multi-injection on HD diesel engine performance and emissions.* Fuel, 2010. **89**(9): p. 2191-2201.
123. Lawes, M., M. Ormsby, C. Sheppard, and R. Woolley, *Variation of turbulent burning rate of methane, methanol, and iso-octane air mixtures with equivalence ratio at elevated pressure.* Combust. Sci. and Tech., 2005. **177**(7): p. 1273-1289.
124. Hult, J., S. Gashi, N. Chakraborty, M. Klein, K.W. Jenkins, S. Cant, and C.F. Kaminski, *Measurement of flame surface density for turbulent premixed flames using PLIF and DNS.* Proceedings of the Combustion Institute, 2007. **31**(1): p. 1319-1326.
125. Bray, K., P. Domingo, and L. Vervisch, *Role of the progress variable in models for partially premixed turbulent combustion.* Combustion and Flame, 2005. **141**(4): p. 431-437.
126. Haq, M., C. Sheppard, R. Woolley, D. Greenhalgh, and R. Lockett, *Wrinkling and curvature of laminar and turbulent premixed flames.* Combustion and Flame, 2002. **131**(1): p. 1-15.
127. Bray, K.N.C., and Peters, N. 1994., *Laminar flamelets in turbulent flames. In Libby, P.A. and Williams, F.A. (Eds.).* Turbulent reacting flows, Academic Press, London, 1994: p. 63–114.

128. Yip, B., J.K. Lam, M. Winter, and M.B. Long, *Time-resolved three-dimensional concentration measurements in a gas jet.* Science, 1987. **235**(4793): p. 1209-1211.
129. Lawes, M., Sheppard, C. G. W., and Woolley, R. *Three dimensional mapping of turbulent flame fronts*. in *Ninth Int. Symp. on Applications of Laser Techniques to Fluid Mechanics, Lisbon, Portugal, July 13-16, vol. 2, 35.2.1.* 1998.
130. Nygren, J., J. Hult, M. Richter, M. Aldén, M. Christensen, A. Hultqvist, and B. Johansson, *Three-dimensional laser induced fluorescence of fuel distributions in an HCCI engine.* Proceedings of the Combustion Institute, 2002. **29**(1): p. 679-685.
131. Hult, J., A. Omrane, J. Nygren, C. Kaminski, B. Axelsson, R. Collin, P.-E. Bengtsson, and M. Aldén, *Quantitative three-dimensional imaging of soot volume fraction in turbulent non-premixed flames.* Experiments in Fluids, 2002. **33**(2): p. 265-269.
132. Mantzaras, J., P.G. Felton, and F.V. Bracco, *Three-dimensional visualization of premixed-charge engine flames: islands of reactants and products; fractal dimensions; and homogeneity*. 1988, SAE Technical Paper.
133. Upton, T., D. Verhoeven, and D. Hudgins, *High-resolution computed tomography of a turbulent reacting flow.* Experiments in Fluids, 2011. **50**(1): p. 125-134.
134. Harker, M., M. Lawes, C. Sheppard, N. Tripathi, and R. Woolley, *Measurements of the Three Dimensional Structure of Flames at Low Turbulence.* Proceedings of the 23th International Colloquium on the Dynamics of Explosion and Reactive Systems, 2011.
135. Ng, W.B. and Y. Zhang, *Stereoscopic imaging and reconstruction of the 3D geometry of flame surfaces.* Experiments in Fluids, 2003. **34**(4): p. 484-493.
136. Bheemul, H.C., G. Lu, and Y. Yan, *Digital imaging-based three-dimensional characterization of flame front structures in a turbulent flame.* IEEE transactions on instrumentation and measurement, 2005. **54**(3): p. 1073-1078.
137. Steinberg, A.M., J.F. Driscoll, and S.L. Ceccio, *Measurements of turbulent premixed flame dynamics using cinema stereoscopic PIV.* Experiments in Fluids, 2008. **44**(6): p. 985-999.
138. Tanahashi, M., S. Inoue, M. Shimura, S. Taka, G.-M. Choi, and T. Miyauchi, *Reconstructed 3D flame structures in noise-controlled swirl-stabilized combustor.* Experiments in Fluids, 2008. **45**(3): p. 447-460.
139. Kang, M., X. Li, and L. Ma, *Three-dimensional flame measurements using fiber-based endoscopes.* Proceedings of the Combustion Institute, 2015. **35**(3): p. 3821-3828.
140. Ma, L., Q. Lei, T. Capil, S.D. Hammack, and C.D. Carter, *Direct comparison of two-dimensional and three-dimensional laser-induced fluorescence measurements on highly turbulent flames.* Optics letters, 2017. **42**(2): p. 267-270.
141. Ma, L., Q. Lei, J. Ikeda, W. Xu, Y. Wu, and C.D. Carter, *Single-shot 3D flame diagnostic based on volumetric laser induced fluorescence*

*(VLIF).* Proceedings of the Combustion Institute, 2017. **36**(3): p. 4575-4583.
142. Wellander, R., M. Richter, and M. Aldén, *Time resolved, 3D imaging (4D) of two phase flow at a repetition rate of 1 kHz.* Optics express, 2011. **19**(22): p. 21508-21514.
143. Wellander, R., M. Richter, and M. Aldén, *Time-resolved (kHz) 3D imaging of OH PLIF in a flame.* Experiments in fluids, 2014. **55**(6): p. 1764.
144. Kristensson, E., E. Berrocal, R. Wellander, M. Ritcher, M. Aldén, and M. Linne, *Structured illumination for 3-D Mie imaging and 2-D attenuation measurements in optically dense sprays.* Proceedings of the Combustion Institute, 2011. **33**(1): p. 855-861.
145. Dave, H.L., A. Mohan, and S. Chaudhuri, *Genesis and evolution of premixed flames in turbulence.* Combustion and Flame, 2018. **196**: p. 386-399.
146. Mason, P., C. Fleischmann, C. Rogers, A. McKinnon, K. Unsworth, and M. Spearpoint, *Estimating thermal radiation fields from 3D flame reconstruction.* Fire technology, 2009. **45**(1): p. 1-22.
147. Meyer, T.R., B.R. Halls, N. Jiang, M.N. Slipchenko, S. Roy, and J.R. Gord, *High-speed, three-dimensional tomographic laser-induced incandescence imaging of soot volume fraction in turbulent flames.* Optics express, 2016. **24**(26): p. 29547-29555.
148. Ma, L., Q. Lei, Y. Wu, T.M. Ombrello, and C.D. Carter, *3D measurements of ignition processes at 20 kHz in a supersonic combustor.* Applied Physics B, 2015. **119**(2): p. 313-318.
149. Shehata, M.M.A.O., *New Fuels, Flame Quenching and DDT*. 2019, University of Leeds.
150. Tripathi, N., *Dynamics of confined premixed laminar explosion flames*. 2012, University of Leeds.
151. Bradley, D., P. Gaskell, X. Gu, M. Lawes, and M. Scott, *Premixed turbulent flame instability and NO formation in a lean-burn swirl burner.* Combustion and Flame, 1998. **115**(4): p. 515-538.
152. Mumby, R.D., *Experimental Characterisation of Fuel Blends, PhD Thesis, Department of Mechanical Engineering, University of Leeds, Leeds U.K.* 2016.
153. Kondo, T., S. Iio, and M. Hiruma, *A study on the mechanism of backfire in external mixture formation hydrogen engines-about backfire occurred by cause of the spark plug.* SAE transactions, 1997: p. 1953-1960.
154. Bradley, D., C. Sheppard, I. Suardjaja, and R. Woolley, *Fundamentals of high-energy spark ignition with lasers.* Combustion and Flame, 2004. **138**(1): p. 55-77.
155. Thorne, B.J.A., *Development of a 3D Laser Imaging System and its Application in Studies of Turbulent Flame Structure*. 2017, University of Leeds.
156. Melling, A., *Tracer particles and seeding for particle image velocimetry.* Measurement Science and Technology, 1997. **8**(12): p. 1406.
157. Harker, M.R., *Experimental Study of Turbulent Flame Structure*. 2009, University of Leeds.

158. Kylafis, G.F., *The explosion and dispersion potential of engineered nanoparticles*. 2016, University of Leeds.
159. Sharpe, G., (2011), Private Communications, cited in R. D. Mumby [2].
160. Andrew, A.M., *Level Set Methods And Fast Marching Methods: Evolving Interfaces In Computational Geometry, Fluid Mechanics, Computer Vision, And Materials Science, by J.A. Sethian, Cambridge University Press, Cambridge, UK, 2nd edn. 1999 (first published 1996 as Level Set Methods) xviii + 420 pp., ISBN (paperback) 0-521-64557-3, (hardback) 0-521-64204-3 (Pbk, £18.95).* Robotica, 1996. **18**(1): p. 89-92.
161. MATLAB R2018b Documentation, h.u.m.c.h.m., 2018.
162. Taubin, G. *A signal processing approach to fair surface design*. in *Proceedings of the 22nd annual conference on Computer graphics and interactive techniques*. 1995. ACM.
163. Zill, D., W.S. Wright, and M.R. Cullen, *Advanced engineering mathematics*. 2011: Jones & Bartlett Learning.
164. Cignoni, P., M. Callieri, M. Corsini, M. Dellepiane, F. Ganovelli, and G. Ranzuglia. *Meshlab: an open-source mesh processing tool*. in *Eurographics Italian chapter conference*. 2008.
165. Corporation, D.S.S., 2002-2019.
166. Kroon, D., *The Mathworks File Exchange, Surface Mesh Voxelisation, Matlab .m File.* 2016.
167. Li, Q., W. Jin, and Z. Huang, *Laminar flame characteristics of C1–C5 primary alcohol-isooctane blends at elevated temperature.* Energies, 2016. **9**(7): p. 511.
168. Bradley, D., M. Lawes, and R. Mumby. *Cellular Flame Instabilities*. in *Proceedings of the Eighth International Seminar on Fire and Explosion Hazards (ISFEH8)*. 2017. USTC Press.
169. Taylor, S.C., *Burning velocity and the influence of flame stretch*. 1991, University of Leeds.
170. Bradley, D. and F.-K. Lung, *Spark ignition and the early stages of turbulent flame propagation.* Combustion and Flame, 1987. **69**(1): p. 71-93.
171. Bradley, D., M. Lawes, K. Liu, S. Verhelst, and R. Woolley, *Laminar burning velocities of lean hydrogen–air mixtures at pressures up to 1.0 MPa.* Combustion and Flame, 2007. **149**(1): p. 162-172.
172. Bradley, D., Shehata, M., Lawes, M., & Pervez Ahmed, *Flame Extinctions: Critical Stretch Rates and Sizes.* Submitted to Journal of Combustion and Flame journal (CNF-D-19-00657), 2019.
173. Wu, F. and C.K. Law, *An experimental and mechanistic study on the laminar flame speed, Markstein length and flame chemistry of the butanol isomers.* Combustion and Flame, 2013. **160**(12): p. 2744-2756.
174. Sarathy, S.M., S. Vranckx, K. Yasunaga, M. Mehl, P. Oßwald, W.K. Metcalfe, C.K. Westbrook, W.J. Pitz, K. Kohse-Höinghaus, and R.X. Fernandes, *A comprehensive chemical kinetic combustion model for the four butanol isomers.* combustion and flame, 2012. **159**(6): p. 2028-2055.
175. Westbrook, C.K., W.J. Pitz, P.R. Westmoreland, F.L. Dryer, M. Chaos, P. Oßwald, K. Kohse-Höinghaus, T.A. Cool, J. Wang, and B. Yang, *A*

*detailed chemical kinetic reaction mechanism for oxidation of four small alkyl esters in laminar premixed flames.* Proceedings of the combustion institute, 2009. **32**(1): p. 221-228.
176. CHEMKIN 10131, R.d.S.D., 2013.
177. Verhelst, S., R. Woolley, M. Lawes, and R. Sierens, *Laminar and unstable burning velocities and Markstein lengths of hydrogen–air mixtures at engine-like conditions.* Proceedings of the Combustion Institute, 2005. **30**(1): p. 209-216.
178. Bradley, D., P. Gaskell, and X. Gu. *The modeling of aerodynamic strain rate and flame curvature effects in premixed turbulent combustion*. in *Symposium (International) on Combustion*. 1998. Elsevier.
179. Bradley, D., C. Sheppart, R. Woolley, D. Greenhalgh, and R. Lockett, *The development and structure of flame instabilities and cellularity at low Markstein numbers in explosions.* Combustion and flame, 2000. **122**(1-2): p. 195-209.
180. Groff, E.G., *The cellular nature of confined spherical propane-air flames.* Combustion and Flame, 1982. **48**: p. 51-62.
181. Yang, S., A. Saha, F. Wu, and C.K. Law, *Morphology and self-acceleration of expanding laminar flames with flame-front cellular instabilities.* Combustion and Flame, 2016. **171**: p. 112-118.
182. Bradley, D., S.E.-D. Habik, and S. El-Sherif, *A generalization of laminar burning velocities and volumetric heat release rates.* Combustion and Flame, 1991. **87**(3-4): p. 336-345.
183. Palacios, A. and D. Bradley, *Generalised correlations of blow-off and flame quenching for sub-sonic and choked jet flames.* Combust. Flame, 2017. **185**: p. 309-318.
184. Al-Shahrany, A., D. Bradley, M. Lawes, K. Liu, and R. Woolley, *Darrieus–Landau and thermo-acoustic instabilities in closed vessel explosions.* Combustion science and technology, 2006. **178**(10-11): p. 1771-1802.
185. Wabel, T.M., A.W. Skiba, and J.F. Driscoll, *Turbulent burning velocity measurements: Extended to extreme levels of turbulence.* Proceedings of the Combustion Institute, 2017. **36**(2): p. 1801-1808.
186. Shepherd, I.G. and R.K. Cheng, *The burning rate of premixed flames in moderate and intense turbulence.* Combustion and Flame, 2001. **127**(3): p. 2066-2075.
187. Mandilas, C., M.P. Ormsby, C.G.W. Sheppard, and R. Woolley, *Effects of hydrogen addition on laminar and turbulent premixed methane and iso-octane–air flames.* Proceedings of the Combustion Institute, 2007. **31**(1): p. 1443-1450.
188. Kitagawa, T., T. Nakahara, K. Maruyama, K. Kado, A. Hayakawa, and S. Kobayashi, *Turbulent burning velocity of hydrogen–air premixed propagating flames at elevated pressures.* International Journal of Hydrogen Energy, 2008. **33**(20): p. 5842-5849.
189. Hicks, R., M. Lawes, C. Sheppard, and B. Whitaker, *Multiple laser sheet imaging investigation of turbulent flame structure in a spark ignition engine.* SAE transactions, 1994: p. 1463-1482.
190. Zhang, M., J. Wang, W. Jin, Z. Huang, H. Kobayashi, and L. Ma, *Estimation of 3D flame surface density and global fuel consumption*

*rate from 2D PLIF images of turbulent premixed flame.* Combustion and Flame, 2015. **162**(5): p. 2087-2097.

191. Hawkes, E.R. and J.H. Chen, *Comparison of direct numerical simulation of lean premixed methane–air flames with strained laminar flame calculations.* Combustion and Flame, 2006. **144**(1-2): p. 112-125.
192. Nivarti, G., R.S. Cant, and S. Hochgreb, *Reconciling turbulent burning velocity with flame surface area in small-scale turbulence.* Journal of Fluid Mechanics, 2019. **858**.
193. Bradley, D., P. Gaskell, and X. Gu, *The mathematical modeling of liftoff and blowoff of turbulent non-premixed methane jet flames at high strain rates.* Symp. (Int.) Combust., 1998. **27**(1): p. 1199-1206.

# Appendix A

This section presents graphs of $u_l$, $Ma_{sr}$ for $CH_4$ and $C_3H_8$ carried out during the course of the PhD work.

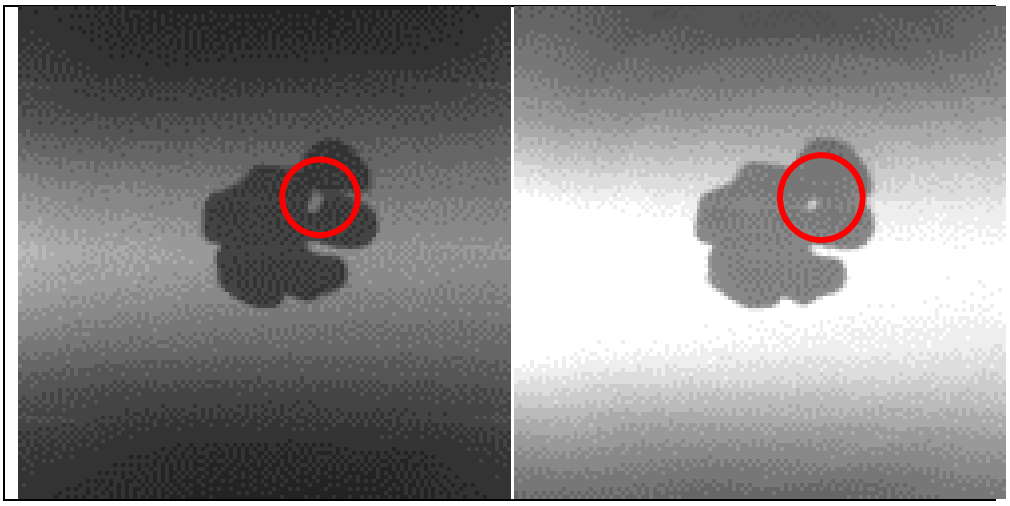

**Figure A.1** Enlarged views of frames 7 and 8 presented in Fig. 4.33.

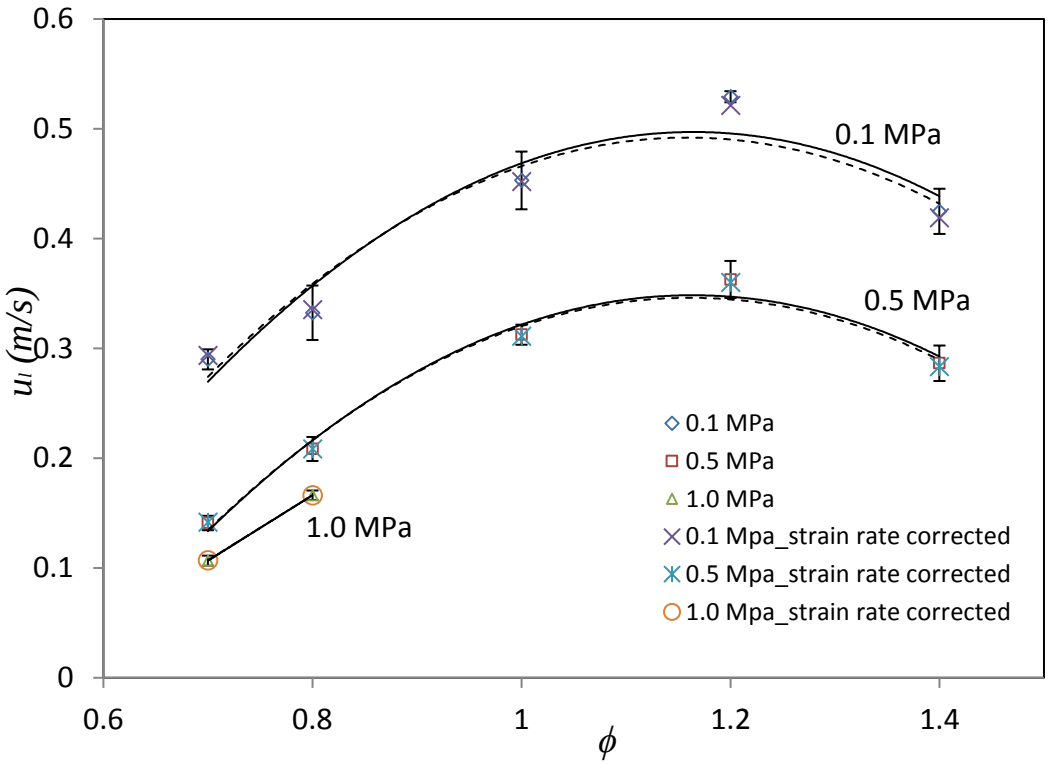


**Figure A.2** Comparison of $u_l$ values from the present work with and without strain rate corrections for $n$-butanol/air mixtures at 360 K. Dashed lines are the $u_l$ values with strain rate corrections.

Figure A.2 compares the values of $u_l$ for $n$-butanol/air mixtures These were measured at 0.5 MPa and 360 K. The solid line shows the best fit through the ul values obtained using Eq. (1.13) and the broken line shows the best fit through the data obtaing using Eq. (1.16) that includes the strain rate corrections discussed in Section 1.3.2. No significant difference was observed between the two methods.

The values of $u_l$ reported in [101] for $CH_4$ /air mixtures at $\phi$ = 1.25 and 1.35 at high pressures and temperatures were simply estimated. No data was found from literature at these conditions until the time of wrirting. Since the values of $u_l$ reported at $\phi$ = 1.25 and 1.35 at 0.5 MPa and 360 K are scare, the present author conducted experimental measurements to obtain them. These were subsequently compared with the data from previous sources.

The values of $S_s$ are found from the $S_n/\alpha$ curves shown in Fig. A. 4. The values of $u_l$ for the $CH_4$ /air mixtures at $\phi$ = 1.25 and 1.35 are obtained from the measured $S_s$ from Fig. A.4 and using Eq.(1.13). These are compared with the data from previous work, shown in Fig. A. 5. These are also compared in Table A.1. A good agrement is found with the experimental data from the previous sources and therefore the present measured $u_l$ values are used in the present study.

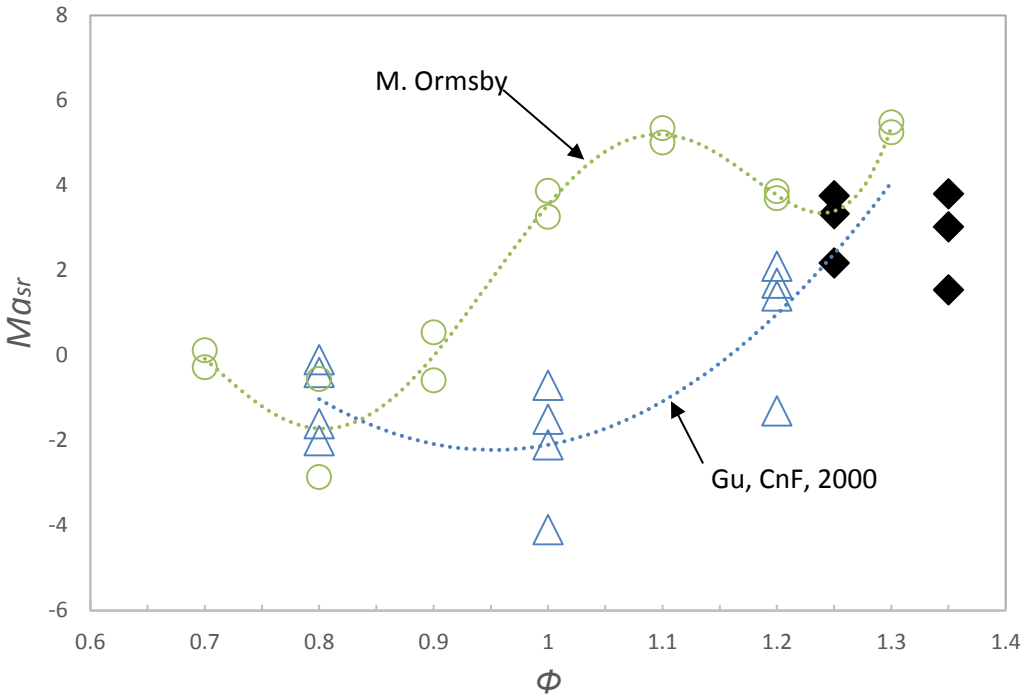


**Figure A.3** $Ma_{sr}$ against $\Phi$ for $CH_4$/air at 0.5 MPa, ~360 K.

Values of $Ma_{sr}$ for $CH_4$/air is found to be inconsistent from the previous data reported. Bradley et al. [101] reported values of 5 and 6 at 0.5 MPa, 365K for $\phi$ =1.25 and 1.35 respectively. However, in a different study they [23] reported values varying between -1.3 and 2.1 at $\phi$ =1.2 for the same mixtures at same pressures and high temperatures. These from different sources are compared along with the measurements carried out during the present work in Fig. A.3. Whilst there is much uncertainty in values of $Ma_{sr}$ for $CH_4$, at high pressures between $\phi$ =0.7 and 1.2, the present author is convinced of the $Ma_{sr}$ values at richest mixtures $\phi$ = 1.25 and 1.35 are close in proximity from all the sources and therefore the ones reported in [101] are used.

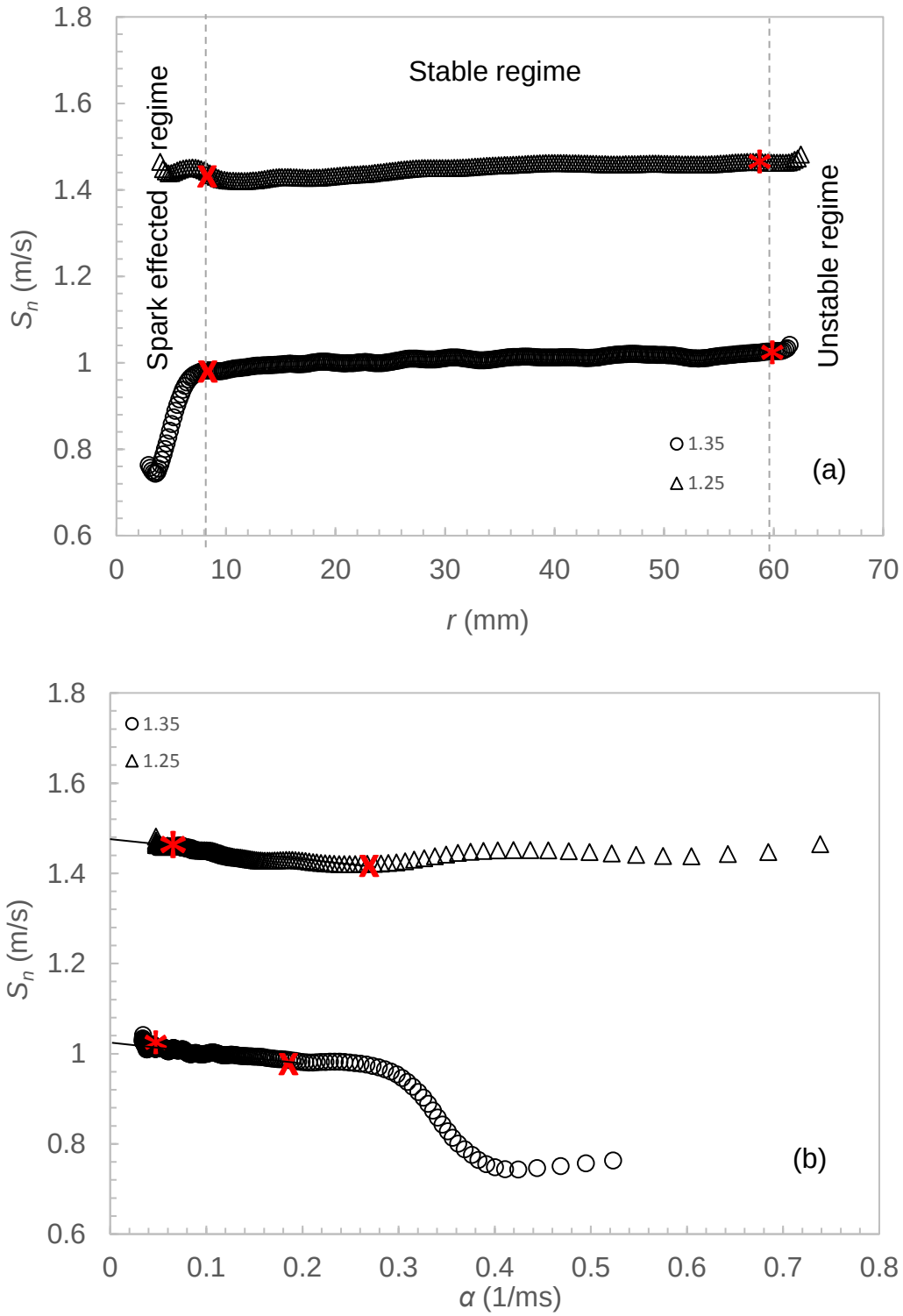


**Figure A.4** Variation of (a) $S_n$ with radius (b) $S_n$ with $\alpha$ for $CH_4$/air at 365K and 0.5MPa.

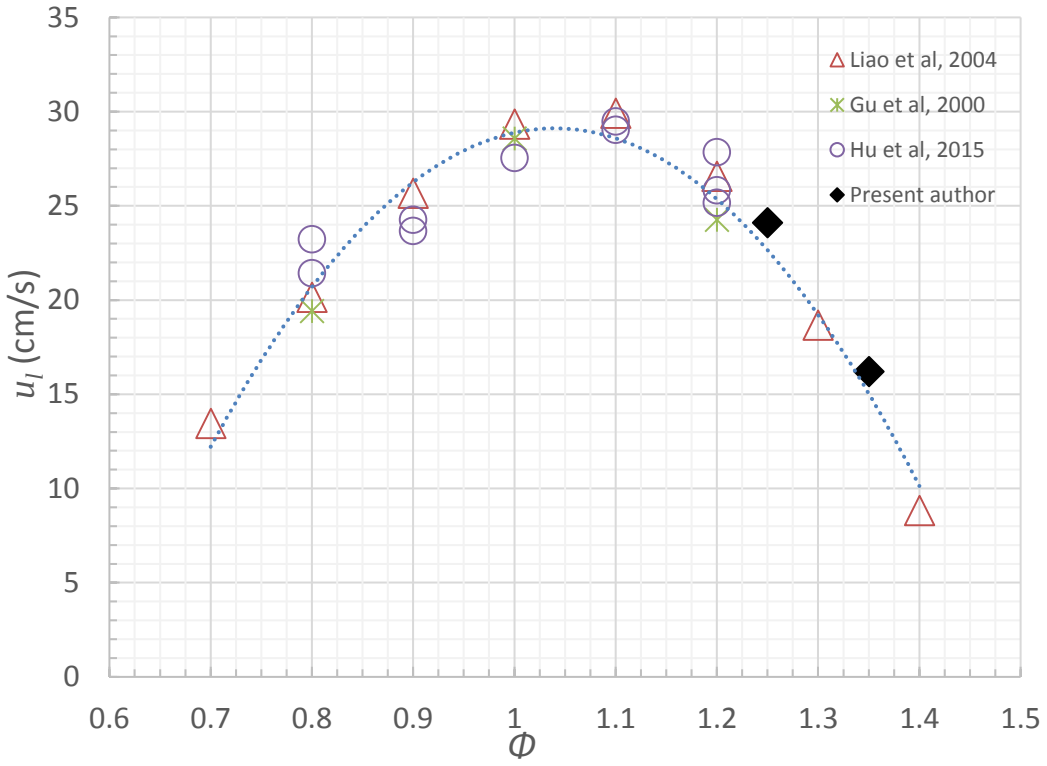


**Figure A.5** Variation of $u_l$ with $\phi$ for $CH_4$/air at 0.5MPa, 365-373K.

**Table A.1** $u_l$ values of $CH_4$/air at 365K

| Φ | P (MPa) | $u_l$ (m/s) Bradley, 2007 | $u_l$ (m/s) Konnov, 20187 | Present work $u_l$ (m/s) |
|---|---|---|---|---|
| 0.6 | 0.1 | 0.189 | | 0.128 |
| 1.25 | 0.5 | 0.18* | 0.23 | 0.241 |
| 1.35 | 0.5 | 0.095* | 0.15 | 0.162 |

*estimated value, presented in Bradley et al. [101].

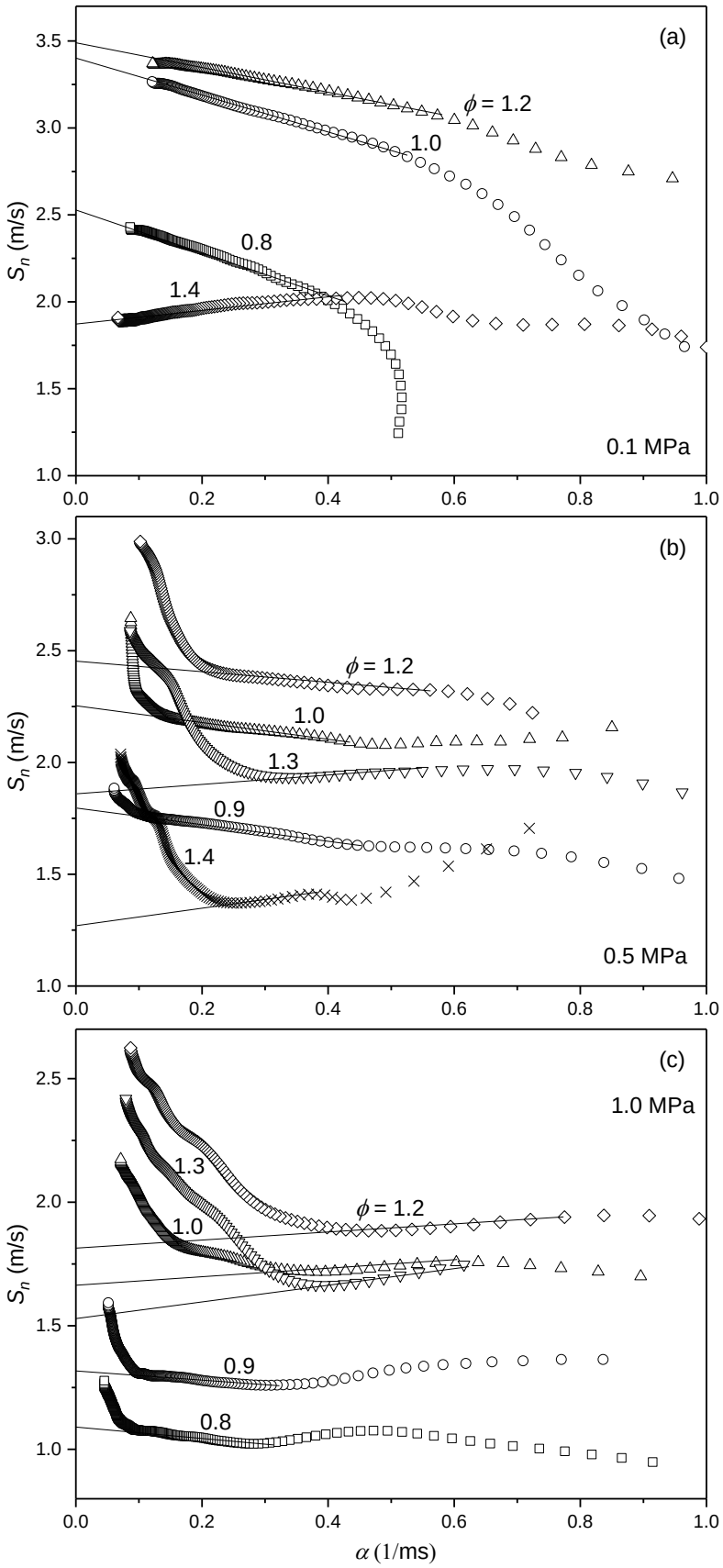


**Figure A.6** Variation of $S_n$ with $\alpha$ for $C_3H_8$/air at 365K and 0.1, 0.5, 1.0 MPa.

## Calculations to determine number of sheets in a sweep

Imaging laser, IL, frequency = 54 kHz

Rotating mirror, RM, frequency = 12 Hz

No. of faces on RM = 16

Time between two consecutive laser sheet = $\frac{1}{54000}$ = 0.0185185 ms

Time for each sweep = $\frac{1}{12*16}$ =5.208 ms

Therefore, the number of sheets in a sweep = $\frac{1.44}{0.0185185}$ =77.7 ~ 78.

# Appendix B

# Data Processing Algorithms in MATLAB

This section presents some of the developed algorithms in MATLAB by the present author and also those developed by others that are used for data processing during the course of the PhD work.

## B.1 Turbulent Mass Burning Rate, $u_{tm}$, Code

---

```
%Code developed by the present author, P. Ahmed, to determine the
%turbulent burning velocities, utm, from pressure %records using the
%equations presented in the appendix of [10]. The code reads the .lvm
%file recorded by the pressure %transducer, smooths the data before
%applying the equations.
clear all
close all
clc
P_D=lvm_import('3.lvm'); % read the data from .lvm file, here P_D
refers presssure data
yk=zeros(25000,2); % assigns a 2 column matrix of 25000; 25000 is
the sampling data of the pressure transducer
yk(:,1)=P_D.Segment1.data(:,1);
x =yk(:,1);
yk(:,2)=P_D.Segment1.data(:,2);
A=sgolayfilt(yk(:,2),1,17); %Uses a Savitzky-Golay filter using 17
data points
B=sgolayfilt(A,1,17);% uses a Savitzky-Golay filter again for
second smoothing
YY = B(1:20:end); % saves every 10th element in B
XX= x(1:20:end); % saves every 10th element in C
plot(P_D.Segment1.data(:,1),P_D.Segment1.data(:,2));
plot(P_D.Segment1.data(:,1),P_D.Segment1.data(:,2));
hold on
scatter(XX,YY,'x')
hold on
xlabel('time (s)', 'FontSize', 12, 'FontName', 'arial')
ylabel('Pressure (bar)', 'FontSize', 12, 'FontName', 'arial')
[row_YY col_YY]=max(YY);
P=YY(1:col_YY);% variable pressure recorded during the explosion
t=XX(1:col_YY);% time at every corresponding P recorded
P0=P(1); % initial pressure
R = 190; % spherical bomb radius in mm based on its measured volume
Y_u = 1.396;
Pf=max(YY);
r_m=R.*((1-((P0./P).^(1./Y_u)).*((Pf-P)./(Pf-P0))).^(1./3)); %falme
radius rm is in mm
r_m=real(r_m(2:numel(r_m)));
dP=ones(numel(P)-1,1);
```

```
dt=zeros(numel(P)-1,1);
for i=1:numel(P)-1
    dP(i,1) = P(i+1,1)-P(i,1);
    dt(i,1) = t(i+1)-t(i);
    i=i+1;
end
P=P(2:numel(P));
u_tm = ((R./1000).*((P0./P).^(1./Y_u)).*(dP./dt))./(3.*(Pf-P0)*(1-
((P0./P).^(1./Y_u)).*((Pf-P)./(Pf-P0))).^(2./3)); % turbulent
burning velocity based on equation A10 in appendix of Cnf2011
ethanol correlation paper.
figure,plot(r_m,u_tm)
xlabel('r_m (mm)', 'FontName', 'arial', 'FontSize', 12)
ylabel('u_t_m (m/s)', 'FontName', 'arial', 'FontSize', 12)
ylim([0 5])
BB=sgolayfilt(u_tm,1,17);
hold on
plot(r_m,BB)
CC=real(sgolayfilt(BB,1,17));
hold on
plot(r_m,CC)
[row1, col1] = find(r_m>29 & r_m<31);
utm_30=mean(CC(row1))% finds the average mean utm, for at 30 mm
[row1, col1] = find(r_m>39 & r_m<41);
utm_40=mean(CC(row1))% finds the average mean utm, for at 40 mm
out(:,1)=real(r_m);
out(:,2)=real(u_tm);
out(:,4)=real(r_m);
out(:,5)=real(BB);
out(:,7)=real(r_m);
out(:,8)=real(CC);
```

---

## B.2 Total flame surface area and volume code

---

```
% Code to import smoothed STL file representing a smoothed flame %and
then calculate the flame surface area and volume. The former %is
achieved using the cross-product of vertex locations to obtain %the
surface area of individual surface triangle "patches", the %latter
voxleises the smoothed  flame then sums the volume of each %voxel
contained within the original flame surface.
clear all
close all
clc
% Set figure properties (axes labels, viewing angle etc.)
axis equal
view(33, 15)
axis([10 640 10 512 10 512])
xlabel('X', 'FontSize', 12, 'FontName', 'arial')
ylabel('Y', 'FontSize', 12, 'FontName', 'arial')
zlabel('Z', 'FontSize', 12, 'FontName', 'arial')
lightangle(-15,30);
lighting gouraud
hcap.AmbientStrength = 0.6;
hiso.SpecularColorReflectance = 0;
hiso.SpecularExponent = 50;
% Import processed STL file
FV=stlread('smoothed_flame_perfect.stl');
```

```
Z = patch(FV, 'facecolor', 'r', 'edgecolor', 'none');
%alpha(0.1)% makes it light
% Calculate and display surface area
verts = get(Z, 'Vertices');
faces = get(Z, 'Faces');
a = verts(faces(:, 2), :)*0.1961 - verts(faces(:, 1), :)*0.1961;
b = verts(faces(:, 3), :)*0.1961 - verts(faces(:, 1), :)*0.1961;
c = cross(a, b, 2);%considers a and b as two vectors and gives the
cross product along rows, for cross(a,b,1) gives the cross product
along columns%
area = (1/2 * sum(sqrt(sum(c.^2, 2))))/100;
radius = sqrt(area/(4*pi));
fprintf('\nThe surface area is (cm2)%f\n\n', area);
fprintf('\nThe value of radius is %f\n\n', radius);
% Voxelise the imported reconstruction
voxel = polygon2voxel(FV, 640, 'none', true);
for i = 1: 640
    A = voxel(:, :, i);
    A = imfill(A, 'holes');
    B(:, :, i) = A(:, :);
end
pix_size=[0.182660081
0.182702086:4.2005E-05:0.209501185];
Array_Sum = (0.1961*0.1961*0.1961*(sum(sum(sum(B)))))/1000; %sums
values in x y and z
fprintf('\nThe flame volume is (cm3)%f\n\n', Array_Sum);
% Calculate the equivalent spherical flame radius from the volume
and % use this to calculate the value of a
eqradius = (Array_Sum./(4*pi/3))^(1/3);
eqarea_a = (4*pi*(eqradius.^2));
fprintf('\nThe value of equivalent area is %f\n\n', eqarea_a);
fprintf('\nThe value of equivalent radius is %f\n\n', eqradius);
Aa = area./eqarea_a;
fprintf('\nA/a =  %f\n\n', Aa);
Tot_vol=0;
for i = 1:640
    slice(i) =
((sum(sum(B(i,:,:))))*pix_size(i)*pix_size(i)*pix_size(i))/1000;%su
ms values in y and z
    Tot_vol=Tot_vol+slice(i);
end
fprintf('\nThe new flame volume is (cm3)%f\n\n', Tot_vol);
new_eqradius = (Tot_vol./(4*pi/3))^(1/3);
new_eqarea_a = (4*pi*(new_eqradius.^2));
fprintf('\nThe value of new equivalent area is %f\n\n',
new_eqarea_a);
fprintf('\nThe value of new equivalent radius is %f\n\n',
new_eqradius);
```

---

## B.3 Flame edge detector code

---

```
% A code to read in a sequence of images in a folder and trace the
%flame edge, if present. This process returns a black flame on a
%white background.
clear all
close all
clc
```

```
% Import a sequence of images and process:
tifFiles = dir('*.tif');
numfiles = length(tifFiles);
mydata = cell(1, numfiles);
mkdir('2');
for k = 1:numfiles
  mydata{k}= imread(tifFiles(k).name);
  A = mydata{k};
  A = A(:, :, 1);
  A = A(:, :);
  AB = edge(A, 'log');
  AC = imfill(AB, 'holes');
  filename = sprintf('Testp%d.tif', k);
  fullFileName = fullfile('2', filename);
  imwrite(AC, fullFileName);
end
disp('Finished');

for k = 1:numfiles
  tic
    mydata{k}= imread(tifFiles(k).name);
  A = mydata{k};
  AB = edge(A, 'log');
  AC = imfill(AB, 'holes');
  AC = bwareafilt(AC, 1);
  AC = imcomplement(AC);
  filename = sprintf('Testp%d.tif', k);
  imwrite(AC, filename);
  toc
end
mkdir('3');
for k = 1:numfiles
  mydata{k} = imread(tifFiles(k).name);
  A = mydata{k};
  AB = imbinarize(A, 'adaptive');
  filename = sprintf('Testp%d.tif', k);
  fullFileName = fullfile('3', filename);
  imwrite(AB, fullFileName);
end
disp('Finished');
```

---

## B.4 Flame sheet assembly code

---

```
%This code was initially developed by Ben Thorne [155]. It was later
%modified and made more efficient by the present author, P. Ahmed.
%This code reads in a number of processed binary flame images for
%wrinkled/slightly broken flames. It then calculates the angles
%between the sheets and the mirror offset and uses this to generate
%a 3D binary matrix. The user specifies the first and last image
%numbers. The user% must change the Current Folder in Matlab to that
%containing the images to be used. Images must be named as "TestX"
%where X is the image number. The previous version of this code
%generated a z = mi + c equation for each sheet and used this to
%change the values of cells in a pre-allocated matrix according o the
%values of the cells in the matrix representing the current image.
%This approach led to incorrect separation between the sheets. This
%code uses an alternative, geometric, approach. DOI: 16.06.2016
```

```
clear all
close all
clc

middlesheet = input('Enter number of middle sheet wrt the bomb');
firstnum = input('Enter number of first image in the sequence');
lastnum = input('Enter number of the last image in the sequence');
 disp('------------------------------------------------------------')
a = 640;
A = ones(a,a,a);
for b = firstnum:lastnum
    % Calculate the angle between successive sheets
    sheetnum = 0-(middlesheet-b);
    omega = (1/laserfqcy)*(motorfqcy/8)*2*pi; % radians angle
between succesive sheets based on mirror fqcy
    sheetangle = (1.92*sheetnum*omega)
    AB = sprintf('Testp%d.tif', b);
    AB = imread(AB);
  for i = 1:resh
    for j = 1: resw
        zd = mirrorwidth/2;
        w = sheetangle/2;
        offset =
(2*zd*tan(w/2)*sin(w/2))/(sin((((45*(pi/180))+(w/2)))))/pixelsize;
        dista = ((498/pixelsize)-(resw/2)) + j;
        opp = dista*tan(sheetangle);
        k = round((opp+(longres/2))+offset);
        A(i, j, k) = AB(i,j);
end
end
end
worldsize = 640;
for h = 1:640
    imagename = sprintf('Sliced_recon%d.tif', h)
    A = imread(imagename);
    A = imcomplement(A);
    SE = strel('disk', 7);
    A = imdilate(A, SE);
    A = imcomplement(A);
    filename = sprintf('Sliced_filled%d.tif', h);
    imwrite(A, filename);
end
AP = ones(640,640,640);
for i = 1:640
    A = sprintf('Sliced_filled%d.tif', i);
    A = imread(A);
    AP(:, :, i)=A(:, :, 1);
end
fv=isosurface(AP,.5);
stlwrite('Unsmoothed_flame.stl', fv);
```

---

## B.5 polygon to voxel, Kroon D

---

```
function Volume=polygon2voxel(FV,VolumeSize,mode,Yxz)
```

```
% This function POLYGON2VOXEL will convert a Triangulated Mesh into
%a  Voxel  Volume  which  will  contain  the  discretized  mesh.
%Discretization of a polygon is done by splitting/refining the face,
%until the longest edge is smaller than 0.5 voxels. Followed by
%setting the voxel beneath the vertice coordinates of that small
%triangle to one. Function is written by D.Kroon University of %Twente
(May 2009)
 if(nargin<4), Yxz=true; end
% Check VolumeSize size
if(length(VolumeSize)==1)
    VolumeSize=[VolumeSize VolumeSize VolumeSize];
end
if(length(VolumeSize)~=3)
    error('polygon2voxel:inputs','VolumeSize must be a array of 3
elements ')
end
% Volume Size must always be an integer value
VolumeSize=round(VolumeSize);
sizev=size(FV.vertices);
% Check size of vertice array
if((sizev(2)~=3)||(length(sizev)~=2))
    error('polygon2voxel:inputs','The vertice list is not a m x 3
array')
end
sizef=size(FV.faces);
% Check size of vertice array
if((sizef(2)~=3)||(length(sizef)~=2))
    error('polygon2voxel:inputs','The vertice list is not a m x 3
array')
end

% Check if vertice indices exist
if(max(FV.faces(:))>size(FV.vertices,1))
    error('polygon2voxel:inputs','The face list contains an
undefined vertex index')
end
% Check if vertice indices exist
if(min(FV.faces(:))<1)
    error('polygon2voxel:inputs','The face list contains an vertex
index smaller then 1')
end
% Matlab dimension convention YXZ
if(Yxz)
    FV.vertices=FV.vertices(:,[2 1 3]);
end
switch(lower(mode(1:2)))
case {'au'} % auto
% Make all vertices-coordinates positive
    FV.vertices=FV.vertices-min(FV.vertices(:));
    scaling=min((VolumeSize-1)./(max(FV.vertices(:))));
    % Make the vertices-coordinates to range from 0 to 100
    FV.vertices=FV.vertices*scaling+1;
    Wrap=0;
case {'ce'} % center
% Center the vertices
FV.vertices=FV.vertices+repmat((VolumeSize/2),size(FV.vertices,1),1
);
    Wrap=0;
case {'wr'} %wrap
    Wrap=1;
```

```
case{'cl'} % clamp
    Wrap=2;
otherwise
    Wrap=0;
end
% Separate the columns;
FacesA=double(FV.faces(:,1));
FacesB=double(FV.faces(:,2));
FacesC=double(FV.faces(:,3));
VerticesX=double(FV.vertices(:,1));
VerticesY=double(FV.vertices(:,2));
VerticesZ=double(FV.vertices(:,3));
% Volume size to double
VolumeSize=double(VolumeSize);
% Call the mex function
Volume=polygon2voxel_double(FacesA,FacesB,FacesC,VerticesX,Vertices
Y,VerticesZ,VolumeSize,Wrap);
```

---

## B.6 Mean flame area based on volume and mass balancing

---

```
% The present code gives the mean radius of a 3D flame from unburned
%andburned gas mixture balancing with respect to Rj based on volume
%as well as mass. It caluclates the centroid of the flame, convert
%the Cartesian coordinates to polar coordinates and then finds the
%tip radius Rt and the root radius Rr. It then iterates from Rj=Rr
%till Rj=Rt to find the burned and unburned gas mixtures outside and
%inside Rj respectively until it finds the radius Rj=Rmean at which
%the volumes and masses becomes equal(both separately)
clear all
close all
clc
% Construct a 3D cube matrix of size 640 voxels with re-sliced and
filled flame images
A = ones(640,640,640); % creates a 3D matrix with 640 side and
filled with ones
% The loop reads all the sliced-filled 2D Mie-scattered images to
% reconstruct the flame based on black (burned) and white pixels
(unburned)
for z = 1:640
Ai = sprintf('Sliced_filled%d.tif', z);
Ai = imread(Ai);
Ai = Ai(:, :, 1);
Ai = Ai(:, :);
% Imported images have cell values of zero where black and
% 255 where white. This part of the code changes white = 255 to 1
for i=1:640
      for j=1:640
            if Ai(i,j)==255
               Ai(i,j)=1;
            else
            end
      end
    end
    A(:, :, z) = Ai;
     end
```

```
%Finds the position of the flame (black pixels) and stores them in
a 3
%column matrix
[row, col, page] = ind2sub(size(A), find(A == 0));
Y = [row, col, page];
% Extracts each column from the above matrix and stores
individually in a
% single column matrix
xY = Y(:,1);
yY = Y(:,2);
zY = Y(:,3);
% calculates the centroid of the flame by calculating the mean in
each
% direction
mxY = round(mean(xY));
myY = round(mean(yY));
mzY = round(mean(zY));
disp('The centroid is located at:')% displays the centroid of the
reconstructed flame
[mxY, myY, mzY]
% Converts cartesian cordinates to polar cordinates of complete
flame
% voxels
xYRtC = xY-mxY;
yYRtC = yY-myY;
zYRtC = zY-mzY;
[TY, RY, ZY] = cart2pol(xYRtC, yYRtC, zYRtC);
HYP = [((RY.^2)+(ZY.^2)).^0.5]; % calculate the hypotenuse
HYPR = round(HYP, 2); % rounds off the above calculated hypoteneuse
to 2 decimal places
HYPR_sorted = sort(HYPR, 'ascend'); % sorts in ascending order
[Rpt_burned HYPR_burned] = hist(HYPR_sorted, unique(HYPR_sorted));
% histogram of HYPOTENUSE of burned voxels
Rpt_burned = Rpt_burned'; % transpose the matrix
% loads a variable containing all the hypotenuse and radii values
for a completely blackened flame occupied 3D cube matrix
load('3DRPV1.mat');
HYPRU = unique(ans); % unburned hypotenuse for all voxels in the
empty cube
Rpt_U=BZ;% repetition of hypotenuse for all voxels in the empty
cubeto extract the surface of the flame and store the surface
voxels in surface_Y
surface_Y=zeros(1500000,3);
RR=zeros(1500000,1);
p=1;
for i = 1:length(Y)
        sumneigh =
A(Y(i,1),Y(i,2)+1,Y(i,3))+A(Y(i,1),Y(i,2),Y(i,3)-
1)+A(Y(i,1)+1,Y(i,2),Y(i,3))+A(Y(i,1),Y(i,2),Y(i,3)+1)+A(Y(i,1)-
1,Y(i,2),Y(i,3))+A(Y(i,1),Y(i,2)-1,Y(i,3));
        if sumneigh ~= 0
            surface_Y(p,:,:) = [Y(i,1),Y(i,2),Y(i,3)];
            RR(p,1)=sqrt((mxY-surface_Y(p,1)).^2+(myY-
surface_Y(p,2)).^2+(mzY-surface_Y(p,3)).^2);
            p=p+1;
        end
end

surface_Y = surface_Y(any(surface_Y,2),:); % removes the extra zero
trailing rows in surface_Y
```

```
RR = RR(any(RR,2),:); % removes the extra zero trailing rows in RR
R_t_verify=max(RR)*0.1961;
R_r_verify=min(RR(RR>0))*0.1961;
R_j_verify=(R_t_verify+R_r_verify)/2
xY_surface_Y = surface_Y(:,1);
yY_surface_Y = surface_Y(:,2); % extract cartesian surface voxels
i, j, k individually in a single column array
zY_surface_Y = surface_Y(:,3);
xY_surface_Y_wRtmxY = xY_surface_Y-mxY;
yY_surface_Y_wRtmyY = yY_surface_Y-myY; % convert x, y, z of
surface voxels with respect to (wRt) centroid (mxY, myY, mzY)
zY_surface_Y_wRtmzY = zY_surface_Y-mzY;
[T_surface_Y, R_surface_Y, Z_surface_Y] =
cart2pol(xY_surface_Y_wRtmxY, yY_surface_Y_wRtmyY,
zY_surface_Y_wRtmzY); % convert cartesian surface voxels to polar
surface voxels
HYP_surface_Y = [((R_surface_Y.^2)+(Z_surface_Y.^2)).^0.5]; %
calculate hypotenuse of surface voxels
HYPR_surface_Y = round(HYP_surface_Y, 2); % rounded to 2 decimals
R_t = max(HYPR_surface_Y);
R_r = min(HYPR_surface_Y(HYPR_surface_Y>0));
R_j_1 = (R_t+R_r)/2 * 0.1961
R_j = (R_t+R_r)/2
n=1;
for R_ji=R_r:0.1:R_t
    [row_b_out col_b_out]=find(HYPR_burned>=R_ji &
HYPR_burned<=R_t);
    sum_burned_out(n,1)=sum(Rpt_burned(row_b_out));% sum of all
burned voxels b/w Rj and Rt
    [row_b_in col_b_in]=find(HYPR_burned>=R_r & HYPR_burned<=R_ji);
    sum_burned_in=sum(Rpt_burned(row_b_in));% sum of all burned
voxels b/w Rr and Rj
    [row_U_in col_U_in]=find(HYPRU>=R_r & HYPRU<=R_ji);
    Total_sum_Unburned_in=sum(Rpt_U(row_U_in));% calculated from
empty cube encludes all the voxels b/w Rr and Rj
    sum_Unburned_in(n,1) = Total_sum_Unburned_in - sum_burned_in; %
sum of all the voxels uburned inside Rj
 Rji(n,1)=R_ji;
 n=n+1;
 end
 Diff = abs(sum_Unburned_in - sum_burned_out);
 min_Diff = min(Diff);
 [row_mean col_mean]=min(Diff);
 R_mean = Rji(col_mean)*0.1961;
 Sum_volume_mean=sum_Unburned_in(col_mean);
 fprintf('\nThe value of mean radius based on volume balance in mm
is %.2f\n', double(R_mean));
 plot((Rji*0.196), (sum_burned_out*0.1961*0.1961*0.1961), '--')
 xlabel('mean radius (mm)', 'FontName', 'arial', 'FontSize', 12)
 ylabel('Volume (mm^3)', 'FontName', 'arial', 'FontSize', 12)
 hold on
 plot((Rji*0.196), (sum_Unburned_in*0.1961*0.1961*0.1961))
  %text(35,3e5,'Unburned \rightarrow')
 legend({'Burned','Unburned'},'Location','northwest')
 hold on
 plot(R_mean,Sum_volume_mean*0.1961*0.1961*0.1961,'r*')
 rho_b = 0.1512;
 rho_u = 1.0951;
 Diff_mass = abs((sum_Unburned_in*(rho_u/1e9)) -
(sum_burned_out*(rho_b/1e9)));
```

```
 min_Diff_mass = min(Diff_mass);
 [row_mean_mass col_mean_mass]=min(Diff_mass);
 R_mean_mass = Rji(col_mean_mass)*0.1961;
 Sum_volume_mean_mass=sum_Unburned_in(col_mean_mass)*(rho_u/1e9);
 fprintf('\nThe value of mean radius based on mass balance in mm is
%.2f\n', double(R_mean_mass));
 figure, plot((Rji*0.196),
(sum_burned_out*0.1961*0.1961*0.1961*(rho_b/1e9)), '--')
 xlabel('mean radius (mm)', 'FontName', 'arial', 'FontSize', 12)
 ylabel('mass (kg)', 'FontName', 'arial', 'FontSize', 12)
 hold on
 plot((Rji*0.196),
(sum_Unburned_in*0.1961*0.1961*0.1961*(rho_u/1e9)))
 legend({'Burned','Unurned'},'Location','northwest')
 hold on
 plot(R_mean_mass,Sum_volume_mean_mass*0.1961*0.1961*0.1961,'r*')
```

---

## B.7 Strain rate Markstein number

---

```
% This code calculates Markstein lengths and Markstein numbers using
%multiple regression method% The input for the code is a text file
%containing (Sn, % r), Sn in m/s and r in mm.
close all;
clear all;
clc;
fileID = fopen('3.txt','r');
formatSpec = '%f %f';
sizeSnr = [2 Inf];
Snr = fscanf(fileID,formatSpec,sizeSnr);
Snr = Snr';
Sn = Snr(:,1);
ru = Snr(:,2);
alpha = (2.*Sn)./ru;
alpha_m = mean(alpha);
Sn_m = mean(Sn);
a = alpha-alpha_m;
b = Sn-Sn_m;
ab=a.*b;
sumab = sum(ab);
sumaa = sum(a.*a);
Lb = -1.*(sumab./sumaa);
Dl = input('\nEnter the value of laminar flame thickness, Dl = ');
Mab = Lb./Dl;
fprintf('\nThe value of burned gas Markstein number, Mab is
%f\n\n', Mab);
D_r = input('\nEnter the value of density ratio rho_u/rho_b, D_r =
');
S = 1+1.2.*((Dl./ru)*(D_r.^2.2))-0.15.*(((Dl./ru)*(D_r.^2.2)).^2);
Un = (Sn.*S)./D_r;
Un_m = mean(Un);
alpha_c = (2.*Un)./ru;
alpha_c_m = mean(alpha_c);
alpha_s = alpha-alpha_c;
alpha_s_m = mean(alpha_s);

A11 = sum((alpha_s-alpha_s_m).^2);
A22 = sum((alpha_c-alpha_c_m).^2);
```

```
A12 = sum((alpha_s-alpha_s_m).*(alpha_c-alpha_c_m));
A10 = sum((alpha_s-alpha_s_m).*(Un-Un_m));
A20 = sum((alpha_c-alpha_c_m).*(Un-Un_m));
fprintf('\nThe value of Lb is %f\n\n', Lb);
Ls = -1.*(((A10.*A22)-(A20.*A12))/((A11.*A22)-(A12.*A12)));
Lc = -1.*(((A20.*A11)-(A10.*A12))/((A11.*A22)-(A12.*A12)));
fprintf('\nThe value of Ls is %f\n\n', Ls);
fprintf('\nThe value of Lc is %f\n\n', Lc);
Lsr = (1/(D_r-1)).*(Lb-Ls);
Lcr = (1/(D_r-1)).*(Lb-Lc);
fprintf('\nThe value of Lsr is %f\n\n', Lsr);
fprintf('\nThe value of Lcr is %f\n\n', Lcr);
Masr = Lsr./Dl;
Macr = Lcr./Dl;
fprintf('\nThe value of strain rate Markstein number, Masr is
%f\n\n', Masr);
fprintf('\nThe value of curvature Markstein number, Macr is
%f\n\n', Macr);
```

---